



**Merkel Cell Carcinoma:  
Investigations on its carcinogenesis and new therapeutic  
approaches**

\*\*\*\*\*

**Merkelzellkarzinom:  
Untersuchungen zur Karzinogenese und neue Therapieansätze**

Doctoral thesis for a doctoral degree  
at the Graduate School of Life Sciences,  
Julius-Maximilians-Universität Würzburg,  
Section Biomedicine

submitted by

**Bhavishya Sarma**

From Madurai, India

Würzburg 2021

**Submitted on:** .....

**Office stamp**

**Members of the Thesis Committee**

**Chairperson:** Prof. Dr. Manfred Gessler

**Primary Supervisor:** PD Dr. Roland Houben

**Supervisor (Second):** Prof. Dr. med. Lars Dölken

**Supervisor (Third):** PD Dr. Matthias Becker

**Supervisor (Fourth):** Dr. David Schrama

**Date of Public Defence:** .....

**Date of Receipt of Certificates:** .....

## **Table of Contents**

<b>Abstract</b> .....	1
<b>Zusammenfassung</b> .....	3
<b>1. Introduction</b> .....	5
1.1 The skin and its cell types .....	5
1.2 Merkel Cell Carcinoma.....	7
1.2.1 Two different molecular pathomechanisms in MCC development .....	7
1.2.2 The Merkel cell polyomavirus and MCC carcinogenesis .....	8
1.2.3 Proteins and pathways involved in MCC .....	11
1.2.3.1 Atonal bHLH transcription factor 1 (ATOH1) .....	12
1.2.3.2 The Hedgehog pathway .....	12
1.2.3.3 The Notch pathway.....	13
1.2.3.4 p53 .....	13
1.2.4 Histology of MCC tumors.....	14
1.2.5 Potential cells of origin of MCC.....	15
1.3 Artesunate: a versatile drug .....	19
1.3.1 Artesunate as an anti-malarial .....	19
1.3.2 Anti-viral properties of artesunate .....	20
1.3.3 Anti-cancer properties of artesunate.....	21
1.3.4 Modes of cell death induced by artesunate in cancer .....	22
1.4 Ferroptosis.....	23
1.4.1 Key antioxidant pathways in ferroptosis.....	26
1.4.2 p53 and ferroptosis .....	27
1.5 Aims and approaches of this study .....	28
1. Generation and evaluation of a vector system that allows independent regulatable expression of key factors of MCC carcinogenesis .....	28
2. Analysis of the use of artesunate as a drug for the treatment of MCC.....	28
<b>2. Materials and Methods</b> .....	29
2.1 Materials .....	29
2.1.1 Devices and equipment .....	29
2.1.2 Laboratory consumables.....	30
2.1.3 Reagents and chemicals.....	31
2.1.4 Cell culture media and supplements.....	32
2.1.5 Pre-prepared buffers and solutions.....	33
2.1.6 Freshly prepared buffers, solutions and media .....	34
2.1.7 Kits.....	36

2.1.8	Antibodies for immunoblotting.....	36
2.1.8.1	Primary antibodies.....	36
2.1.8.2	Secondary antibodies.....	37
2.1.9	Antibodies for flow cytometry.....	37
2.1.9.1	Primary antibodies.....	37
2.1.9.2	Secondary antibodies.....	38
2.1.10	Enzymes.....	38
2.1.11	Primers and oligos.....	39
2.1.11.1	Primers used for PCR and qPCR.....	39
2.1.11.2	Primers and oligos used for cloning, mutagenesis and sequencing.....	41
2.1.12	Antibiotics.....	43
2.1.13	Inducers, inhibitors and drugs.....	43
2.1.14	Mammalian cell lines and primary cells.....	43
2.1.15	Mice for <i>in vivo</i> experiments.....	45
2.1.16	Bacteria for transformation.....	45
2.1.17	Plasmids.....	46
2.1.17.1	Previously generated plasmids.....	46
2.1.17.2	Newly generated plasmids.....	47
2.1.17.3	Plasmids obtained from external sources.....	48
2.1.18	Software and online tools.....	49
2.2	Methods.....	50
2.2.1	Cell biological methods.....	50
2.2.1.1	Cell culture and handling of mammalian cells.....	50
2.2.1.1.1	Maintenance of cell cultures.....	50
2.2.1.1.2	Splitting of cells.....	50
2.2.1.1.3	Thawing cells to bring them into culture.....	51
2.2.1.1.4	Preparation of cell culture freeze downs.....	51
2.2.1.1.5	Dissociation of cells for flow cytometry.....	51
2.2.1.1.6	Trypan blue cell counting.....	51
2.2.1.2	Cell viability assays.....	52
2.2.1.2.1	Trypan blue cell viability assay.....	52
2.2.1.2.2	Cell cycle analysis.....	52
2.2.1.3	Flow cytometric staining and cell sorting.....	53
2.2.1.3.1	Staining for HLA and PD-L1.....	53
2.2.1.3.2	Staining for cell surface proteins.....	53
2.2.1.3.3	Flow cytometric cell sorting.....	54
2.2.1.4	Transformation assay.....	54

2.2.1.4.1	Lentiviral transduction of NIH3T3 cells .....	54
2.2.1.4.2	Crystal violet staining .....	55
2.2.1.5	Single cell cloning.....	55
2.2.1.6	Time lapse microscopy.....	56
2.2.2	Molecular biological methods.....	56
2.2.2.1	Cloning methods.....	56
2.2.2.1.1	Classical cloning of vectors .....	56
2.2.2.1.1.1	Amplification of Inserts .....	56
2.2.2.1.1.2	Restriction Digestion .....	58
2.2.2.1.1.3	Ligation .....	59
2.2.2.1.1.4	Transformation of E.coli, clone PCR and Sanger sequencing	59
2.2.2.1.2	Mutagenesis.....	61
2.2.2.1.3	Golden gate cloning .....	62
2.2.2.2	DNA isolation.....	63
2.2.2.3	Polymerase chain reaction .....	63
2.2.2.5	Complementary DNA (cDNA) synthesis .....	64
2.2.2.6	Quantitative PCR (qPCR).....	65
2.2.3	Methods for genetic modification of mammalian cells.....	66
2.2.3.1	Lentiviral transduction.....	66
2.2.3.2	Co-transfection of cell lines .....	67
2.2.3.3	CRISPR/Cas9 genome editing .....	68
2.2.3.4	A potential approach to study MCPyV-positive MCC oncogenesis and differentiation.....	69
2.2.4	Biochemical methods.....	71
2.2.4.1	Immunoblotting for proteins .....	71
2.2.4.1.1	Preparation of cell lysates .....	71
2.2.4.1.2	Protein estimation .....	71
2.2.4.1.3	Sodium dodecyl sulphate-polyacrylamide gel electrophoresis (SDS-PAGE) .....	71
2.2.4.1.4	Immunoblotting.....	72
2.2.5	<i>In vivo</i> mouse experiments .....	73
2.2.6	Statistical Analysis .....	74
<b>3.</b>	<b>Results</b> .....	<b>75</b>
3.1	Generation and evaluation of a vector system expressing factors implicated in MCC oncogenesis.....	75
3.1.1	RNA sequencing of MCPyV-positive MCC cells for the identification of suitable cell surface markers .....	75

3.1.2 Successful establishment of a KRT20 fluorescence reporter system using CRISPR/Cas9 technology .....	79
3.1.3 Generation of inducible expression vectors for the expression of proteins implicated in MCPyV-positive MCC oncogenesis .....	83
3.1.3.1 Doxycycline-inducible T antigen (TA) and small T antigen (sT) expression vectors .....	83
3.1.3.2 RheoSwitch-inducible Atonal Homolog BHLH Transcription Factor 1 (ATOH1) expression vector .....	86
3.1.3.3 IPTG-inducible GLI family zinc finger 1 (GLI1) and dominant-negative Mastermind-like1 (dnMAML) expression vectors.....	88
3.1.4 Genetic manipulations in primary fibroblasts .....	91
3.1.4.1 Integration of the KRT20 donor into primary fibroblasts .....	91
3.1.4.2 The use of human telomerase reverse transcriptase (hTERT) to increase the proliferative lifespan of primary fibroblasts .....	92
3.1.4.3 Lentiviral transduction of primary fibroblasts with the various inducible expression vectors .....	94
3.1.4.4 Single cell cloning to identify optimal genetically manipulated clones	97
3.1.5 The use of HaCaT cells as an alternative starting point for the approach to study MCC oncogenesis .....	99
3.1.5.1 Integration of the KRT20 donor into HaCaT cells .....	99
3.1.5.2 Lentiviral transduction of HaCaT cells with the various inducible expression vectors .....	100
3.1.5.3 Expression of MCPyV-TA, ATOH1 and DNAML1 in HaCaT cells does not induce expression of the MCC marker KRT20.....	102
3.2 Analysis of the use of artesunate as a potential drug for MCC treatment .....	107
3.2.1 Artesunate exerts strong cytotoxic effects towards MCPyV-positive MCC cell lines <i>in vitro</i> .....	107
3.2.2 Artesunate downregulates LT expression in MCPyV-positive MCC cell lines .....	108
3.2.3 Repression of T antigen expression is not the sole mechanism of artesunate-induced cell death in MCPyV-positive MCCs.....	112
3.2.4 WaGa cells are sensitized to artesunate by the expression of the T antigens .....	114
3.2.5 Absence of typical apoptotic signatures in most artesunate-treated MCPyV-positive MCC cell lines .....	116
3.2.6 Artesunate induces a ferroptotic mode of cell death in MCPyV-positive MCC cell lines.....	118
3.2.7 Ferroptosis suppressor protein 1 (FSP1) does not suppress artesunate-induced ferroptosis in MCPyV-positive MCCs .....	121
3.2.8 Absence of a pro-ferroptotic role of p53 in MCPyV-positive MCCs.....	124
3.2.9 Artesunate suppresses MCC tumor growth <i>in vivo</i> .....	126

3.2.10 Artesunate does not interfere with upregulation of crucial immune-relevant molecules on MCPyV-positive MCC cells .....	127
<b>4. Discussion .....</b>	<b>133</b>
4.1 Models for MCC oncogenesis .....	133
4.1.1 Why has the cell of origin of MCC not yet been identified? .....	133
4.1.2 Generation of a vector system to aid in the study of MCC oncogenesis. ....	134
4.1.3 Efficiency of the generated inducible expression vectors in primary fibroblasts and HaCaT cells .....	134
4.1.4 Challenges faced with primary fibroblast proliferation, single cell clone generation and the integrated KRT20 donor .....	136
4.1.5 Expression of potential MCC-promoting factors in HaCaT cells .....	137
4.1.6 Future implications for our lentiviral vector system for multiple independently-inducible factors .....	138
4.1.7 Conclusion .....	138
4.2 Artesunate as a potential MCC treatment .....	139
4.2.1 The need for alternative treatments for MCC .....	139
4.2.2 Artesunate as a potential treatment option for MCPyV-positive MCC.....	139
4.2.3 Artesunate inhibits the growth of MCPyV-positive MCCs and represses MCPyV oncoproteins .....	140
4.2.4 Further mechanisms in addition to MCPyV T antigen repression are crucial in artesunate-induced cytotoxicity towards MCPyV-positive MCCs .....	142
4.2.5 Artesunate-induces ferroptosis in MCPyV-positive MCCs and does not depend on suppressing the FSP1 antioxidant pathway in these cells .....	143
4.2.6 The tumor suppressor protein p53 does not promote artesunate-induced ferroptosis in MCPyV-positive MCCs .....	148
4.2.7 First positive indications for the potential use of artesunte in combinatorial MCPyV-positive MCC immunotherapy .....	150
4.2.8 Conclusion .....	151
<b>5. References .....</b>	<b>152</b>
<b>6. Appendix .....</b>	<b>175</b>
6.1 List of tables .....	175
6.2 List of figures .....	175
6.3 Abbreviations .....	177
6.4 Copyright clearance .....	180
6.5 Affidavit .....	181
6.6 Acknowledgements .....	182
6.7 Publication list .....	184

## Abstract

Merkel cell carcinoma (MCC) is a rare and aggressive skin cancer with an increasing incidence. The majority of MCC cases (approximately 80%) are associated with the Merkel cell polyomavirus (MCPyV). This virus encodes for the MCPyV T antigens (small T (sT) and large T (LT)), which are oncoproteins that drive MCC carcinogenesis. However, the precise cells of the skin that are transformed by the T antigens are not known i.e., the cells of origin of MCC are yet to be discovered. Therefore, the first part of this study involved the generation and evaluation of a vector system that could be used to study MCC oncogenesis. To this end, a set of lentiviral vectors was cloned that allows independent, inducible expression of potential key factors in MCC oncogenesis. In addition, a CRISPR/Cas9 knock in was established that allows the coding sequence for a fluorescent protein to be placed under the control of the promoter of *KRT20*, one of the most crucial markers of MCC. The functionality of this *KRT20* reporter was proven in the MCPyV-positive MCC cell line, WaGa. The different inducible vector systems (doxycycline-inducible MCPyV T antigens or MCPyV sT, RheoSwitch-inducible ATOH1 and IPTG-inducible dnMAML1 and GLI1) were found to have different efficacies in various cellular systems and in particular, a considerable reduction in efficiency was observed at times upon the interaction of several vectors in one cell.

In the second and more important part of this study, the role of the well-established anti-malarial drug, artesunate, which possesses additional anti-tumor and anti-viral activity, in the treatment of MCPyV-positive MCC was analyzed. In our study, artesunate was found to be cytotoxic towards MCPyV-positive MCC cell lines *in vitro* and repressed tumor growth *in vivo* in a mouse model. Artesunate was also found to downregulate T antigen expression, which is critical for the proliferation of MCPyV-positive MCC cells. The repression of T antigen expression, however, was not the sole mechanism of artesunate's cytotoxic action; instead, the MCPyV-positive MCC cell line, WaGa, was found to be even less sensitive to artesunate after shRNA knockdown of the T antigens. Since loss of membrane integrity occurred more rapidly than degradation/loss of genomic DNA under the influence of artesunate in four of five MCPyV-positive MCC cell lines examined, apoptosis, although widely described as a *modus operandi* for artesunate, did not appear to be a determinant of the cytotoxicity of artesunate against MCPyV-positive MCC cells. Instead, we were able to demonstrate that artesunate induced the recently described iron-dependent and lipid peroxide-associated form of cell death known as "ferroptosis". This was achieved primarily through the use of inhibitors that can suppress specific individual steps of the ferroptotic process. Thus, artesunate-induced cell death of MCPyV-positive MCC cells could be suppressed by iron chelators and by the inhibition of lipid peroxidation and lysosomal transport. Surprising results were obtained from the analysis of two proteins associated with the ferroptotic process, namely, ferroptosis suppressor protein 1 (FSP1) and tumor suppressor protein p53. Here, we showed that ectopically-

expressed FSP1 cannot suppress artesunate-induced ferroptosis in MCPyV-positive MCC cells and that p53 does not play a pro-ferroptotic role in artesunate-induced cell death of MCPyV-positive MCCs. Since artesunate did not suppress the interferon- $\gamma$ -induced expression of immune-related molecules such as HLA and PD-L1 on the surface of MCPyV-positive MCCs, our study also provided the first positive evidence for its use in combinatorial immunotherapy. Overall, this study showed that artesunate appears to be an effective drug for the treatment of MCPyV-positive MCC and might also be considered for its use in combinatorial MCC immunotherapy in the future.

## Zusammenfassung

Das Merkelzellkarzinom (MCC) ist ein seltener und aggressiver Hautkrebs mit einer steigenden Inzidenz. Die Mehrzahl der MCC-Fälle (ca. 80%) sind mit dem Merkelzell-Polyomavirus (MCPyV) assoziiert. Dieses Virus kodiert für die MCPyV T Antigene (small T (sT) und Large T (LT)), die als Onkoproteine die MCC Karzinogenese vorantreiben. Unbekannt ist jedoch welche Zellen der Haut durch die T Antigene transformiert werden, was also die Ursprungszellen des MCC sind. Der erste Teil dieser Arbeit befasste sich daher mit der Generierung und Evaluierung eines Vektorsystems, das zur Untersuchung der MCC-Onkogenese genutzt werden könnte. Dazu wurde ein Set von lentiviralen Vektoren kloniert, das die voneinander unabhängige, induzierbare Expression von potentiellen Schlüsselfaktoren der MCC-Onkogenese erlaubt. Außerdem wurde ein CRISPR/Cas9 *knock in* etabliert, der es erlaubt die kodierende Sequenz für ein fluoreszierendes Protein unter die Kontrolle des Promoters von *KRT20*, dessen Expression eines der wichtigsten MCC Marker ist, zu bringen. Die Funktionalität dieses KRT20 Reporters konnte in einer MCPyV-positive MCC Linie, WaGa, nachgewiesen werden. Die verschiedenen induzierbaren Vektorsysteme (Doxycyclin-induzierbare MCPyV T Antigene bzw. MCPyV sT, RheoSwitch-induzierbare ATOH1, IPTG-induzierbares dnMAML1 und GLI1) zeigten sich unterschiedlich effektiv in unterschiedlichen Zellsystemen und insbesondere im Zusammenspiel mehrerer Vektoren in einer Zelle war die Induzierbarkeit teilweise erheblich reduziert.

Im zweiten, und wichtigeren Teil dieser Arbeit, habe ich mich mit der Frage auseinandergesetzt, ob ein etabliertes Anti-Malaria-Medikament, dem zusätzlich anti-tumorale und anti-virale Aktivität zugeschrieben werden, sich für die Behandlung des MCPyV-positiven MCC anbieten könnte. In unserer Studie wurde festgestellt, dass Artesunat *in vitro* zytotoxisch auf MCPyV-positive MCC Zelllinien wirkt und *in vivo* im Mausmodell das Tumorstadium verlangsamen kann. Es wurde zudem beobachtet, dass Artesunat die T Antigen Expression unterdrückt, das für die Proliferation von MCPyV-positiven MCC-Zellen entscheidend ist. Allerdings spielt die Repression der T Antigen Expression keine Rolle für den zytotoxischen Effekt von Artesunat, sondern es zeigte sich, dass die MCC-Zelllinie WaGa nach shRNA *knockdown* der T Antigene sogar weniger sensitiv gegenüber Artesunat war. Da unter dem Einfluss von Artesunat in vier von fünf untersuchten MCC Zelllinien der Verlust der Membranintegrität schneller eintrat als eine Degradation/Verlust der genomischen DNA scheint Apoptose, obwohl vielfach als *Modus Operandi* für Artesunat beschrieben, nicht bestimmend für die Zytotoxizität von Artesunat gegenüber MCPyV-positiven MCC Zellen zu sein. Stattdessen konnten wir die kürzlich beschriebene eisenabhängige und Lipidperoxid-assoziierte Form des Zelltods, die sogenannte "Ferroptose", nachweisen. Dies gelang vor allem durch den Einsatz von Inhibitoren, die spezifische Einzelschritte des ferroptotischen Prozesses unterdrücken können. So ließ sich der durch Artesunat induzierte Zelltod von MCPyV-positiven Zellen durch

Eisenchelatformer und Inhibition der Lipidperoxidation und des lysosomalen Transports unterdrücken. Überraschende Ergebnisse lieferte die Analyse von zwei Proteinen, die mit dem ferroptotischen Prozess in Verbindung gebracht werden, nämlich dem Ferroptose-Suppressor-Protein 1 (FSP1) und dem Tumorsuppressor-Protein p53. Hier zeigte sich, dass ektopisch-exprimiertes FSP1 die Artesunat-induzierte Ferroptose in MCC Zellen nicht unterdrücken kann und dass p53 keine pro-ferroptotische Rolle beim Artesunat-induzierten Zelltod von MCPyV-positiven MCCs spielt. Da Artesunat die Interferon- $\gamma$  induzierte Expression von immunrelevanten Molekülen wie HLA und PD-L1 auf der Oberfläche von MCPyV-positiven MCCs nicht unterdrückte, ergaben sich auch erste positive Hinweise auf seinen Einsatz in der kombinatorischen Immuntherapie. Insgesamt zeigte diese Studie, dass Artesunat ein wirksames Medikament für die Behandlung von MCPyV-positivem MCC zu sein scheint und in Zukunft auch für den Einsatz in der kombinatorischen MCC-Immuntherapie in Frage kommen könnte.

# **1. Introduction**

## **1.1 The skin and its cell types**

The largest organ of the human body is the skin [1, 2]. It is a complex organ composed of many different layers and cell types [1-3]. The outermost layer, the epidermis, forms a multilayered epithelium (Fig. 1a), which serves to protect the body from external infectious agents, UV light, injury and water loss [1, 2]. The predominant cell type found here are the keratin-secreting keratinocytes [1, 2]. These cells are arranged in progressive stages of differentiation with the basal layer consisting of mitotically active cells (expressing Keratin 4 and 15), the middle layers consisting of differentiating cells (expressing Keratin 1 and 10) and the outermost layer consisting of terminally differentiated cells [2, 4-6]. Besides keratinocytes, several further cell types are present in the epidermis (Fig. 1a). In the basal layer and surrounding hair follicles, Merkel cells which interact with cutaneous nerves and provide a sensation to touch can be detected [1, 7]. Furthermore, melanocytes support keratinocytes by synthesizing pigments [1, 8] and Langerhans cells and dendritic cells are important for antigen presentation [1, 9, 10]. The epidermis is also inclusive of structures such as the hair follicles, sebaceous glands and sweat glands [1-3]. There are several stem cell populations found in the skin to enable regeneration of the various cell types. Epidermal stem cells are located in hair follicles and in the surrounding interfollicular epidermis and aid in the continuous renewal of the cells of the epidermis (Fig. 1b) [11, 12]. Stem cells from the hair follicle can also give rise to Merkel cells [13]. In addition, Merkel cells have a further progenitor population which are epidermal keratinocytes found in specialized structures called touch domes in the interfollicular epidermis (Fig. 1b) [14, 15]. An extracellular matrix-rich basement membrane separates the upper epidermis from the underlying layer, the dermis which is a connective tissue layer that supports the epidermis (Fig. 1a) and provides it with nourishment [1-3]. It consists predominantly of collagen-secreting fibroblasts [2, 3]. Blood vessels, lymphatic vessels, nerves and muscle fibres are also found in this layer [1-3].

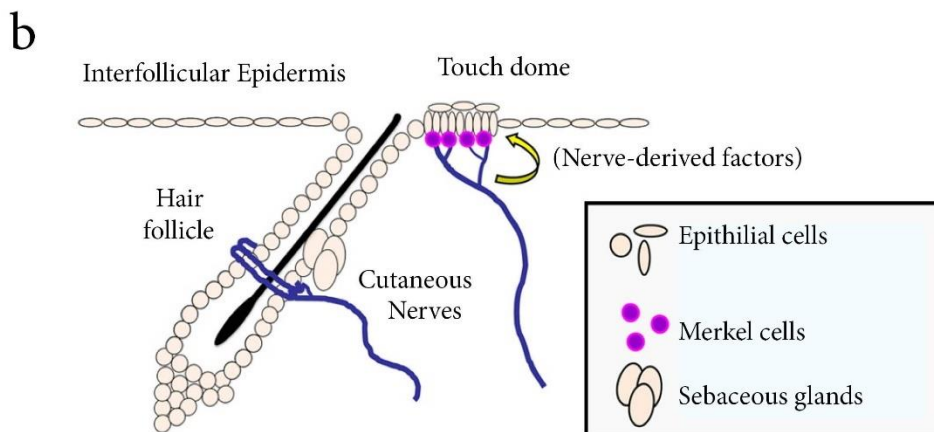
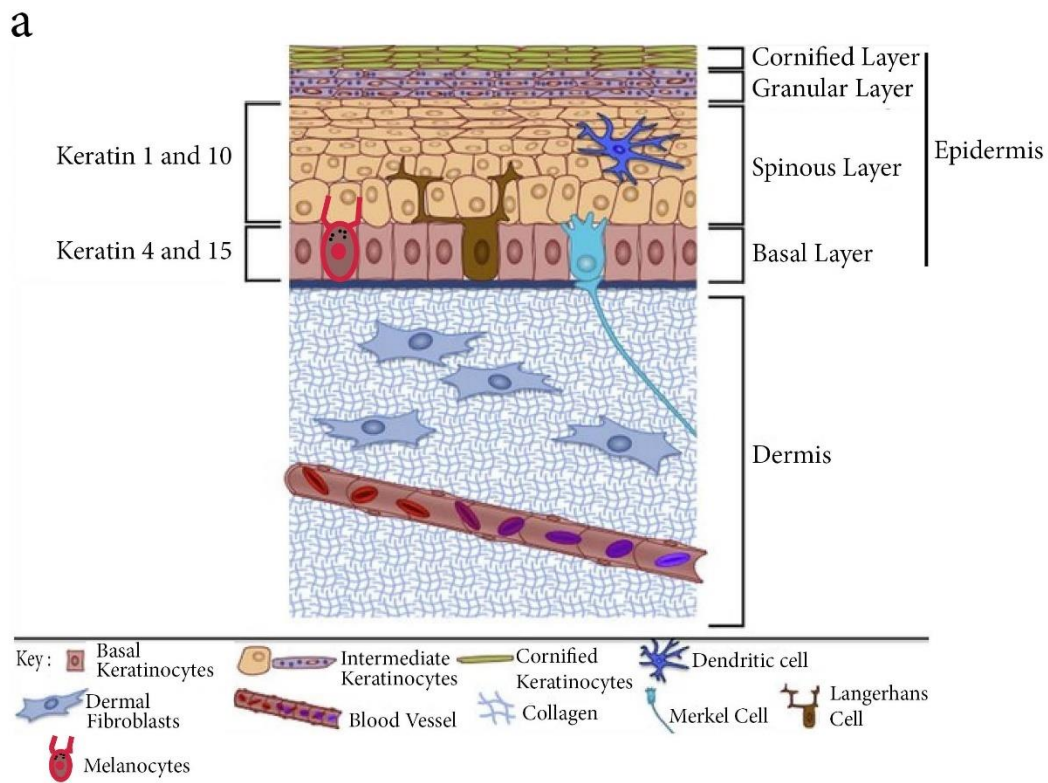


**Figure 1: Schematic representation of the skin and location of epidermal stem cells.** a) The outer layer of the skin, the epidermis and the inner layer, the dermis are depicted. The various layers of the epidermis (cornified, granular, spinous and basal layers) are predominantly made up of keratinocytes which secrete the protein keratin. Some of the other cell types found in the epidermis are Merkel cells, melanocytes, dendritic cells and Langerhans cells. The underlying dermis is predominantly made up of fibroblasts which secrete the protein collagen. Blood vessels are also found in this layer (Figure adapted from [16] with permission from Elsevier, Copyright 2017). b) Epidermal stem cells are located in the hair follicle and the surrounding interfollicular epidermis. Specialized keratinocytes in the touch dome serve as progenitors for Merkel cells (Figure adapted from [17] with permission from Elsevier, Copyright 2015).

## **1.2 Merkel Cell Carcinoma**

Merkel cell carcinoma (MCC) is a rare but highly aggressive and lethal neuroendocrine carcinoma of the skin [18]. It was discovered in the year 1972 by Toker [19] and was later named 'Merkel cell carcinoma' due to phenotypic similarities between MCC and Merkel cells [20, 21]. It commonly occurs in fair-skinned, immunosuppressed and elderly individuals (95% over 50 years old) with increasing ultraviolet (UV) exposure [22]. It presents as painless, reddish-purple, fast growing nodules on the skin (Fig. 2) in sun-exposed areas like the head and neck [23-25]. In 2013, the incidence rate of MCC in the United States of America was 0.7 per 100,000 person-years and a 14% increase in the incidence is predicted by the year 2025 [26]. The mortality rate associated with MCC is between 33% to 46% and is much higher than that for the more commonly observed skin cancer, melanoma [27]. A 5-year overall survival rate of 51%, 35% and 14% for local disease, nodal involvement and metastasis has recently been estimated by the MCC staging system from the American Joint Committee on Cancer [24, 28].



**Figure 2: Appearance of MCC tumors on the skin.** A Merkel cell carcinoma nodule on the skin is depicted (Figure adapted from [29]; Copyright: Creative Commons Attribution License (CC BY 4.0)).

### **1.2.1 Two different molecular pathomechanisms in MCC development**

Due to the elevated incidence of MCC in immunosuppressed patients like those suffering from acquired immunodeficiency syndrome (AIDS), an infectious origin for MCC was suspected [24, 30]. Accordingly, in 2008, the human Merkel cell polyomavirus (MCPyV) was identified [31] and is nowadays believed to be the oncogenic trigger in 80% of MCC cases [32-34] while the remaining cases are believed to be caused by UV-induced mutations [35]. Indeed, while MCPyV-positive MCC tumors expressing viral oncoproteins as supposed oncogenic drivers are among the tumors with lowest frequencies of somatic mutations, MCPyV-negative MCC tumors are characterized by the almost highest mutational burden among all cancers with prominent UV-mutational signatures like cytosine to thymidine (C > T) transitions [36-38]. Some of the genes recurrently found to be mutated in MCPyV-negative MCC tumors include the tumor suppressors *RB1* and *TP53*, signaling pathway genes such as *NOTCH1* and *NOTCH2*, DNA damage pathway genes like *ATM* and chromatin modifying genes like *ASXL1* [36]. Notably, the absence of characteristic driver

mutations in MCPyV-positive MCC highlights the importance of MCPyV in the oncogenesis of these cases [36, 37].

### **1.2.2 The Merkel cell polyomavirus and MCC carcinogenesis**

The Merkel cell polyomavirus (MCPyV) is a human polyomavirus which belongs to the Polyomaviridae family [39] and is the first polyomavirus to be associated with human cancer [40]. It is a small circular double-stranded DNA virus with a genome size of approximately 5400 bp (Fig. 3a) [41, 42]. It has two transcriptional units, comprising an early and a late region [41]. An early gene region encodes for the differentially spliced tumor (T) antigens including the small T antigen (sT), large T antigen (LT) and 57kT (a splice variant of LT) [41]. Additionally, in an alternate reading frame, a further protein termed ALTO (alternate frame of the large T open reading frame) [43] is encoded by the early region. The late region encodes for the viral coat proteins VP1 and VP2 [41]. Polyomaviruses express the early region genes upon infection and the resulting proteins are involved in viral DNA replication while the late region is expressed at later stages of infection for the encapsulation of progeny virions [40]. The non-coding control region (NCCR) is found between the early and late regions [41]. It contains the origin of replication (ori) for initiation of viral DNA replication as well as bidirectional promoters and enhancers for transcription of the early and the late region genes [40, 44].

sT, LT and 57kT are three unique T antigens generated by alternative splicing from a single T antigen transcript (Fig. 3b) [41, 45]. Several molecular functions of the MCPyV T antigens have been described and will be discussed in the following paragraphs.

All T antigens share a common N-terminal domain (78 aa) consisting of the DnaJ domain with a conserved CR1 motif (LXXLL) (13–17 aa) and an Hsc70 binding domain (HPDKGG) (42–47 aa) (Fig. 3c) [31, 46]. Hsc70 is a heat shock protein with which LT interacts to enable efficient viral replication [47]. Owing to alternative splicing, the other domains vary among the T antigens. MCPyV-LT (817 aa) has a two unique regions distinct from other human polyomaviruses which are the MCPyV unique regions (MUR), MUR1 (102-207 aa) and MUR2 (220-258 aa), found downstream of the DnaJ domain (Fig. 3c) [24, 46, 48]. LT binds to the human cytosolic protein Vam6p via a Vam6p binding motif in the MUR1 region, thereby shuttling this protein to the nucleus and preventing lysosomal clustering [46, 49]. A conserved Rb-binding motif (LXCXE) (212–216 aa) is found between two MUR regions [46]. The binding of LT to the retinoblastoma tumor suppressor protein (RB1), enables RB1 sequestration which in turn activates expression of proteins like cyclinE and E2F1 which promote cell cycle entry into the S phase [45, 46, 50]. This interaction is crucial in MCPyV-positive MCC for the maintenance of tumor cell proliferation [51, 52]. Following the second MUR region, a short nuclear localization signal (NLS) (277–280 aa) is present (Fig. 3c) [46].

The NLS aids in nuclear localization of LT in those MCC tumors where the NLS sequence is still retained following LT truncation [53]. The C-terminally located origin binding domain (OBD) (308–433 aa), zinc-finger motif (437–528 aa) and helicase/ATPase domain (441–817 aa) (Fig. 3c) in LT are important for viral DNA replication [46]. LT binds to the origin of replication in the NCCR by its OBD [54], oligomerizes and initiates replication via the zinc-finger motif and the helicase/ATPase domains [46]. In MCPyV-positive MCC tumors the C-terminal of LT is truncated (tLT) such only that the DnaJ domain, RB-binding domain and in some cases, the NLS is retained [45, 53]. The OBD and helicase/ATPase domain which are involved in viral replication are lost following truncation due to frame shift mutations and the insertion of premature stop codons [45]. As a result, viral replication does not take place in these tumors serving as a mechanism for the virus to evade the replication-associated DNA damage response in the host [24, 45]. Furthermore, this C-terminal region has also been described to possess growth inhibitory properties and the ability to induce host cell apoptosis upon phosphorylation of serine 816 [44, 55]. These properties are lost upon truncation of viral LT enabling successful proliferation of tumor cells [24, 56, 57].

In addition to the common N-terminal region, sT (186 aa) has two protein phosphatase 2A (PP2A) binding domains (119–124 and 147–152 aa) (Fig. 3c) [46] by means of which it binds and inhibits several components of the PP2A and PP4 complexes such as PP2A A $\alpha$ , PP2A A $\beta$ , and PP4C [58]. While other polyomaviruses such as SV40 rely on the sT-PP2A interaction for cellular transformation [59], this is not the case for the MCPyV sT [58, 60]. On the other hand, the LT-Stabilization Domain (LSD) (1–95 aa) of sT (Fig. 3c) is crucial for the transforming properties of sT as demonstrated in mice [61]. This LSD domain is required for the binding of sT to the eukaryotic translation initiation factor 4E-binding protein 1 (4E-BP1) that is hyperphosphorylated by sT leading to dysregulated cap-dependent translation [46, 60]. This inhibition of 4E-BP1 by sT is required for cellular transformation [60]. As suggested by the nomenclature, sT also stabilizes the viral replication helicase protein LT via the LSD domain thereby promoting viral replication [46, 62]. Although this function of sT was previously attributed to its binding and sequestering of the cellular SCF<sup>Fbw7</sup> E3 ubiquitin ligase from LT [62], subsequent studies either indicate an SCF<sup>Fbw7</sup>-independent mechanism for this function of sT [63] or demonstrate that this function of sT can occur only in the presence of a positively charged LSD domain [64]. sT inhibits activation of the NF- $\kappa$ B pathway via its PP4C/NEMO interaction domain (95–111 aa) (Fig. 3c) [46, 65]. This domain facilitates interaction of sT with protein phosphatase 4C (PP4C) which in turn enables interaction of PP4C with NF- $\kappa$ B essential modulator (NEMO) which is part of a kinase complex involved in NF- $\kappa$ B signaling [46, 65]. PP4C inhibits phosphorylation of I $\kappa$ B by inhibition of the kinase complex as a result of which NF- $\kappa$ B cannot translocate to the nucleus and activate downstream genes [44, 65]. The interaction of sT with PP4C is also responsible for microtubule destabilisation and consequent increase in cellular motility and migration [66].

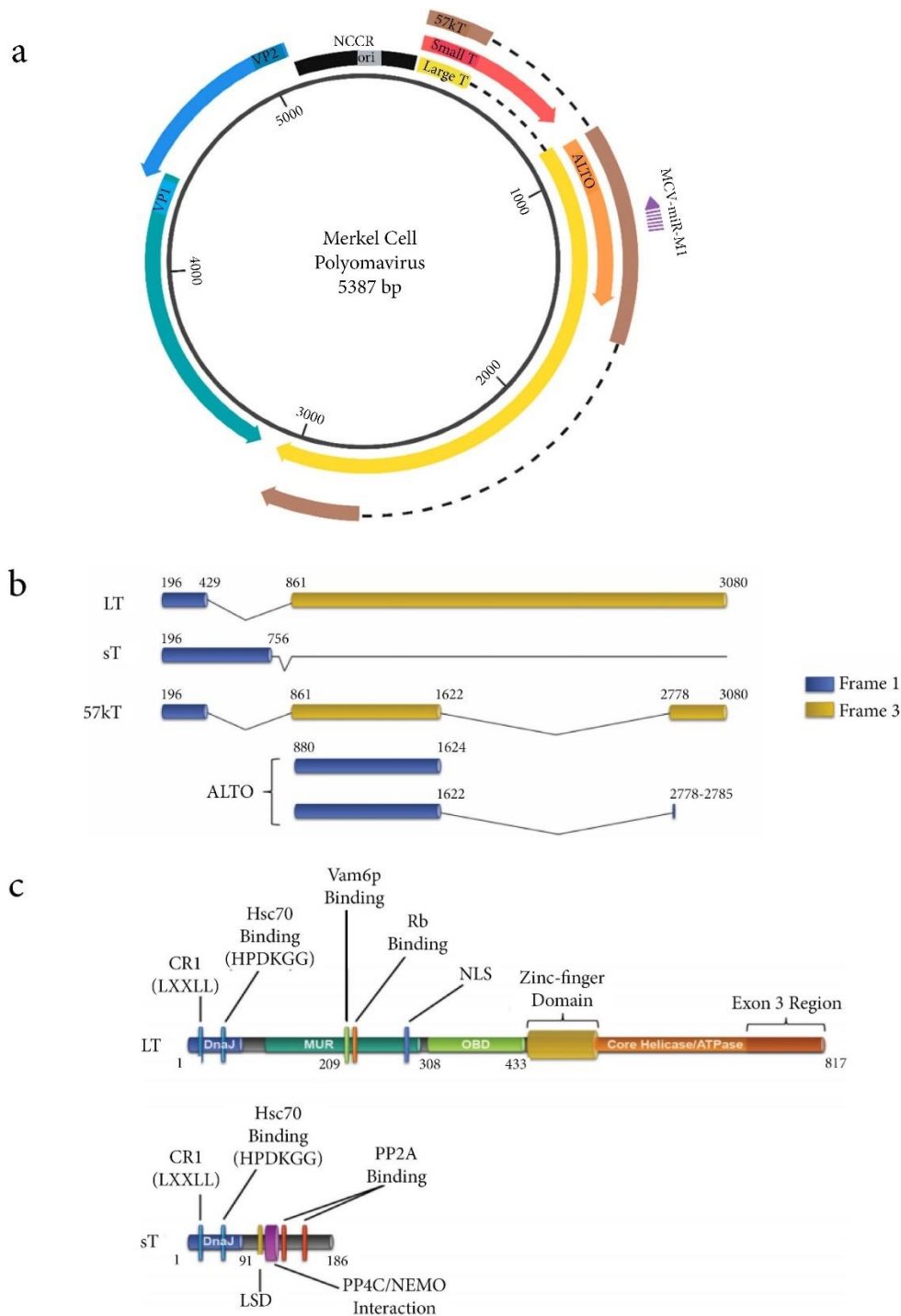


**Figure 3: Schematic representation of the MCPyV genome and its early region transcripts/proteins.** a) The 5387 bp genome of MCPyV is depicted. Within the non-coding control region (NCCR), is an origin of replication (ori) and bidirectional promoters for the transcription of both the early region (small T (sT), large T (LT), 57kT and the alternate frame of the large T open reading frame (ALTO)) and the late region (VP1 and VP2 coat proteins). The MCPyV late region also encodes for the microRNA, MCV-miR-M1 (Figure adapted from [41]; Copyright: Creative Commons Attribution license (CC BY 4.0)). b) The alternatively spliced MCPyV early region transcripts, LT, sT, 57kT and ALTO are depicted. c) The various functional domains of LT and sT are represented (MUR: MCPyV unique region, Rb: retinoblastoma, NLS: nuclear localization signal, OBD: origin binding domain, PP2A: protein phosphatase 2A, PP4C: protein phosphatase 4C, LSD: LT stabilizing domain, NEMO: NF- $\kappa$ B essential modulator) (Figures b and c adapted from [46] with permission from Elsevier, Copyright 2015).

57kT, the splice variant of LT, retains the CR1 motif, DnaJ domain, Rb-binding region and additionally contains 100 C-terminal residues encoded for by Exon 3 which are absent in the MCC tumor-specific truncated LT [46, 56]. These 100 residues are known to possess growth inhibitory properties [56] which might explain why LT is always found to be genetically truncated in MCC tumors which are composed of rapidly proliferating cells. The expression of ALTO is not a necessity for viral replication or for the proliferation of MCPyV-positive MCC tumor cells [43, 44, 53].

MCV-miR-M1-5p is a 22-nucleotide mature microRNA encoded for by the late region of MCPyV, antisense to a coding region of LT (Fig. 3a) [67, 68]. This miRNA, as in the case of other polyomaviruses, regulates expression of the early region genes [68, 69].

Truncated LT and sT are the most important factors involved in MCC carcinogenesis [70]. When the T antigens are knocked down in MCPyV-positive MCC cell lines, the cells arrest in the G1 phase, limit entry into the S and G2/M phases, show reduced proliferation and exhibit increased cell death [70]. In this context, studies have demonstrated a crucial role for LT in the maintenance of tumor cell proliferation via its interaction with RB1 for which phosphorylation of LT at serine 220 is essential [51, 71]. Accordingly, cell death of MCPyV-positive MCC cell lines caused by T antigen knockdown was found to be rescued by the overexpression of LT alone [72]. On the contrary, other reports have suggested that sT is crucial for the initiation of tumorigenesis in mice [61, 73] wherein no appreciable alteration in tumor initiation upon coexpression of LT was observed [61]. Notably, sT is associated with the ability to induce transformation as was observed following its overexpression in rodent and murine fibroblasts [60]. This transforming property of sT has been attributed to its LSD domain-mediated interactions [58, 73] and has also been partly associated with its ability to elevate aerobic glycolysis as studied in human fibroblasts [74]. Coexpression of sT with the Merkel cell transcription factor Atonal BHLH Transcription Factor 1 (ATOH1) in the epidermis of murine skin results in the development of intraepidermal MCC-like lesions [61]. In other *in vivo* experiments in mice, ectopic keratin 14-directed expression of the T antigens in stratified squamous epithelial cells led to hyperplasia and development of papillomas [75]. A recent report in these keratin 14-directed MCPyV T antigen expressing transgenic mice, a widely used model of skin carcinogenesis was used to define the role of the MCPyV T antigens as ‘tumor promoters’ rather than ‘initiators’ in the stages of cancer development [76, 77]. In summary, several studies performed so far have highlighted the significance of the MCPyV T antigens in MCPyV-positive MCC carcinogenesis.

### **1.2.3 Proteins and pathways involved in MCC**

Several proteins and cell signaling pathways have been implicated in MCC oncogenesis and have been discussed in the subsequent sections.

### **1.2.3.1 Atonal bHLH transcription factor 1 (ATOH1)**

Atonal bHLH transcription factor 1 (ATOH1) is a basic helix-loop-helix transcription factor, which is essential for Merkel cell development [78-80]. Although initial studies reported a tumor suppressor role for ATOH1 in MCC [81], it was later found to be overexpressed especially in aggressive MCCs and was associated with worse prognosis [82]. Upon co-expression of MCPyV sT and ATOH1 in the epidermis of mice, this resulted in the development of cellular aggregates with an MCC-like phenotype [61]. ATOH1 has also recently been described as a lineage-dependency oncogene in MCC [83]. In this regard, ATOH1 was found to upregulate expression of the MCC associated microRNA, miR-375 [83]. Moreover, its overexpression was associated with the development of a neuroendocrine phenotype as evidenced by a change in the morphology of fibroblasts and MCPyV-negative MCC cell lines from an adherent to a suspension phenotype [83]. In further studies, MCPyV LT was found to stabilize the ATOH1 protein via its MUR1 region [84] and based on the cellular context was shown to upregulate ATOH1 transcription in *in vitro* experiments [85]. Recent studies showed that following T antigen knock down in MCPyV-positive MCC cell lines cocultured with keratinocytes, a subsequent reduction of ATOH1 and SOX2 expression with concomitant differentiation into neurite<sup>+</sup> cells was observed highlighting the importance of ATOH1 in the maintenance of a Merkel-cell like phenotype in MCC tumors [85]. Interestingly, sT in the form of the ST-MYCL-EP400 complex activates an LSD1 transcriptional repressor complex that opposes ATOH1 transcriptional activity which potentially occurs as a mechanism to prevent complete differentiation into Merkel cells [24, 86]. In summary, both, increased as well as decreased ATOH1 function induced by the MCPyV T antigens have been described.

### **1.2.3.2 The Hedgehog pathway**

Hedgehog signaling is a developmental pathway that is functional during embryogenesis and organogenesis in humans [87, 88]. When the signaling cascade is activated, the 3 mammalian hedgehog protein homologues, Sonic, Indian and Desert, bind to their receptor (Patched) which in turn activates a transmembrane protein (Smoothed) [87, 89]. As a result, downstream signaling can take place and the GLI family zinc finger (GLI) transcription factors translocate to the nucleus where they are responsible for switching on development related genes [87-89]. In mammalian skin, Sonic hedgehog (Shh) signaling is important for the specification of Merkel cells [90]. Progenitors for Merkel cells in touch domes establish a connection with nerve endings thereby activating the Shh pathway and subsequently the expression of GLI1 [91, 92]. Notably, high levels of the hedgehog proteins including GLI1 have been detected in MCCs indicating activation of this pathway in these tumors [89, 93]. Interestingly, analysis of combined a trichoblastoma-MCPyV-positive MCC

tumor has shown that the development of the MCC part of the tumor occurred following integration of the MCPyV in a cell from the trichoblastoma which in turn was rich in GLI1+ cells [94]. Additionally, subsequent experiments performed in keratinocytes *in vitro* demonstrated the induction of a Merkel cell phenotype in these cells upon coexpression of GLI1 and the MCPyV T antigens [84]. Therefore, activation of the Hedgehog pathway appears to have a connection with MCC.

### **1.2.3.3 The Notch pathway**

In humans, the Notch pathway has several important functions for development such as cell type specification and organogenesis [95]. This signaling pathway is activated when a Notch receptor (NOTCH 1-4) on a signal-receiving cell binds to Notch ligands (such as Delta-like and Jagged) on a neighbouring signaling-sending cell [96]. This interaction initiates the cleavage of the Notch receptor resulting in the release of the Notch intracellular domain (NICD) from the membrane and its translocation into the nucleus [96]. Within the nucleus the NICD forms a transcriptional complex with proteins like Mastermind-like (MAML) and other transcriptional coactivators to activate downstream Notch target genes such as *HES1* [96]. In the epidermal layer of the skin, the Notch pathway functions in basal stem cells of the epidermis to facilitate differentiation into mature keratinocytes [97]. Interestingly, it has also been shown that the Notch pathway suppresses the expression of ATOH1, the transcription factor for Merkel cell specification [98]. In this context, experiments have shown that the disruption of Notch signaling increases Merkel cell numbers in mouse skin [99]. Indeed, the Notch pathway has been found to be inactivated in both MCPyV-positive and MCPyV-negative MCCs with cancer-promoting damaging mutations found in the Notch receptor genes, *NOTCH1* and *NOTCH2* [36]. Therefore, it is possible that the suppression of the Notch pathway in MCC promotes the development of a Merkel-cell like phenotype. Furthermore, the role of miR-375, a microRNA highly expressed in MCC tumors, as a post-transcriptional repressor of Notch receptor genes like *NOTCH2* has also been demonstrated [100]. Studies in MCC patients have also shown that those with higher expression of NOTCH3 have a more favorable overall survival [101]. Taken together, studies performed until date implicate suppression of the Notch pathway in MCCs.

### **1.2.3.4 p53**

While MCPyV-negative MCCs harbour inactivating mutations in the tumor suppressor proteins p53 and RB1, these proteins are expressed in their wildtype form in MCPyV-positive MCCs [102]. It has been found that truncated LT expressed in MCPyV-positive MCCs can bind and inhibit RB1 [51] however, in contrast to LT from other

polyomaviruses, such an interaction with p53 does not take place [24, 56]. Infact, it can activate p53, partly through inactivation of RB1 [24, 103]. MCPyV sT, however, forms a part of the ST-MYCL-EP400 complex which activates downstream targets such as the E3 ubiquitin ligase MDM2, which inhibits p53 [24, 103, 104]. Furthermore, MCPyV-positive MCC cells are also described to have higher levels of MDM4, another p53 inhibitor [103]. Therefore, although wild type p53 is expressed in MCCs, its transcriptional activity is not high enough to inhibit tumor cell growth and survival [102].

#### **1.2.4 Histology of MCC tumors**

MCC tumors display high-grade neuroendocrine carcinoma features and are located primarily within the dermis of the skin [105, 106] (Fig. 4a). However, subcutaneous and intraepidermal tumors can also occasionally be found [105, 107]. These tumors are referred to as ‘small blue cell tumors’ as staining with haematoxylin and eosin reveals a high nuclear to cytoplasmic ratio in these cells indicative of large nuclei with scant cytoplasm (Fig. 4b) [24, 105, 106]. The high proliferative rate of these tumors is represented by the frequent mitotic figures seen in tumor nuclei [24, 105, 106]. A widely used epithelial marker for the identification of MCC is Keratin 20 (KRT20), an intermediate filament protein normally expressed in the gastrointestinal epithelium, urothelium, and in Merkel cells [108-110]. A paranuclear dot-like pattern is observed upon staining of MCCs with this marker (Fig. 4c) [24, 105, 106]. KRT20 positivity and thyroid-specific transcription factor 1 (TTF-1) negativity is useful for distinguishing between MCC and other common neuroendocrine tumors such as small cell lung carcinoma (SCLC) [111, 112]. MCC also stains positive for neuroendocrine markers such as synaptophysin, chromogranin A, CD56 and insulinoma-associated 1 (INSM1) [106, 113-115]. Additionally, MCPyV-positive MCC tumors are identified by means of their positivity for the Merkel cell polyomavirus large T antigen [116]. Special AT-rich sequence-binding protein 2 (SATB2) is a further nuclear marker used for specific and sensitive detection of MCC tumors [106, 116, 117].

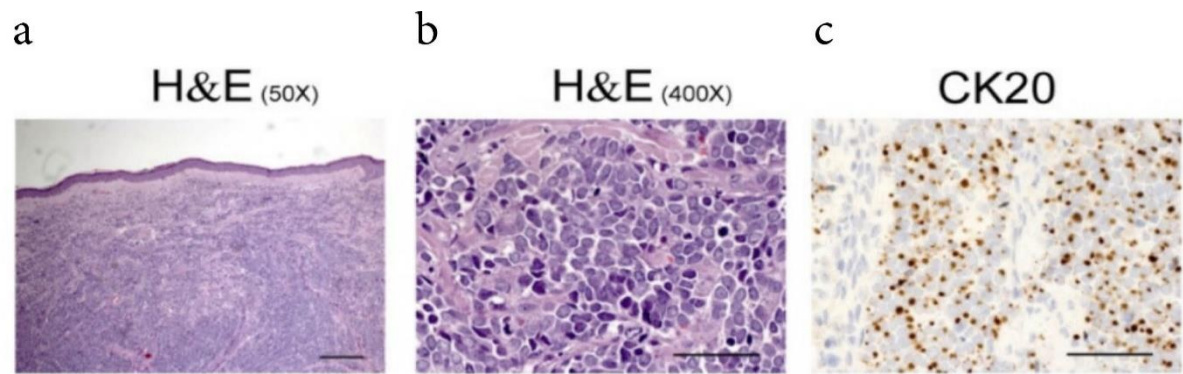


**Figure 4: Histology of MCC tumors.** Staining of an MCC tumor a) with Hematoxylin/Eosin (H/E) revealing a dermal location (50X, scale bar 200  $\mu\text{m}$ ) b) with H/E depicting round blue cells with scant cytoplasm and a high nuclear to cytoplasmic ratio (400X, scale bar 50  $\mu\text{m}$ ) c) for cytokeratin 20 (CK20) revealing a paranuclear dot-like pattern of staining (400X, scale bar 50  $\mu\text{m}$ ) (Figure adapted from [118]; Copyright: Creative Commons Attribution license (CC BY 4.0)).

### 1.2.5 Potential cells of origin of MCC

Knowledge of the cell of origin of cancer can prove very valuable not only for its treatment and prevention but also for enabling the generation of suitable disease models for understanding the pathogenesis of the disease. Several cell types deriving from the epithelial, mesenchymal and lymphoidal origins have been discussed as potential cells of origin of MCC. However, this is yet to be discovered (reviewed in [106]).

Since the majority of MCC tumors are located within the dermis, cell types such as fibroblasts, dermal stem cells and pro/pre-B cells have been discussed as possible cells of origin [106]. Nevertheless, studies have shown that epidermally located Merkel cells, their precursors and epidermal stem cells are closer to the speculated cell of origin [106].

MCC initially got its name from Merkel cells, the epithelial neuroendocrine mechanoreceptor cells in the epidermis [106, 119]. MCCs were originally thought to arise from this cell type (Fig. 5) owing to the extensive phenotypic similarities between the two [106, 119]. Both MCCs and Merkel cells express dense core neuroendocrine granules [119] and show positive immunohistochemical staining for keratin 20 [108, 120], ATOH1 [79, 121] as well as for neuroendocrine markers like chromogranin A and synaptophysin [113, 122, 123]. Nevertheless, several lines of evidence disagree with Merkel cells being the cells of origin for MCC. At first, Merkel cells are well-differentiated and post-mitotic in contrast to typical cells of origin of cancer which possess proliferative potential [124]. Furthermore, keratin 20 (Merkel cell marker) positive human fetal scalp cells were poorly infected by pseudo MCPyV virions *in vitro* hinting at the unlikelihood of MCPyV infecting the already differentiated Merkel cells

[106, 125]. Moreover, experiments in mice showed that ectopic sT overexpression in Merkel cells was unable to induce proliferation and transformation in these cells [106, 126]. MCCs are also most often located within the dermis and therefore the epidermal location of Merkel cells is a further point making it a less likely candidate [106, 127]

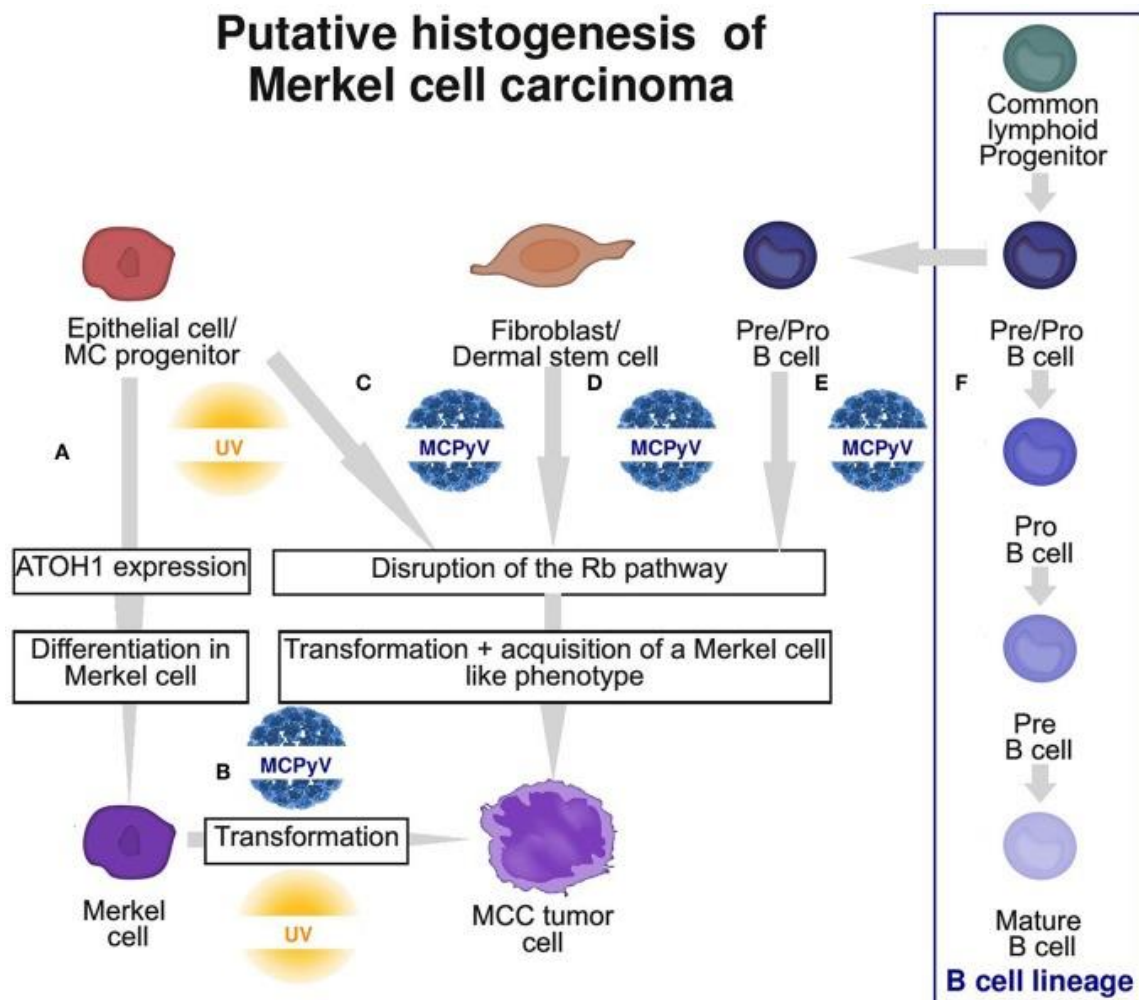


**Figure 5: Speculated cells of origin of MCC.** A) Differentiation pathway for the specification of ATOH1 expressing Merkel cells (MCs) from epithelial stem cells or MC progenitors. Potential origin of MCC from B) Merkel cells C) Epithelial stem cells or MC progenitors D) Fibroblasts/Dermal stem cells E) Pre/Pro B cells or F) the B cell lineage (Figure adapted from [106]; Copyright: Creative Commons Attribution license (CC BY 4.0))

A more likely cell of origin of MCC is an epidermal progenitor cell (Fig. 5) which has the capacity to differentiate into a Merkel cell and being a stem cell, has increased proliferative potential [94]. This was strongly supported by recent work in a combined MCPyV-positive MCC-trichoblastoma tumor which demonstrated that the MCPyV-positive MCC tumor developed following the integration of MCPyV in a cell from the neighbouring epithelial trichoblastoma tumor wherein the latter possessed both the

capacity for proliferation and for Merkel cell differentiation [94]. Expression of characteristic markers like KRT17, SOX9 and nuclear GLI1 showed that the cells of this trichoblastoma tumor were found to phenotypically resemble Merkel cell progenitor cells found in the bulge region of the hair follicle [94]. Since the bulge region of the hair follicle is dermally embedded, this further serves as an explanation for the predominantly dermal location of MCCs [94, 106]. Notably, other skin cancers such as basal cell carcinoma have also been found to arise from hair follicle stem cells showing that these stem cells are indeed susceptible to oncogenic stimuli [17]. Therefore, it is conceivable that MCPyV integrates into a Merkel cell precursor stem cell which results in the acquisition of a Merkel-cell like phenotype in MCCs during the oncogenic process [84, 106].

Owing to their dermal location, fibroblasts are yet another suspected cell of origin of MCC (Fig. 5) [106, 125]. In addition, a fibroblastic origin was strongly favoured in an *ex vivo* study which showed that dermal fibroblasts were not only robustly infected by MCPyV pseudovirions but were also able to efficiently support MCPyV replication and transcription of genes like *LT* and *VP1* [125]. Other cell types like Merkel cells and keratinocytes which were tested in parallel in this study were only poorly infected and did not support viral replication or transcription [125]. Moreover, the induction of cellular transformation by the viral T antigens, specifically sT, has so far only been evident in fibroblasts [126]. Dermally located stem cells called skin-derived precursors [128] are in close proximity to fibroblasts and have the additional advantages of having a broad differentiation potential, expressing pluripotent factors and of being able to reprogram into an epithelial or neuronal state [106, 129]. Therefore, these cells are also considered under the list of potential origin cells for MCC (Fig. 5) [106]. Nevertheless, fibroblasts have not shown the ability to acquire a Merkel-cell like phenotype up to date and have also never been identified as cells of origin of other neuroendocrine carcinomas [106]. MCPyV DNA has also never been detected in skin-derived precursors so far [130], questioning the origin of MCC from these cell types.

Pro/pre-B cells or pre-B cells have also been discussed as potential cells of origin of MCC (Fig. 5) [106]. This was following the finding that MCCs coexpressed the B cell differentiation markers terminal deoxynucleotidyl transferase (TdT) and paired box gene 5 (PAX 5) [131]. According to the same group, MCCs were also found to express immunoglobulins and exhibited clonal immunoglobulin rearrangements as seen in immature B cells [131]. Certain studies have indicated an association between the occurrence of MCC and B-cell neoplasias such as chronic lymphocytic leukemia (CLL) and non-Hodgkin lymphoma [132-134]. In a few CLL cases, integrated MCPyV with a truncated *LT* was also found [135, 136]. Despite all these findings, there is currently no evidence for the development of an MCC phenotype or Merkel cell-like differentiation from B cells [106]. Furthermore, the neuroendocrine nature of MCC argues against the possibility of B cells as the cells of origin [106].

Therefore, future studies aimed at elucidating the mechanisms of MCC oncogenesis and differentiation might throw light upon the cellular origin of this cancer.

### **1.2.6 Current treatment options for MCC**

There are several options currently available for the treatment of MCC. Primary MCCs are surgically excised along with a defined margin in accordance with the current National Comprehensive Cancer Network (NCCN) guidelines [137]. Complete lymph node dissection and adjuvant radiotherapy of the tumor location and lymph node region is performed for those patients with a node-positive disease [137]. For those with a node-negative disease, a sentinel lymph node biopsy is required to determine the lymph node status and radiotherapy of the primary tumor site alone is considered [137, 138]. Chemotherapy with drugs such as carboplatin, cisplatin and etoposide is a further commonly used option for the treatment of metastatic MCC [139, 140]. Despite the high response rate of patients to first-line chemotherapy, the response to these treatments is not durable, progression-free survival is typically low and chemotherapeutic drugs are quite toxic especially for elderly patients [139, 140]. Notably, MCC tumor cells (specifically MCPyV-positive MCCs) downregulate the expression of tumor antigen-presenting major histocompatibility complex class I (MHC-I) on their cell surface [141]. This is however reversible as was observed following treatment with interferon gamma indicating a positive role for the use of immunotherapy for MCC treatment [141]. In this regard, checkpoint blockade immunotherapy targeting of immune checkpoint proteins like programmed death-1 (PD-1) [142] or its ligand programmed death-ligand 1 (PD-L1) [143] has emerged as an effective treatment option for MCC. PD-1 is expressed on the cell surface of activated and tumor-specific T cells while PD-L1 is expressed on the cell surface of certain tumor cell types and antigen presenting cells [144, 145]. Tumor cells frequently upregulate their expression of PD-L1 which upon binding to PD-1, inhibits T cell activation thereby aiding the tumor cells in evading the immune response [144, 145]. In this context, a study in MCPyV-positive MCC tumors showed that a large number of these tumors indeed expressed PD-L1 [146]. Accordingly, anti-PD-1 and anti-PD-L1 antibody treatments of MCC patients with stage IV disease were found to be associated with a high response rate of 56% and 32% in first and second line treatment respectively [147, 148]. Immunotherapies have also been associated with frequent long lasting responses, for instance, recent studies reported a median a progression free survival of 16.8 months in MCC patients following treatment with the PD-1 inhibitor pembrolizumab [149] as compared to previous studies which reported a median progression free survival of 94 days in MCC patients following chemotherapy [139]. In fact, the PD-L1 inhibitor, Avelumab, which is additionally safe with no adverse side effects, was approved by the FDA and the EMA for its use as the first-line treatment for metastatic MCC [148, 150, 151]. Similar to PD-1, CTLA-4 is a T cell intrinsic checkpoint which is expressed on the surface of T cells and often competes with other immunostimulatory T cell surface proteins to inhibit T cell proliferation and activation [144, 145]. In fact, in a recent study, the anti-CTLA-4 antibody Ipilimumab was used in combination with the anti-PD-1 antibody Nivolumab in Avelumab-refractory MCC

patients and also was found to be safe and was associated with a high response rate [152]. Despite the tremendous progress with immune checkpoint blockade as a therapy for MCC, lack of a response to treatment, relapse of MCC tumors and acquired resistance to these treatments persist as problems in a subset of patients [142]. Moreover, the high costs of immunotherapy serve as a limitation for its usage in developing countries, highlighting the need for alternative cost-effective MCC therapies [153]. In addition, studies so far have demonstrated that these immune checkpoint inhibitors function regardless of the viral state of the MCC tumors, also urging the need for viral specific treatments owing to the frequently observed MCPyV-positive MCC cases [44].

### **1.3 Artesunate: a versatile drug**

#### **1.3.1 Artesunate as an anti-malarial**

Artesunate is a semi-synthetic derivative of artemisinin, a metabolite isolated from *Artemisia annua* (Fig. 6a) which has been used in Chinese medicine for centuries [154, 155]. Both artesunate and artemisinin are used for the treatment of malaria caused by the protozoan parasites *Plasmodium falciparum* and *Plasmodium vivax* [156-160]. In fact, due to its efficacy and safety profile, artesunate was approved in 2020 by the United States Food and Drug Administration (FDA) as the first-line drug for the treatment of severe malaria [161] and is commonly administered to patients at a dosage of 2.4 mg/kg body weight intravenously or intramuscularly [162]. In children with severe malaria, pretreatment with rectal administration of artesunate is recommended [163]. Structurally, artesunate is a sesquiterpene lactone compound characterized by the presence of a 1,2,4-endoperoxide bridge that plays a central role for its anti-malarial activity (Fig. 6b) [161]. This bridge is cleaved in the presence of intraparasitic heme iron by the Fenton reaction resulting in the release of reactive oxygen species (ROS) such as hydroxyl radicals which are toxic for the parasite [164]. Importantly, this large amount of ROS produced by artesunate depolarizes and damages mitochondria of plasmodium species but not mammalian mitochondria making it an ideal drug candidate in humans [165]. Artesunate is also described to bring about DNA damage in the parasite [166] and alkylates and impairs the function of parasitic proteins [167] in the process of exerting its cytotoxic effects [166, 168].

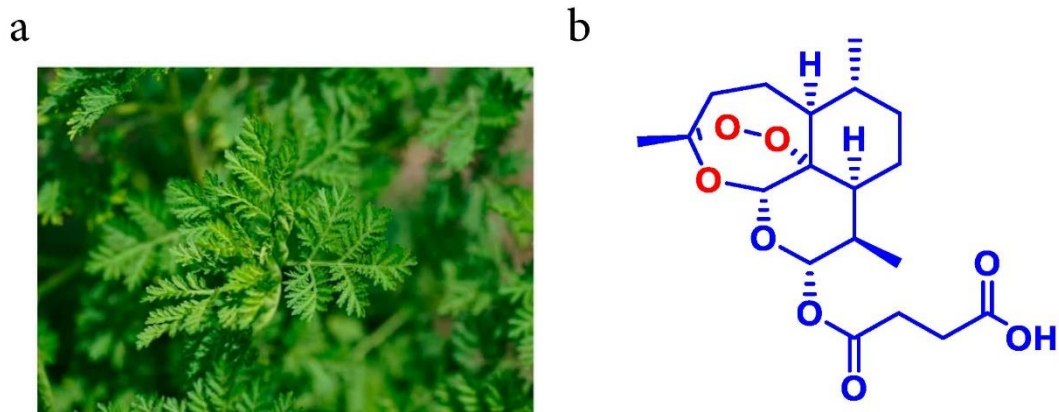


**Figure 6: The source and structure of artesunate.** a) The Sweet Wormwood plant (*Artemisia annua*) from which artemisinin is isolated for the synthesis of artesunate (Figure adapted from [169]; Copyright: Creative Commons Attribution license (CC BY 4.0)). b) The structure of artesunate wherein the oxygen atoms marked in red form a part of the 1,2,4-endoperoxide bridge [161]. (Figure adapted from [170]; Copyright: Creative Commons Attribution license (CC BY 4.0)).

### 1.3.2 Anti-viral properties of artesunate

In addition to its anti-malarial properties, anti-viral activities of artesunate have also been reported in the literature [171, 172]. Early experiments revealed the capacity of artesunate to inhibit the replication of viruses such as the herpes simplex virus type 1 (HSV-1) and Human Cytomegalovirus (HCMV) *in vitro* [173, 174]. Artesunate inhibited replication by decreasing the expression of HCMV proteins such as IE1-72 which are important for host cell dysregulation [175] as well as by inhibition of Akt in infected host cells, thereby inhibiting the PI3-K pathway which is required for HCMV DNA replication [174]. In one case of a patient with late drug-resistant CMV infection, potent anti-viral effects of artesunate were observed since artesunate treatment resulted in a 1.7–2.1-log reduction of viral load in the patient [176]. Interestingly, artesunate was also found to inhibit *in vitro* replication of members of the polyomavirus family, such as the human JC polyomavirus (JCPyV) and BK Polyomavirus (BKV) [177-179]. Artesunate's anti-viral efficacy against Epstein Barr virus (EBV) [180], hepatitis B virus (HBV) [181] and hepatitis C virus (HCV) [182] has also been demonstrated as observed by the inhibition of viral replication upon artesunate treatment [171]. Furthermore, artesunate also proved to be effective in the treatment of cervical intraepithelial neoplasia 2/3 (CIN2/3) in a Phase I dose-escalation study wherein the clearance of HPV genotypes was detected in 47.4% of the patients who demonstrated regression of tumors in response to artesunate [183]. In summary, the anti-viral activity of artesunate against a large number of pathogenic viruses might support its future use in anti-viral therapies.

### **1.3.3 Anti-cancer properties of artesunate**

In addition to its effect on human pathogens, artesunate has also been described to possess anti-cancer activity [184]. In this respect, cytotoxicity of artesunate towards several cancer types including colon cancer, pancreatic cancer, renal cancer, colorectal cancer, breast cancer, ovarian cancer, bladder cancer, esophageal cancer, glioblastoma and leukemia has been demonstrated in cell lines and in some cases also in animal models [185-197]. Moreover, there are also several ongoing or in few cases successfully completed Phase I and Phase II clinical trials for testing the efficacy of artesunate in patients with colorectal cancer, hepatocellular carcinoma, metastatic breast cancer and cervical epithelial neoplasias (<https://clinicaltrials.gov>) [183, 198, 199]. In Phase I trials for patients with advanced solid tumors, the maximum tolerable dose of intravenous artesunate was identified as 18 mg/kg [198]. Based on the experiments performed this far, artesunate has been described to exert its tumor-specific cytotoxic effects via various mechanisms of action. Numerous cell signaling pathways have also been implicated to be disrupted in the process [200]. In this regard, artesunate-induced inhibition of tumor cellular proliferation via interference with cell cycle progression has frequently been observed [201]. Breast cancer cells arrest in the G2/M phase with a concomitant increase of the cell cycle inhibitor protein p21 [202, 203] while bladder cancer cells arrest in G0/G1 and express lower levels of cell cycle activating proteins like CDK2 and CDK4 [197] upon artesunate treatment. For esophageal cancer, it has been shown that artesunate increases the levels of phosphorylated histone  $\gamma$ -H2AX (an indicator of DNA-double stranded breaks) and consequently promotes DNA damage and further enhances their radiosensitivity [204]. Like described for its antimalarial action, cleavage of the endoperoxide bridge of artesunate resulting in ROS production and oxidative damage is important also for artesunate's anti-cancer activity as evidenced in renal cancer cell lines and leukemic T cells [205, 206]. Experiments in mice with renal cell carcinoma xenografts have revealed that artesunate can also demonstrate anti-angiogenic and anti-metastatic properties and is responsible for the inhibition of vascular endothelial growth factor receptor 2 (VEGFR2) signaling [187]. Migration and invasiveness in embryonal Rhabdomyosarcoma cells is reduced upon artesunate treatment due to increased expression of adhesion molecules such as neural cell adhesion molecule (NCAM) and integrin  $\beta$ 1 [207]. Notably, cancer cells ensure their survival by several means including uncontrolled proliferation, altering host metabolism and escaping host immune surveillance [208, 209]. Artesunate has been found to interfere with one or more of these pathways upon exerting its cytotoxic effects on cancer cells. In this context, artesunate suppresses the hyperactive Wnt/ $\beta$ -catenin pathway in colorectal cancer cells [210]. Dihydroartemisinin (DHA), a further derivative of artemisinin [211], inhibits glycolytic metabolism in non-small cell lung cancer cells by inhibition of the mTOR pathway [212]. In lung cancer cells, artesunate was found to downregulate epidermal growth factor receptor (EGFR) and its phosphorylation and also prevented activation of its downstream kinase Akt [213], a pathway frequently activated in lung cancer to promote proliferation [214]. Inflammation in the tumor microenvironment is

another a key factor for cancer progression and in this respect artesunate has also been associated with anti-inflammatory properties in a rat model of colorectal cancer via the suppression of pro-inflammatory cytokines such as TNF- $\alpha$  [215]. In conclusion, observations derived from several cancer entities and models suggest that the well established anti-malarial drug artesunate might be a safe and promising alternative to cytotoxic chemotherapeutic drugs for cancer therapy.

#### **1.3.4 Modes of cell death induced by artesunate in cancer**

Cytotoxicity of drugs can be mediated by different genetically encoded mechanisms which have evolved in multicellular organisms for the elimination of superfluous, irreversibly damaged or potentially harmful cells [216-218]. These different cell death modes also have different consequences for the environment of the dying cell [219-221]. For the cytotoxic action of artesunate on cancer cells, apoptosis, ferroptosis, oncosis and autophagy have been reported to occur [186, 202, 222, 223]. A summary of the characteristics of the various modes of cell death is provided in table 1. In retinoblastoma cells, artesunate-induced mitochondrial apoptosis by the upregulation of the tumor suppressor Kruppel-like factor 6 (KLF6) [222]. Mitochondrial apoptosis also occurred in breast cancer cells treated with artesunate via its upregulation of pro-apoptotic proteins such as Bax and Bcl-2 and increased caspase 3 and caspase 9 activity [224]. As determined by artesunate-induced depletion of ATP, generation of ROS and activation of the protease calpain in renal cancer cells, an oncosis-like cell death was identified to occur in this case [187]. An oncosis-like morphology characterized by a swollen cytoplasm and several cytoplasmic vacuoles, was also observed in pancreatic and gastric cancer cells treated with artesunate [223, 225]. In another study in breast cancer cells, artesunate upregulated markers for the initiation of autophagy like Beclin1 [202]. In bladder cancer cells, artesunate treatment resulted in the formation of double membraned vesicles with cytoplasmic contents, a characteristic morphology of autophagy and increased expression of the autophagy marker LC3B-II [226]. Ferroptosis is a more recently described form of non-apoptotic cell death [227] and is introduced in detail in the subsequent section 1.4. Ferroptosis has been identified as a novel mechanism of cell death induction by several anti-cancer drugs [217]. In this context, artesunate has also been associated with ferroptosis induction for instance in pancreatic cancer where characteristic features of ferroptosis such as lipid peroxidation, iron dependency and ROS generation were observed following artesunate treatment [186]. Head and neck cancer and Burkitt's lymphoma are few other types of cancers where artesunate-induced ferroptosis was observed as detected by lipid peroxidation and ROS generation [228, 229]. Taken together, artesunate has been associated with the induction of several modes of cell death in different cancer entities.

	Mode of cell death				
	Apoptosis	Ferroptosis	Oncosis	Autophagy	Necrosis
Morphology	Cytoplasmic and nuclear condensation , DNA damage, apoptotic body formation, membrane blebbing [230, 231]	Cell swelling prior to cell rupture [232], small mitochondria with ruptured outer mitochondrial membrane [231, 233]	Cell swelling, coagulation of cytoplasm [234]	Vacuolization (double membraned autolysosomes), degradation of cytoplasmic contents within autophagic vacuoles, slight chromatin condensation [230, 231]	Cell swelling, membrane rupture and subsequent loss of organelles [233]
Biochemical features	Caspase activation [230]	Iron accumulation, lipid peroxidation, ROS generation [231]	Intracellular ATP depletion [234]	Increased lysosomal activity resulting in degradation of cytoplasmic contents [231, 233]	Release of cytosolic enzymes including lactate dehydrogenase [230]
Key proteins/ markers involved	Caspases, BAX, BCL2 [230, 231, 233]	GPX4, xCT, TFR1 [231, 233]	UCP-2 [235], calpains [236]	ATGs, LC3, Beclin 1 [231, 233, 237]	- [233]

**Table 1: Characteristics of various modes of cell death.**

## **1.4 Ferroptosis**

The term ferroptosis was coined in 2012 and represents a non-apoptotic, iron-dependent form of cell death characterized by extensive lipid peroxidation [227]. The physiological relevance of ferroptosis for instance in development of the human body is yet to be elucidated. Nevertheless, several studies have highlighted the significance of ferroptosis in various pathological conditions. Ferroptosis has been identified as the cause for severe cellular damage and death occurring in ischemic heart disease [238], lung epithelial cell death in cigarette smoking-associated chronic obstructive pulmonary disease [239] and accumulation of brain iron, loss of glutathione and lipid peroxidation in neurodegenerative conditions such as Alzheimer's disease [240, 241]. In addition, the potential of tumor suppressors such as p53 and BRCA1-associated protein 1 (BAP1) to prevent tumor development by promoting ferroptosis has also been described implicating a role for ferroptosis in tumor suppression [241-243].

The morphological features of ferroptosis are quite distinct from apoptosis however some necrosis-like morphological changes (see table 1) are found to occur [244].

Contrary to cell shrinkage and plasma membrane blebbing seen in apoptosis [245, 246], cells undergoing ferroptosis swell prior to cell death [232], similar to necrotic cells [247]. This swelling was identified to occur due to the formation of pores on the plasma membrane [232]. Interestingly, ferroptotic cell death is found to propagate from cell to cell in a wave like manner [248]. Moreover, chromatin condensation is not typically observed. Ultrastructurally, ferroptosis is characterized by shrunken mitochondria that have increased bilayer membrane density and reduction in cristae [227, 244].

The biochemical hallmarks of ferroptosis are iron accumulation and lipid peroxidation [227, 244] and will be discussed in the subsequent paragraphs. Under physiological conditions, ferrous iron ( $\text{Fe}^{2+}$ ) is required for regulation of metabolic processes like oxygen transport and energy metabolism [244]. During ferroptosis, the large amounts of free intracellular ferrous iron ( $\text{Fe}^{2+}$ ) interact with substrates like hydrogen peroxide ( $\text{H}_2\text{O}_2$ ) to generate hydroxyl or peroxide radicals via the Fenton reaction (Fig. 7a) [249, 250]. These radicals in turn aid in the generation of toxic lipid hydroperoxides (LOOH) and reactive oxygen species (ROS) which trigger ferroptotic cell death [227, 244, 251]. In this regard, one of the inducers of ferroptosis is transferrin, the iron-carrier protein [238]. Under normal circumstances, transferrin binds to its transferrin receptor 1 (TFR1) found on the surface of cells to enable the release of iron into the cytosol [238, 249]. This iron import is balanced by iron efflux mediated by the iron exporter ferroportin, found on the cell surface [249, 252]. Notably, malignant cancer cells often express a larger number of transferrin receptors (Fig. 7a) due to their higher demand for iron to enable proliferation [249, 253-255] and a downregulation of ferroportin has also been found in several cancer cell types [249, 255, 256]. As a result, this makes them more susceptible to ferroptosis inducers such as erastin and artemisinin derivatives [257-259]. Iron accumulation also occurs within cellular organelles called lysosomes (Fig. 7b) [260]. In this context, the role of functional lysosomes for the ferroptotic process has also been established [261]. Lysosomes are responsible for the autophagic degradation of ferritin, a cytosolic iron storage protein, via a process called ferritinophagy [244, 262]. This process which is mediated by nuclear receptor coactivator 4 (NCOA4) releases free ferrous iron into the lysosomes which is subsequently released into the cytoplasm [244, 262, 263]. Several experiments have demonstrated the successful inhibition of ferroptotic cell death upon the lack of iron availability. The potent iron chelator deferoxamine (DFO) was found to prevent ferroptosis in fibrosarcoma cells [227] as well as in rat models of spinal cord injury [264]. Another inhibitor, bafilomycin A1 (BAF-A1), inhibits the vacuolar-type  $\text{H}^+$ -ATPase, a pump present on the lysosomal membrane which is responsible for acidification of the lysosome (Fig. 7b) [265]. Functional lysosomes require this acidic environment for proper ferrous iron efflux [263]. Therefore, the use of BAF-A1, results in impaired lysosomal acidification, iron accumulation within the lysosome and thereby a deficiency in cytoplasmic ferrous iron [263]. Accordingly, pancreatic ductal adenocarcinoma cells and human fibrosarcoma cells were protected from ferroptotic cell death upon treatment with BAF-A1 emphasizing the importance of iron and functional lysosomes for ferroptosis [266, 267].

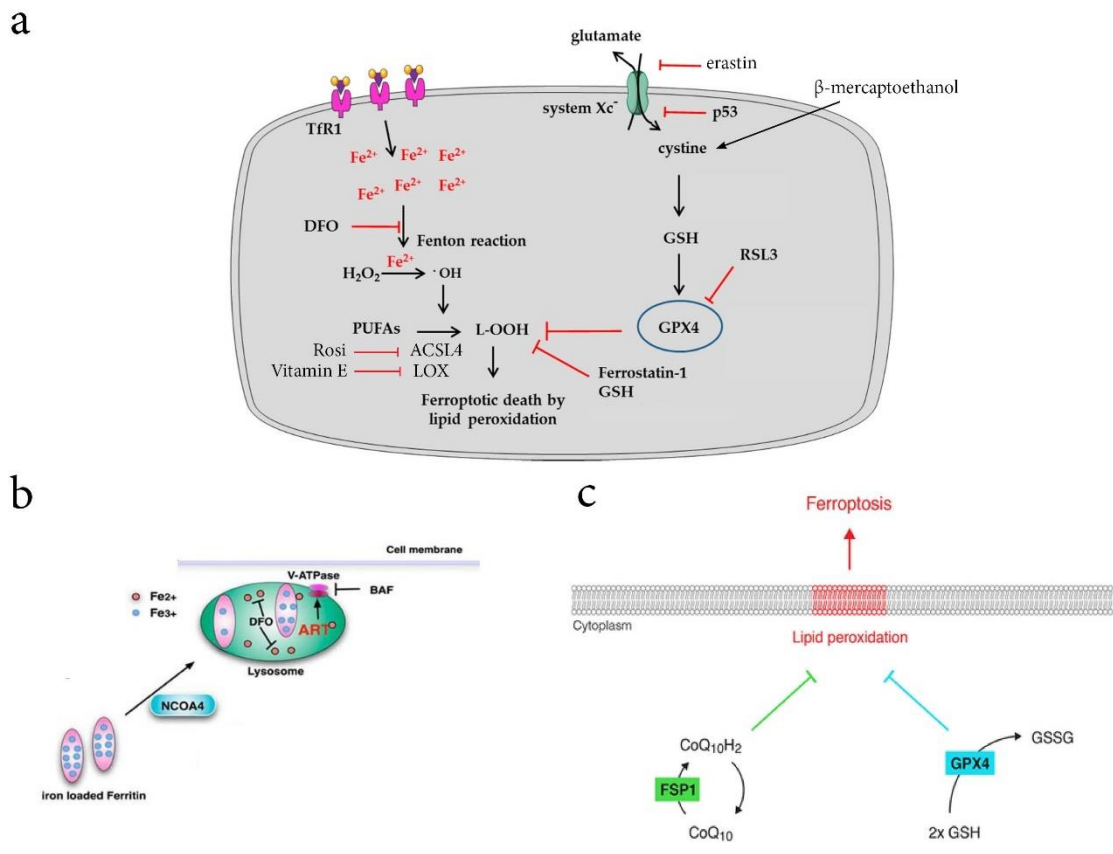


**Figure 7: Important aspects of ferroptosis.** a) The schematic diagram highlights the various pathways involved in ferroptosis including relevant ferroptosis inhibitors/inducers and their targets (Figure adapted from [249]; Copyright: Creative Commons Attribution license (CC BY 4.0)). b) The role of the lysosome in iron metabolism is depicted in the schematic image. In addition, the action of the lysosomal inhibitor (BAF) and the iron chelator (DFO) in the lysosome is represented. The image also demonstrates ART accumulation in the lysosomes and its promotion of lysosomal V-ATPase activity as per a study in human cervical cancer cells. (Figure adapted from [268]; Copyright: Creative Commons Attribution license (CC BY 4.0)). c) The two independent antioxidant pathways involving FSP1 and GPX4 which prevent lipid peroxide-mediated ferroptosis are depicted (Figure adapted from [269] with permission from American Chemical Society, Copyright 2020) (TFR1: Transferrin receptor 1; Fe<sup>2+</sup>: Ferrous iron; DFO: Deferoxamine; H<sub>2</sub>O<sub>2</sub>: Hydrogen peroxide; •OH: Hydroxyl radical; PUFAs: Polyunsaturated fatty acids; Rosi: Rosiglitazone; ACSL4: Acyl-CoA synthetase long-chain family member 4; LOX: Lipoxygenase; L-OOH: Lipid hydroperoxide; GSH: Glutathione; GPX4: Glutathione peroxidase 4; RSL3: RAS-selective lethal 3; ART: artesunate; BAF: Bafilomycin; NCOA4: nuclear receptor coactivator 4; V-ATPase: vacuolar H<sup>+</sup>-ATPase; FSP1: Ferroptosis suppressor protein 1; GSSG: Glutathione disulfide; CoQ<sub>10</sub>: Coenzyme Q<sub>10</sub>; CoQ<sub>10</sub>H<sub>2</sub>: Reduced Coenzyme Q<sub>10</sub>).

As part of the normal lipid metabolic process, polyunsaturated fatty acids (PUFAs) are esterified into membrane phospholipids [270, 271]. Ferroptosis-associated free radical-mediated oxidation of membrane phospholipids such as phosphatidylethanolamines (PEs), especially those containing arachidonic acid (AA) or adrenic acid (AdA), generates toxic lipid hydroperoxides (LOOH) which are the key mediators of ferroptosis (Fig. 7a) [270]. Under normal conditions, oxidative stress caused by excess lipid hydroperoxides is prevented by their reduction into the

respective lipid alcohols (LOH) [272, 273]. However, ferroptosis occurs when there is a fatal accumulation of such lipid hydroperoxides [274]. Acyl-CoA synthetase long-chain family member 4 (ACSL4) is an enzyme which activates PUFAs into their corresponding PUFA-CoA variants for their incorporation into membrane phospholipids [275]. In several studies, ACSL4 expression was found to positively correlate with ferroptosis sensitivity (Fig. 7a) [276-278]. In this regard, the use of the ACSL4 inhibitor, Rosiglitazone (Rosi) (a thiazolidinedione often used as an anti-diabetic [279]), ameliorated tissue damage in a ferroptotic mouse model [277]. Another set of important enzymes catalysing the peroxidation of PUFAs in phospholipids are the non-heme iron-containing dioxygenases called lipoxygenases (LOXs) (Fig. 7a) [280, 281]. The LOX enzyme, LOX-15 was found to aid in ferroptosis induced in human fibrosarcoma cells [280, 282, 283]. In this context, it was demonstrated that inhibition of LOX-15 by Vitamin E homologues (tocopherols and tocotrienols) was associated with a suppression of ferroptosis in various *in vitro* cellular models [284, 285]. Potent radical trapping antioxidants like ferrostatin-1 (Fer-1) and lipoxstatin-1 (Lip-1) have also demonstrated excellent potential to inhibit ferroptosis in cancer cells by slowing down the accumulation of lipid peroxides [227, 286].

In summary, despite its recent discovery [227], several hallmarks of ferroptosis and its associated proteins have already been described in the literature.

#### **1.4.1 Key antioxidant pathways in ferroptosis**

As a protective mechanism, several antioxidant pathways exist which are known to counteract ferroptotic cell death [244]. One such important component of the antioxidant system is the amino acid antiporter, System  $X_c^-$  (Fig. 7a) [227]. The antiporter consists of two components, a light-chain subunit (SLC7A11) and a heavy-chain subunit (SLC3A2) which function together to import cystine molecules into the cell and export glutamate molecules to the exterior in a 1:1 ratio [251, 287]. The imported cystine is ultimately involved in the synthesis of glutathione (GSH) [251, 288]. GSH is used as a cofactor by the selenoenzyme Glutathione peroxidase 4 (GPX4), which plays a pivotal role in controlling ferroptosis (Fig. 7a) [289]. GPX4 serves as a lipid hydroperoxidase and reduces toxic lipid peroxides to corresponding alcohols [289, 290]. Experiments have shown that inhibition of System  $X_c^-$  or the direct inhibition of GPX4 by the use of ferroptosis inducers such as erastin or RAS-selective lethal 3 (RSL3) respectively, triggered ferroptotic cell death via lipid peroxidation in cancer cells but not normal cells [291-293]. Notably, in fibrosarcoma cells sensitized to ferroptosis by the inhibition of System  $X_c^-$ , a promoter of cystine import,  $\beta$ -mercaptoethanol, was able to rescue ferroptotic cell death [227, 294]. In this manner, these experiments were able to reinforce the role of the system  $X_c^-$ /GPX4 axis as a crucial antioxidant pathway in the prevention of ferroptosis.

A further antioxidant protein acting independent of the GPX4 pathway is ferroptosis suppressor protein 1 (FSP1) (Fig. 7c) [295]. FSP1 is a flavoprotein which was initially found to complement the loss of *GPX4* in a ferroptosis-resistant breast cancer cell line [295]. FSP1 is recruited to the plasma membrane upon myristoylation following which it functions as an oxidoreductase to generate a reduced version of coenzyme Q10 (CoQ<sub>10</sub>) using NADPH, which in turn serves as a potent antioxidant to prevent lethal lipid peroxidation [296]. FSP1 was found to be expressed in several human cancer cells such as those from the lung and kidney and inhibition of FSP1 sensitized them to RSL3 (GPX4 inhibitor) induced ferroptosis [295, 296]. Therefore, the FSP1–CoQ<sub>10</sub>–NADPH pathway has been identified to act in parallel with the GPX4 pathway to prevent lipid peroxide-mediated ferroptosis [295].

#### **1.4.2 p53 and ferroptosis**

The tumor suppressor protein p53 is one of the most important regulators of programmed cell death [297, 298]. With respect to ferroptosis, pro as well as anti-ferroptotic functions have been described for p53 depending on the cellular context [251]. With regards to its role in supporting ferroptosis, studies have shown that p53 can downregulate the expression of *SLC7A11*, one of the components of the amino acid antiporter, System X<sub>c</sub><sup>-</sup>, thereby inhibiting cystine uptake and consequently promoting ferroptosis [243]. Furthermore, p53 can also activate its downstream target spermidine/spermine N1-acetyltransferase 1 (SAT1), an enzyme involved in polyamine metabolism, which in turn elevates levels of LOX-15 that promotes oxidative stress induced ferroptosis [299, 300]. Certain studies also demonstrated that p53 can inhibit ferroptosis, for instance, by the upregulation of its target gene *CDKN1A* (encoding p21) which promoted conservation of the antioxidant GSH [301]. In another study, p53 was shown to bind and subsequently block the activity of dipeptidyl-peptidase-4 (DPP4), an enzyme which was found to promote lipid peroxidation and ferroptosis [302]. Therefore, p53-regulated ferroptosis is highly context dependent with further studies underway to understand the basis for this observation [300].

## **1.5 Aims and approaches of this study**

The rising incidence of MCC cases urges the need for a thorough understanding of its carcinogenesis as well as for the development of novel safe and effective therapies for its treatment. In this regard, this study comprised two main goals:

### **1. Generation and evaluation of a vector system that allows independent regulatable expression of key factors of MCC carcinogenesis**

There are currently no perfect experimental models to study MCPyV-induced MCC development and information on the cell of origin of this cancer is lacking [44]. Although no recurrent genetic alterations in addition to MCPyV integration have been identified, there are candidate signaling pathways which likely contribute to MCC oncogenesis [36, 82, 94]. To allow testing of several factors for their possible contribution to MCC development in a temporal pattern, we wished to generate a set of antibiotic-selectable lentiviral vectors allowing the independent inducible expression of oncogenes and differentiation factors that might promote the development of MCC-like cells. The vectors to be generated and tested included doxycycline-inducible T antigens (MCPyV-positive MCC oncoproteins [70]), RheoSwitch-inducible atonal bHLH transcription factor 1 (ATOH1) (an MCC transcription factor [121]), IPTG-inducible GLI family zinc finger 1 (GLI1) (a transcription factor widely expressed in potential MCC precursor cells [94]) and IPTG-inducible dominant-negative Mastermind-like1 (dnMAML1) (a dominant negative version of a transcription factor to enable downregulation of the Notch pathway which is suppressed in MCCs [36]). In addition, to allow straight forward identification of an MCC-like phenotype we aimed to generate a fluorescence reporter allowing to monitor promoter activity of the MCC marker Keratin 20 (KRT20).

### **2. Analysis of the use of artesunate as a drug for the treatment of MCC**

In an attempt to identify further promising options for MCC treatment, we wished to test the cytotoxicity of the anti-malarial drug, artesunate, which additionally possesses anti-cancer and anti-viral properties [161, 172], towards MCPyV-positive MCC cell lines *in vitro* as well as in MCC xenotransplantation mice models *in vivo*. In order to get a clear understanding into the mechanism of action of artesunate, its influence on the T antigen oncoproteins driving MCPyV-positive MCC carcinogenesis was to be analyzed. In addition, we also wished to obtain information regarding the mode of cell death which artesunate might induce in MCPyV-positive MCCs and the possibility for its use in combinatorial immunotherapy in the future.

## **2. Materials and Methods**

### **2.1 Materials**

#### **2.1.1 Devices and equipment**

<b><u>Device/Equipment</u></b>	<b><u>Name</u></b>	<b><u>Manufacturer/Seller</u></b>
Autoclave	Tecnoclav 135S	Fedegari Autoclavi SPA Varioklav
Cell counting chamber	Neubauer Chamber	Paul Marienfeld GmbH & Co. KG
Cell culture benches	Heraeus	Hera Cell
	Hood Safe 2020	Thermo Scientific
Cell culture incubator	Hera cell	Heraeus
Centrifuges	Biofuge fresco Heraeus	Thermo Fisher Scientific
	Biofuge pico Heraeus	Thermo Electron Corporation
	Megafuge 2.0R	Thermo Fisher Scientific
	Mega Star 3.0R	VWR
	Micro Star 17	VWR
	Rotina 420 R	Hettich
Flow cytometers	Cytoflex LX	Beckman Coulter
	FACS Canto	BD Biosciences
Freezer (-20°C)	Comfort	Liebherr
Freezer (-80°C)	Forma -86C ULT Freezer	Thermo Electron Corporation
Fridge (4°C)	Mediline	Liebherr
Gel documentation system	Intas Science Imager	Intas Science Imaging
Gel electrophoresis chamber	Owl™ A2 Large Gel Systems	Thermo Fisher Scientific
Heating block/shaker	TCR 100 Test Tube Thermostat	Carl Roth GmbH & Co. KG
	Thermomixer 5436	Eppendorf
Ice machine	Scotsman AF 20	Scotsman Ice Systems
Incubator shaker (for bacterial cultures)	Innova	New Brunswick Scientific
Microbiological incubator	BM 200	Memmert

Micropipettes (2 µl, 10 µl, 20 µl, 100 µl, 200 µl, 1000 µl)	Eppendorf Research Plus	Eppendorf
	PIPETMAN®	Gilson
Micropipetting aid	accu-jet pro	Brand
Microplate reader (spectrophotometer)	Infinite M Nano	Tecan
Microscopes	Leica DMI1	Leica Microsystems
	Eclipse Ti	Nikon
Microwave	Sharp R-3V10	Sharp Electronics GmbH
Nanodrop	DS-11 Spectrophotometer	DeNovix
Nitrogen tank	Biosafe® 120 MD-Smart	Cryotherm GmbH & Co. KG
PCR/qPCR machines	Biometra TRIO	Analytik Jena
	PCR System 9700	Applied Biosystems
	qTOWER <sup>3</sup> G	Analytik Jena
	Veriti™ Thermal Cycler	Applied Biosystems
pH-Meter	inoLab pH 720	WTW
Power supplies	Electrophoresis EPS 600	Pharmacia Biotech
	PowerPac 300	Bio-Rad
Vortexer	Vibrofix VF1 Electronic	IKA-Werke GmbH & Co. KG
Water bath	-	Köttermann
Weighing balance	Ohaus LS 5000	Ohaus
Western Blot equipment	Mini Trans-Blot® Cell	Bio-Rad
Western Blot imaging system	Amersham Imager 600	GE Healthcare

### **2.1.2 Laboratory consumables**

<b><u>Consumable</u></b>	<b><u>Manufacturer/Seller</u></b>
µ-Slide 4 well chamber	Ibidi
Cell culture flasks (T25, T75 and T175)	Greiner Bio-One
Cell scraper	BD Biosciences
Clone cylinders	VWR
Cryopreservation tubes	Thermo Scientific

Eppendorf tubes (1.5 ml)	Sarstedt
Falcon tubes (15 ml and 50 ml)	Greiner Bio-One
Glass beakers, glass bottles and Erlenmeyer flasks	Schott
MicroAmp Optical 96 Well Reaction Plate (for qPCR)	Applied Biosystems
MicroAmp™ Optical Adhesive Film (for qPCR)	Applied Biosystems
Nitrocellulosemembranes (0.2 µm and 0.45 µm)	GE Healthcare
Parafilm	Bemis
PCR tubes	Sarstedt
Petri dishes (100 and 150 mm)	Thermo Fisher Scientific
Pipette tips (with and without filter)	Nerbe plus
Serological pipettes	Greiner Bio-One
Syringe	BD Discardit™ II
Syringe needles	BD Biosciences
Syringe (sterile) filter	Sarstedt
Terralin® liquid	Schülke
Well plates (6, 12, 24, 48 and 96 wells)	Greiner Bio-One
Whatman® filter paper	Hartenstein

### **2.1.3 Reagents and chemicals**

<b><u>Reagent/Chemical</u></b>	<b><u>Manufacturer/Seller</u></b>
Acrylamide 4 K solution 30% Mix (29:1)	AppliChem
Agarose	Biozym Scientific GmbH
Ammonium persulfate (APS)	Sigma Aldrich
β-Glycerophosphate	Sigma Aldrich
β-Mercaptoethanol	Sigma Aldrich
Boric acid	Sigma Aldrich
Bovine Serum Albumin (BSA)	Sigma Aldrich
Distilled water (dH <sub>2</sub> O)	Gibco
Dimethyl sulfoxide (DMSO)	Sigma Aldrich
Deoxyribonucleoside triphosphates (dNTPs) (100mM)	Invitrogen
Ethanol absolute	Chemsolute

Glycerin	neoLab
Glycine	Roth
Hydrogen Peroxide solution (30%)	Sigma Aldrich
Isopropanol	VWR Chemicals
LB agar	Invitrogen
LB broth base	Invitrogen
Luminol	Sigma Aldrich
Matrigel®	Corning®
Methanol	Sigma Aldrich
Milk powder	Roth
NP-40	Sigma Aldrich
P-Coumaric acid	Sigma Aldrich
Phosphate buffered saline (PBS)	Sigma Aldrich
Polybrene	EMD Millipore
Propidium Iodide	Sigma Aldrich
Protease inhibitor cocktail tablets	Roche
Tetramethylethylenediamine (TEMED)	Roth
Tris	Roth
Tris Hydrochloride (Tris-HCl)	Roth
Trypsin/EDTA (10X TE) (0.5/0.2% in PBS)	Sigma Aldrich
Tween 20	Sigma Aldrich
Sodium Chloride (NaCl)	Sigma Aldrich
Sodium Orthovanadate	Sigma Aldrich
Ultra-pure SDS-Solution (10%)	Invitrogen

#### **2.1.4 Cell culture media and supplements**

<b><u>Medium/Supplement</u></b>	<b><u>Manufacturer/Seller</u></b>
Bovine pituitary extract	Invitrogen Life Technologies
Epidermal growth factor	Invitrogen Life Technologies
Fetal Bovine Serum (FBS) Superior	Biochrom GmbH
Keratinocyte serum-free medium	Invitrogen Life Technologies
Penicillin/Streptomycin (Pen/Strep) (10000 U/ml/10 mg/ml)	Sigma Aldrich

RPMI-1640	Sigma Aldrich
-----------	---------------

### **2.1.5 Pre-prepared buffers and solutions**

<b><u>Buffer</u></b>	<b><u>Manufacturer/Seller</u></b>
10X T4 Ligation buffer	New England Biolabs
10X T4 Ligation buffer (containing 10 mM ATP)	New England Biolabs
ATP solution (25 mM)	Epicentre
BamHI Buffer	Thermo Scientific
Cfr9I Buffer	Thermo Scientific
Dithiothreitol (DTT, 100 mM)	Invitrogen
DNase/RNase free water	Invitrogen
Ethylenediaminetetraacetic acid (EDTA, 0.5 M)	Sigma Aldrich
First Strand Buffer (5x)	Invitrogen
Gel loading dye orange (6X)	New England Biolabs
Gene ruler 100 bp plus DNA ladder	Thermo Scientific
Gram's crystal violet solution	Merck
HD green Plus DNA stain	Intas Science
JetPrime® buffer	Polyplus Transfection®
JetPrime® transfection reagent	Polyplus Transfection®
Lane Marker Reducing Sample Buffer	Thermo Scientific
Low ROX SYBR Master Mix dTTP blue	Takyon
Oligo dT 12-18 Primer (0.5 µg/µl)	Life Technologies
Page Ruler Plus Prestained Protein Ladder	Thermo Scientific
PonceauS	Chem Cruz
Q5 reaction buffer	New England Biolabs
Random Primers (3 µg/µl)	Invitrogen
Tango Buffer (10X)	Thermo Scientific
Trypan Blue Solution	Sigma Aldrich

## 2.1.6 Freshly prepared buffers, solutions and media

<u>Buffer/Solution</u>	<u>Preparation</u>
Agarose gel (1%)	<ul style="list-style-type: none"> <li>- 1 g Agarose</li> <li>- 100 ml 1X TBE</li> <li>- Boil in the microwave to dissolve</li> <li>- 5 µl HD green Plus DNA stain once cool</li> <li>- Pour into gel chamber for solidification</li> </ul>
APS solution (10%)	<ul style="list-style-type: none"> <li>- 1 g APS</li> <li>- Dissolve in 10 ml dH<sub>2</sub>O</li> </ul>
Bacterial culture preservation medium (LB + 60% Glycerin)	<ul style="list-style-type: none"> <li>- 20 ml LB medium</li> <li>- 30 ml Glycerin</li> </ul>
Blotting buffer (10X)	<ul style="list-style-type: none"> <li>- 144.1 g Glycine</li> <li>- 30.3 g Tris-HCl</li> <li>- Dissolve in 1 l dH<sub>2</sub>O</li> </ul>
Blotting buffer (1X)	<ul style="list-style-type: none"> <li>- 70 ml 10X Blotting buffer</li> <li>- 140 ml Methanol</li> <li>- Mix with dH<sub>2</sub>O up to 700 ml</li> </ul>
Buffer B	<ul style="list-style-type: none"> <li>- 125 ml Tris-HCl (pH 8.8)</li> <li>- 5 ml 10% SDS</li> <li>- Mix with dH<sub>2</sub>O up to 250 ml</li> </ul>
Buffer C	<ul style="list-style-type: none"> <li>- 125 ml Tris-HCl (pH 6.8)</li> <li>- 5 ml 10% SDS</li> <li>- Mix with dH<sub>2</sub>O up to 250 ml</li> </ul>
Cell culture freezing medium (FBS + 10% DMSO)	<ul style="list-style-type: none"> <li>- 5 ml DMSO</li> <li>- Mix with FBS up to 50 ml</li> </ul>
E1A lysis buffer	<ul style="list-style-type: none"> <li>- 20 mg β-Glycerophosphate</li> <li>- 25 ml Sodium Orthovanadate</li> <li>- 200 µl Protease inhibitor</li> <li>- Dissolve in ELB lysis buffer up to 5 ml</li> </ul>
ELB Lysis buffer	<ul style="list-style-type: none"> <li>- 3 ml 5 M NaCl</li> <li>- 5 ml 1 M Hepes (pH 7.5)</li> <li>- 1 ml 0.5 M EDTA</li> <li>- 100 µl NP-40</li> <li>- Mix with dH<sub>2</sub>O up to 100 ml</li> </ul>
Electrophoresis buffer (10X)	<ul style="list-style-type: none"> <li>- 144.1 g Glycine</li> <li>- 30.3 g Tris-HCl</li> <li>- 100 µl 10% SDS</li> <li>- Dissolve in 1 l dH<sub>2</sub>O</li> </ul>
Electrophoresis buffer (1X)	<ul style="list-style-type: none"> <li>- 100 ml 10X Electrophoresis buffer</li> <li>- Mix with dH<sub>2</sub>O up to 1 l</li> </ul>
Enhanced Chemiluminescence (ECL) buffer	<ul style="list-style-type: none"> <li>- 12.1 g Tris-HCl</li> <li>- Dissolve in 800 ml dH<sub>2</sub>O</li> <li>- Adjust pH to 8.5</li> <li>- Mix with dH<sub>2</sub>O up to 1 l</li> </ul>
Flow cytometry wash buffer (PBS + 1% FBS)	<ul style="list-style-type: none"> <li>- 500 µl FBS</li> <li>- Mix with PBS up to 50 ml</li> </ul>

Flow cytometry wash buffer (PBS + 0.1% BSA)	<ul style="list-style-type: none"> <li>- 50 mg BSA</li> <li>- Dissolve in 50 ml PBS</li> </ul>
LB agar for bacterial cultures	<ul style="list-style-type: none"> <li>- 32 g LB Agar</li> <li>- Mix with 1 l dH<sub>2</sub>O and autoclave</li> <li>- 1 ml ampicillin after cooling to 50 °C</li> <li>- Pour into 10 cm petri dishes and leave to solidify</li> </ul>
LB medium for bacterial cultures	<ul style="list-style-type: none"> <li>- 20 g LB broth base</li> <li>- Dissolve in 1 l dH<sub>2</sub>O and autoclave</li> </ul>
Luminol solution	<ul style="list-style-type: none"> <li>- 0.44 g Luminol</li> <li>- Dissolve in 10 ml DMSO</li> </ul>
Milk (5% in TBST)	<ul style="list-style-type: none"> <li>- 5 g milk powder</li> <li>- Dissolve in 100 ml TBS-T</li> </ul>
NaCl solution (5M)	<ul style="list-style-type: none"> <li>- 146.1 g NaCl</li> <li>- Dissolve in 500 ml dH<sub>2</sub>O</li> </ul>
Sodium Orthovanadate solution	<ul style="list-style-type: none"> <li>- 18.39 mg sodium orthovanadate</li> <li>- Dissolve in 10 ml dH<sub>2</sub>O</li> </ul>
P-coumaric acid solution	<ul style="list-style-type: none"> <li>- 0.15 g p-coumaric acid</li> <li>- Dissolve in 10 ml DMSO</li> </ul>
Protease inhibitor solution	<ul style="list-style-type: none"> <li>- 1 tablet</li> <li>- Dissolve in 2 ml dH<sub>2</sub>O</li> </ul>
RPMI complete medium (RPMI + 10% FBS and 1% Pen/Strep)	<ul style="list-style-type: none"> <li>- 500 ml RPMI 1640</li> <li>- 50 ml FBS</li> <li>- 5 ml Pen/Strep</li> </ul>
Stripping buffer stock	<ul style="list-style-type: none"> <li>- 200 ml 10% SDS</li> <li>- 125 ml 0.5 M Tris-HCl (pH 6.7)</li> <li>- Mix with dH<sub>2</sub>O up to 1 l</li> </ul>
Stripping buffer (used for immunoblots)	<ul style="list-style-type: none"> <li>- 100 ml Stripping buffer stock</li> <li>- 800 µl β-mercaptoethanol</li> </ul>
Tris-Borate EDTA (TBE) 1X	<ul style="list-style-type: none"> <li>- 200 ml 5X TBE</li> <li>- Mix with dH<sub>2</sub>O up to 1 l</li> </ul>
Tris-Borate EDTA (TBE) 5X	<ul style="list-style-type: none"> <li>- 54 g Tris-HCl</li> <li>- 27.5 g of Boric acid</li> <li>- 20 ml 0.5 M EDTA</li> <li>- Dissolve in dH<sub>2</sub>O up to 700 ml</li> <li>- Adjust pH to 8.0</li> <li>- Mix with dH<sub>2</sub>O up to 1 l</li> </ul>
Tris buffered saline (TBS) 10X	<ul style="list-style-type: none"> <li>- 24.2 g Tris-HCl</li> <li>- 80 g NaCl</li> <li>- Dissolve in dH<sub>2</sub>O up to 700 ml</li> <li>- Adjust pH to 7.6</li> <li>- Mix with dH<sub>2</sub>O up to 1 l</li> </ul>
Tris buffered saline (TBS) 1X	<ul style="list-style-type: none"> <li>- 100 ml 10X TBS</li> <li>- Mix with dH<sub>2</sub>O up to 1 l</li> </ul>
Tris buffered saline - Tween 20 (TBS-T) 1X	<ul style="list-style-type: none"> <li>- 100 ml 10X TBS</li> <li>- Mix with dH<sub>2</sub>O up to 1 l</li> <li>- Add 500 µl Tween 20</li> </ul>
Tris-HCl solution pH 6.7 (0.5 M)	<ul style="list-style-type: none"> <li>- 60.56 g of Tris-HCl</li> <li>- Dissolve in dH<sub>2</sub>O up to 600 ml</li> </ul>

	<ul style="list-style-type: none"> <li>- Adjust pH to 6.7</li> <li>- Mix with dH<sub>2</sub>O up to 1 l</li> </ul>
Tris-HCl solution pH 6.8 (0.5 M)	<ul style="list-style-type: none"> <li>- 60.56 g of Tris-HCl</li> <li>- Dissolve in dH<sub>2</sub>O up to 600 ml</li> <li>- Adjust pH to 6.8</li> <li>- Mix with dH<sub>2</sub>O up to 1 l</li> </ul>
Tris-HCl solution pH 8.8 (1.5 M)	<ul style="list-style-type: none"> <li>- 181.71 g of Tris-HCl</li> <li>- Dissolve in dH<sub>2</sub>O up to 600 ml</li> <li>- Adjust pH to 8.8</li> <li>- Mix with dH<sub>2</sub>O up to 1 l</li> </ul>

### **2.1.7 Kits**

<b><u>Kit</u></b>	<b><u>Manufacturer/Seller</u></b>
jetPRIME® Polyplus-transfection	Polyplus
PeqGOLD Total RNA Kit	VWR
Pierce™ BCA Protein Assay Kit	Thermo Fisher Scientific
Presto™ Mini Plasmid Kit	Geneaid
QIAamp® DNA Mini Kit	Qiagen
QuikChange Lightning Site-Directed Mutagenesis Kit # 210518	Agilent
Wizard® SV Gel and PCR Clean-Up System	Promega

### **2.1.8 Antibodies for immunoblotting**

#### **2.1.8.1 Primary antibodies**

<b><u>Antibody</u></b>	<b><u>Source and clonality</u></b>	<b><u>Manufacturer/Seller</u></b>	<b><u>Concentration used</u></b>
2T2 (against MCPyV T antigens)	Hybridoma cell supernatant α Mouse	Prepared in our laboratory	1:10
β-Actin (AC-15)	Mouse, monoclonal	Sigma Aldrich	1:1000
β-Tubulin (TUB2.1)	Mouse, monoclonal	Sigma Aldrich	1:5000
FSP1	Rat, monoclonal	AG Friedmann Angeli (University of Würzburg)	1:10
HA-tag	Mouse, monoclonal	Abcam	1:1000

LSD1	Rabbit, monoclonal	Cell Signaling Technology	1:1000
MCPyV LT (CM2B4)	Mouse, monoclonal	Santa Cruz Biotechnology, Inc.	1:200
p53 (DO-1)	Mouse, monoclonal	Santa Cruz Biotechnology, Inc.	1:200
TERT (A-6)	Mouse, monoclonal	Santa Cruz Biotechnology, Inc.	1:100
Vinculin	Mouse, monoclonal	Sigma Aldrich	1:1000

### **2.1.8.2 Secondary antibodies**

<b><u>Antibody</u></b>	<b><u>Manufacturer/Seller</u></b>	<b><u>Concentration used</u></b>
Anti-Mouse HRP	Dako	1:1000
Anti-Rabbit HRP	Dako	1:1000
Anti-Rat HRP	Dako	1:1000

### **2.1.9 Antibodies for flow cytometry**

#### **2.1.9.1 Primary antibodies**

<b><u>Antibody</u></b>	<b><u>Manufacturer/Seller</u></b>	<b><u>Concentration used</u></b>
ADRA2C	Biorbyt	1:100
CELSR3-APC	Macs miltenyi	1:50
Contactin 2 (F-1)	Santa Cruz Biotechnology, Inc.	1:50
FITC anti-human HLA-A,B,C (clone W6/32)	BioLegend	1:20
FITC mouse IgG2a, κ isotype control	BioLegend	1:20
Glypican-3 (F-3)	Santa Cruz Biotechnology, Inc.	1:50
Human Carbonic Anhydrase IX/CA9 Alexa Fluor® 405	R&D Systems	1:50
Human DLL3	R&D Systems	1:50
Human LINGO-1 Alexa Fluor® 750	R&D Systems	1:50
Neurensin-1	Santa Cruz Biotechnology, Inc.	1:50

Neuritin	Thermo Fisher Scientific	1:50
PE/Cy7 anti-human CD274 (B7-H1, PD-L1)	BioLegend	1:20
PE/Cyanine7 mouse IgG2b, $\kappa$ isotype contol	BioLegend	1:20
Slit1 (G-4) AF680	Santa Cruz Biotechnology, Inc.	1:50

### **2.1.9.2 Secondary antibodies**

<b><u>Antibody</u></b>	<b><u>Manufacturer/Seller</u></b>	<b><u>Concentration used</u></b>
Mouse anti-goat IgG-CFL 647	Santa Cruz Biotechnology, Inc.	1:100
Mouse anti-rabbit IgG-CFL 647	Santa Cruz Biotechnology, Inc.	1:100
Polyclonal Rabbit Anti-Mouse Immunoglobulins/FITC	Dako	1:50

### **2.1.10 Enzymes**

<b><u>Enzyme</u></b>	<b><u>Manufacturer/Seller</u></b>
AsiSI	Thermo Scientific
BamHI	Thermo Scientific
BglII	Thermo Scientific
BseJI	Thermo Scientific
BshTI (AgeI)	Thermo Scientific
BsmBI	Thermo Scientific
Bsp119I	Thermo Scientific
EcoRI	Thermo Scientific
KfII	Thermo Scientific
NdeI	Thermo Scientific
NotI	Thermo Scientific
PacI	Thermo Scientific
Q5 High-Fidelity DNA Polymerase	New England Biolabs
RNase A	Fermentas
Sall	Thermo Scientific
SfaAI	Thermo Scientific

SpeI	Thermo Scientific
Super Script II Reverse Transcriptase	Invitrogen
T4 DNA Ligase	New England Biolabs
T4 PNK (polynucleotide kinase)	Thermo Scientific
T7 DNA Ligase	Enzymatics
XbaI	Thermo Scientific
XhoI	Thermo Scientific

### **2.1.11 Primers and oligos**

#### **2.1.11.1 Primers used for PCR and qPCR**

The primers were ordered from Sigma Aldrich. The primers marked with a star (\*) were used for nested PCRs.

<b><u>Primer</u></b>	<b><u>Sequence (5'-3')</u></b>
ADRA2C_sybr_fw	AGAAGCGCTTCACCTTTGTG
ADRA2C_sybr_rv	AGGCTGTAGCTGAAGAAGAAGG
AIFM2 (FSP1) fw	ATTCTCTGCACCGGCATCAA
AIFM2 (FSP1) rv	GCTCGTTCACTCTCAGAGCA
ATOH1_sybr_fw	CAGCCAGTGCAGGAGGAAAA
ATOH1_sybr_rv	GAAAATTCCCCGTCGCTTCT
BSD 5 prime rev	ATGTCAGATTGCCTGCTGCT
CA9_sybr_fw	AGAAGAGGGCTCCCTGAAGT
CA9_sybr_rv	CCTCCATAGCGCCAATGACT
CELSR3_sybr_fw	TTACGCTGTCCCTCTCGTTC
CELSR3_sybr_rv	AGTCGTGCTTCTCGTTCAGG
CNTN2_sybr_fw	GTGGCCCTTGTCTCCTCTTC
CNTN2_sybr_rv	GTCTTCAAAGACAGGCCCGA
DLL3_sybr_fw	GCTCGAGGACGAATGTGAGG
DLL3_sybr_rv	TCTAGGCATCGGCATTCACC
dnMAML1 Sybr fw	GCCAACACACCTTCGCCC
Gli1 Sybr fw (2)	TGACCCCACCACCAATCAGTA
Gli1 Sybr rv (2)	AGACAGTCCTTCTGTCCCCACA
GPC3_sybr_fw	TGAAGAAACCTTATCCAGCCGA

GPC3_sybr_rv	TGCAGATGTAGCCAGGCAAA
KRT20 mNeon integ fw*	GCCCGTTACAGCAGCCAGTTAG
KRT20 mNeon integ rev*	ACGTCCCCCGCTTGTTTCAGTAG
KRT20 mNeon integ vor fw*	GCGCCGCACTGAAAGAACA
KRT20 mNeon integ vor rev*	GGCGCCGTCCTCAAAGTGC
KRT20_sybr_fw	GGACGACACCCAGCGTTTAT
KRT20_sybr_rv	CGCTCCCATAGTTCACCGTG
LINGO1_sybr_fw	CCAGTCTGTTTGCCTCCCAA
LINGO1_sybr_rv	CAGCACCAGCAGGAGGATG
LT_sybr_mRNA_fw2	CTCGTCAACCTCATCAAAC
LT_sybr_mRNA_rv2	GGAGCAAATTCCAGCAAA
mNeon Sybr fw	TGGCCGCCAACTATCTGAAG
mNeon Sybr rv	AGCTCTGTCTTGCTGTGCTT
NRN1_sybr_fw	CCTGGACGACAAGACGAACA
NRN1_sybr_rv	AATCCGTAAGGGCTGTGACC
NRSN1_sybr_fw	CACCTAACAGGTGGAGCTCAG
NRSN1_sybr_rv	GCTTCGCAAATGCTTCGAT
RPLP0 fw	CCATCAGCACCACAGCCTTC
RPLP0 rv	GGCGACCTGGAAGTCCAAC
SLIT1_sybr_fw	CAGCGCCTGGAACCTCAATG
SLIT1_sybr_rv	TCCACTGCTCCAATCTGGTTC
St-fw2_sg	TACTTCCTTCCTCTGTTGAC
sT-rv_sg	TCCTGATCTCCACCATTCT
T2A 3 prime fw	AGGAGTGGCAGAAGGCCT
TA Exon1 endo fw	ATGGCAACATCCCTCTGATGA
TA Exon1 endo rv	AAGTCACTTCTGAGCTTGTGG
V5 dnMAML1 Sybr rv	AGGGATAGGCTTACCGTGC

### **2.1.11.2 Primers and oligos used for cloning, mutagenesis and sequencing**

The primers were ordered from Sigma Aldrich.

<b><u>Primer</u></b>	<b><u>Sequence (5'-3')</u></b>
2ndStop_sT_fw	ATCTGCACCTTTTCTAGTGAAGGGAGTGGAGCAAC
AsiSI_AToh1_rv	ACACACGCGATCGCCGACCTAACTTGCCTCATCC G
BseJI_LacO_fw	ACACACGATTGGAATCGGAGCTCCACCGCGGT
BshT1_LH_KRT20_840_fw	ACACACACCGGTTGGCTCACAGTTCTGGAGGC
Bsp119I-flag_fw	ACACACTTCGAAGCCACCATGGACTACAAGGACG
Bsp119I_LH_KRT20_840_rv	ACACACTTCGAACACGACTTCAGATGACACGACCT TG
Contig 3 Fw	TGCTTACTGCATCTGCACCT
Donor_seq	CAAATAGGGGTTCGCGC
EcoRI_HygR_rv	ACACACGAATTCCTATTCTTTGCCCTCGGAC
EcoRI_pCW_Flag_fw	ACACACGAATTCGCCACCATGGACTACAAGG
EcoRI_PGK_rv	ACACACGAATTCCTGCAGGTCGAAAGGCC
EF1a_5prime_seq_rv	CCAACTTCTCGGGGACTGT
ERK5_sybr_fw	CTAAGTCACAGGTGGAGGACC
Gblock_clono_fw	GGGTCGTTTGTTCACTAGT
induc_shRNA_clone PCR_rv	CGGAAGGATCAGGACGCTC
induc_shRNA_seq1	TCGGGTTTATTACAGGGACAGC
KflI_LacO_rv	ACACACGGGTCCCCTGCTCCCTGCTTGTGTGT
KRt20_shRNA_E_fw	TCCCGCAGTCCAACCTCAAACCTTGATGTGCTTTCA AGTTTGGAGTTGGACTGCTTTTT
KRt20_shRNA_E_rv	CGGGAAAAAGCAGTCCAACCTCAAACCTTGAAAGCA CATCAAGTTTGGAGTTGGACTGC
Krt_LH_850_rv	CTTACAAGATGCCGGCAC
LT_WaGa_Stop_fw	CTCCATTCTCAAGAAAGTAGGAAGGGAGTGGAGC AACG
minCMV_fw	CGGTAGAAGGTAGGCGTGTACGGTGGGAGGCCTA TATAAGCAGAGCTCGTTTGTAGTGAACCGTCAGATCG CCTGG
minCMV_rv	CTAGCCAGGCGATCTGACGGTTCCTAAACGAGC TCTGCTTATATAGGCCTCCACCGTACACGCCTAC CTTCTAC
NdeI_RH_KRT20_1050_fw	ACACACCATATGAATATCTAAATAGCTACCAGAAG G

Neondonor_clono_rv	GTTATCCTAGGTGGGCCG
NLUC_3prime_clono_fw	TCAACGGAGTGACCGGCT
NLUC_rv	CACCGCTCAGGACAATCCT
NotI_dnMAML1_rv	AGATCCTTCGCGGCCG
NotI_eGFP_rv	ACACACGCGGCCGCTTACTTGTACAGCTCGTCCAT GC
NotI_pCW_rv	ACACACGCGGCCGCGAGCCAATCCCCTCCTT
Oligo_KRT20RH_fw	CTAGTCATATGGGTCCTCCACCTGTGACTTAGCAG G
Oligo_KRT20RH_rv	TCGACCTGCTAAGTCACAGGTGGAGGACCCATAT GA
Ori_Seq	GCCACCTCTGACTTGAGCG
pCDH_NFAT_clono_rv	GTGCGCTCTGCCACTGA
pCW_ST_stop_fw	CTGCATCTGCACCTTTTCTAGGAAGGGAGTGGAG CAA
PeTa_stop_fw	CAGATCCTCCTCCTTCACCA
pIH-seq_fw	CGTCTAGGCCCCCCGAAC
pgreen_ltr_puro_bb_rv	CCCATCGCGATCTAATTC
pgreen_NCCR_neon-clono_rv	GCCTTCACCGACGTGATGG
pSLIK_seq_vector_fw	CGACAGGCCCGAAGGAAT
Sall_Gli1	ACACACGTCGACCGCCACCATGGACTACAAAG
Sall__RH_KRT20_1050_rv	ACACACGTCGACATGAAATGTCCAGAGTAGG
SfaAI_Lacl_rv	ACACACGCGATCGCGCGCTCAAACCTTCCTCTTC
SpeI_HygR_fw	ACACACACTAGTATGAAAAAGCCTGAACTCAC
T7	TAATACGACTCACTATAGG
UAS_clono_fw	GGATCAACAGCTCCTGGG
WPRE_3prime_fw	CGAGTCGGATCTCCCTTTG
XbaI_lacl_fw	GCGATCGTCTAGAGGTACCC
XbaI_PGK_fw	ACACACTCTAGATAATAACTTCGTATAGCATAACATT ATACGAAGTTATTGCTAGCAATTCTACCGGGTAGG
XhoI_dnMaml1_fw	ACACACCTCGAGAATTCGCCACCATGCTGC
XhoI_eGFP_fw	ACACACCTCGAGGCCACCATGGTGAGCAAGGGCG AG

### **2.1.12 Antibiotics**

<b><u>Antibiotic</u></b>	<b><u>Manufacturer/Seller</u></b>
Ampicillin (50 mg/ml)	Sigma Aldrich
Blasticidin (10 mg/ml)	InvivoGen
G418 (Neomycin) (100 mg/ml)	InvivoGen
Hygromycin (100 mg/ml)	InvivoGen
Puromycin (10 mg/ml)	InvivoGen
Zeocin™ (100 mg/ml)	InvivoGen

### **2.1.13 Inducers, inhibitors and drugs**

<b><u>Inducer/Inhibitor/Drug</u></b>	<b><u>Manufacturer/Seller</u></b>
(1S,3R)-RSL3	Cayman Chemical
Artesunate	Sigma Aldrich
Bafilomycin A1	Hycultec
Deferoxamine	Hycultec
Doxycycline	Sigma Aldrich
Ferrostatin-1	Cayman Chemical
Interferon- $\gamma$ (IF002)	Sigma Aldrich
IPTG	Cayman Chemical
Nutlin-3a	Sigma Aldrich
Rosiglitazone	Cayman Chemical
RSL1 (RG 102240)	Tocris
Vitamin E ( $\alpha$ -Tocotrienol)	Cayman Chemical
Z-VAD-FMK	MedChemExpress

### **2.1.14 Mammalian cell lines and primary cells**

Of the several cell lines used in this study, the MCPyV-positive MCC cell lines, WaGa and BroLi, were established in the department of dermatology in Würzburg while PeTa was established in the department of dermatology in Mannheim [70, 303]. The other MCPyV-positive MCC cell lines, MKL-1 [304], MKL-2 [305] and MS-1 [306] were established and characterized previously by other groups [303]. The MCPyV-negative

MCC cell lines, MCC13 [307], MCC26 [305] and UIISO [308] have been described previously. The primary keratinocytes were obtained from the University Hospital Center of Tours (France) [84] and the primary fibroblasts were obtained from Promocell. Further cell lines used included HaCaT (CLS Cat# 300493/p800\_HaCaT, RRID:CVCL\_0038) [309], NIH3T3 (RCB Cat# RCB2767, RRID:CVCL\_0594) [310], U2OS (DSMZ Cat# ACC-785, RRID:CVCL\_0042) [311], HEK293T (CCLV Cat# CCLV-RIE 1018, RRID:CVCL\_0063) [312] and MDA-MB-213 (ECACC Cat# 92020424, RRID:CVCL\_0062) [313].

A brief overview of the MCC cell lines used in this study is provided in the table below.

<b><u>MCC cell lines</u></b>	<b><u>MCPyV Status</u></b>	<b><u>Origin</u></b>	<b><u>Morphology and cell growth</u></b>
BroLi	+	Pleural effusion from a 54 year old male	Spheroids in suspension
MKL-1	+	Nodal metastasis from a 26 year old male	Spheroids in suspension
MKL-2	+	Isolated from a 72 year old male MCC patient	Spheroids in suspension
MS-1	+	Tumor biopsy from a female MCC patient	Spheroids in suspension
PeTa	+	Primary back tumor from a 65 year old male	Single cells in suspension
WaGa	+	Ascites from a 66 year old male	Single cells in suspension
MCC13	-	Metastatic cervical node biopsy from an 80 year old female	Adherent
MCC26	-	Isolated from an 82 year old female MCC patient	Adherent
UIISO	-	Isolated from a 46 year old female MCC patient	Adherent

A brief overview of the other cell lines and primary cell types used in this study is provided in the table below.

<b><u>Primary cell type/ Cell lines</u></b>	<b><u>Source/Description</u></b>	<b><u>Cell growth</u></b>
Primary keratinocytes	Isolated from human abdominal samples	Adherent
Primary fibroblasts	Isolated from the dermis of juvenile foreskin (Promocell)	Adherent
HaCaT	Immortalized human adult skin keratinocytes	Adherent

HEK293T	Human embryonic kidney cells expressing an allele of the SV40 T antigen	Adherent
MDA-MB-231	Human epithelial breast cancer cells	Adherent
NIH3T3	Murine embryonic fibroblasts	Adherent
U2OS	Human osteosarcoma epithelial cells	Adherent

Cell lines that were previously transduced in the laboratory were also used for our study and are summarized in the table below.

<u>Cell Line</u>	<u>Name of the vector</u>
MKL-1	pLVX NCCR mNeonGreen mRuby3
MKL-1, WaGa	pIH LT_(254) sh6 TA
MKL-1, MKL-2, WaGa	TA.shRNA.tet
MKL-1, MKL-2, WaGa	RB1 shRNA
MKL-1, WaGa	pGreenFire

### **2.1.15 Mice for *in vivo* experiments**

Five-week-old NOD.CB17/Prkdcscid female mice were used for this study and were obtained from Charles River. They were housed under pathogen-free conditions.

### **2.1.16 Bacteria for transformation**

<u>Bacterial cell type</u>	<u>Seller</u>
Competent <i>E. coli</i> K12	Bioline

## 2.1.17 Plasmids

### 2.1.17.1 Previously generated plasmids

<u>Name of the vector</u>	<u>Description</u>	<u>Antibiotic resistance</u>	
		<u>Bacteria</u>	<u>Mammalian cells</u>
64221 mCherry KRT20 A	Constitutive expression of KRT20 gRNA and Cas9 endonuclease	Ampicillin	-
64222 mCherry KRT20 A	Constitutive expression of KRT20 gRNA and Cas9 endonuclease	Ampicillin	-
Induc p53 shRNA puro	Expression of doxycycline-inducible shRNA to p53	Ampicillin	Puromycin
pCDH	Empty vector	Ampicillin	-
pCDH BRAFV600E	Constitutive expression of the potent oncogene BRAF <sup>V600E</sup>	Ampicillin	-
pCDH Cre puro	Constitutive expression of the Cre recombinase enzyme	Ampicillin	Puromycin
pCDH Flag HA ATOH1 puro	Constitutive expression of ATOH1	Ampicillin	Puromycin
pCDH NIC puro (N1CD)	Constitutive expression of the Notch intracellular domain (ICN1)	Ampicillin	Puromycin
pCDH puro	Empty vector	Ampicillin	Puromycin
pCDH TA WaGa sh6	Constitutive expression of the WaGa T antigen oncoproteins	Ampicillin	-
plH LT_(254) sh6 TA	Constitutive expression of the LoKe large T antigen	Ampicillin	Hygromycin
pLVX NCCR mNeonGreen mRuby3	Contains a bidirectional NCCR reporter cassette expressing mNeonGreen (in frame with the MCPyV early region) and mRuby3 (in frame with the MCPyV late region)	Ampicillin	Puromycin
PX459 pitch gRNA	Constitutive expression of pitch gRNA and Cas9 endonuclease	Ampicillin	-
RB1 shRNA	Constitutive expression of an shRNA to RB1	Ampicillin	-
TA.shRNA.tet	Expression of doxycycline-inducible shRNA to the MCPyV T antigens	Ampicillin	-

### 2.1.17.2 Newly generated plasmids

<u>Name of the vector</u>	<u>Description</u>	<u>Antibiotic resistance</u>	
		<u>Bacteria</u>	<u>Mammalian cells</u>
Induc KRT20 shRNA E Zeo	Inducible expression of KRT20 shRNA with doxycycline	Ampicillin	Zeocin
KRT20 Donor mNeon BSD	KRT20 Donor for the CRISPR/Cas9 knock-in of mNeonGreen in frame with the KRT20 gene	Ampicillin	Blasticidin
pCDH GLI IRES ATOH1 puro	Constitutive expression of GLI1 and ATOH1	Ampicillin	Puromycin
pCDH IPTG dnMAML1 V5	Inducible expression of dnMAML1 with IPTG	Ampicillin	Puromycin
pCDH IPTG eGFP	Inducible expression of eGFP with IPTG	Ampicillin	Puromycin
pCDH IPTG Flag GLI1 Puro	Inducible expression of GLI1 with IPTG	Ampicillin	Puromycin
pCDH PGK hTERT mRuby	Constitutive expression of loxP flanked hTERT and mRuby	Ampicillin	-
pCDH PGK minCMV Rheo r Zeo	Constitutive expression of the Rheo receptor and Rheo activator which together form a heterodimeric transcription factor that is activated with RSL1	Ampicillin	Zeocin
pCDH Rheo eGFP Neo	Inducible expression of eGFP with RSL1	Ampicillin	Neomycin
pCDH Rheo X Neo ATOH1 Flag HA	Inducible expression of ATOH1 with RSL1	Ampicillin	Neomycin
pCW sT2xstop rtTA Hygro	Inducible expression of MCPyV sT with doxycycline	Ampicillin	Hygromycin
pCW TA278stop rtTA Hygro	Inducible expression of MCPyV TAs with doxycycline	Ampicillin	Hygromycin

### 2.1.17.3 Plasmids obtained from external sources

<u>Name of the vector</u>	<u>Description</u>	<u>Antibiotic resistance</u>		<u>Source</u>
		<u>Bacteria</u>	<u>Mammalian cells</u>	
HES1-DSRedExpress-DR	Contains a reporter cassette with the <i>HES1</i> promoter and a downstream red fluorescent protein (DsRed-Express)	Kanamycin	-	Obtained from the authors of [314].
p442 hAIFM2 E156A Flag IRES puro	Expression of the inactive mutant (E156A) of AIFM2 (FSP1)	Ampicillin	Puromycin	AG Friedmann Angeli (University of Würzburg)
p442 hAIFM2 G2A eGFP IRES Neo	Expression of the inactive mutant (G2A) of AIFM2 (FSP1) fused to eGFP	Ampicillin	Neomycin	AG Friedmann Angeli (University of Würzburg)
p442 hAIFM2 WT eGFP IRES Neo	Expression of the wild type AIFM2 (FSP1)-eGFP fusion protein	Ampicillin	Neomycin	AG Friedmann Angeli (University of Würzburg)
p442 hAIFM2 WT Flag IRES puro	Expression of wild type AIFM2 (FSP1)	Ampicillin	Puromycin	AG Friedmann Angeli (University of Würzburg)
pGreenFire	Reporter construct expressing GFP upon the activation of p53	Ampicillin	Puromycin	System Biosciences, Mountain View, CA
pMD2.G (p60)	VSV-G envelope expressing plasmid	Ampicillin	-	Addgene
pMDLg/ pRRE (p61)	3rd generation lentiviral packaging plasmid containing Gag and Pol	Ampicillin	-	Addgene
pRSV-Rev (p59)	3rd generation lentiviral packaging plasmid containing Rev	Ampicillin	-	Addgene

### **2.1.18 Software and online tools**

<b><u>Software</u></b>	<b><u>Analysis</u></b>	<b><u>Producer/Website</u></b>
Adobe Photoshop and Indesign	Preparation of figures	Adobe Inc.
BLOCK-iT™ RNAi Designer	Design of shRNAs	Thermo Fisher Scientific
FloJo	Flow cytometric analysis	Tree Star Inc.
GraphPad Prism 5.03	Statistical analysis and graph preparation	GraphPad Software
Magellan™	Analysis of protein concentrations in lysates	Tecan
Microsoft Office	Analysis, documentation and presentation of scientific data	Microsoft
NEB Tm Calculator	Estimation of annealing temperature for PCR	New England Biolabs
Primer-BLAST	Design of primers	NCBI
SnapGene	Design of cloning strategies and alignment of DNA sequences	GSL Biotech LLC

## **2.2 Methods**

### **2.2.1 Cell biological methods**

#### **2.2.1.1 Cell culture and handling of mammalian cells**

##### **2.2.1.1.1 Maintenance of cell cultures**

All cell lines used this study were maintained in RPMI-1640 medium supplemented with 10% FBS and 1% Pen/Strep (100 U/mL penicillin and 0.1 mg/mL streptomycin) at 37 °C with 5% CO<sub>2</sub> concentration and at 95% humidity. Keratinocytes were maintained in keratinocyte serum-free medium which was supplemented with epidermal growth factor (5 ng/mL) and bovine pituitary extract (50 µg/mL).

##### **2.2.1.1.2 Splitting of cells**

The splitting procedure depended upon whether the cells were adherent or suspension cells. To split adherent cells, the old medium was discarded from the cell culture flasks and the cells were then washed in 10 ml PBS. This was followed by the incubation of the cells in the presence of 1 ml of 1X TE for five minutes at 37 °C. The cell culture flasks were then tapped at sides to release the trypsinized cells from the base of the flask. For cell lines such as HaCaT which adhered strongly to the flask, cell scrapers were used to further aid in the release of the cells. The trypsinization process was stopped once all cells were released from the flask by the addition of 9 ml of medium. This cellular suspension was mixed gently and split according to requirement (1:10 for rapidly proliferating cells such as HaCaT or 1:2 for slower proliferating cells like primary fibroblasts).

To add fresh medium to suspension cells, the spheroids and single cells were allowed to settle at the base of the flask. The old medium was then discarded using a pipette and fresh medium was added into the flasks. In order to split these cells, in addition to the old medium, a few spheroids or single cells were also aspirated using a pipette and fresh medium was then added to the flask. The precise volumes of medium added depended upon the size of the flask or well plate and is provided in the table below.

<b><u>Well plates/Flask</u></b>	<b><u>Volume of medium (ml)</u></b>
6 well plate	5
T25	5
T75	20
T175	30

#### **2.2.1.1.3 Thawing cells to bring them into culture**

In order to thaw cells frozen at -80 °C or in liquid nitrogen, the cryovials containing the frozen cells were incubated for five minutes in a 37 °C water bath. Once thawed, the cells were transferred into a 15 ml falcon containing 10 ml PBS and centrifuged at 400 x g for five minutes at RT. The supernatant was discarded, the cell pellet was resuspended in 1 ml medium and then transferred to a new cell culture flask containing fresh medium.

#### **2.2.1.1.4 Preparation of cell culture freeze downs**

In order to freeze down cells, cell suspensions were at first centrifuged at 400 x g for five minutes at RT. The supernatant was discarded and the pellet was resuspended in 1 ml of FBS + 10% DMSO. The suspension was transferred into cryovials labeled with the name of the cell line, passage number as well as the date of the freeze down. The cryovials were stored at -80 °C or in liquid nitrogen for long term storage.

#### **2.2.1.1.5 Dissociation of cells for flow cytometry**

While adherent and single cell suspension cell lines were prepared for flow cytometric analysis by extracting a small part of the cell suspension during the splitting procedure (explained in section 2.2.1.1.2), it was crucial to dissociate spheroidal cell lines into single cell suspensions for flow cytometric analysis. For this purpose, the flasks were at first maintained in a tilted position for a few minutes until the spheroids settled in the bottom corner of the flask. These spheroids were harvested into 1 ml Eppendorf tubes and centrifuged at 400 x g for five minutes at RT. The supernatant was discarded, the cell pellets were resuspended in 1 ml of 1X TE and centrifuged again at 400 x g for five minutes at RT. The supernatant was discarded. This was followed by the addition of 0.5 ml of 1X TE and 1 ml of medium to the pellet after which it was vigorously resuspended to generate a single cell suspension. Since a minimum of 10000 events were recorded on the flow cytometer, at least  $1 \times 10^5$  cells were harvested from each cell suspension to be analyzed.

#### **2.2.1.1.6 Trypan blue cell counting**

In order to perform trypan blue cell counting, 10 µl of the desired single cell suspension was mixed with 10 µl of trypan blue. 10 µl of this mixture was added into a Neubauer chamber already sealed with a cover slip. The chamber was divided into four areas each with 16 squares. The living cells in these squares were counted under the light microscope and were identified as shiny and transparent in contrast to the dead cells

which were stained blue. The number of cells per ml was then determined using the following formula given below.

$$(\text{Total number of living cells counted}/\text{Number of squares counted}) \times \text{Dilution factor} \times 10^4 = \text{Number of cells per ml}$$

The dilution factor was considered as “2” since the single cell suspension was diluted in an equal volume of trypan blue.

### **2.2.1.2 Cell viability assays**

#### **2.2.1.2.1 Trypan blue cell viability assay**

In order to assess cell viability using the trypan blue assay,  $2 \times 10^4$  cells were seeded per well into 48 well plates. A total of 1.25 ml of medium with or without the drug/combination of drugs to be tested was added into each well at the required concentrations. The cells were incubated at 37 °C for a defined period depending upon the treatment being tested. Following the incubation period, trypan blue cell counting was performed as described in section 2.2.1.1.6. Importantly, in addition to the living cells, the dead cells were also counted. The ratio of the living cells to the total number of cells (living + dead) was determined next for every treatment condition. The ratio of every treatment condition was then divided by the ratio obtained for the reference treatment condition. The obtained normalized ratios were then displayed as percentages for the final analysis with the reference set to 100%.

#### **2.2.1.2.2 Cell cycle analysis**

For cell cycle analysis, cell pellets of parental, untreated or artesunate-treated cells with approximately  $1 \times 10^6$  cells were resuspended in 100 µl of PBS + 1% FBS and then fixed using 90% ice-cold ethanol which was added dropwise to the cells while vortexing them. The cells were incubated for a minimum of one hour at 4 °C. The cells were then centrifuged at 400 x g for five minutes at RT. The supernatant was discarded and the fixed cells were resuspended in 200 µl of PBS + 1% FBS containing propidium iodide (0.1 mg/ml) and RNase A (0.1 mg/ml). Following an incubation for one hour at 37 °C, the cells were analyzed on the flow cytometer. The data obtained was analyzed using the FloJo software to determine the percentage of cells in the Sub-G1 phase of the cell cycle.

### **2.2.1.3 Flow cytometric staining and cell sorting**

#### **2.2.1.3.1 Staining for HLA and PD-L1**

The first step of this procedure was to seed  $2 \times 10^5$  cells per well in 5 ml of medium in a 6 well plate. Depending upon the treatment to be performed, artesunate (10  $\mu$ M), interferon gamma (200U/ml) or a combination of both were added to the cell culture media. The cells were incubated for 48 hours at 37 °C. The cells were then harvested into 15 ml falcons and centrifuged at 400 x g for five minutes at RT. The supernatant was discarded and the pellets were resuspended in 600  $\mu$ l of 0.1% BSA in PBS. If MKL-1 cells were used, they were dissociated at this step as described in section 2.2.1.1.5. The suspension was distributed equally into 3 Eppendorf tubes each with 200  $\mu$ l of the suspension (for treatment of each distributed part of sample with the required antibodies, isotype controls or with no antibodies respectively). The suspension was centrifuged at 1000 x g for five minutes at RT. The supernatant was discarded, the pellets were resuspended in 100  $\mu$ l of 0.1% BSA in PBS and the tubes were centrifuged again at 1000 x g for five minutes at RT. The supernatant was discarded and the respective antibodies/isotype controls were added to the cells from master mixes prepared in advance. As further controls, one part of the cells was treated without any antibodies. The amount of the antibodies required for one tube is provided in the table below.

<b><u>Component</u></b>	<b><u>Volume for one tube (<math>\mu</math>l)</u></b>
FACS wash buffer (0.1% BSA-PBS)	45
HLA antibody or isotype control	2.5
PD-L1 antibody or isotype control	2.5

The cells were incubated in the dark for 30 minutes at RT. The cells were then centrifuged at 1000 x g for five minutes at RT and the supernatant was discarded. This is followed by two washing steps with 100  $\mu$ l of 0.1% BSA-PBS with centrifugation steps at 1000 x g for five minutes at RT in between the washes. The cells were then resuspended in 200  $\mu$ l of 0.1% BSA-PBS and were analyzed on the flow cytometer.

#### **2.2.1.3.2 Staining for cell surface proteins**

In order to stain cell surface proteins,  $1 \times 10^5$  cells to be stained were centrifuged at 400 x g for five minutes at RT. The supernatant was discarded and the pellet was resuspended in 600  $\mu$ l of PBS + 1% FBS. The suspension was distributed to two Eppendorf tubes (for treatment with and without antibodies respectively) and centrifuged at 1000 x g for three minutes at RT. The supernatant was discarded and the primary fluorescence-conjugated antibody was added at the appropriate dilution in

PBS + 1% FBS. The cells were incubated in the dark for 30 minutes on ice following which they were centrifuged at 1000 x g for three minutes at RT. The supernatant was discarded and the pellet was washed twice with 300 µl of PBS + 1% FBS with centrifugation steps at 1000 x g for three minutes at RT in between the washes. In those cases where the primary antibody was not fluorescence-conjugated, the secondary antibody was added at this stage and the cells were incubated in the dark for 30 minutes at RT which was followed by two washing steps with PBS + 1% FBS. Following the last centrifugation step, the cells were resuspended in 200 µl of PBS + 1% FBS and were analyzed on the flow cytometer.

### **2.2.1.3.3 Flow cytometric cell sorting**

In order to sort for the mNeonGreen positive population of lentiviral cre-transduced WaGa cells harbouring the KRT20 donor construct, the cells were sorted by a staff member in the cell sorting facility in the institute for virology and immunology in the University of Würzburg.

### **2.2.1.4 Transformation assay**

#### **2.2.1.4.1 Lentiviral transduction of NIH3T3 cells**

In order to test for the transforming potential of sT in our T antigen constructs, the transformation assay was performed using NIH3T3 cells. As the first step, NIH3T3 cells were transduced (see subsequent section 2.2.3.1) with the generated TA and sT lentiviral inducible expression vectors as well as with vectors constitutively expressing BRAF<sup>V600E</sup>, the WaGa T antigens and an empty vector as controls. The table below provides an overview of the plasmids used for the transformation assay and the purpose of their usage.

<b><u>Plasmid</u></b>	<b><u>Protein expressed</u></b>	<b><u>Purpose</u></b>
pCDH BRAFV600E	BRAF <sup>V600E</sup>	Overexpression of the potent oncogene BRAF <sup>V600E</sup> as a positive control for transformation
pCDH TA WaGa sh6	WaGa T antigens	Overexpression of the WaGa T antigen oncoproteins as a positive control for MCPyV T antigen-induced transformation
pCDH	-	An empty vector used as a negative control

pCW TA278stop rtTA Hygro	Doxycycline-inducible expression of the T antigens	To test the capacity of inducibly expressed sT in the TA construct to promote transformation
pCW sT2xstop rtTA Hygro	Doxycycline-inducible expression of sT	To test the capacity of inducibly expressed sT in the sT construct to promote transformation

The following day, the infected cells were split (see section 2.2.1.1.2) and were transferred into T75 flasks containing 20 ml fresh medium. The cells infected with the inducible TA and sT vectors were split into two parts and seeded into two separate flasks with and without 1  $\mu$ M doxycycline. The cells were maintained in culture for three weeks and the medium was changed once in four or five days when the color of the medium changed from red-pink to orange-yellow. After three weeks the cells were prepared for crystal violet staining in order to visualize transformation-induced foci.

#### **2.2.1.4.2 Crystal violet staining**

To perform crystal violet staining, the flasks containing the cells to be stained were placed for one minute on ice. The medium was discarded and the cells were washed twice in PBS, pre-cooled at 4 °C. This was followed by the fixation of the cells by the addition of 20 ml of ice-cold methanol to the cells for 10 minutes on ice (performed in the fume hood). The methanol was discarded and 10 ml of Gram's crystal violet stain was added to the cells for 10 minutes at RT. The stain was then removed from the cell surface and the cells were washed several times with dH<sub>2</sub>O until the excess stain was washed away. Following the last wash, the flasks were left open in the fume hood overnight until the excess dH<sub>2</sub>O evaporated. The following day, the images of the stained foci were captured and documented.

#### **2.2.1.5 Single cell cloning**

For cells which could grow as single cells, such as HaCaT cells, single cell cloning was performed in 96 well plates. The cells were diluted in medium to arrive at a concentration of 0.3 cells per well in 200  $\mu$ l of medium and then seeded into the plates. These plates were placed in moist growth chambers and were incubated at 37 °C. The plates were periodically monitored under the microscope until wells with cell growth were observed. These proliferating cells were identified as single cell clones and were expanded by sequentially transferring them into 48 well plates, 24 well plates, 12 well plates, 6 well plates and finally into cell culture flasks.

For cells such as primary fibroblasts which could not grow as single cell colonies, we established a variant method for single cell cloning. In this method, parental fibroblasts

were initially used for supporting the growth of single cell clones of the genetically manipulated KRT20-fibroblasts. For this purpose, the genetically manipulated KRT20-fibroblasts and parental fibroblasts were mixed in a 1:500 ratio and seeded into 150 mm petri dishes ( $1.2 \times 10^6$  parental fibroblasts per dish) in a total volume of 20 ml. Three such dishes were prepared for every clone that had to be isolated. The dishes were incubated at 37 °C for approximately one week until the cells on the dishes were confluent. The medium was then exchanged with BSD containing medium (5 µg/ml) and incubated at 37 °C for approximately one week until the parental fibroblasts were killed due to the antibiotic. The plate was then closely observed under the light microscope. Colonies of single cell clones of the genetically manipulated KRT20-fibroblasts (BSD-resistant) were identified and markings around these colonies were made on the base of the dish. These clones were then isolated into 48 well plates using sterile cloning cylinders. The expansion of these single cell clones was performed as described for the HaCaT cells in this section.

#### **2.2.1.6 Time lapse microscopy**

The cells to be filmed were seeded at a density of  $1 \times 10^5$  cells per well in µ-Slides from Ibidi in 800 µl of medium in the presence or absence of artesunate (50 µM). The cells were then monitored under the Nikon Eclipse Ti microscope at a magnification of 20X over a defined time period and morphological changes were recorded.

### **2.2.2 Molecular biological methods**

#### **2.2.2.1 Cloning methods**

##### **2.2.2.1.1 Classical cloning of vectors**

###### **2.2.2.1.1.1 Amplification of Inserts**

The classical cloning procedure was followed for the cloning of inducible and expression vectors. DNA inserts were amplified from parental vectors by PCR using the Q5 High-Fidelity DNA Polymerase to minimize the error rate. The primers used were designed to introduce suitable restriction enzyme sites at the flanking ends of the amplified inserts to enable subsequent restriction digestion and ligation into the desired vector backbone. The volumes of the reagents required for the master mix for the PCR are depicted in the table below.

<b><u>Reagent</u></b>	<b><u>Volume for one reaction (µl)</u></b>
Q5 Reaction Buffer	4
Forward primer (10µM)	1
Reverse primer (10µM)	1
dNTPs	0.4
Q5 High-Fidelity DNA Polymerase	0.2
DNase/RNase free H <sub>2</sub> O	12.4
Plasmid DNA	1

The PCR was performed in the PCR machine using the program given in the table below.

<b><u>Temperature °C</u></b>	<b><u>Time</u></b>	<b><u>Number of Cycles</u></b>	<b><u>Step</u></b>
98	1 minute	-	Initial denaturation
98	10 seconds	35 cycles	Denaturation
x	30 seconds		Annealing
72	y seconds		Extension
72	72 minutes	-	Final extension
4	∞	-	Cooling

The optimal annealing temperature (x) was determined by entering the primer sequences into the NEB T<sub>m</sub> calculator website. The extension time (y) depended upon the length of the final product that was to be amplified and was calculated by estimating the extension efficiency of the Q5 polymerase as approximately one kilobase per minute. In order to check for successful amplification of the insert, agarose gel electrophoresis was performed. 3 µl of the PCR product was mixed with a 1 µl of the gel loading dye orange and run on a 1% agarose gel set to run at 130 V for 20 minutes. The gel were also loaded with 5 µl of the Gene ruler 100 bp plus DNA ladder in order to estimate the size of amplified DNA insert running through the gel. The amplified DNA insert was visualized under UV light and upon observing a band at the right height, images were captured using the Intas Science Imager. The amplified DNA insert was then isolated from PCR mixture using the Wizard® SV Gel and PCR Clean-Up System as per the manufacturer's protocol.

### **2.2.2.1.1.2 Restriction Digestion**

As the next step, 2.5 µg of both the purified amplified insert and the vector backbone were digested separately with suitable restriction enzymes in a buffer preferably enabling optimal activity of both enzymes (in the best case 100% activity for both enzymes). The buffer was determined by entering the names of both enzymes on the DoubleDigest calculator by Thermo Scientific. A mastermix containing the buffer and enzymes was prepared as given in the table below and 4 µl of this mix used for every digestion reaction.

<b><u>Reagent</u></b>	<b><u>Volume for one reaction (µl)</u></b>
Buffer	2
Enzyme 1	1
Enzyme 2	1

The total volume of the reaction was made up to 20 µl with dH<sub>2</sub>O and the digestion reaction was carried out according to the protocol provided in the table below.

<b><u>Temperature °C</u></b>	<b><u>Time</u></b>	<b><u>Step</u></b>
37	60 minutes	Digestion
37	60 minutes	
x	20 minutes	Inactivation of enzyme 1
y	20 minutes	Inactivation of enzyme 2
4	∞	Cooling

The inactivation temperatures (x) and (y) for the first and second enzyme respectively were also determined using the DoubleDigest calculator by Thermo Scientific.

In order to isolate the successfully digested insert and vector, agarose gel electrophoresis was performed as described in section 2.2.2.1.1.1. In this case, 20 µl of the digests were mixed with 5 µl of the gel loading dye and the electrophoresis was performed at 100 V for one hour. The digested DNA bands were visualized and cut out under UV light and were transferred into Eppendorf tubes. Images of the bands were captured using the Intas Science Imager. The digested DNA was isolated from the gel slices using the Wizard® SV Gel and PCR Clean-Up System as per the manufacturer's protocol.

### **2.2.2.1.1.3 Ligation**

The purified and digested insert and vector DNA were ligated using T4 DNA Ligase. The table below provides the volumes of the components required for one ligation reaction.

<b><u>Component</u></b>	<b><u>Volume for one reaction (µl)</u></b>
Digested Vector	1
Digested Insert	3
T4 DNA ligase Buffer	2
T4 DNA ligase	1
DNase/RNase free H <sub>2</sub> O	13

The ligation mixture was incubated for one hour at RT following which it was stored at 4 °C if not used immediately for the subsequent transformation steps.

### **2.2.2.1.1.4 Transformation of *E.coli*, clone PCR and Sanger sequencing**

In order to generate several copies of the ligated plasmid, the ligation mixture was transformed into competent K12 *E.coli* cells. For this purpose, 1 µl of the ligation mixture was added to a 20 µl suspension of *E.coli* cells for 30 minutes on ice. This was followed by a heat shock to the cells for 30 seconds at 42 °C followed by the incubation of the cells for two minutes on ice. 100 µl of pre-warmed LB medium was then added to the cells. The cells were then placed in the incubator shaker at 600 rpm for one hour at 37 °C. The cells were then plated onto LB agar plates containing ampicillin to select for cells successfully transformed with the plasmid. The plates were incubated overnight at 37 °C. In order to identify *E.coli* clones which were successfully transformed with the genetically engineered plasmid, clone PCRs were performed the following day. The primers used for clone PCRs were designed to amplify a short sequence (typically under 200 base pairs) with one primer within the insert and the other, in the vector backbone thereby enabling confirmation of a successfully ligated product. Individual clones were picked from the plates and resuspended in 20 µl of DNase/RNase free water. 10 µl of each clonal suspension was treated for 10 minutes at 100 °C prior to its use for the clone PCR. The table below provides the volumes of the components used for one clone PCR reaction.

<b><u>Component</u></b>	<b><u>Volume for one reaction (µl)</u></b>
Low ROX SYBR Master Mix dTTP blue	5
Forward primer (10 µM)	0,75
Reverse primer (10 µM)	0.75
DNase/RNase free water	2.5
DNA template (clonal suspension)	1

The clone PCR was then performed in the thermal cycler using the program provided in the table below.

<b><u>Temperature °C</u></b>	<b><u>Time</u></b>	<b><u>Number of Cycles</u></b>	<b><u>Step</u></b>
98	10 minutes	-	Initial denaturation
98	10 seconds	30 cycles	Denaturation
55	30 seconds		Annealing
72	2 minutes		Extension
72	7 minutes	-	Final extension
4	∞	-	Cooling

Positive clones were identified as those for which amplification was detected. These clones were transferred into 15 ml falcons containing 5 ml of LB medium with ampicillin (100 µg/ml). The falcons were placed in the incubator shaker at 225 rpm overnight at 37 °C. The following day, plasmid DNA was isolated from the cells using the Presto™ Mini Plasmid Kit as per the manufacturer's instructions. The concentration of the eluted DNA was measured on the Nanodrop. The elution buffer from the kit was used for the blank measurement.

In order to confirm the sequences of the generated plasmids, they were sent for sequencing to Microsynth Seqlab GmbH. For this purpose, ideally a minimum of 400 ng of plasmid was sent for sequencing to enable the generation of good quality sequences. The rest of the volume was made up to 12 µl with DNase/RNase dH<sub>2</sub>O. The sequencing primer was chosen such that it would amplify a region of the insert as well as the flanking vector backbone sequence. 3 µl of this primer was added to the plasmid preparation. A Seqlab barcode was pasted onto the Eppendorf tube and the sample was then sent for sequencing. The sequences were obtained the following day and were aligned with the expected sequences using SnapGene. Upon correct alignment, the *E.coli* cultures harbouring these plasmids were to be preserved. This was carried out by mixing 500 µl of these *E.coli* cultures with 500 µl of the LB + 60% Glycerin preservation medium. This stock was then frozen at -80 °C. When plasmids were to be replenished, a small aliquot of the preserved stock was inoculated into fresh

LB-ampicillin medium for preparing overnight bacterial cultures. The plasmids were isolated the following day as described previously in this section.

### **2.2.2.1.2 Mutagenesis**

Mutagenesis was performed in order to insert stop codons at the end of the coding sequence of the T antigens for the inducible TA and sT expression vectors. The procedure was carried out using the QuikChange Lightning Site-Directed Mutagenesis Kit and the table below provides the amounts of the components required for one reaction.

<b><u>Reagent</u></b>	<b><u>Volume for one reaction (µl)</u></b>
10× QuikChange Lightning Buffer	2.5
Forward primer (10µM)	0.5
Reverse primer (10µM)	0.5
dNTP mix	0.5
QuikSolution reagent	0.75
QuikChange Lightning Enzyme	0.5
DNase/RNase free H <sub>2</sub> O	18.75
Plasmid DNA	1

The plasmid DNA was diluted in DNase/RNase free H<sub>2</sub>O so as to contain 25 ng/µl of which 1 µl was used per reaction. The mutagenesis reaction was then performed in the PCR machine using the program provided in the table below.

<b><u>Temperature °C</u></b>	<b><u>Time</u></b>
95	2 minutes
95	20 seconds
60	10 seconds
68	4.5 minutes
68	5 minutes
4	∞

This was followed by the addition of 1 µl of the DPN1 enzyme (provided in the kit) to the amplicon for specific digestion of the parental template DNA. The reaction was incubated for five minutes at 37 °C. Competent bacterial cells were then to be

transformed with the DNA. At first, 1  $\mu$ l of XL10-Gold  $\beta$ -mercaptoethanol mix ( $\beta$ -ME) was added to XL10-Gold ultracompetent bacterial cells (both provided in the kit) in order to increase the transformation efficiency of the cells and incubated for two minutes on ice. 1  $\mu$ l of the DPN1 digested DNA was added to these competent cells which were then incubated for 30 minutes on ice. The subsequent transformation procedure and identification of positive clones was carried out as described in section 2.2.2.1.1.4.

### **2.2.2.1.3 Golden gate cloning**

Golden gate cloning was performed to generate the lentiviral vector expressing doxycycline-inducible KRT20 shRNA. shRNAs were designed using the BLOCK-iT™ RNAi Designer from Thermo Fisher Scientific and were ordered from Sigma Aldrich. The first step was to anneal the shRNA oligos. The table below provides the amounts of the components required for one reaction.

<b><u>Reagent</u></b>	<b><u>Volume for one reaction (<math>\mu</math>l)</u></b>
Forward oligo (100 $\mu$ M)	1
Reverse oligo (100 $\mu$ M)	1
10X T4 Ligation buffer (containing 10 mM ATP)	1
DNase/RNase free H <sub>2</sub> O	6.5
T4 PNK (polynucleotide kinase)	0.5

The oligos were annealed in the PCR machine using the program provided in the table below.

<b><u>Temperature °C</u></b>	<b><u>Time</u></b>
37	30 minutes
95	5 minutes
Ramp down 5° per minute to 25 °C	

The digestion-ligation reaction was performed subsequently to introduce the annealed oligos into the target vector. For this purpose, the annealed oligos were diluted 1:250 and the target vector was diluted to a concentration of 100 ng/ $\mu$ l in DNase/RNase free H<sub>2</sub>O. The amounts of the components used for one reaction are provided in the table below.

<b><u>Reagent</u></b>	<b><u>Volume for one reaction (µl)</u></b>
Vector	1
Annealed oligos (1:250 diluted)	2
10X Tango Buffer	2
DTT (10 mM)	2
ATP (10 mM)	2
BsmBI (restriction enzyme)	1
T7 DNA ligase	0.5
DNase/RNase free H <sub>2</sub> O	9.5

The reaction was performed in the PCR machine using the program provided in the table below.

<b><u>Temperature °C</u></b>	<b><u>Time</u></b>	<b><u>Number of Cycles</u></b>
37	5 minutes	6 cycles
23	5 minutes	
4	∞	-

Competent bacterial cells were then transformed with the ligated plasmid as described in section 2.2.2.1.1.4 and positive clones were identified by sequencing.

### **2.2.2.2 DNA isolation**

Genomic DNA was isolated from the cells using the QIAamp® DNA Mini Kit from Qiagen and the performed as per the manufacturer's protocol. The concentration of the eluted DNA was measured on the Nanodrop and the blank measurement was performed using the elution buffer from the kit. DNA samples were stored at 4 °C for short term storage and at -20 °C for long term storage.

### **2.2.2.3 Polymerase chain reaction**

PCR was performed using the Q5 High-Fidelity DNA Polymerase and the PCR products were checked using agarose gel electrophoresis as described in section 2.2.2.1.1.1. The DNA was subsequently purified using the Wizard® SV Gel and PCR Clean-Up System as per the manufacturer's protocol and subsequently sent for sequencing as described in section 2.2.2.1.1.4. 18 ng per 100 bp were required to be sent for sequencing of PCR products in a total volume of 12 µl.

#### **2.2.2.4 RNA isolation from cells**

The PeqGOLD Total RNA Kit was used for the isolation of RNA from the cells and was performed as per the manufacturer's protocol. Approximately  $2 \times 10^6$  cells were used for the RNA isolation procedure. The concentration of the isolated RNA was measured on the Nanodrop and the RNase free water provided in the kit was used for the blank measurement. If not used immediately for cDNA synthesis, the RNA was stored at  $-80\text{ }^{\circ}\text{C}$  until further use.

#### **2.2.2.5 Complementary DNA (cDNA) synthesis**

Prior to performing cDNA synthesis, the RNA sample with the lowest concentration was identified. Every other RNA sample was diluted with RNase free water to reach the lowest concentration of RNA in the sample set in a total volume of  $4.9\text{ }\mu\text{l}$ . An ideal concentration of the total RNA used for cDNA synthesis per reaction ranged from 400 to 900 ng. Subsequently, a master mix containing the various reagents required for the cDNA synthesis process was prepared. The volumes of the reagents required for a single reaction are provided in the table below.

<b><u>Reagent</u></b>	<b><u>Volume for one reaction (<math>\mu\text{l}</math>)</u></b>
First Strand Buffer	2
DTT (100 mM)	1
dNTPs (10 mM)	0.5
Oligo dT (10 pmol/ $\mu\text{l}$ )	0.5
Random Primer 1:150	0.5
Super Script II reverse transcriptase (200 U/ $\mu\text{l}$ )	0.6
RNA	4.9

$4.9\text{ }\mu\text{l}$  of each RNA sample was mixed with  $5.1\text{ }\mu\text{l}$  of the master mix and then loaded into the PCR machine. The PCR program for cDNA synthesis is provided in the table below.

<b><u>Temperature <math>^{\circ}\text{C}</math></u></b>	<b><u>Time</u></b>
42	30 minutes
45	30 minutes
72	2 minutes
4	$\infty$

The prepared cDNA was stored at 4 °C until further use.

### **2.2.2.6 Quantitative PCR (qPCR)**

qPCR was performed in order to analyze and compare levels of transcription of various genes between cell samples. *RPLP0* was used as the internal control gene for every sample analyzed. The prepared cDNA was diluted 1:10 in dH<sub>2</sub>O prior to its use for qPCR. A master mix containing the various reagents required for qPCR was prepared as depicted in the table below.

<b><u>Reagent</u></b>	<b><u>Volume for one reaction (µl)</u></b>
Low ROX SYBR Master Mix dTTP blue	10
Forward primer (10 µM)	1.5
Reverse primer (10 µM)	1.5
DNase/RNase free water	6
cDNA template	1

At first, 19 µl of the prepared master mix was pipetted into each well of a MicroAmp Optical 96 well reaction plate. This was followed by the addition of 1 µl of the respective cDNA samples into independent wells. In order to account for manual errors, every sample was loaded in triplicates for every gene analyzed. The addition of DNase/RNase in the place of cDNA served as a negative control. The plate was covered with a protective adhesive film and centrifuged at 400 x g for five minutes at RT. The plate was loaded into the real time thermal cycler. The program used for qPCR is presented in the table below.

<b><u>Temperature °C</u></b>	<b><u>Time</u></b>	<b><u>Number of Cycles</u></b>	<b><u>Step</u></b>
95	3 minutes	-	Initial denaturation
95	10 seconds	40 cycles	Denaturation
60	45 seconds		Annealing and Extension

The analysis of the qPCR data was performed using the  $2^{-\Delta\Delta C_T}$  method as previously described by Livak and Schmittgen [315]. The data was obtained as threshold cycle (Ct) values for every gene analyzed. As the first step, the Ct value of RPLP0 was subtracted from the Ct value of the target gene for every sample analyzed ( $\Delta C_t$ ). The next step involved subtraction of the  $\Delta C_t$  values of every sample from the  $\Delta C_t$  value

of a reference sample ( $\Delta\Delta C_t$ ). As the last step to obtain relative expression values, the formula  $2^{-\Delta\Delta C_T}$  was used.

### **2.2.2.7 RNA sequencing**

For RNA sequencing, total RNA was isolated from the cells of interest ( $2 \times 10^6$  cells per sample) as described in section 2.2.2.4. For every cell type to be sequenced, three independent RNA replicates were prepared from different freeze-down batches. cDNA library preparation as well as paired-end 150 bp RNA sequencing on an Illumina NovaSeq 6000 sequencing system was performed by a company (Novogene). Results were obtained as FPKM (Fragments Per Kilobase per Million mapped reads) values.

## **2.2.3 Methods for genetic modification of mammalian cells**

### **2.2.3.1 Lentiviral transduction**

The first step of the lentiviral transduction procedure was to transfect the producer HEK293T cells with the plasmid containing the gene of interest. For this purpose, the HEK293T cells were seeded one day prior to the transfection into 6 well plates at a density of  $7.5 \times 10^5$  cells per well in a volume of 2 ml per well. At this density, the cells reached a confluency of approximately 80% the following day which was an ideal density for transfection. Furthermore, the cells were seeded in medium with 10% FBS and without Pen/Strep to enhance transfection efficiency. The following day, the HEK293T cells were transfected with the plasmid containing the gene of interest along with the relevant lentiviral helper plasmids (p59, p60 and p61/p61\*) as per the Polyplus jetPRIME® transfection protocol provided in the table below. The p61\* helper plasmid was a mutated version of the p61 plasmid which was used for performing non-integrating lentiviral infections such as the Cre recombinase infection performed in this study. The table below provides the amounts of DNA and jetPRIME® reagents used for the transfection of cells plated in one well.

<b><u>Component</u></b>		<b><u>Amount for one well</u></b>	<b><u>Treatment and incubation time</u></b>
DNA	Plasmid	0.89 µg	Vortex, briefly spin down
	p59	0.22 µg	
	p60	0.31 µg	
	p61 or p61*	0.58 µg	
jetPRIME® buffer		200 µl	
jetPRIME® transfection reagent		4 µl	Vortex, briefly spin down, incubate 10 minutes at RT
Add the mixture dropwise to the cells and incubate overnight at 37 °C			

The following day, the transfection medium was aspirated and replaced with 3 ml of medium with 10% FBS and 1% Pen/Strep. Furthermore, the adherent cells to be transduced were plated at a density of  $2 \times 10^5$  cells per 6 well in 2 ml of medium with 10% FBS and without Pen/Strep in order to reach a confluency of approximately 70-80% for the transduction procedure the following day. Suspension cells were harvested on the day of the transduction shortly before the procedure as  $1 \times 10^6$  cells in 50 µl per 6 well. In order to transduce the cells, the virus containing supernatant was harvested from the HEK293T cells into syringes in the S2 laboratory. Using a 0.45 µm filter, the supernatant was filtered into falcons containing polybrene (1 µg/ml) to increase the efficiency of the viral transduction procedure. This supernatant was then added onto the cells to be transduced and incubated overnight at 37 °C. The following day, the viral supernatant was aspirated from adherent cells. The cells were washed with 5 ml of PBS which was followed by the addition of 3 ml of medium with 10% FBS and 1% Pen/Strep. Suspension cells on the other hand, were harvested along with the viral supernatant into 15 ml falcons containing 10 ml of PBS. Most suspension cells were centrifuged once at 400 x g for five minutes at RT while WaGa cells being highly sensitive, were centrifuged twice to wash away any remnants of the viral supernatant. Following the centrifugation steps, the supernatant was discarded and the pellet was resuspended in 1 ml of medium and transferred into T25 flasks containing 5 ml fresh medium. The cells were then allowed to recover from the transduction procedure for two days following which the respective antibiotic containing medium was added onto the cells to select for successfully transduced cells. Non-transduced cells treated with medium and polybrene only were also selected as a negative controls.

### **2.2.3.2 Co-transfection of cell lines**

In order to perform co-transfections in this study, U2OS cells were plated at a density of  $2 \times 10^5$  cells per 6 well one day prior to the transfection in medium with 10% FBS.

The next day, the following amounts of plasmids, as shown in the table below, were combined for the co-transfections.

<b><u>Plasmid</u></b>	<b><u>Amount for co-transfection (µg)</u></b>
HES1-DSRedExpress-DR (Notch reporter)	0.66
x/y/z	0.66
x/y/z	0.66

Where x: pCDH puro; y: pCDH NIC puro (N1CD); z: pCDH IPTG dnMAML1 V5

Co-transfection mixes of the Notch reporter plasmid with the combinations xx, xy, xz and yz of the other plasmids were then prepared. The transfection procedure was then carried out using the Polyplus jetPRIME® transfection protocol as described in section 2.2.3.1.

### **2.2.3.3 CRISPR/Cas9 genome editing**

The cells to be used for CRISPR/Cas9 genome editing for the integration of the KRT20 donor into their genome were seeded in T25 flasks in medium with 10% FBS one day prior to the transfection. The number of the cells seeded depended upon the cell type and their proliferation rate and is provided in the table below.

<b><u>Cell line/Primary cell type</u></b>	<b><u>Number of cells seeded per T25 flask prior to transfection</u></b>
WaGa	1 x 10 <sup>6</sup>
Primary fibroblasts	5 x 10 <sup>5</sup>
HaCaT cells	3 x 10 <sup>5</sup>

The following day, the cells were transfected with the KRT20 donor and the plasmids encoding for the guide RNAs (gRNAs) (amounts used for transfection in table below) as per the Polyplus jetPRIME® transfection protocol (described in section 2.2.3.1). A flask with non-transfected cells served as a negative control.

<b><u>Plasmid</u></b>	<b><u>Type</u></b>	<b><u>Amount for CRISPR/Cas9 transfection (µg)</u></b>
KRT20 Donor mNeon BSD	Donor DNA	1
64222_mCherry_KRT20_A	Guide	0.33
64221_mCherry_KRT20_A	Guide	0.33
Pitch gRNA	Guide	0.33

The guide RNA harbouring plasmids, 64222\_mCherry\_KRT20\_A, 64221\_mCherry\_KRT20\_A and Pitch gRNA used in this study, additionally encoded for the Cas9 endonuclease and were previously tested in our laboratory for their efficiency. The pitch guide RNA was used as PITCh (Precise Integration into Target Chromosome) systems are known to enable linearisation of the donor DNA in the host and increase the precision of intergation [316]. The pitch gRNA target sequences were present on the KRT20 donor plasmid shortly before and after the left homology and right homolgy arm sequences respectively. The sequences recognized by these gRNAs are provided in the table below.

<b><u>gRNA</u></b>	<b><u>Recognition sequence (5'-3')</u></b>
KRT20 gRNA	CGTGTCATCTGAAGTCAAAG
Pitch gRNA	CATCGTACGCGTACGTGTT

On the day following the transfection, the cells were washed with PBS and 5 ml of fresh medium was added to the flasks. The next day, the old medium was aspirated from the control and transfected flasks and replaced with antibiotic (BSD) containing medium. The cells were selected for one month until the non-transfected cells as well as those containing the donor plasmid episomally were killed in the presence of BSD.

#### **2.2.3.4 A potential approach to study MCPyV-positive MCC oncogenesis and differentiation**

The figure below provides a schematic representation of a potential method to study MCPyV-positive MCC oncogenesis and differentiation using the *in vitro* genetic tools generated in this study.

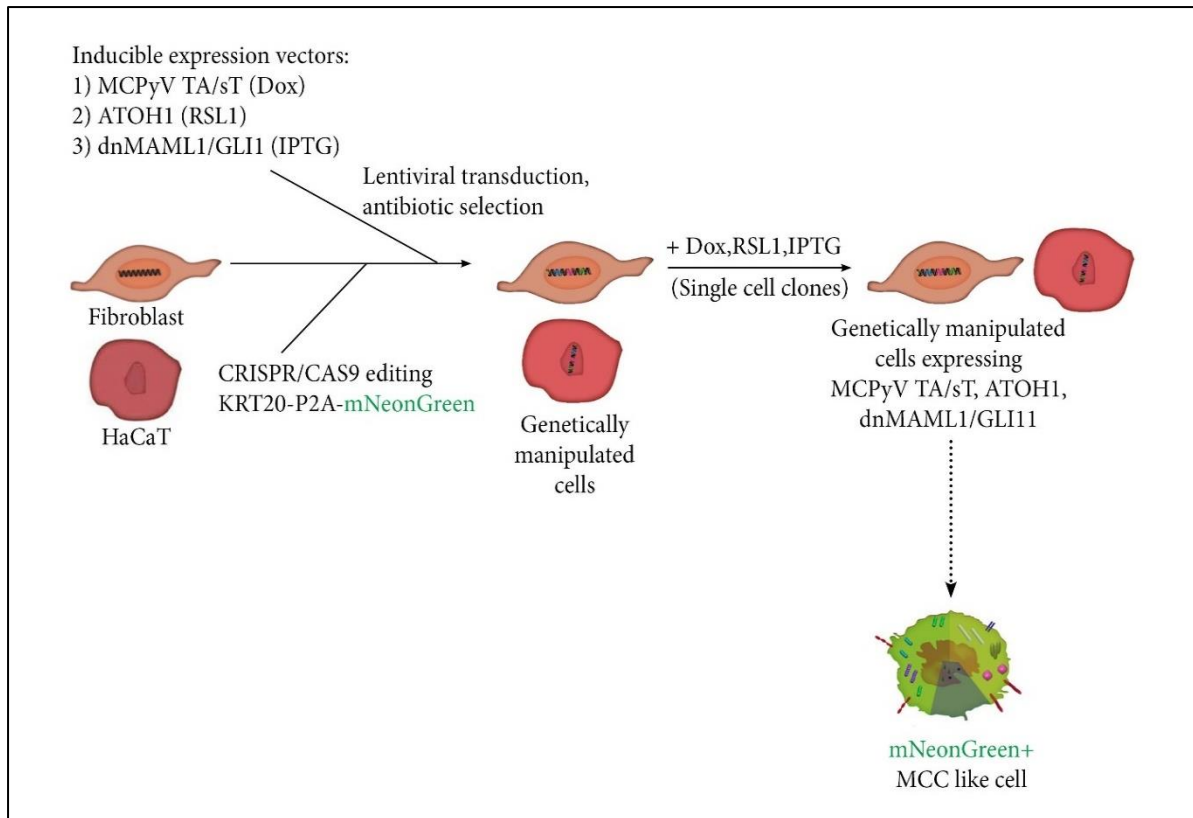


**Figure 8: Schematic representation of a potential approach to study *in vitro* oncogenesis and differentiation processes of MCPyV-positive MCC.** The figure depicts an attempt to study MCPyV-positive MCC oncogenesis from *in vitro* generated potential cells of origin of MCPyV-positive MCC which could subsequently be monitored for the differentiation into an MCC-like cell. In this study, our generated vector system was introduced into primary fibroblasts and HaCaT cells. The vectors included a KRT20-P2A-mNeonGreen fluorescence reporter (to monitor potentially developing KRT20+ MCC-like cells) and several lentiviral inducible expression vectors encoding MCC oncoproteins (MCPyV TA/sT) and differentiation factors (ATOH1/dnMAML/GLI1) (to potentially promote MCC-like differentiation). Each vector was selectable with a different antibiotic and was independently inducible with a unique inducible system (Dox for MCPyV TA/sT, RSL1 for ATOH1 and IPTG for dnMAML/GLI1). The KRT20-P2A-mNeonGreen fluorescence reporter and the various inducible expression vectors were introduced into the cells by CRISPR/Cas9 genome editing and lentiviral transduction respectively. Following selection with the respective antibiotics, the genetically manipulated cells were then induced with the various inducers (Dox, RSL1 and IPTG) to identify clones with the highest inducible expression of MCPyV TA/sT, ATOH1 and dnMAML/GLI1. The selected clones were further analyzed for differentiation into an MCC-like cell by monitoring induction of mNeonGreen deriving from an activated KRT20 endogenous promoter. (MCPyV-TA/sT: Merkel cell polyomavirus T antigens/small T antigen; Dox: Doxycycline; ATOH1: Atonal bHLH transcription factor 1; RSL1: Rheoswitch ligand 1; GLI1: GLI family zinc finger 1; dnMAML1: dominant-negative Mastermind-like1; IPTG: Isopropyl  $\beta$ -d-1-thiogalactopyranoside; MCC: Merkel cell carcinoma)

## **2.2.4 Biochemical methods**

### **2.2.4.1 Immunoblotting for proteins**

#### **2.2.4.1.1 Preparation of cell lysates**

To prepare protein lysates, cellular suspensions of the cells of interest were transferred to Eppendorf tubes and centrifuged at 900 x g for five minutes at 4 °C. The pellets were washed twice in 1 ml PBS and centrifuged between each wash at 200 x g for five minutes at 4 °C. The pellets were then resuspended in E1A lysis buffer in a volume ranging from 30 µl to 200 µl depending upon the size of the pellet. The cells were incubated for a minimum of one hour at 4 °C which was followed by a centrifugation step at 10,000 x g for 10 min at 4 °C. The supernatants (lysates) were carefully pipetted into new Eppendorf tubes and were used for subsequent protein estimation. The lysates were stored at -20 °C until further use.

#### **2.2.4.1.2 Protein estimation**

The concentration of protein in our generated protein lysates was estimated using 'Pierce™ BCA Protein Assay Kit' as per the manufacturer's protocol. The samples were analyzed on the spectrophotometer using the Magellan7.2 software. Standard curves were generated following the subtraction of the blank absorbance value from the absorbance values obtained for every standard sample. The protein concentrations of our lysates were determined using this generated standard curve such that every sample was normalized to contain an ideal amount of 20 µg total protein. In order to obtain this concentration, all lysates were appropriately diluted in ELB lysis buffer and 5 µl of Lane Marker Reducing Sample Buffer was added to each sample. The lysates were then denatured for five minutes at 95 °C and stored at RT until further use.

#### **2.2.4.1.3 Sodium dodecyl sulphate-polyacrylamide gel electrophoresis (SDS-PAGE)**

To enable the separation of proteins based on their mass, SDS-PAGE was performed. The proteins were separated on polyacrylamide gels which were composed of upper stacking gels and lower separation gels. The percentage of the separation gels used depended upon the size of the proteins to be separated such that the smaller the protein to be separated, the higher was the percentage of the gel prepared. The tables below depict the components required for the preparation of stacking gels as well as separation gels of various percentages.

<b><u>Component of Stacking Gel</u></b>	<b><u>Volume for 3 gels</u></b>
Acrylamide	1 ml
Buffer B	5 ml
dH <sub>2</sub> O	4 ml
APS (10%)	150 µl
TEMED	10 µl

<b><u>Component of Separation Gel</u></b>	<b><u>8%</u></b>	<b><u>10%</u></b>	<b><u>12%</u></b>	<b><u>15%</u></b>
Acrylamide	2.66 ml	3.33 ml	4 ml	5 ml
Buffer B	5 ml	5 ml	5 ml	5ml
dH <sub>2</sub> O	2.33 ml	1.66 ml	1 ml	-
APS (10%)	100 µl	100 µl	100 µl	100 µl
TEMED	4 µl	4 µl	4 µl	4 µl

A total of 25 µl of each pre-prepared denatured protein lysate was loaded onto the gels. 5 µl of the Page Ruler Plus Prestained Protein Ladder was loaded onto every gel as a reference for estimating protein size. The loaded gels were placed in electrophoresis buffer and run at a constant voltage of 100V for a minimum of 90 minutes.

#### **2.2.4.1.4 Immunoblotting**

Immunoblotting was performed following SDS-PAGE (described in section 2.2.4.1.3) in order to aid in the transfer of the separated proteins onto nitrocellulose membranes. The blotting procedure was performed in blotting chambers. The sponges, filter papers, the gels and the membranes used for this process were soaked in blotting buffer prior to use. The blotting sandwich was set up in a sequential order to contain the blotting cassette, a sponge, a filter paper, the gel containing the separated proteins, a nitrocellulose membrane (0.2 µm for small proteins and 0.45 µm for large proteins), another filter paper and another sponge. This assembly was sealed, placed into the blotting chamber filled with pre-cooled blotting buffer and the set-up was placed into a box containing ice to prevent overheating. Ice packs were also added into the chamber to prevent excess heating of the assembly. Blotting was performed at a constant current of 400 mA for 70 minutes. Once the blotting procedure was complete, the membrane was washed in TBS-T for two minutes at RT. This buffer was then discarded and the membrane was stained with PonceauS for three minutes at RT to check for equal protein loading in every lane. The membrane was then washed in distilled water at RT to remove the excess stain, dried in filter papers and scanned. This was followed by the washing of the membrane in TBS-T three times for 10

minutes each at RT to completely remove the PonceauS stain from the proteins. The membrane was then blocked in 5% milk in TBS-T for one hour at RT. For the preparation of the primary antibody, the appropriate dilution was noted from the antibody data sheet and was prepared by diluting the antibody in 5% milk in TBS-T in a total volume of 1 ml. The antibody was added onto the membrane which was then sealed in parafilm and incubated overnight at 4°C. The following day, the membrane was washed in TBS-T three times for 10 minutes each at RT. The Horseradish Peroxidase (HRP)-conjugated secondary antibody was added next at a dilution of 1:1000 in a total volume of 7 ml of 5% milk in TBS-T. The membrane was incubated on the shaker for one hour at RT. The membrane was then washed in TBS-T two times for 10 minutes each at RT. Following the last 10 minute washing step in TBS at RT, the membrane was prepared for detection of proteins. The ECL solution was used for detection. 20 ml of this solution was placed into two separate 50 ml falcons. 12 µl of hydrogen peroxide was added to one falcon while 88 µl of p-Coumaric acid and 200 µl of Luminol was added to the other falcon prior to detection. The solutions were then combined into a tray and the membrane was incubated in this solution in the dark for one minute at RT. The membrane was then placed into the western blot imager and pictures of the protein bands were captured. In order to enable detection of further proteins on the same membrane, the membrane was washed in TBS-T three times for 10 minutes each at RT and then placed into stripping buffer for 30 minutes at 50 °C. The membrane was washed three times in TBS-T again for 10 minutes each at RT, blocked in 5% milk in TBS-T for one hour at RT and the next primary antibody was added onto the membrane as described earlier in this section.

### **2.2.5 In vivo mouse experiments**

The animal experiments performed in this study were carried out in accordance with legal requirements and were approved by the Regierung von Unterfranken (RUF 55.2.2 -22532.2 -925-18). The first step was to generate xenotransplantation mouse models with MCC tumors deriving from the MCPyV MCC cell line, MKL-1. For this purpose, five-week-old female NOD.CB17/*Prkdc*<sup>scid</sup> female mice grown in a pathogen-free environment were used. Each mouse was subcutaneously injected with  $5 \times 10^6$  MKL-1 cells in a 100 µl suspension containing equal volumes of medium and Matrigel®. The mice were closely monitored for increases in tumor volume which were measured daily using a vernier calipers. The calculation of tumor volume (V) was performed using the formula ( $V = (\pi/6) \times (\text{length})^2 \times \text{height}$ ). Treatments of the mice were started once the tumors reached a size of approximately 150 mm<sup>3</sup>. Six mice were allotted to the artesunate treatment group and five mice were allotted to the control group (owing to the absence of tumor growth in one mouse). Daily intraperitoneal injections of artesunate were then carried out such that each mouse from the treatment group was administered 100 mg/kg of artesunate which was dissolved at first in DMSO following which the volume was made up to 200 µl with PBS shortly before the treatment. The same volume of DMSO dissolved in a total volume of 200 µl of PBS

was administered to the control group (2% DMSO). The tumor sizes were measured until the maximum tolerable size was reached following which the mice were sacrificed.

### **2.2.6 Statistical Analysis**

GraphPad Prism was used for statistical analysis. Significant differences between cell survival observed following the treatment of cells with artesunate with and without apoptosis and ferroptosis inhibitors were estimated using ANOVA followed by suitable post hoc tests. This significance was calculated by comparing cell survival in each condition to cell survival upon artesunate treatment. The non-parametric Mann-Whitney test was used for comparing cell volume differences obtained by time lapse microscopy. Adjusted p-values were obtained following Dunnett multiple comparison testing. For the mouse experiments, tumor growth curves were plotted and the unpaired t-test was used to compare the values for the area under the curves.

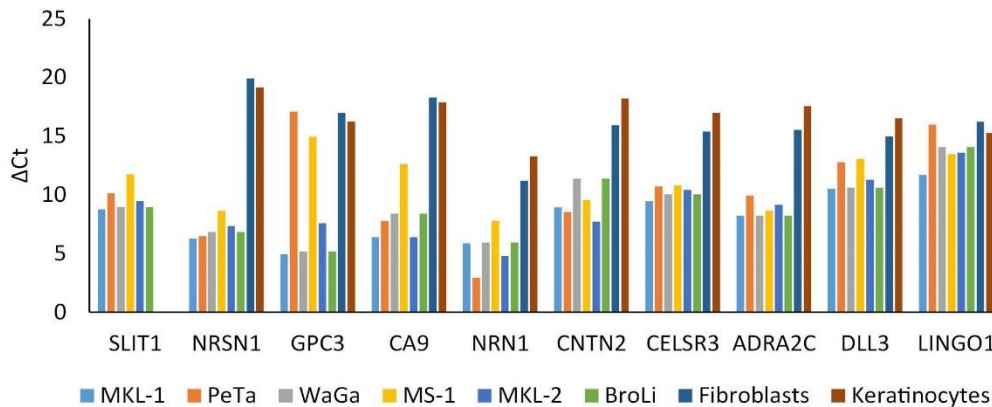
## **3. Results**

### **3.1 Generation and evaluation of a vector system expressing factors implicated in MCC oncogenesis**

#### **3.1.1 RNA sequencing of MCPyV-positive MCC cells for the identification of suitable cell surface markers**

Since the mechanisms of MCPyV-positive MCC carcinogenesis demand further investigation [44], we wished to generate and evaluate a vector system which might help to study aspects of MCPyV-positive MCC oncogenesis *in vitro*. An important point, in such an approach, would be the availability of suitable markers to identify and isolate cells undergoing MCC-like differentiation. To allow this in living and intact cells, we wished to identify proteins that are highly and selectively expressed on the cell surface of MCPyV-positive MCC cells as compared to the expression on other skin cell types like fibroblasts and keratinocytes. Therefore, paired-end RNA sequencing was performed for two MCPyV-positive MCC cell lines, MKL-1 and WaGa, as well as for primary keratinocytes and fibroblasts. The FPKM (Fragments Per Kilobase per Million mapped reads) values obtained for a total of 60448 genes were compared between each of the cell types to identify differentially expressed genes. 543 genes were identified which were expressed more than 20-fold by both MCPyV-positive MCC cell lines as compared to both control cells. Since we were interested in identifying cell surface markers, these 543 genes were manually screened further and 122 of them were found to be plasma membrane bound proteins with an extracellular domain. It was important to further screen these cell surface markers based on the availability of suitable antibodies for flow cytometric identification. Following this detailed screening, ten cell surface markers for which antibodies were available, were finally shortlisted and these markers were then used for the subsequent analysis.

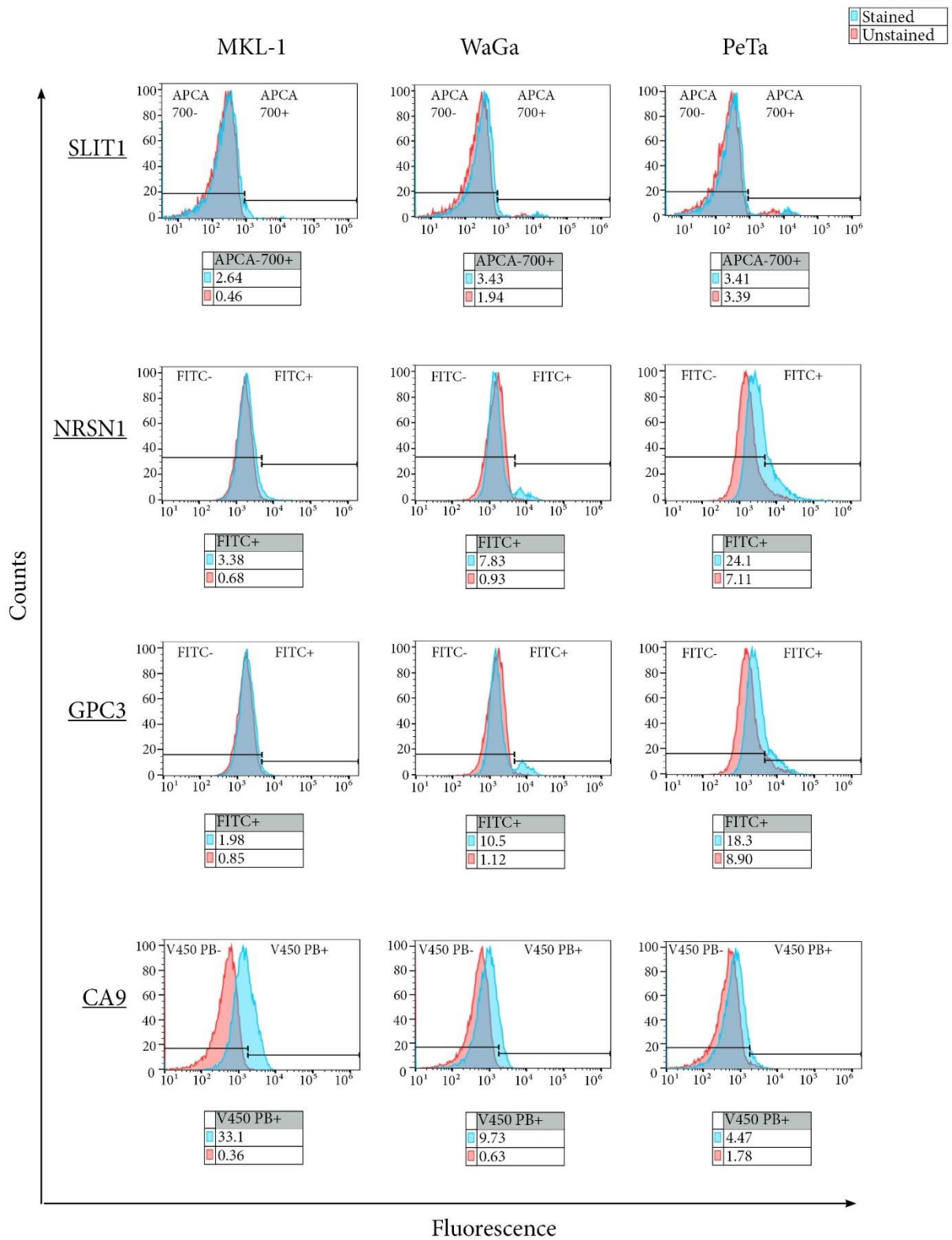
At first, expression of the ten shortlisted genes was analyzed using qPCR to confirm the results obtained by RNA sequencing. The expression was analyzed in six MCPyV-positive MCC cell lines (MKL-1, PeTa, WaGa, MS-1, MKL-2 and BroLi) and was compared with expression levels observed in primary fibroblasts and keratinocytes as controls (Fig. 9). With the exception of *LINGO1*, the RNA sequencing results of more than 20-fold difference between MKL-1/WaGa and fibroblasts/keratinocytes could be confirmed by qPCR ( $\Delta C_t$  values  $> 4.5$ ) and an MCC-specific high expression was suggested for most of the investigated mRNAs. However, since PeTa and MS-1 demonstrated mRNA levels comparable to keratinocytes and fibroblasts for GPC3 and DLL3, these two genes may be less robust MCC markers.

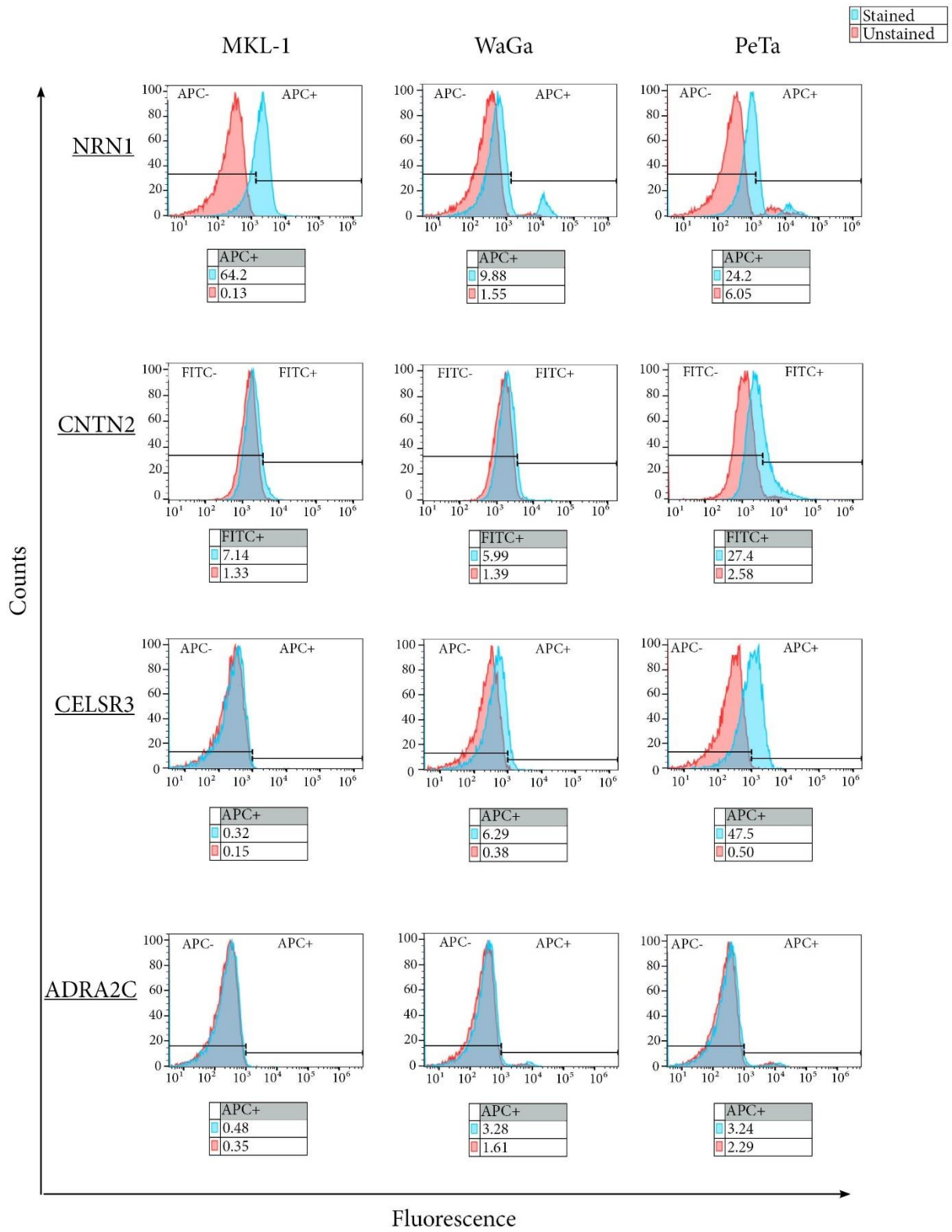


**Figure 9: Gene expression of ten MCPyV-positive MCC cell surface markers shortlisted post-RNA sequencing.** Six MCPyV-positive MCC cell lines (MKL-1, PeTa, WaGa, MS-1, MKL-2 and BroLi) were subjected to qPCR for ten cell surface marker genes that were shortlisted post-RNA sequencing. The expression levels of these genes in the MCPyV-positive MCC cell lines were compared with the expression levels in fibroblasts and keratinocytes as controls. The housekeeping gene, *RPLP0*, was used for the normalisation of target gene expression. Expression is plotted as the delta Ct ( $\Delta Ct$ ) values wherein low  $\Delta Ct$  values represent high expression and vice versa. (*SLIT1* - Slit Guidance Ligand 1, *NRSN1* - Neurensin 1, *GPC3* - Glypican 3, *CA9* - Carbonic Anhydrase 9, *NRN1* - Neuritin 1, *CNTN2* - Contactin 2, *CELSR3* - Cadherin EGF LAG Seven-Pass G-Type Receptor 3, *ADRA2C* - Adrenoceptor Alpha 2C, *DLL3* - Delta Like Canonical Notch Ligand 3, *LINGO1* - Leucine Rich Repeat And Ig Domain Containing Protein 1)

We went on to test commercially available antibodies against the shortlisted markers suggested to be MCC-specific by the RNA data by performing flow cytometric staining of three MCPyV-positive MCC cell lines (MKL-1, WaGa and PeTa). The results from these experiments showed that for most of the analyzed cell surface proteins, fluorescence staining did not correlate with the qPCR results (Fig. 9 and Fig. 10) and most of the antibodies produced hardly any signal (Fig. 10) raising doubts that they might be useful for distinguishing MCC-like cells from potential precursors. The only exception was the DLL3 antibody which produced a significant signal with all three investigated MCC cell lines (Fig 10), although mRNA expression was among the lowest in the MCPyV-positive MCCs when compared with the other shortlisted genes (Fig. 9). Because, particularly in PeTa, DLL3 mRNA expression was very similar to fibroblasts, we decided that also DLL3 might not be regarded as a suitable cell surface marker.

In conclusion, the RNA sequencing approach had not generated tools that could be used for the identification of living MCC-like cells and therefore, there was a need for an alternative approach to enable this crucial step for studying MCC oncogenesis.





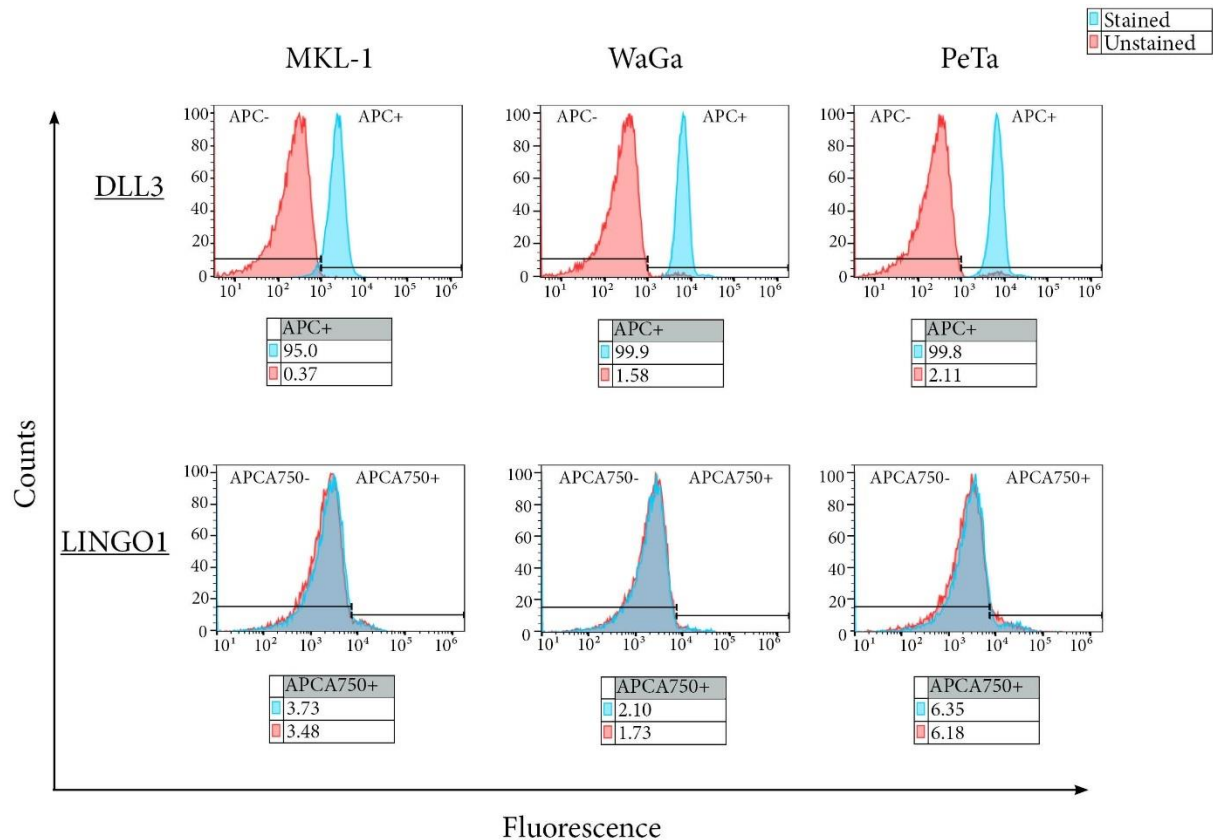


**Figure 10: Flow cytometric staining for the ten cell surface markers shortlisted post-RNA sequencing.** Three MCPyV-positive MCC cell lines (MKL-1, WaGa and PeTa) were stained with antibodies that were supposed to recognize the ten cell surface marker proteins that were shortlisted post-RNA sequencing. The antibodies against the markers SLIT1, CA9 and LINGO1 were conjugated to the fluorophores APCA700, V450 PB and APCA750 respectively. The antibodies against the markers NRN1, CELSR3, ADRA2C and DLL3 were conjugated to the fluorophore APC. Since the antibodies against the other markers (NRSN1, GPC3, CNT2) were not conjugated to fluorophores, secondary antibodies conjugated to FITC were used. Post-staining, fluorescence was analyzed on the flow cytometer in the respective fluorescence channels. The red peaks represent unstained cells while the blue peaks represent stained cells. The percentages of the fluorescence-positive populations of the unstained (red) and stained (blue) samples are provided in the boxes below each histogram. (SLIT1 - Slit Guidance Ligand 1, NRSN1 - Neurensin 1, GPC3 - Glypican 3, CA9 - Carbonic Anhydrase 9, NRN1 - Neuritin 1, CNTN2 - Contactin 2, CELSR3 - Cadherin EGF LAG Seven-Pass G-Type Receptor 3, ADRA2C - Adrenoceptor Alpha 2C, DLL3 - Delta Like Canonical Notch Ligand 3, LINGO1 - Leucine Rich Repeat And Ig Domain Containing Protein 1)

### 3.1.2 Successful establishment of a KRT20 fluorescence reporter system using CRISPR/Cas9 technology

A widely used marker for the diagnosis of MCC as well as for the identification of Merkel cells is the intermediate filament protein, Keratin 20 (KRT20) [24, 108, 111, 317]. Therefore, as the next attempt to enable easy identification of MCC-like cells *in vitro*, we aimed to establish a KRT20 fluorescence reporter system in which KRT20 expression would be coupled to expression of a green fluorescent protein. To this end,

we wanted to use CRISPR/Cas9 technology to integrate an mNeonGreen cDNA in frame with the *KRT20* coding sequence in the genome such that when the *KRT20* promoter would get activated, green fluorescence could be used to specifically isolate these cells.

The donor construct was designed such that its flanking ends contained sequences homologous to the *KRT20* genome (Fig. 11a). This would ensure insertion of the construct in frame with and at the end of the coding sequence the *KRT20* gene such that expression of *KRT20* would not be interfered with. Immediately following *KRT20* and in frame with it, the sequence for the fluorescent protein, mNeonGreen, was placed such that mNeonGreen expression would always accompany *KRT20* expression. mNeonGreen was flanked by the P2A and T2A self-cleaving peptide sequences that would enable its expression as a protein separate from *KRT20* and not as a fusion protein. Furthermore, the construct also contained a constitutively active CMV promoter that was controlling the expression of the antibiotic blasticidin (BSD) which would enable selection of cells that would successfully integrate the construct into their genome following transfection. The *loxP* sites flanking the CMV promoter were included to enable removal of the CMV promoter using the Cre-*loxP* system at later stages of the genetic manipulation procedure so that MCC-like cells with an active *KRT20* promoter could also be selected by means of their resistance to BSD.

At first, we tested the functionality of this reporter system in cells which already actively expressed *KRT20*. For this purpose, the MCC cell line WaGa was transfected with the *KRT20* donor construct using CRISPR-Cas9 genome editing. The cells were selected in BSD for a month to ensure the exclusion of cells which were not transfected as well as those which contained the donor plasmid episomally for a short duration. Correct integration of the donor construct in the survivor cells was confirmed by PCR (Fig. 11b) and subsequent Sanger sequencing of the PCR product. Furthermore, removal of the CMV promoter was also tested in these cells by PCR (Fig. 11b) following their transduction with a non-integrating, puromycin-selectable lentiviral vector carrying the Cre recombinase enzyme. A non-integrating lentiviral vector was used in this case because puromycin was to be used again as a selection marker in the constructs needed at later stages of the genetic manipulation procedure. In addition, the successfully transfected cells with the correctly integrated donor were analyzed on the flow cytometer to check for mNeonGreen fluorescence. Indeed, around 33% of the cells were positive for mNeonGreen and were identified as high expressors of *KRT20* (Fig. 11c). Post-Cre treatment and with continued selection in BSD, this mNeonGreen positive population of cells segregated from the negative population (as observed by the shift of the peak to the right) and exhibited slightly increased fluorescence (40%) (Fig. 11c). This implied that we were able to enrich for these high *KRT20* expressors. Since we wished to work exclusively with this enriched population, the cells were sorted out to isolate these mNeonGreen positive cells which was confirmed using flow cytometry (Fig. 11c). In order to test for the functionality of this *KRT20* reporter system,

we tested whether inhibition of KRT20 would result in a concomitant reduction of mNeonGreen expression. To this end, the sorted population of WaGa cells was transduced with a vector expressing a doxycycline-inducible shRNA to KRT20. Indeed, following induction, downregulation of both *KRT20* as well as mNeonGreen expression was observed as determined by qPCR analysis (Fig. 11d). Additionally, upon analyzing the cells on the flow cytometer, reduction of mNeonGreen fluorescence was also observed following doxycycline induction of the KRT20 shRNA (Fig. 11e).

These experiments led to the conclusion that the KRT20 donor construct could successfully be directed into the genome of target cells and the subsequent shRNA experiments confirmed the functionality of this KRT20 reporter system.

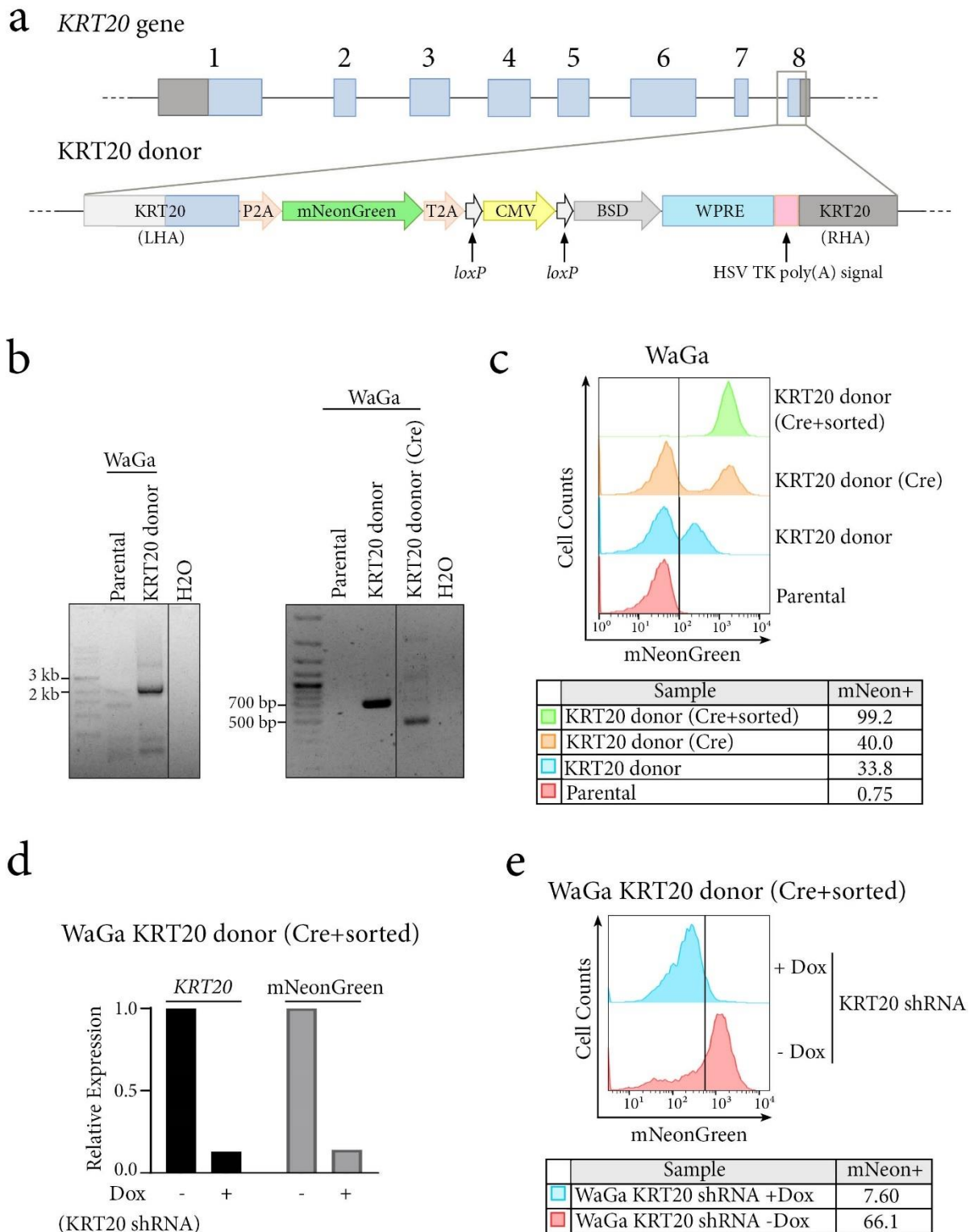


**Figure 11: Design of the *KRT20* donor and confirmation of the functionality of the *KRT20* fluorescence reporter system in WaGa cells.** a) The schematic representation on top is that of the *KRT20* gene depicting its eight exons represented by boxes and the spaces in between them represent the introns. Within the exons, the coding sequence is depicted in blue and the non-coding sequence in grey. The schematic representation of the *KRT20* donor is depicted below. The flanking ends of the donor consisted of the left homology arm (LHA) and the right homology arm (RHA) which were sequences homologous to the *KRT20* genome and enabled correct insertion of the reporter cassette in frame with and at the end of the coding sequence of *KRT20* (as depicted by the grey box). The

sequence for the fluorescent protein, mNeonGreen, was present in frame with the *KRT20* coding sequence and was flanked by the self-cleaving peptide sequences, P2A and T2A. This was followed by the sequence for the constitutive CMV promoter that was flanked by *loxP* sites to aid in its removal using the Cre-*loxP* system when necessary. Following this was the sequence for the antibiotic blasticidin (BSD), the expression of which was controlled by the CMV promoter. Additional elements included the woodchuck hepatitis virus post-transcriptional regulatory element (WPRE) to enhance transgene expression [318] and the herpes simplex virus thymidine kinase polyadenylation signal (HSV TK poly(A) signal) to increase polyadenylation efficiency [319]. b) (left) WaGa cells were transfected with the *KRT20* donor and with plasmids encoding Cas9 and a guide targeting the last coding exon of *KRT20*. DNA was then isolated from the cells that successfully survived one month of BSD (5 µg/ml) selection. A nested PCR was performed to check for correct integration of the donor in the genome of these cells. The primers used were designed such that one primer would bind within the donor and the other within the genome of *KRT20* outside the LHA. The expected size of the PCR product was 2001 bp. DNA from parental WaGa cells was used as a control. (right) WaGa cells which had successfully integrated the *KRT20* donor were transduced with a lentiviral vector expressing the Cre recombinase enzyme for the removal of the CMV promoter. DNA was isolated before and after the transduction and a PCR was performed for checking for the removal of the CMV promoter. The expected size of the PCR product with the CMV promoter was 658 bp and without the CMV promoter was 420 bp. DNA from parental WaGa cells was used as a negative control. c) The flow cytometric analysis depicts mNeonGreen fluorescence in WaGa cells with the integrated *KRT20* donor before and after transduction with the lentiviral Cre recombinase vector, in the sorted mNeonGreen positive population and in parental cells as controls. d) The sorted population of WaGa cells were transduced with a doxycycline (Dox)-inducible shRNA to *KRT20* and were induced with 1 µM Dox for four days. Subsequently, RNA was isolated and qPCR for *KRT20* and mNeonGreen was performed. Relative expression of *KRT20* and mNeonGreen is depicted as normalized to the uninduced state in both cases. *RPLP0* was used as the housekeeping gene for normalisation of target gene expression. e) The sorted population of WaGa cells which were transduced with the Dox-inducible shRNA to *KRT20* were induced with and without 1 µM Dox for four days and were then analyzed on the flow cytometer for mNeonGreen fluorescence.

### **3.1.3 Generation of inducible expression vectors for the expression of proteins implicated in MCPyV-positive MCC oncogenesis**

Since a deeper understanding into the mechanisms of MCPyV-positive MCC oncogenesis and differentiation is needed [44], we wished to establish a vector system that might aid in studies addressing these aspects. To this end, we generated several independently-inducible lentiviral vectors (described in subsequent sections 3.1.3.1 to 3.1.3.3) that would enable the inducible expression of proteins that have previously been implicated in MCPyV-positive MCC oncogenesis [36, 70, 82, 94]. In order to enable testing of the several inducible proteins at the same time, different inducible systems and antibiotic selection markers were utilized in every vector.

#### **3.1.3.1 Doxycycline-inducible T antigen (TA) and small T antigen (sT) expression vectors**

In MCPyV-positive MCC tumors, the Merkel cell polyomavirus (MCPyV) clonally integrates into the genome of the host and expresses the small T antigen (sT) and the

C-terminally truncated large T antigen (LT) which serve as oncogenic drivers of MCC [31, 45, 70]. Therefore, the most important vectors generated for enabling the study of MCPyV-positive MCC oncogenesis were the T antigen expression vectors. Furthermore, we also generated a vector expressing only sT and not LT. This would aid in analyzing the independent influence of sT in MCC formation as previous experiments in mice have demonstrated the initiation of intraepidermal MCC-like tumors upon co-expression of sT and the Merkel cell determinant, ATOH1 [61]. Moreover, analysis of established MCC cells strongly suggests sT involvement in MCC tumorigenesis [60, 70].

The T antigen expression vectors were designed to express sT and the truncated version of LT from the WaGa cell line [53]. Two separate vectors, one expressing both the T antigens and the other expressing sT alone were generated (Fig. 12a). The vectors relied on the Tet-On doxycycline-inducible system [320, 321] such that the T antigens would be expressed only following induction with doxycycline. The P2A and NLuc elements present in between the two promoters, the Tight TRE and EF-1 $\alpha$ , were not expressed but were nevertheless retained in the vector. This was because several attempts at optimisation of the vectors revealed that the presence of these additional elements enabled the best possible inducible expression of the T antigens, probably owing to the additional distance between the two promoters [322]. Furthermore, the vectors also expressed hygromycin as an antibiotic resistance marker in order to enable selection.

At first, the inducibility and functionality of these vectors was tested in the murine fibroblast cell line, NIH3T3. NIH3T3 cells have frequently been used in previous studies to test the transforming capability of potential oncogenes [323-325]. Under normal circumstances, these cells rely on strong contact inhibition and grow in monolayers. However, upon transformation, they lose their contact inhibition and grow as multilayered colonies of transformed cells called foci. These foci are thereby indicative of oncogenes with transforming capabilities [325, 326]. MCPyV sT has been shown to possess some transforming capabilities both *in vitro* and *in vivo* [24, 60, 61, 126]. Therefore, in this experiment, the transformation assay was used to confirm the transforming capacity of sT in our T antigen vectors and to thereby prove its functionality. To this end, NIH3T3 cells were transduced with either the TA or sT vectors and were then selected in hygromycin. Doxycycline-inducible T antigen expression in the survivor cells was then confirmed by immunoblot (Fig. 12b). An 87-fold induction of LT and a 19-fold induction of sT compared to the uninduced state was observed for the NIH3T3 cells transduced with the TA vector. For the NIH3T3 cells transduced with the sT vector, a 15-fold induction of sT as compared to the uninduced state was observed. In parallel, the transduced NIH3T3 cells were also seeded at low densities in flasks with or without doxycycline in the medium and the transforming potential of inducible sT was analyzed by the transformation assay. Using crystal violet staining, it was found that focus formation occurred only in those flasks where the T

antigens were inducibly expressed following doxycycline treatment, confirming that these vectors were functional (Fig. 12c).

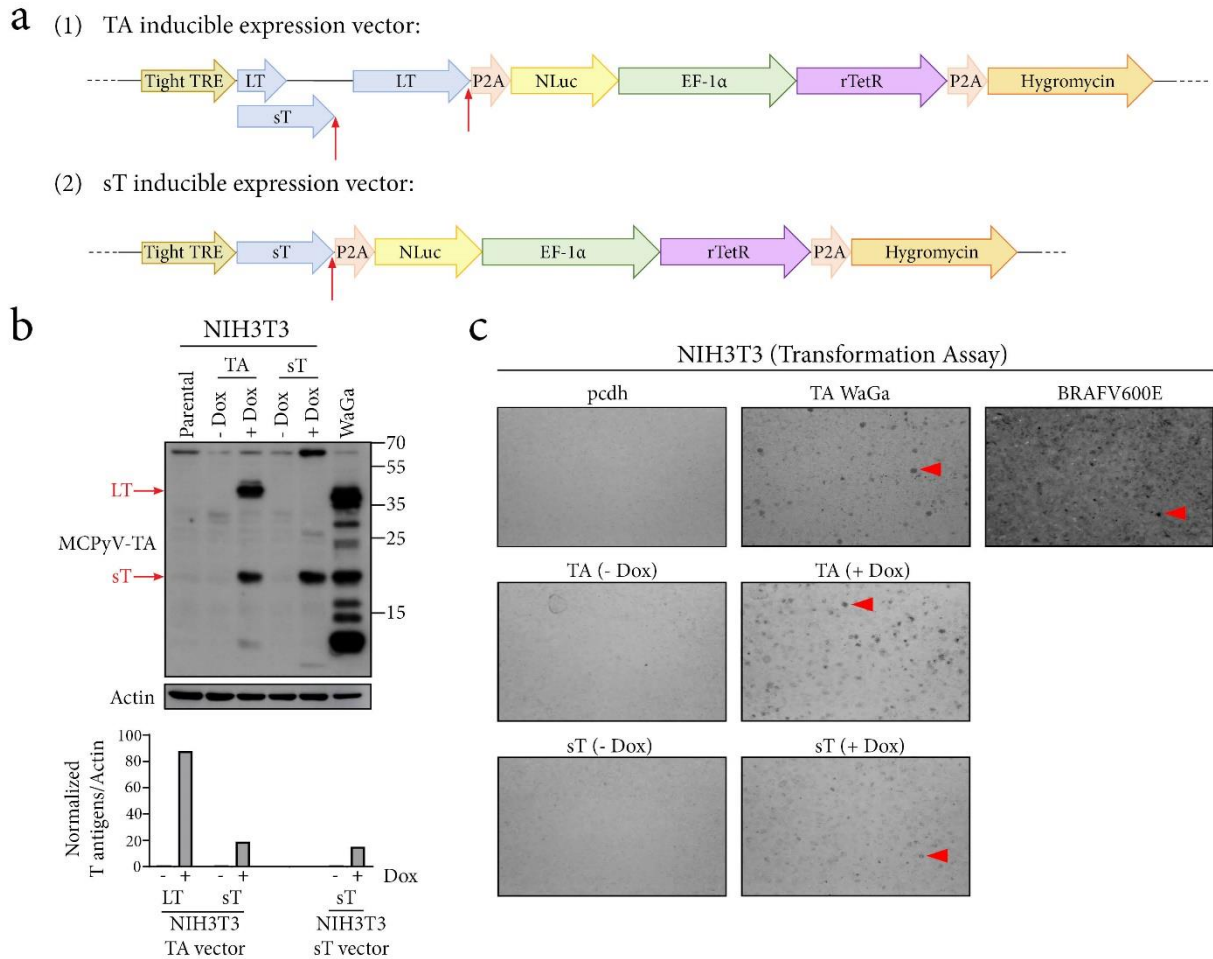


**Figure 12: Design and confirmation of inducibility and functionality of the T antigen expression vectors.** a) Schematic representations of the lentiviral (1) TA and (2) sT inducible expression vectors are depicted. The sequences for WaGa-derived sT and truncated LT are placed under the control of the inducible Tet-responsive promoter (Tight TRE). At the ends of the T antigen sequences, stop codons are placed (indicated by red arrows). The EF-1 $\alpha$  promoter aids in constitutive expression of the reverse tetracycline-controlled transactivator (rTetR) element as well as hygromycin as the antibiotic resistance marker separated from rTetR by a P2A self cleavage peptide sequence. The tight TRE promoter and rTetR element are both part of the Tet-On doxycycline-inducible expression system. In the absence of doxycycline (Dox), the rTetR, which is fused to a transcription activation domain, cannot bind to the operator sequences in the tight TRE promoter preventing transcription. When present, Dox binds to rTetR bringing about a change in its conformation and therefore enables binding to the operator and activation of transcription [320, 321]. Additional elements present are the P2A and NanoLuc (NLuc) sequences, which however are not expressed. b) NIH3T3 cells were transduced with either the TA or sT vectors and were selected in hygromycin (100  $\mu$ g/ml) for a week. The survivor cells were induced with or without 1  $\mu$ M Dox for four days following which an immunoblot for the T antigens was performed using the 2T2 antibody. Parental NIH3T3 cells and WaGa cells were included as negative and positive controls respectively. Actin was used as the loading control. The bar graphs depict quantification for the immunoblot signals for LT and sT normalized to actin and represented relative to the respective uninduced states. c) NIH3T3 cells that were transduced with either the TA or sT vectors were seeded

at low densities into T75 cell culture flasks either in the presence or absence of 1  $\mu$ M Dox. The cells were maintained in the flask for three weeks and the medium was periodically replenished. NIH3T3 cells transduced with an empty vector (pcdh) as a negative control and either with constitutively expressed WaGa T antigen (TA WaGa) or the potent oncogene BRAF<sup>V600E</sup> [327, 328] as positive controls were included. After three weeks, the cells were stained with crystal violet. Foci are indicated by red pointers.

### **3.1.3.2 RheoSwitch-inducible Atonal Homolog BHLH Transcription Factor 1 (ATOH1) expression vector**

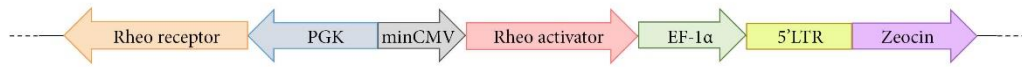
The basic helix-loop-helix transcription factor, atonal bHLH transcription factor 1 (ATOH1), is crucial for the development of Merkel cells from epidermal progenitors in the skin [78-80, 329]. ATOH1 overexpression has also been witnessed in MCCs and is correlated with poor prognosis [82]. In addition, experiments have shown that co-expression of ATOH1 and MCPyV sT in the epidermis of mice results in the development of intraepidermal MCC-like tumors [61]. Therefore, we generated a vector for the inducible expression of ATOH1.

The RheoSwitch system was used for the inducible expression of ATOH1. Two vectors were used as part of this system, the first expressing a RheoSwitch transcription factor and the second, consisting of the inducible promoter for ATOH1 expression (Fig. 13a). The RheoSwitch transcription factor consisted of the Rheo receptor and Rheo activator. Together, these fusion proteins formed a heterodimeric transcription factor which stabilized and activated transcription of ATOH1 from the inducible promoter lacP only upon induction with the ligand RSL1 [330-332].

In order to test the inducibility of this system, an eGFP inducible test vector was generated. In place of ATOH1, a sequence for eGFP was cloned in the second RheoSwitch vector. These vectors were tested in primary fibroblasts and in HaCaT cells (immortalized human keratinocytes). Sequential transduction of the cells with both the RheoSwitch vectors was performed. After each transduction, the cells were selected with the antibiotics, zeocin and neomycin respectively. The survivor cells were then cultured with or without RSL1 following which the cells were analyzed for the induction of eGFP on the flow cytometer. A 61-fold and 54-fold induction of eGFP compared to the uninduced state was observed in RSL1-induced fibroblasts and HaCaT cells respectively confirming the inducibility of the RheoSwitch vectors although some differences between induction in the the two cell types were observed (Fig. 13b). While 90% of the fibroblasts expressed eGFP following RSL1 induction, only a fraction of the HaCaT cells (55%) were found to be positive post-induction. Notably, however, some background fluorescence (11.9%) was observed in fibroblasts while in HaCaT cells, no leakiness was evident.

**a** Rheoswitch two component vector system

(1) Rheoswitch transcription factor:



(2) ATOH1 inducible expression vector:



(3) eGFP inducible test vector:



**b**

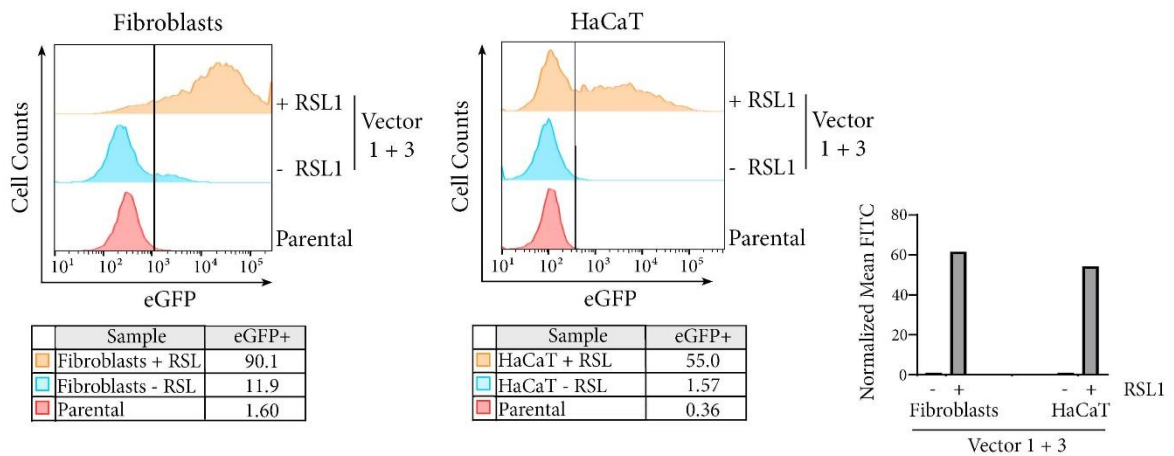


**Figure 13: Design and functionality of the RheoSwitch-inducible lentiviral vector intended for the inducible expression of ATOH1.**

**a)** Schematic representations of the lentiviral vectors expressing (1) the RheoSwitch transcription factor, (2) inducible ATOH1 and (3) inducible eGFP are depicted. In the first vector, the Rheo receptor and Rheo activator, encoded for by the PGK and minimal CMV (min CMV) promoters respectively, each express a part of a heterodimeric transcription factor. The Rheo receptor encodes for the ecdysone receptor (EcR) from *Choristoneura fumiferana* with a ligand binding domain fused to a DNA binding domain of the GAL4 transcriptional activator from yeast. The Rheo activator encodes for the retinoic acid receptor RXR-beta fused to the transcriptional activation domain of herpes simplex virus protein VP16 [330-332]. The EF-1 $\alpha$  promoter controls expression of the antibiotic selection marker zeocin. The second vector consists of the inducible promoter lacP which expresses Flag-HA-tagged ATOH1 upon activation by the heterodimeric transcription factor only following induction with the inducer RSL1. The EF-1 $\alpha$  promoter controls expression of the antibiotic selection marker neomycin. The third vector is a variant of the second vector wherein the sequence for Flag-HA tagged ATOH1 is replaced by that of an eGFP. It serves as a test vector to test the inducibility of the RheoSwitch system. Additional elements present are the lac operator lacO, the 5X UAS which consists of five tandem copies of the "Scal site", a 17-mer sequence (CGGAGTACTGTCCTCCG), which serves as an upstream activating sequence (UAS) that efficiently binds yeast Gal4 [333, 334] and the 5' LTR which represents the truncated 5' long terminal repeat (LTR) from human T-cell leukemia virus (HTLV) type 1. **b)** Fibroblasts and HaCaT cells were transduced with the RheoSwitch transcription factor vector (vector 1) and the eGFP inducible test vector (vector 3), sequentially, following selection with zeocin (400  $\mu$ g/ml) and neomycin (400  $\mu$ g/ml) after each transduction. The survivor cells were treated with or without RSL1 (2  $\mu$ M) for three days and subsequently analyzed on the flow cytometer for eGFP fluorescence. The corresponding parental cells were analyzed as negative controls. The bar graphs depict normalized mean FITC values represented relative to the uninduced states.

### **3.1.3.3 IPTG-inducible GLI family zinc finger 1 (GLI1) and dominant-negative Mastermind-like1 (dnMAML) expression vectors**

The transcription factor GLI Family Zinc Finger 1 (GLI1) is part of the Hedgehog signaling cascade which is involved in embryogenesis and organogenesis in humans [87, 89]. The activation of this cascade and subsequent GLI1 expression is known to be required for the differentiation of Merkel cells and the maintenance of their progenitors [84, 90, 91]. Interestingly, previous reports to identify the cellular origin of MCC, have strongly supported its origin from GLI1-expressing epithelial progenitor cells [84, 94]. As a result, an inducible expression vector for GLI1 was generated.

The multifaceted Notch signaling pathway is important for cell growth, regeneration and cell fate determination [335]. The pathway is activated upon the binding of a ligand to Notch receptors on the cell surface [336, 337]. This results in the proteolytic cleavage and translocation of the intracellular domain of Notch into the nucleus which is responsible for the activation of Notch target genes [336, 337]. Mastermind-like (MAML) proteins such as MAML1, form a part of a large transcription activation complex associated with the intracellular domain of Notch to amplify Notch-induced transcription of target genes such as *HES1* [338]. Inactivation of the Notch pathway has been described in MCC [36]. Therefore, an inducible vector expressing a dominant negative version of MAML1 (dnMAML1), a previously well-established system for Notch inhibition [339], was generated.

Isopropyl  $\beta$ -D-thiogalactopyranoside (IPTG)-inducible vectors were generated for GLI1 and dnMAML1 (Fig. 14a). In an uninduced state, the constitutively expressed lac repressor (lacI) binds to the lac operator located within the promoter for the respective cDNA, thereby inhibiting transcription. The inducer, IPTG, binds to the lac repressor when present in the medium, thereby permitting expression of the target gene [340, 341]. Similar to the RheoSwitch system, an eGFP inducible test vector was generated to confirm the inducibility of these vectors following treatment with IPTG. For this purpose, U2OS cells (Human Bone Osteosarcoma Epithelial Cells) were transduced with this eGFP vector and puromycin selection was performed. The survivor cells were cultured with or without IPTG and were subsequently analyzed for eGFP fluorescence on the flow cytometer. A 9-fold induction of eGFP compared to the uninduced state was observed in the IPTG-induced cells confirming that the system was inducible (Fig. 14b). Although the fold-induction levels were much lower than that observed upon using a similar eGFP test vector for the RheoSwitch system (Fig. 13b), eGFP induction was observed in a large number of cells (70%) and no background fluorescence was observed.

In addition, we also tested the functionality of IPTG-inducible dnMAML1 in our generated vector. For this purpose, a Notch reporter system was made use of to test the influence of IPTG-inducible dnMAML1 expression on the suppression of Notch signaling. To this end, a reporter plasmid for Notch signaling activation was used

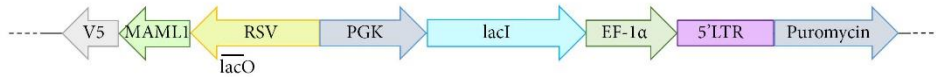
(hereafter referred to as the Notch reporter) which consisted of the promoter for the Notch downstream target gene *HES1*, downstream of which the sequence of a red fluorescent protein (DsRed-Express) was present (Fig. 14c). Furthermore, a plasmid for overexpression of the Notch intracellular domain (hereafter referred to as NIC) for the upregulation of Notch signaling was also used in order to more easily visualize a potential suppression of Notch signaling by dnMAML1. A series of co-transfections in U2OS cells were then performed. All cells were transfected with the Notch reporter. In addition, the cells were either transfected with NIC, IPTG-inducible dnMAML1 or a combination of the two plasmids and as controls, with empty vectors. Following two days of induction with or without IPTG, the cells were analyzed on the flow cytometer. The cells co-transfected with the Notch reporter and NIC demonstrated an approximately 11-fold increase in red fluorescence as compared to the co-transfected controls both in the presence and absence of IPTG indicating that Notch signaling was upregulated in these cells because of NIC overexpression. No changes in red fluorescence were evident upon IPTG-induced expression of dnMAML1 in cells co-transfected with the Notch reporter and IPTG-inducible dnMAML1 alone. Notably, however, the cells co-transfected with the Notch reporter, NIC and IPTG-inducible dnMAML1 demonstrated only a 5.5-fold increase in red fluorescence in the presence IPTG as compared to the co-transfected controls. In contrast, the same set of co-transfected cells, in the absence of IPTG, demonstrated a 10-fold increase in red fluorescence. Therefore, since the NIC induced upregulation of Notch signaling was reduced by approximately 2-fold upon the IPTG-induced expression of dnMAML1, this experiment demonstrated the functionality of inducible dnMAML1 in our generated vector.

**a** IPTG-inducible system

(1) GLI1 inducible expression vector:



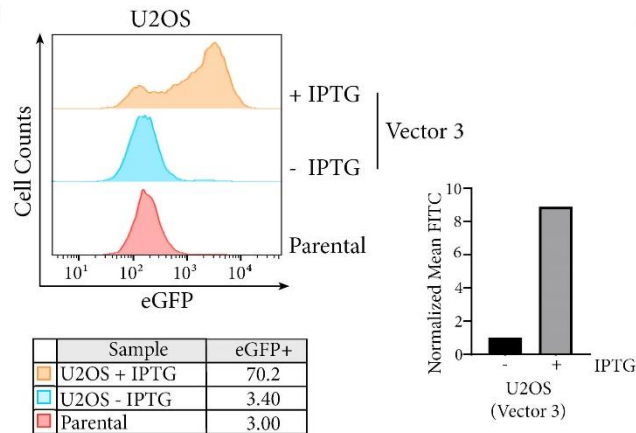
(2) dnMAML1 inducible expression vector:



(3) eGFP inducible test vector:



**b**



**c**

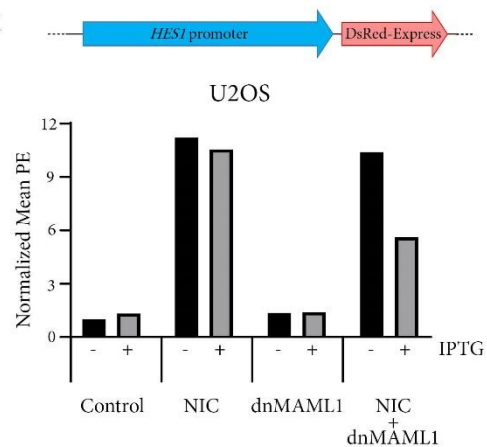


**Figure 14: Design and functionality of the IPTG-inducible lentiviral vector intended for the inducible expression of GLI1 and dnMAML1.** a) Schematic representations of the lentiviral vectors expressing (1) inducible GLI1, (2) inducible dnMAML1 and (3) inducible eGFP are depicted. The inducible promoter RSV controls the expression of (1) Flag-tagged GLI1, (2) V5-tagged dnMAML1 or (3) eGFP in each of the vectors. The PGK promoter drives expression of lacI (the lac repressor) which binds to the lac operator (lacO) present within the RSV promoter, preventing transcription. When IPTG is present, it binds to the lac repressor releasing it from the RSV promoter thereby facilitating expression of the target genes [340, 341]. The EF-1 $\alpha$  promoter and the truncated 5' long terminal repeat (LTR) from human T-cell leukemia virus (HTLV) type 1 control expression of the antibiotic selection marker puromycin. b) U2OS cells were transduced with the eGFP inducible test vector and selected with puromycin (5  $\mu$ g/ml). The survivor cells were treated with or without IPTG (400  $\mu$ M) and analyzed on the flow cytometer for induction of eGFP three days after treatment. U2OS parental cells were analyzed as negative controls. The bar graphs depict normalized mean FITC values represented relative to the uninduced state. c) A schematic representation of the reporter cassette of the Notch reporter plasmid is provided above the bar graphs and depicts the promoter for the Notch target gene, *HES1* and the downstream red fluorescent protein, DsRed-Express. The bar graphs depict normalized mean PE (red fluorescence) as determined by flow cytometric analysis of U2OS co-transfected cells treated in the presence or absence of 400  $\mu$ M IPTG for two days. All cells were transfected with the Notch reporter. In addition, the cells were co-transfected either with NIC, IPTG-inducible dnMAML1 or a combination of both and as controls, with empty vectors. All values are represented as relative to the control treated in the absence of IPTG.

Since the eGFP test vectors were able to confirm the inducibility of the RheoSwitch and IPTG systems, this served as an indication that ATOH1 and GLI1 should also respectively be efficiently induced using these systems. Therefore, inducible expression of these proteins was directly tested in subsequent experiments wherein the influence of these vectors was analyzed in specific cellular backgrounds.

### **3.1.4 Genetic manipulations in primary fibroblasts**

Following the successful generation and testing of the KRT20 fluorescence reporter system as well as the various vectors for the inducible expression of MCC relevant factors, we went on to introduce these vectors into various cell types in an attempt to test for a potential influence of these factors in MCC development. Since primary fibroblasts are easy to genetically manipulate and additionally possess the potential of dedifferentiation into iPSCs [342-344], we initially used primary fibroblasts as the starter cells for this approach (See Fig. 8 in section 2.2.3.4). Furthermore, fibroblasts are known to be the only cell type which support robust replication of the MCPyV [125].

#### **3.1.4.1 Integration of the KRT20 donor into primary fibroblasts**

Primary fibroblasts were transfected with the KRT20 donor construct using CRISPR/Cas9 as described for WaGa cells (Section 3.1.2) and were selected with BSD for one month. The fibroblasts that survived were tested for correct integration of the donor by PCR (Fig. 15a) and subsequent Sanger sequencing. They were found to integrate the donor at the right location in the genome. Since later stages of the genetic manipulation procedure would require the removal of the CMV promoter, this was tested in a subset of fibroblasts with correctly integrated donor following their transduction with the non-integrating lentiviral Cre vector as described for WaGa cells (Section 3.1.2). PCR was used to confirm the loss of the CMV promoter (Fig. 15b). These primary fibroblasts with correctly integrated KRT20 donor are henceforth referred to as KRT20-fibroblasts.

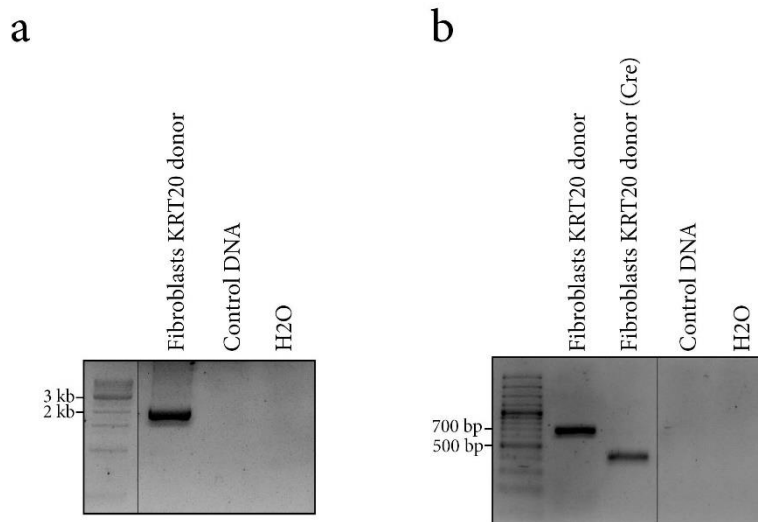


**Figure 15: Introduction of the KRT20 donor construct in primary fibroblasts.** a) Primary fibroblasts were transfected with plasmids encoding Cas9 and a guide targeting the last coding exon of KRT20 as well as the KRT20 donor construct. Following selection in BSD (5  $\mu$ g/ml) for one month, DNA was isolated from the survivor cells. Nested PCR was performed to check for correct integration of the donor in the genome of these cells. The expected size of the PCR product was 2001 bp. b) A subset of primary fibroblasts which had successfully integrated the KRT20 donor were transduced with a non-integrating lentiviral vector expressing the Cre recombinase enzyme for the removal of the CMV promoter. DNA was isolated before and after the transduction and a PCR was performed for checking for the removal of the CMV promoter. The expected size of the PCR product with the CMV promoter was 658 bp and without the CMV promoter was 420 bp. Human random control DNA was used as a negative control for both PCRs.

### **3.1.4.2 The use of human telomerase reverse transcriptase (hTERT) to increase the proliferative lifespan of primary fibroblasts**

Since we used primary cells for our genetic manipulations, we often observed that the cells ran into senescence and failed to proliferate after being maintained in culture for a long period of time. The role of human telomerase reverse transcriptase (hTERT) in extending the proliferative capacity of primary cells has previously been described [345, 346]. Hence, to circumvent our problem, an hTERT vector was designed and its usefulness in prolonging the lifespan of our primary cells during the course of the genetic manipulations was tested.

The vector was designed to constitutively express hTERT (Fig. 16a). Since the available antibiotic selection markers were already used for the other vectors, mRuby was used as a fluorescence marker to identify successfully transduced cells. Certain studies demonstrated that long term expression of hTERT resulted in the development of a transformed phenotype in primary fibroblasts [347]. We speculated that the event of such an occurrence in our cells might aid in the long term goal which was the generation of tumor-like cells *in vitro*. Nevertheless, the long term effect of hTERT overexpression in our primary cells and its influence on future MCC-like cells in our

experimental setting was unknown. Hence, we included *LoxP* sites flanking the ends of the vector to enable its removal from the cells if required, after performing the genetic manipulations.

The lentiviral hTERT vector was transduced into the KRT20-fibroblasts. The cells were then maintained in culture to enable a possible enrichment of hTERT positive cells over time. mRuby fluorescence deriving from these transduced cells was compared immediately post-transduction as well as after maintaining these cells in culture for one month post-transduction. We observed that 76.5% of the cells were positive for mRuby fluorescence immediately post-transduction indicative of a high efficiency of transduction (Fig. 16b). The fluorescence increased further to 91.2% after maintaining these cells in culture one month, indicative of an enrichment of hTERT expressing cells in this time frame (Fig. 16b). We also performed an immunoblot and could confirm hTERT expression in the cells transduced with the hTERT vector (Fig. 16c). Semiquantitative and morphological comparison of hTERT-transduced and non-transduced cells, suggested that fibroblasts expressing hTERT regained their proliferative potential, appeared healthier and also lost their senescent phenotype (Fig. 16d). In conclusion, we found that hTERT expression had a positive influence on the growth potential of our primary fibroblasts making it easier to work with these cells for the rest of the genetic manipulation procedure.

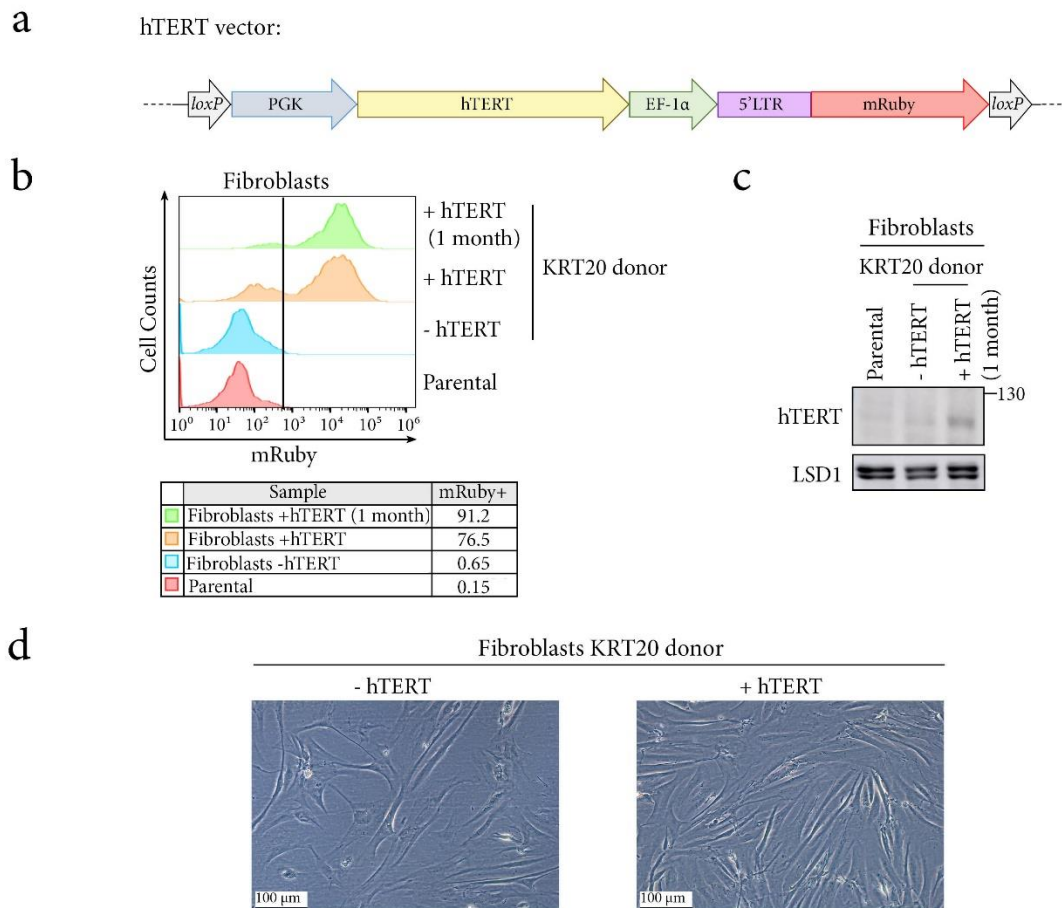


**Figure 16: hTERT expression increased the proliferative potential of primary fibroblasts.** a) The schematic representation of the lentiviral hTERT expression vector is depicted. The PGK and EF-1 $\alpha$  promoters constitutively expressed hTERT and mRuby respectively. The *loxP* sites found at the flanking ends of the vector were placed to enable removal of the vector from the cells using Cre treatment. Additional elements present were the 5' LTR which represented the truncated 5' long terminal repeat (LTR) from human T-cell leukemia virus (HTLV) type 1. b) KRT20-fibroblasts were transduced with the hTERT vector and were analyzed on the flow cytometer for mRuby fluorescence immediately following transduction (+hTERT) as well as one month post-transduction (+hTERT (1 month)). Parental fibroblasts as well as non-transduced KRT20-fibroblasts were included as a negative controls. c) KRT20-fibroblasts which were transduced with the hTERT vector were analyzed by immunoblot for hTERT expression one month post-transduction. The expected size of hTERT was 126 kDa. LSD1 was used as a loading control. d) Light microscopic images of confluent KRT20-fibroblasts transduced (and maintained in culture for one month) or not transduced with the hTERT vector are depicted. Scale bars = 100  $\mu$ m.

### 3.1.4.3 Lentiviral transduction of primary fibroblasts with the various inducible expression vectors

The next step was to sequentially introduce the various inducible expression vectors into the KRT20-fibroblasts via lentiviral transduction. At first, the KRT20-fibroblasts were sequentially transduced with the two RheoSwitch-inducible ATOH1 vectors and

were selected with zeocin and neomycin following each of the two transduction steps. Low levels of ATOH1 expression (approximately 3-fold compared to the uninduced state) following RSL1 induction were observed in these cells by immunoblot (Fig. 17a) which was lower than the levels of induction observed upon initial testing of the RheoSwitch vectors (Fig. 13b). Therefore, we decided at this stage that single cell cloning would be performed at the end of the genetic manipulation procedure to enable the potential isolation of clones with high levels of induction. The cells were then split into two parts and each was then transduced either with the doxycycline-inducible TA or sT vectors. After hygromycin selection, the survivor cells were induced with doxycycline and inducible T antigen expression was confirmed by immunoblot (Fig. 17b). While a 46-fold induction of sT was observed in the cells expressing the sT vector following doxycycline induction, for the cells expressing the TA vector, a 5-fold and 15-fold induction of sT and LT respectively was observed as compared to the respective uninduced states in each case. The two cell populations expressing either inducible TA or sT were then infected either with the IPTG-inducible dnMAML1 or GLI1 vectors and selected with puromycin. Induction of *DNMAML1* and *GLI1* following IPTG treatment was tested using qPCR (Fig. 17c and d). IPTG-induced expression of *dnMAML1* increased by 11-fold and 3-fold for the cells harbouring the TA and sT vectors respectively as compared to the uninduced states (Fig. 17d). With respect to IPTG-induced expression of *GLI1*, very small increases in *GLI1* expression, under 2-fold compared to the uninduced states, were observed for both the TA and sT vector harbouring cell populations (Fig. 17d). Moreover, it was also evident that the expression of *GLI1* from this vector was very leaky as observed by the 15-fold and 17-fold increase in *GLI1* expression for the TA and sT vector harbouring cells respectively in the uninduced states compared to parental fibroblasts (Fig. 17d). Therefore, single cell cloning was performed subsequently to search for clones demonstrating optimal induction.

In addition, we attempted performing Cre treatment in these fibroblasts in order to remove the CMV promoter controlling BSD expression in the KRT20 donor construct. As described in section 3.1.2, this would serve as an additional tool in enabling the selection of MCC-like cells which would then express BSD under the control of their own active KRT20 promoter. Soon after the Cre treatment, the fibroblasts appeared senescent and stopped actively proliferating. This occurred most likely due to the concomitant removal of the hTERT vector that was enhancing the proliferative potential of these cells. Therefore, the Cre treatment step was omitted.

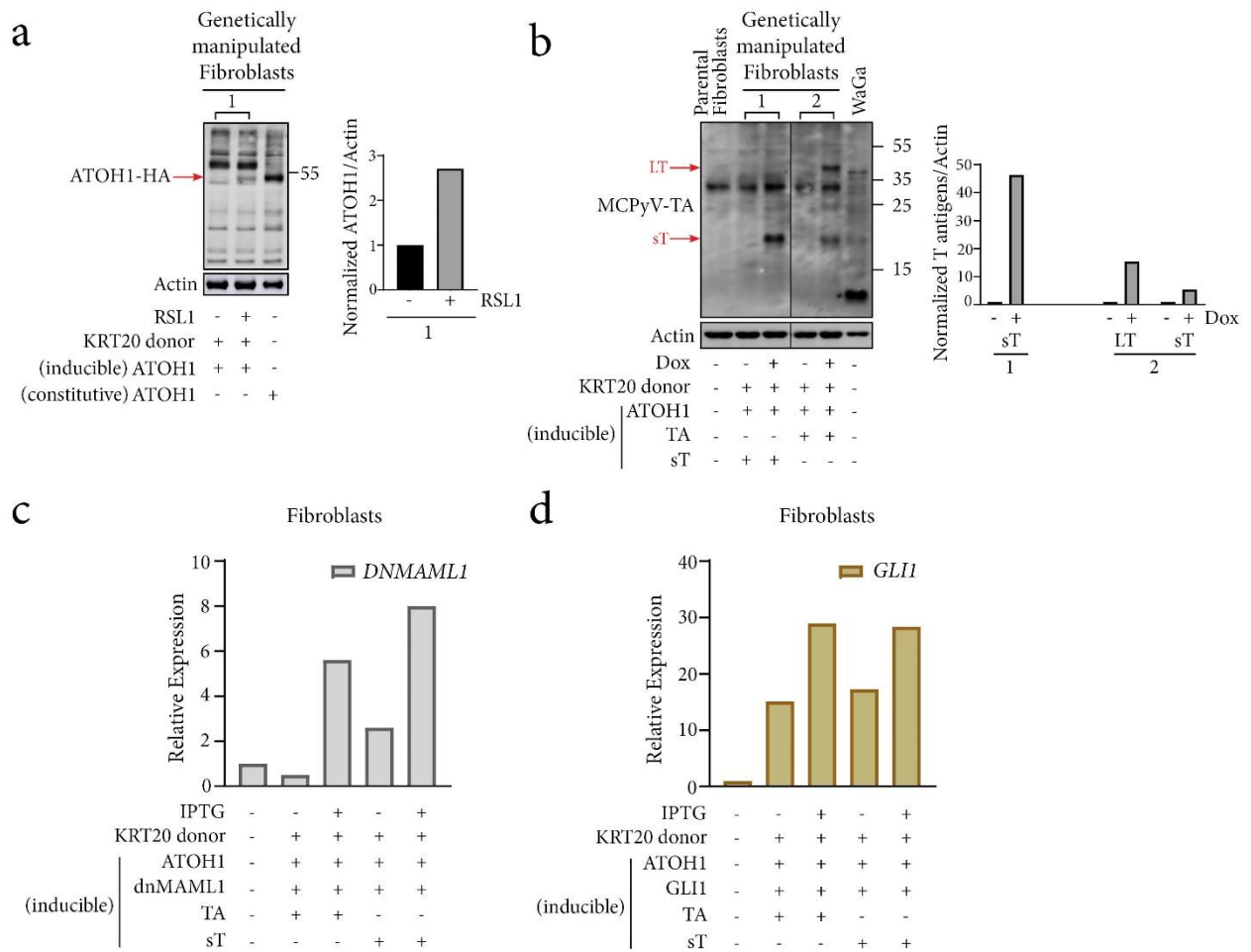


**Figure 17: Inducibility testing of the various vectors in KRT20-fibroblasts.** a) KRT20-fibroblasts were sequentially transduced with the two RheoSwitch-inducible ATOH1 expression vectors and were selected with zeocin (400  $\mu\text{g}/\text{ml}$ ) and neomycin (400  $\mu\text{g}/\text{ml}$ ) following each transduction. The survivor fibroblasts were induced with 2  $\mu\text{M}$  RSL1 for three days after which an immunoblot for HA-tagged ATOH1 was performed. Fibroblasts constitutively expressing HA-tagged ATOH1 were used as a positive control. Actin was used as the loading control. The bar graphs depict quantification for the immunoblot signals for ATOH1 normalized to actin and represented relative to the respective uninduced state. b) KRT20-fibroblasts transduced with the RheoSwitch-inducible ATOH1 vectors were further transduced either with the doxycycline (Dox)-inducible TA or sT vectors and were selected in hygromycin (100  $\mu\text{g}/\text{ml}$ ). The survivor fibroblasts were induced with 1  $\mu\text{M}$  Dox for four days and an immunoblot for the T antigens was performed. Parental fibroblasts and WaGa cells were used as negative and positive controls respectively. The bar graphs depict quantification for the immunoblot signals for sT and LT normalized to actin and represented relative to the respective uninduced states. c and d) KRT20 fibroblasts transduced with both the ATOH1 and TA/sT inducible expression vectors were transduced with either the IPTG-inducible (c) dnMAML1 or (d) GLI1 expression vectors. Following selection with puromycin (5  $\mu\text{g}/\text{ml}$ ), the survivor fibroblasts were induced with 400  $\mu\text{M}$  IPTG for three days and qPCR for (c) *DNMAML1* and (d) *GLI1* was performed. Parental fibroblasts are represented in the first columns of the graphs and were included as negative controls. The expression of the genes was normalized to that of the parental cells. *RPLP0* was used as the housekeeping gene for normalisation of target gene expression.

#### **3.1.4.4 Single cell cloning to identify optimal genetically manipulated clones**

From the polyclonal population of genetically manipulated KRT20-fibroblasts, we wished to generate single cell clones in order to be able to pick out clones which exhibited excellent inducible expression of all three vectors, preferably with no leaky expression. Since our primary fibroblasts did not grow as single cells upon seeding at very low densities, a variant method for single cell cloning had to be established. To this end, the genetically manipulated KRT20-fibroblasts were mixed with parental fibroblasts in a 1:500 ratio and seeded into petri-dishes. Once the dish was nearly confluent, the cells were selected in BSD. The parental cells, due to the lack of this selection marker, died seven days after selection. Individual clones of the genetically manipulated KRT20-fibroblasts, that were able to use the parental cells for contact-dependent growth during the seeding stage, survived and proliferated as clonal colonies in the presence of BSD. They were isolated using specialized single cell cloning cylinders, were expanded and then induced with doxycycline, RSL1 and IPTG. qPCR was used to test for inducible expression of the target genes since it was the fastest available method for the detection of several clones at once.

Several hurdles were faced during and after the single cell cloning process. The isolated single cell clones harbouring the most important doxycycline-inducible TA vector appeared stressed and did not actively proliferate making it challenging to work with these clones. Nevertheless 30 clones with the doxycycline-inducible *sT* construct survived the procedure and they were tested for their inducible expression. Almost every clone analyzed demonstrated excellent inducibility of *sT* without any leaky expression indicating that the doxycycline system worked very well in the primary fibroblasts. The qPCR data for two representative clones (clones 1 and 4) showing over 1000-fold induction of *sT* upon doxycycline induction is depicted (Fig. 18a). With respect to the RheoSwitch and IPTG systems, very low inducible expression of *ATOH1* and *DNMAML1/GLI1* respectively was observed for all clones tested. The maximum inducible expression observed was around 8 and 5-fold for *ATOH1* and *DNMAML1* as seen for clone 1 (Fig. 18b and c). Since WaGa cells endogenously express the T antigens and *ATOH1*, expression levels of these two genes in the two representative clones following induction were also compared to that of WaGa cells. While the expression of induced *sT* in the tested clones reached about one-fourth the expression levels of *sT* seen in WaGa cells, almost no induced *ATOH1* expression could be detected in the clones relative to WaGa *ATOH1* expression levels (Fig. 18d). This further reinforced the low levels of inducible expression for *ATOH1* obtained from the RheoSwitch system in the fibroblasts. A further concern was the observation that these KRT20-fibroblast single cell clones contained a small subpopulation displaying increased green fluorescence manifesting as “shoulders” in the mNeonGreen plot and in some cases also as a distinct population in flow cytometric analysis (Fig. 18e). Since the KRT20 donor construct was designed such that mNeonGreen fluorescence was under the control of the endogenous KRT20 promoter, we checked whether the

KRT20 promoter was activated in these cells due to an unforeseen event during the genetic manipulations. However, qPCR analysis showed that KRT20 was not expressed in these cells (Fig. 18f) indicating that the observed mNeonGreen fluorescence was not deriving from an active KRT20 promoter. Alternatively, fluorescence might arise from donor randomly integrated in the genome although in such a case it would be expected that all cells of a single cell clone would express mNeonGreen at a similar level. However, the more important conclusion of this phenomenon was that it challenged the use of the KRT20 fluorescence reporter system for the future detection of developing KRT20-positive MCC-like cells.

In conclusion, the lack of clones with the crucial TA vector, the low inducibility of the RheoSwitch and IPTG systems and the unaccountable mNeonGreen fluorescence observed in the KRT20-fibroblast single cell clones served as critical barriers for the continuation of the genetic manipulation procedure. Therefore, the series of genetic manipulations was subsequently attempted in alternative starter cells.

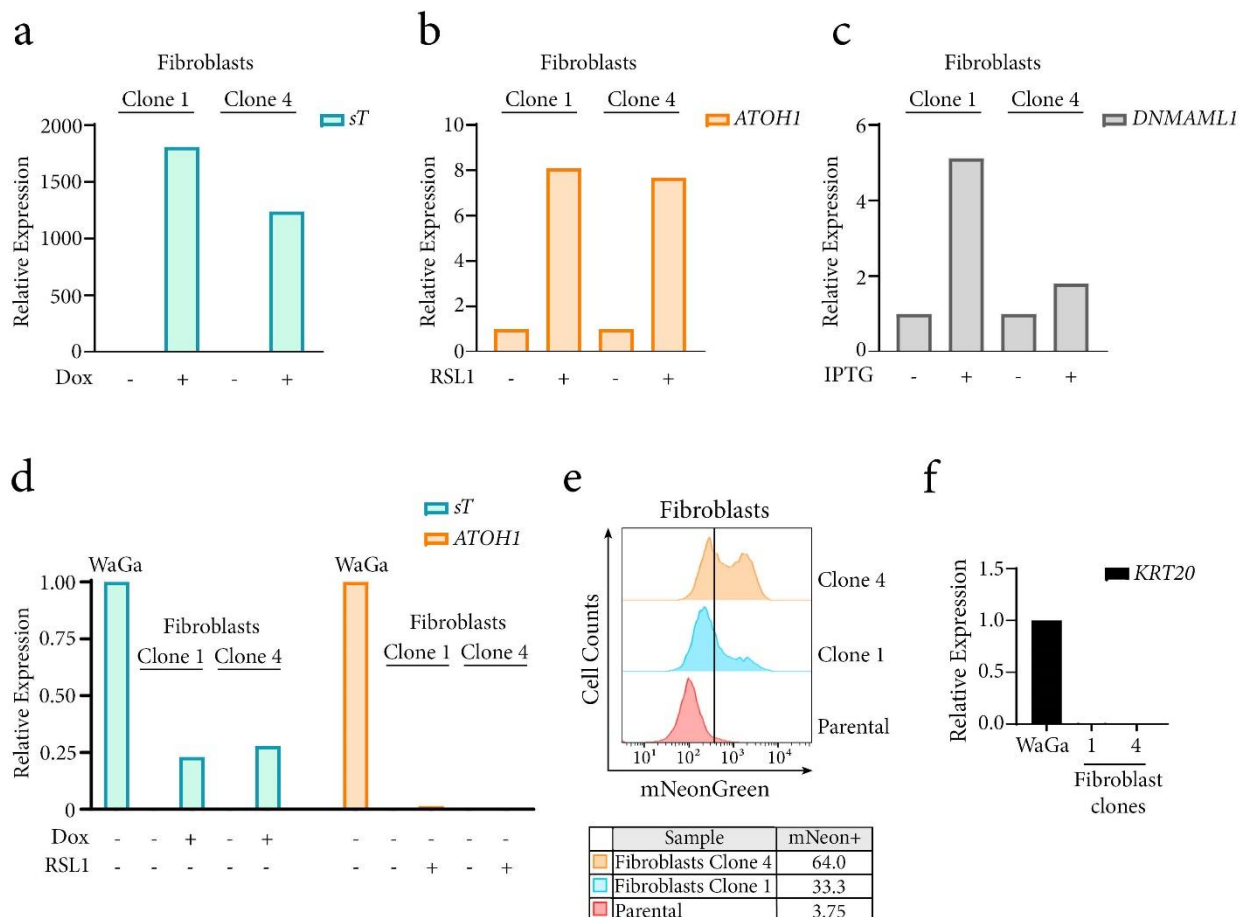


**Figure 18: Inducibility testing of representative single cell clones of genetically manipulated KRT20-fibroblasts.** Two representative clones (clones 1 and 4) of KRT20-fibroblasts with the inducible expression vectors for sT, ATOH1 and dnMAM1L were induced with 1  $\mu$ M doxycycline (Dox), 2  $\mu$ M RSL1 and 400  $\mu$ M IPTG for four days following which qPCR was performed. Relative expression of a)

sT b) *ATOH1* and c) *DNMAML1* are depicted for the two clones wherein expression of every gene is normalized to the respective uninduced state. d) Dox-induced sT and RSL1-induced *ATOH1* expression of the two clones was estimated in relation to that of WaGa cells. The relative expression of every gene was normalized to that of WaGa. The housekeeping gene, *RPLP0*, was used for the normalisation of target gene expression for every qPCR analysis. e) Clones 1 and 4 were analyzed for mNeonGreen fluorescence on the flow cytometer. Fibroblast parental cells were analyzed as a negative control. f) qPCR for *KRT20* expression was performed for clones 1 and 4 and WaGa cells were analyzed as a positive control. The relative expression of every gene was normalized to that of WaGa. The housekeeping gene, *RPLP0*, was used for the normalisation of target gene expression.

### **3.1.5 The use of HaCaT cells as an alternative starting point for the approach to study MCC oncogenesis**

Since in fibroblasts, independent inducible expression of the candidate drivers of MCC oncogenesis could not be achieved, the immortalized human keratinocytic cell line, HaCaT, was used as an alternative starting point for this approach. Being a cell line, HaCaT have the disadvantage of possessing several mutations [348, 349] which might interfere with the process of MCC-like differentiation. On the other hand, however, owing to its keratinocytic origin HaCaT cells are close to the previously supported epithelial cell of origin of MCC [94] and therefore crucial differentiation steps might be directly observable without the need to dedifferentiate these cells. Hence, following introduction of the *KRT20* donor and the various inducible vectors potentially promoting MCC formation, we wished to directly analyze the MCC marker *KRT20* in these cells upon induction of expression from the lentiviral vectors (See Fig. 8 in section 2.2.3.4).

#### **3.1.5.1 Integration of the *KRT20* donor into HaCaT cells**

HaCaT cells were transfected with the *KRT20* donor construct as described for WaGa cells (section 3.1.2) and fibroblasts (section 3.1.4.1). Following one month of BSD selection, the cells were tested for correct integration of the donor by PCR (Fig. 19). Sequencing of the PCR product obtained at the correct height (2001 bp), confirmed integration of the donor at the right location. These HaCaT cells with correctly integrated *KRT20* donor are henceforth referred to as *KRT20*-HaCaT cells.

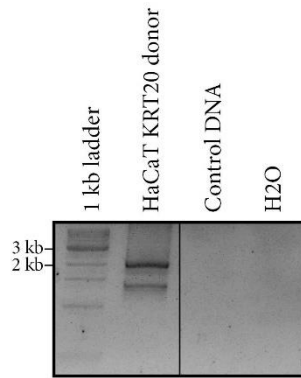


**Figure 19: Introduction of the KRT20 donor construct in HaCaT cells.** HaCaT cells were transfected with the KRT20 donor and with plasmids encoding Cas9 and a guide targeting the last coding exon of KRT20. Following one month of BSD (5  $\mu\text{g}/\text{ml}$ ) selection, DNA was isolated from the survivor cells. Nested PCR was performed to check for correct integration of the donor in the genome of these cells. The expected size of the PCR product was 2001 bp.

### 3.1.5.2 Lentiviral transduction of HaCaT cells with the various inducible expression vectors

Since HaCaT cells proliferate rapidly, the series of lentiviral transductions with the various expression vectors was performed at first. Testing of the inducibility of the vectors was performed subsequently after successfully completing the transductions. In this case, the KRT20-HaCaT cells were first infected either with the TA or sT vectors, followed by the two vectors for ATOH1 expression and at last with either the dnMAML1 or the GLI1 expression vectors. As described for the fibroblasts, each transduction was followed by selection with the respective antibiotics and the survivor cells were used for the subsequent transductions. As a result of the transductions, four unique cell populations of genetically manipulated KRT20-HaCaT cells were generated each of which were subsequently induced with doxycycline, RSL1 and IPTG. As confirmed by immunoblot, doxycycline-induced T antigen expression was observed in all four cell populations with sT expression ranging from 17 to 44-fold and LT expression ranging from 30 to 35-fold as compared to the respective uninduced states (Fig. 20a). Similarly, RSL1-induced ATOH1 expression was confirmed by immunoblot in all four cell populations wherein a 10 to 30-fold increase in ATOH1 expression from the respective uninduced states was observed (Fig. 20b). The induction of *DNMAML1* (Fig. 20c) and *GLI1* (Fig. 20d) as determined by qPCR was quite poor (approximately 2-fold induction of *DNMAML1* and less than 2-fold for *GLI1* as compared to the respective uninduced states). Furthermore, the expression of *DNMAML1* was also very leaky with an 8 to 15-fold background induction in the uninduced state as compared to the parental cells (Fig. 20c). Therefore, as performed for the fibroblasts, single cell cloning was subsequently performed also for the HaCaT cells in order to identify optimal clones.

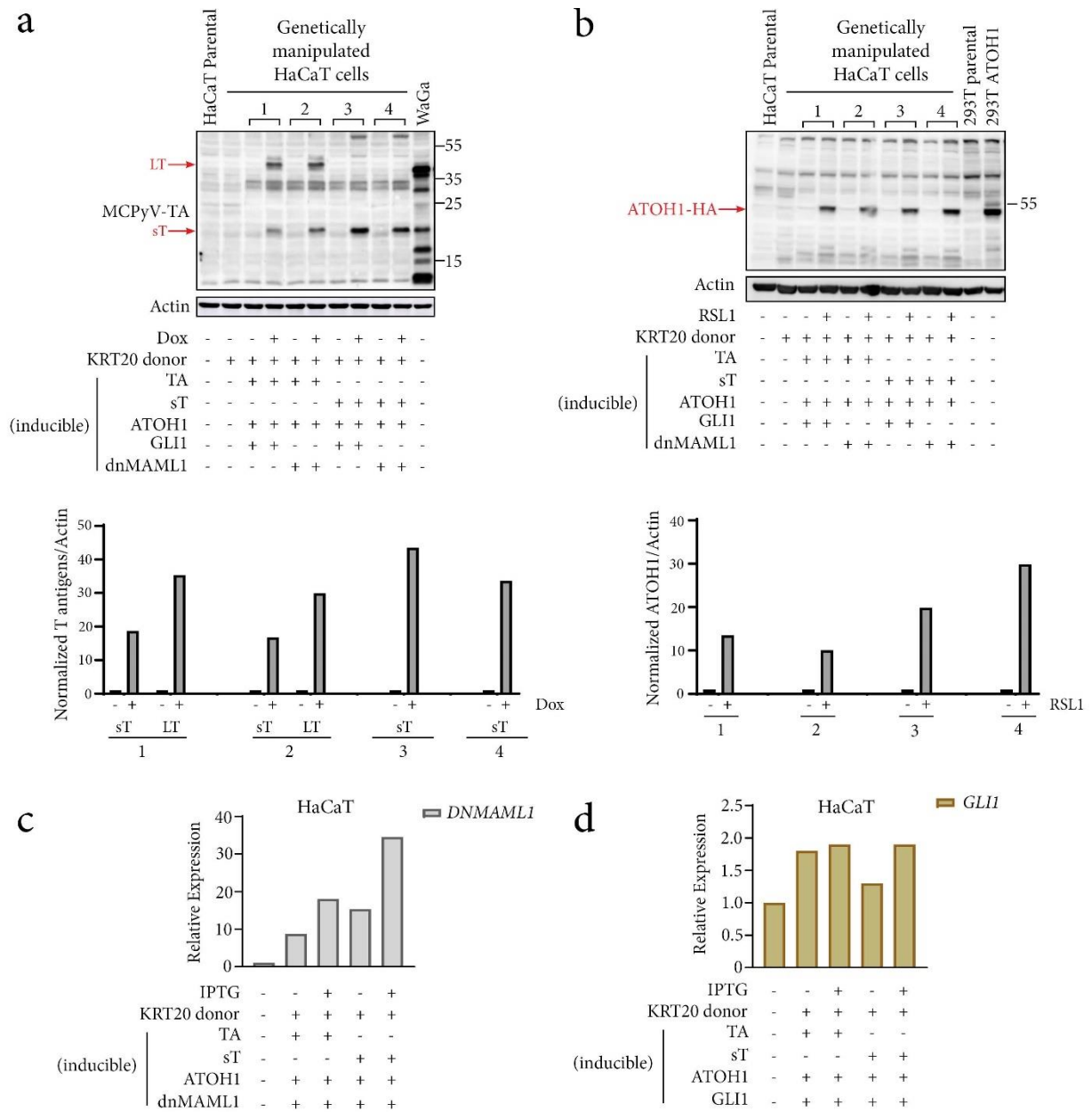


**Figure 20: Inducibility testing of the various vectors in genetically manipulated KRT20-HaCaT cells.** KRT20-HaCaT cells were sequentially transduced with the doxycycline (Dox)-inducible TA or sT vectors, the two RheoSwitch-inducible ATOH1 expression vectors and finally with either the IPTG-inducible dnMAML1 or GLI1 expression vectors. The cells were selected with hygromycin (100  $\mu\text{g/ml}$ ) (after the TA/sT transduction), zeocin (400  $\mu\text{g/ml}$ ) and neomycin (400  $\mu\text{g/ml}$ ) (after the ATOH1 transductions) and with puromycin (5  $\mu\text{g/ml}$ ) (after the dnMAML1/GLI1 transductions). The survivor cells were used for every subsequent transduction. The successfully transduced cells were induced with 1  $\mu\text{M}$  Dox, 2  $\mu\text{M}$  RSL1 and 400  $\mu\text{M}$  IPTG for four days and inducible expression was tested for a) the T antigens (immunoblot) b) HA-tagged ATOH1 (immunoblot) c) *DNMAML1* (qPCR) and d) *GLI1* (qPCR). For the immunoblots performed, parental HaCaT cells were used as a negative control, WaGa cells were used as a positive control for the T antigens and 293T cells transfected with a constitutively expressed HA-tagged ATOH1 vector were used as a positive control for ATOH1. Actin was used as a loading control. The bar graphs below each immunoblot depict quantification for the immunoblot signals for the T antigens (sT and LT) and ATOH1 normalized to actin and represented relative to the respective

uninduced states. For the qPCRs performed, parental HaCaT cells, represented in the first columns of the graphs, were used as negative controls. Relative expression of *DNMAML1* and *GLI1* is depicted as normalized to that of parental cells. *RPLP0* was used as the housekeeping gene for normalisation of target gene expression.

### **3.1.5.3 Expression of *MCPyV-TA*, *ATOH1* and *DNMAML1* in HaCaT cells does not induce expression of the MCC marker KRT20**

Similar to the observation made for fibroblasts, inducible expression deriving the IPTG system, was not only low but also leaky as observed in the polyclonal populations of genetically manipulated HaCaT cells. Therefore, it was necessary to perform single cell cloning for the HaCaT cells. Since HaCaT cells are capable of regeneration from a single cell, single cell cloning was performed by seeding the cells at very low densities in 96 well plates. The plates were screened for individual clones which were then expanded and characterized using qPCR. Since we most often observed very good inducible expression from the doxycycline-inducible system, we first searched for clones which were able to show inducible expression from the other two systems. In the 58 clones isolated, the induction of RheoSwitch-inducible *ATOH1* was not very high in the majority of clones. Nevertheless, a few clones showed higher induction levels as compared to that seen for the fibroblasts. One shortlisted clone (clone 3), showed 15-fold induction of *ATOH1* from the uninduced state (Fig. 21b). Notably however, a higher basal *ATOH1* expression in the uninduced state compared to parental HaCaTs was also detected for most clones. Induction of *GLI1* and *DNMAML1* by the IPTG system was very low and exhibited leaky expression. However, the selected clone 3 showed around 27-fold induction of *DNMAML1* from the uninduced state which was higher than that observed for any of the other tested HaCaT and fibroblast clones (Fig. 21c). As expected, very high levels of doxycycline-inducible expression of *TA* and *sT* with no leaky expression were observed for most of the isolated HaCaT single cell clones. Clone 3 demonstrated over 1000-fold induction of *TA* (Fig. 21a). Upon comparison of expression levels of *TA* and *ATOH1* observed for clone 3 with endogenous expression in WaGa, this clone was found to express *TA* at a level of about one-fourth that of WaGa cells and *ATOH1* at a level of about one-third that of WaGa cells (Fig. 21d). Overall, since this clone showed good *TA* and *ATOH1* inducible expression and the highest ever observed inducible expression of *DNMAML1* from the IPTG system, we proceeded with this clone for the further analysis. Previous studies in keratinocytes have demonstrated the induction of KRT20 two weeks after ectopic overexpression of the T antigens in combination with GLI1 [84]. Although we could not generate clones with good inducible expression of GLI1 with no leakiness, we tested whether *ATOH1* and *dnMAML* in combination with the T antigens might have a similar influence on our selected HaCaT single cell clone. We induced this clone with all inducers and then analyzed whether it might result in induction of the MCC marker KRT20 over a period of time. This was analyzed by

monitoring mNeonGreen fluorescence as an indicator for KRT20 induction. These HaCaT cells were constantly monitored after induction at several time points for up to 20 days post-induction. However, no induction of KRT20 was observed as seen by the absence of mNeonGreen fluorescence induction for any of the time points tested (Fig. 21e).

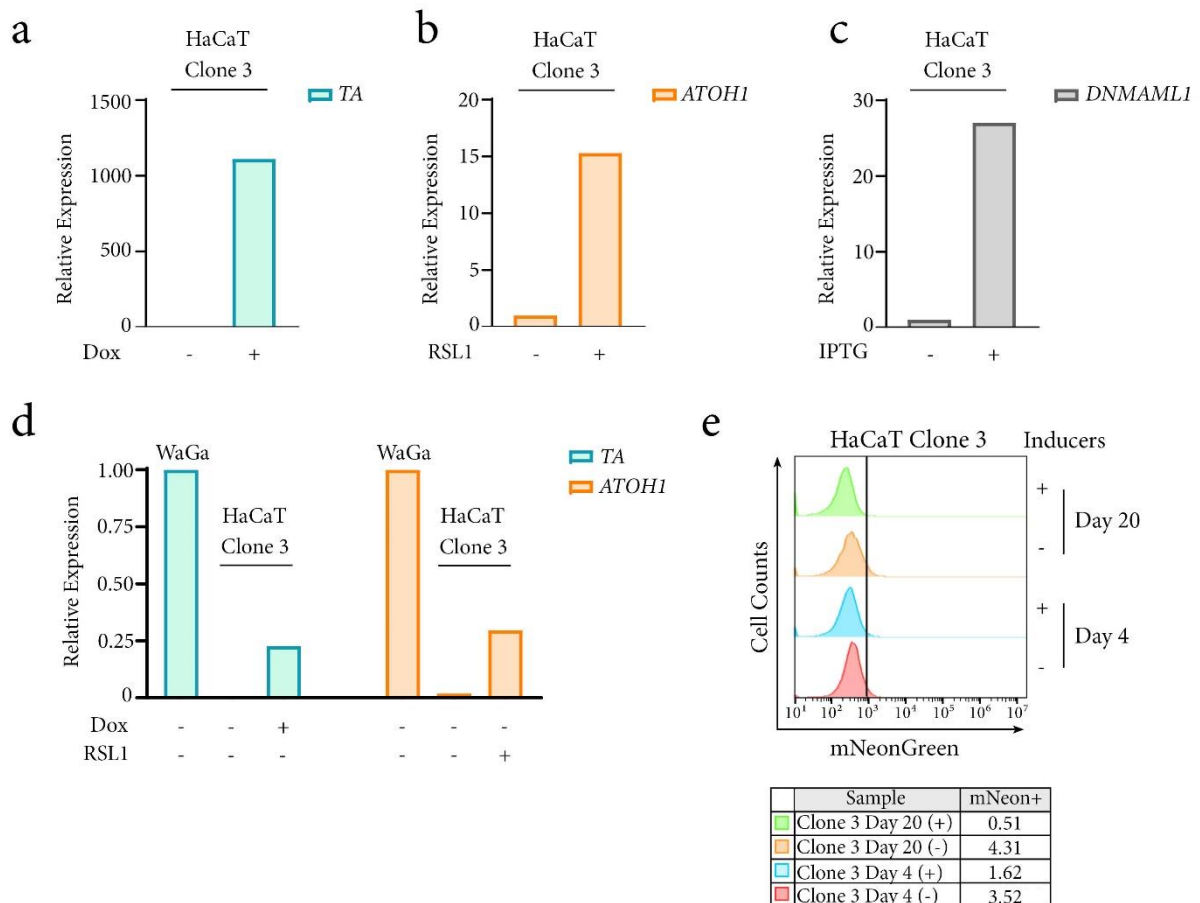


**Figure 21: Testing of the genetically manipulated KRT20-HaCaT single cell clone 3 as a precursor for MCC-like cell formation.** A representative clone (clone 3) of KRT20-HaCaTs with the inducible expression vectors for TA, ATOH1 and dnMAML1 were induced with 1  $\mu$ M doxycycline (Dox), 2  $\mu$ M RSL1 and 400  $\mu$ M IPTG for four days following which qPCR was performed. Relative expression of a) TA b) ATOH1 and c) DNAMML1 are depicted for the clone wherein expression of every gene is normalized to the respective uninduced state. d) Dox-induced TA and RSL1-induced ATOH1 expression of clone 3 was estimated in relation to that of WaGa cells. The relative expression of every gene was normalized to that of WaGa. The housekeeping gene, *RPLP0*, was used for the normalisation of target gene expression for every qPCR analysis. e) After treatment with or without all three inducers, Clone 3 was analyzed for mNeonGreen fluorescence at several time points for up to 20 days on the flow cytometer. Data from day four and day 20 of induction are depicted in the figure.

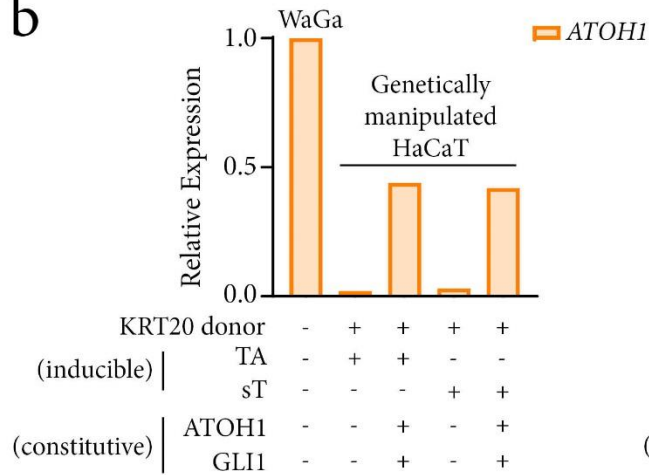
The results from the single cell cloning procedure showed that only one HaCaT clone with detectable expression of both ATOH1 and DNAMML1 could be identified.

Moreover, the IPTG system was found to be associated with leakiness and very low inducibility. In addition, no suitable clones expressing good levels of inducible GLI1 could be identified, a transcription factor that from recent work appears to be quite an important prerequisite in progenitor cells for MCC development [84]. The doxycycline system, on the other hand, consistently yielded excellent expression of the T antigens. Therefore, we decided to pursue one further attempt using the polyclonal population of KRT20-HaCaT cells harbouring only the doxycycline-inducible TA or sT vectors (described in 1.5.2). We transduced these two populations with a vector which would constitutively express ATOH1 and GLI1 (Fig. 22a) thereby circumventing the problems faced earlier regarding very low levels of inducible expression. *ATOH1* and *GLI1* overexpression in the two transduced cell lines was determined using qPCR (Fig. 22b and c). *ATOH1* overexpression in these cells was now found to be almost half of the expression observed in WaGa cells. *GLI1* overexpression was found to be over 1000-fold for the KRT20-HaCaT inducible TA-cells and 400 fold for KRT20-HaCaT inducible sT-cells as compared to the expression in the cells prior to transduction. The cells were induced with doxycycline to enable T antigen expression. As analyzed previously, these cells were then monitored regularly for a period of 20 days for the induction of KRT20 by means of mNeonGreen fluorescence. In these cells too, no major increase of mNeonGreen fluorescence was observed indicating the absence of induction of KRT20 over the time course studied (Fig. 22d and e). In addition, this batch of transduced cells also appeared stressed and exhibited increased cell death. It is possible that the increased overexpression of these tumor-promoting proteins induced apoptosis in our cells [350, 351]. Therefore, the small shoulder of mNeongreen fluorescence seen for the ATOH1 and GLI1 overexpressing KRT20-HaCaT inducible sT-cells at day 20 most likely arises due to autofluorescence from dying cells (Fig. 22e).

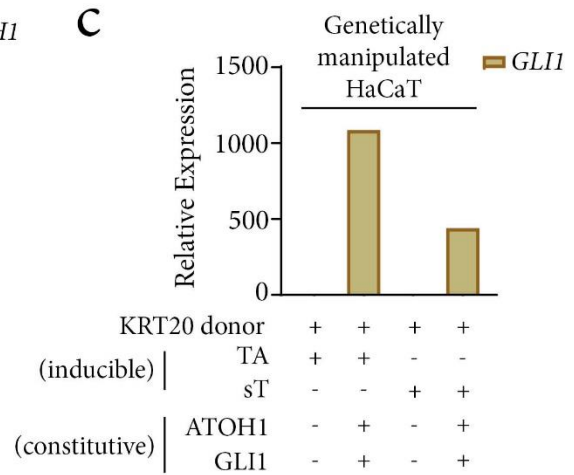
**a** GLI1 and ATOH1 constitutive expression construct:



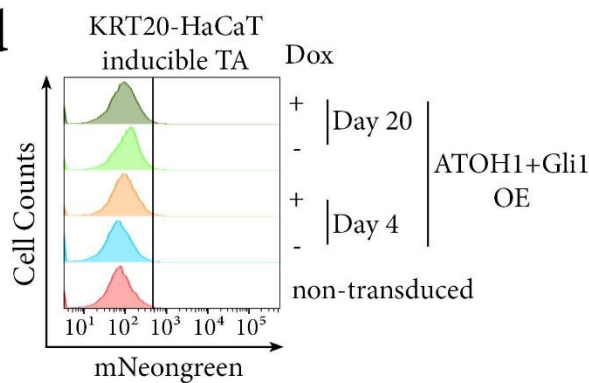
**b**



**c**

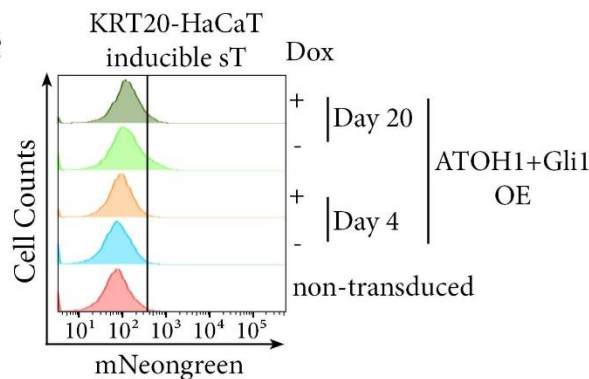


**d**



Sample	mNeon+
KRT20 HaCaT induc. TA (OE) Day 20 (+)	1.04
KRT20 HaCaT induc. TA (OE) Day 20 (-)	1.00
KRT20 HaCaT induc. TA (OE) Day 4 (+)	1.02
KRT20 HaCaT induc. TA (OE) Day 4 (-)	0.37
KRT20 HaCaT induc. TA non-transduced	0.58

**e**



Sample	mNeon+
KRT20 HaCaT induc. sT (OE) Day 20 (+)	5.09
KRT20 HaCaT induc. sT (OE) Day 20 (-)	9.43
KRT20 HaCaT induc. sT (OE) Day 4 (+)	1.06
KRT20 HaCaT induc. sT (OE) Day 4 (-)	1.01
KRT20 HaCaT induc. sT non-transduced	1.18

**Figure 22: Testing of the genetically manipulated KRT20-HaCaT cells expressing inducible T antigens and overexpressing ATOH1 and GLI1 as precursors for MCC-like cell formation.** A) The vector for overexpression of ATOH1 and GLI1 is depicted. The CMV promoter controlled the expression of Flag-tagged GLI1 and Flag-HA-tagged ATOH1. An intra-ribosomal entry site (IRES) sequence was

placed in between the coding sequences of the two genes to enable their expression as separate proteins. The EF-1 $\alpha$  promoter constitutively expressed the antibiotic selection marker puromycin. Additional elements present were the 5' LTR which represented the truncated 5' long terminal repeat (LTR) from human T-cell leukemia virus (HTLV) type 1. b and c) The polyclonal population of KRT20-HaCaTs harbouring the inducible expression vectors for TA and sT were transduced with the vector constitutively expressing ATOH1 and GLI1 and selected in puromycin. qPCR was performed using mRNA from the cells before and after successful transduction. Expression was normalized to that of b) WaGa cells for *ATOH1* expression c) the cells prior to the transduction for *GLI1* expression. The housekeeping gene, *RPLP0*, was used for the normalisation of target gene expression. d and e) KRT20-HaCaTs with the inducible expression vectors for d) TA and e) sT which overexpressed ATOH1 and GLI1 were induced with and without 1  $\mu$ M doxycycline (Dox) over a period of 20 days. The cells were analyzed for mNeonGreen fluorescence at several time points post-induction. Non-transduced cells were included as negative controls. Data from day four and day 20 of induction are depicted in the figure (OE - Overexpression).

In conclusion, co-expression of the T antigens, ATOH1 and either dnMAML1 or GLI1 in in HaCaT cells did not result in the induction of KRT20 over the analyzed time course in our experimental set-up.

## **3.2 Analysis of the use of artesunate as a potential drug for MCC treatment**

### **3.2.1 Artesunate exerts strong cytotoxic effects towards MCPyV-positive MCC cell lines *in vitro***

Since the majority of MCC cases are associated with the Merkel cell polyomavirus [31, 352], it was interesting to test the response of MCCs to the anti-malarial drug artesunate, which is additionally known to possess anti-viral [172, 174] and anti-cancer [184, 185, 353, 354] properties. Three MCPyV-positive (MKL-1, WaGa and PeTa) and three non-classical MCPyV-negative (MCC13, MCC26 and UIISO) MCC cell lines were treated with artesunate in an initial experiment and their viability was analyzed using cell cycle analysis. Cell death was estimated by measuring an increase in the sub-G1 fraction represented by cells with DNA content less than 2N. Upon four days of artesunate treatment, all three MCPyV-positive MCC cell lines and two MCPyV-negative MCC cell lines, MCC26 and UIISO, showed an increase in the sub-G1 fraction indicative of cytotoxicity towards the drug (Fig. 23a and 23b). After seven days of treatment, the MCPyV-positive MCC cell lines demonstrated a larger percentage of dead cells as compared to the MCPyV-negative MCC cell lines (Fig. 23b). Furthermore, the cell cycle profiles for the MCPyV-positive MCC cells, especially for WaGa and PeTa, were almost completely distorted by this time point in comparison to that of MCC26 and UIISO (Fig. 23a). The MCPyV-negative MCC cell line MCC13 appeared to be fairly resistant to artesunate and showed only a very minor increase in the sub-G1 fraction following treatment (Fig. 23a and 23b). The results indicated that artesunate was cytotoxic towards most MCC cell lines *in vitro* and exerted a stronger cytotoxic effect on MCPyV-positive MCC cell lines over time as compared to MCPyV-negative MCC cell lines.

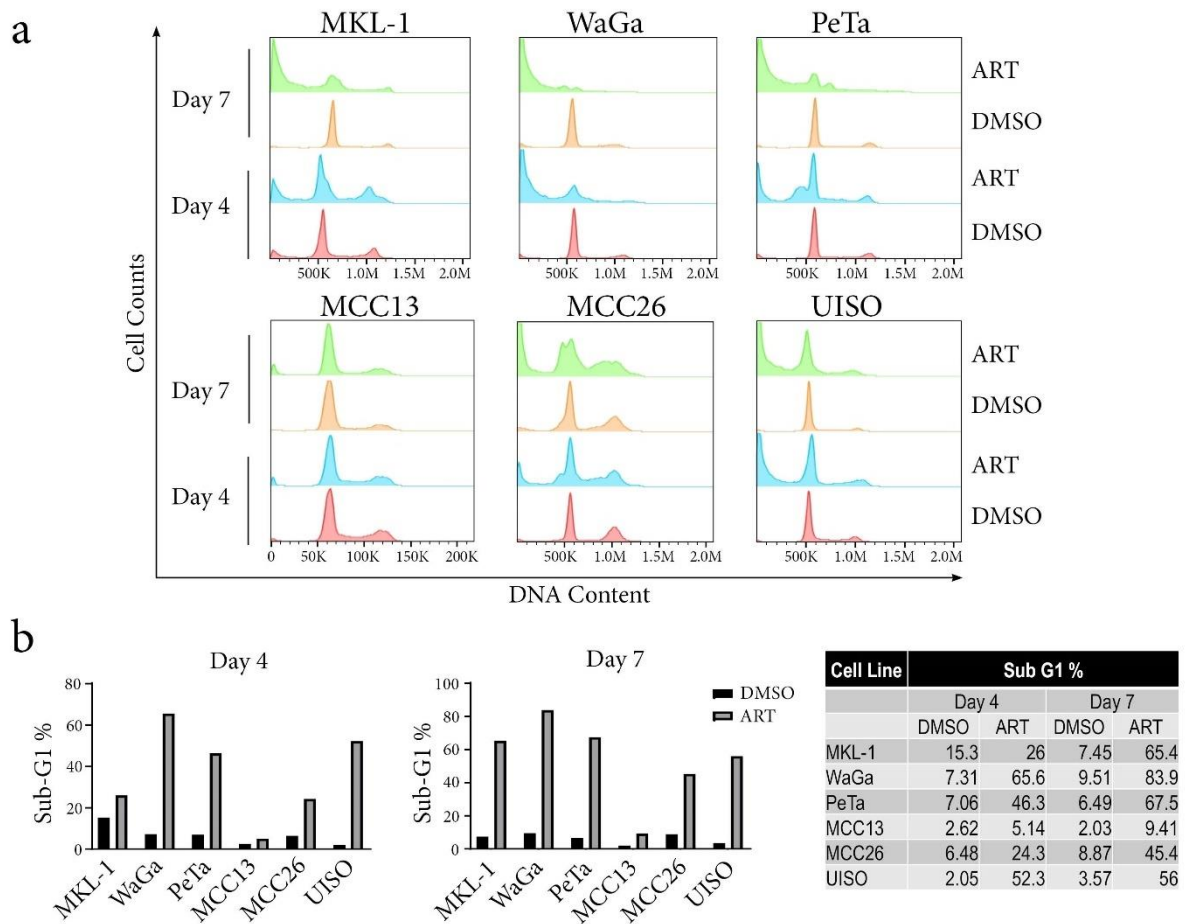


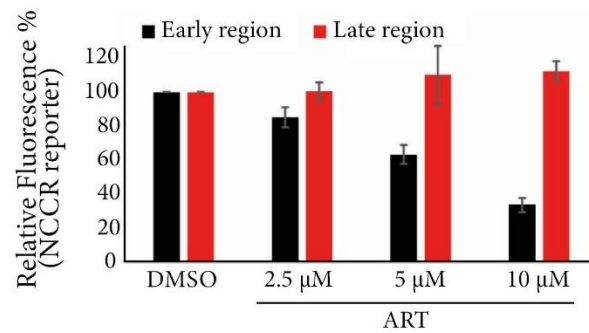
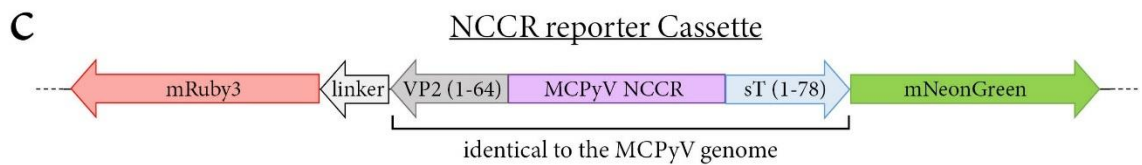
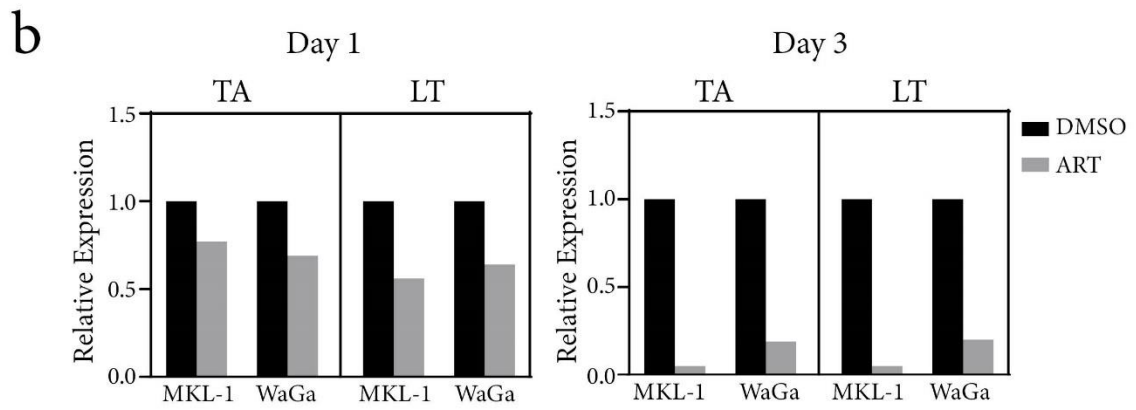
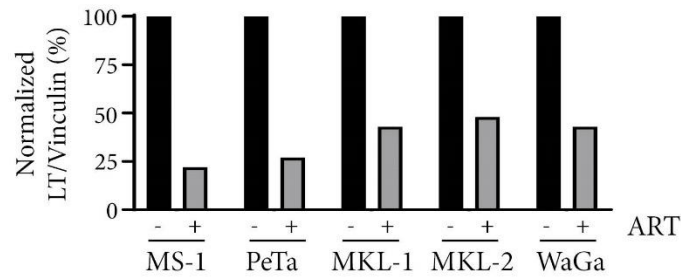
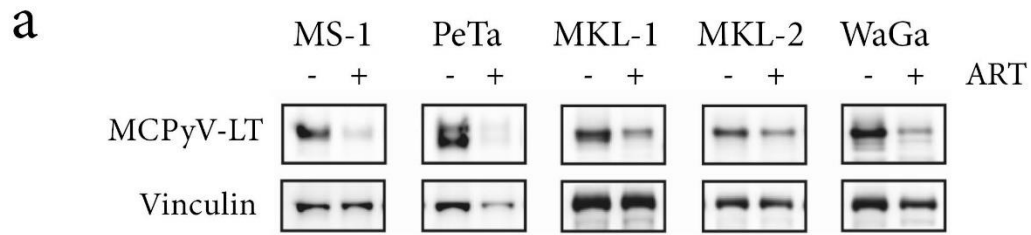
**Figure 23: Artesunate is strongly cytotoxic towards MCPyV-positive MCC cell lines *in vitro*.** a) The indicated MCC cell lines were treated either with 10  $\mu$ M artesunate (ART) or with DMSO as a control. Upon four and seven days of treatment, the cells were fixed, stained with propidium iodide and cell cycle profiles were analyzed by flow cytometry. b) The graphs depict the percentage of cells in the sub-G1 fraction for each cell line treated either with 10  $\mu$ M ART or DMSO for four and seven days. The corresponding values are provided in the adjoining table.

### **3.2.2 Artesunate downregulates LT expression in MCPyV-positive MCC cell lines**

The cytotoxicity studies suggested a slightly increased sensitivity of MCPyV-positive MCC cell lines towards artesunate. These MCPyV-positive MCC cells depend on the expression of viral proteins (i.e., small T (sT) and large T (LT) antigen) [51, 53, 70] and since artesunate had been shown to repress gene expression of other viruses [179, 355], the influence of artesunate on T antigen expression was examined next. To this end, five MCPyV-positive MCC cell lines (MKL-1, MKL-2, WaGa, PeTa and MS-1) were treated with artesunate and immunoblot for LT was performed. All cell lines showed reduced LT protein levels compared to the loading control vinculin upon treatment (Fig. 24a) indicating that the cytotoxic effects of artesunate are associated with reduced LT expression.

Next, we analyzed whether the observed LT repression by artesunate might occur at the transcriptional level. For this purpose, two MCPyV-positive MCC cell lines (MKL-1 and WaGa), were treated with artesunate and qPCR for total T antigen (TA) and LT transcripts was performed. Indeed, both cell lines demonstrated a decline in TA and LT transcripts already one day post-treatment (Fig. 24b). Subsequent analysis after three days of treatment showed that artesunate strongly repressed these transcripts by approximately 20-fold in MKL-1 and 5-fold in WaGa.

To confirm these results suggesting transcriptional repression of the T antigen mRNA by artesunate, we next used a reporter construct containing the MCPyV non-coding control region (NCCR), a bidirectional promoter known to independently regulate polyomavirus early and late gene expression [40, 356, 357]. In frame with sT (early region), we placed the coding sequence of mNeogreen and in frame with VP2 (late region), that of mRuby (Fig. 24c). The cells were treated with several increasing concentrations of artesunate and fluorescence was then analyzed by flow cytometry. A dose-dependent loss of green but not red fluorescence was noticed (Fig. 24c). This indicated that artesunate might downregulate T antigen transcription by specifically regulating the NCCR driven early-gene expression.



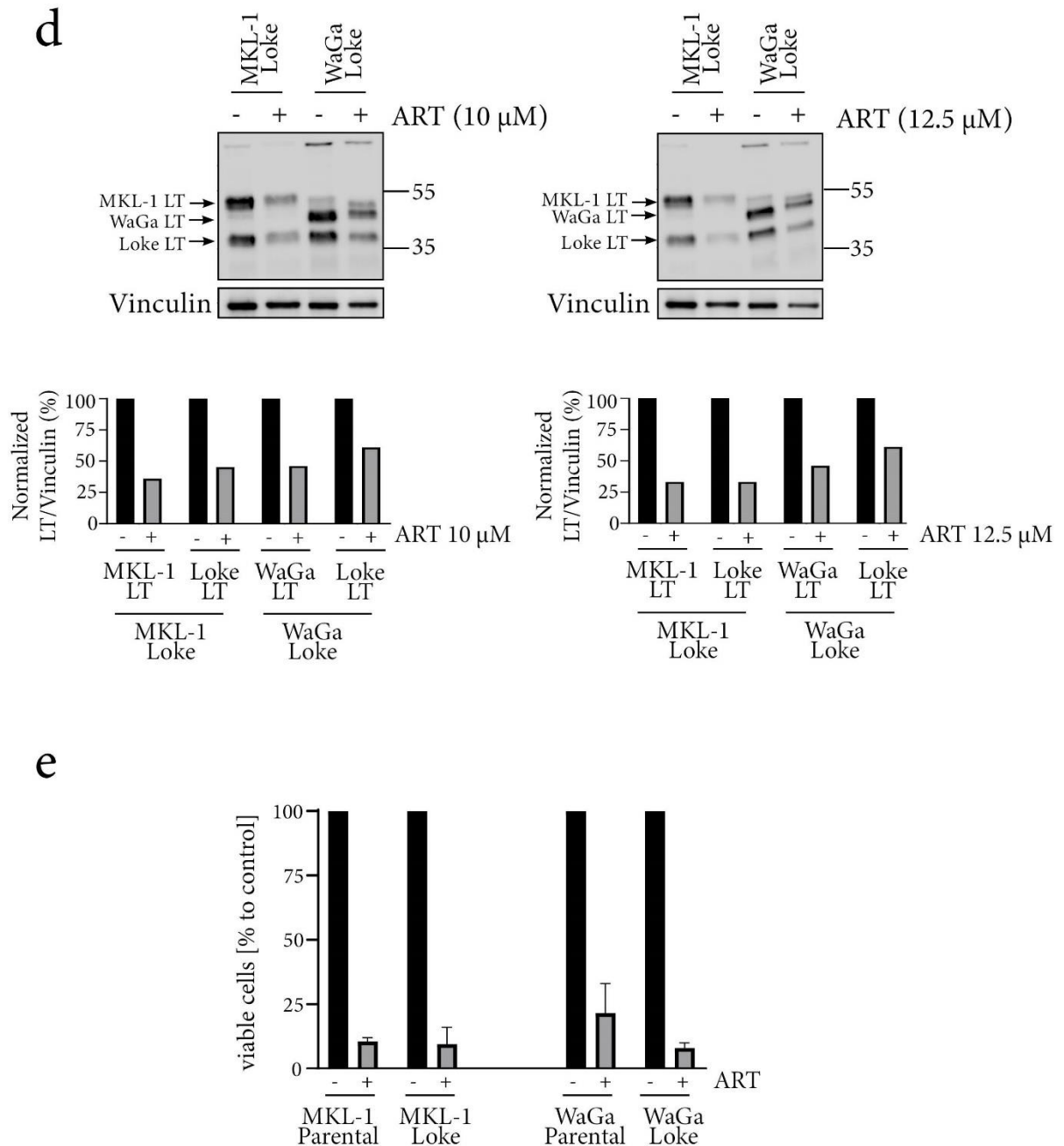


**Figure 24: Artesunate downregulates LT expression in MCPyV-positive MCC cell lines.** a) Five MCPyV-positive MCC cell lines were treated with 10 μM (MKL-1, MKL-2, WaGa) or 12 μM (MS-1, PeTa) artesunate (ART) and DMSO as a control. After three days, protein lysates were subjected to immunoblotting for MCPyV-LT and vinculin as a loading control. The bar graphs depict quantification for the immunoblot signals for LT normalized to vinculin and represented relative to the respective DMSO control treatments. b) MKL-1 and WaGa cells were treated with 10 μM ART or DMSO as a control. qPCR for total T antigen (TA) and LT was performed after one and three days. Bar graphs depict relative expression normalized to the respective DMSO controls. c) A schematic representation NCCR reporter cassette is depicted with the central bidirectional MCPyV NCCR. mNeonGreen and mRuby3 are in frame with partial sequences of sT and VP2 respectively. MKL-1 cell lines transduced with the NCCR reporter construct were treated for five days with ART (2.5 μM, 5 μM and 10 μM) or DMSO as a control and were then subjected to flow cytometric analysis. The bar graphs depict relative fluorescence normalized to DMSO controls. Mean fluorescence values ± SD are displayed. d) MKL-1

and WaGa cells overexpressing the Loke T antigen were treated with 10  $\mu$ M or 12.5  $\mu$ M ART and DMSO as a control. After three days, protein lysates were subjected to immunoblotting for MCPyV-LT and vinculin as a loading control. The bar graphs depict quantification for the immunoblot signals for LT normalized to vinculin and represented relative to the respective DMSO control treatments. e) The cells described in d) (those treated with 12.5  $\mu$ M ART and the respective DMSO-treated controls), were counted to assess cell viability using the trypan blue assay. The bar graphs depict the percentage of viable cells normalized to the respective DMSO controls. Mean values from two independent experiments are represented. Statistical analysis (t-test) was used to compare artesunate treatments between parental cell lines and the respective T antigen overexpression (Loke) cell lines. No significant differences were obtained. Figures a and c adapted from [358].

To further study the effect of artesunate on the NCCR, we hypothesized that given an LT regulation exclusively based on modifying its NCCR-controlled transcription, LT repression would not occur if T antigens were ectopically expressed controlled by another promoter. To test this hypothesis, two MCPyV-positive MCC cell lines, MKL-1 and WaGa, transduced with a construct expressing T antigens under the control of a CMV promoter were used [53]. Following treatment with two different concentrations of artesunate, LT protein levels were examined by immunoblotting. The ectopically expressed LT used in this case was that of the MCPyV-positive MCC cell line Loke, that harbours a larger C terminal LT truncation than MKL-1 and WaGa [359], enabling to differentiate between the endogenous and ectopically expressed LT by immunoblot. Interestingly, upon artesunate treatment, in addition to endogenous LT, ectopic LT was also repressed at the protein level (Fig. 24d) suggesting that either expression from the CMV promoter is also affected by artesunate or that artesunate also exerts a translational repression. Moreover, cell viability analysis performed in parallel with the immunoblot experiments also revealed no differences in cell survival between artesunate-treated parental cells and those overexpressing ectopic Loke T antigen (Fig. 24e).

In summary, while downregulation of also CMV-driven LT expression raises doubts about a specific effect of artesunate on NCCR-driven early region transcription, repression relative to different other proteins in immunoblot analysis, real time PCR and reporter gene assays suggest a selective repression of LT expression.

### **3.2.3 Repression of T antigen expression is not the sole mechanism of artesunate-induced cell death in MCPyV-positive MCCs**

The initial report on TA dependence of MCC cells reported that besides cell cycle arrest, apoptosis is also induced in MCPyV-positive MCC cells upon TA repression [70]. Therefore, the massive suppression of LT expression by artesunate in all MCPyV-positive MCC cell lines made it appear that this process might be crucial for artesunate's cytotoxic action. Consequently, to test the following, cell death induced by shRNA-mediated T antigen knockdown was compared with artesunate-induced cell

death in two MCPyV-positive MCC cell lines (MKL-1 and WaGa). To this end, cell lines transduced with a vector allowing knockdown of T antigens upon doxycycline addition were used [360]. After treatment with either doxycycline or artesunate, LT expression was determined by immunoblotting and cell viability was monitored over a time course using the trypan blue assay. The repression of LT expression achieved in both cases was comparable (Fig. 25a). On the contrary, the survival curves showed that while T antigen knockdown only resulted in a minor increase in cell death over time, artesunate was able to completely eliminate the cells over the time course studied (Fig. 25b). The results showed that there exist further mechanisms along with T antigen inhibition by which artesunate kills MCPyV-positive MCCs.

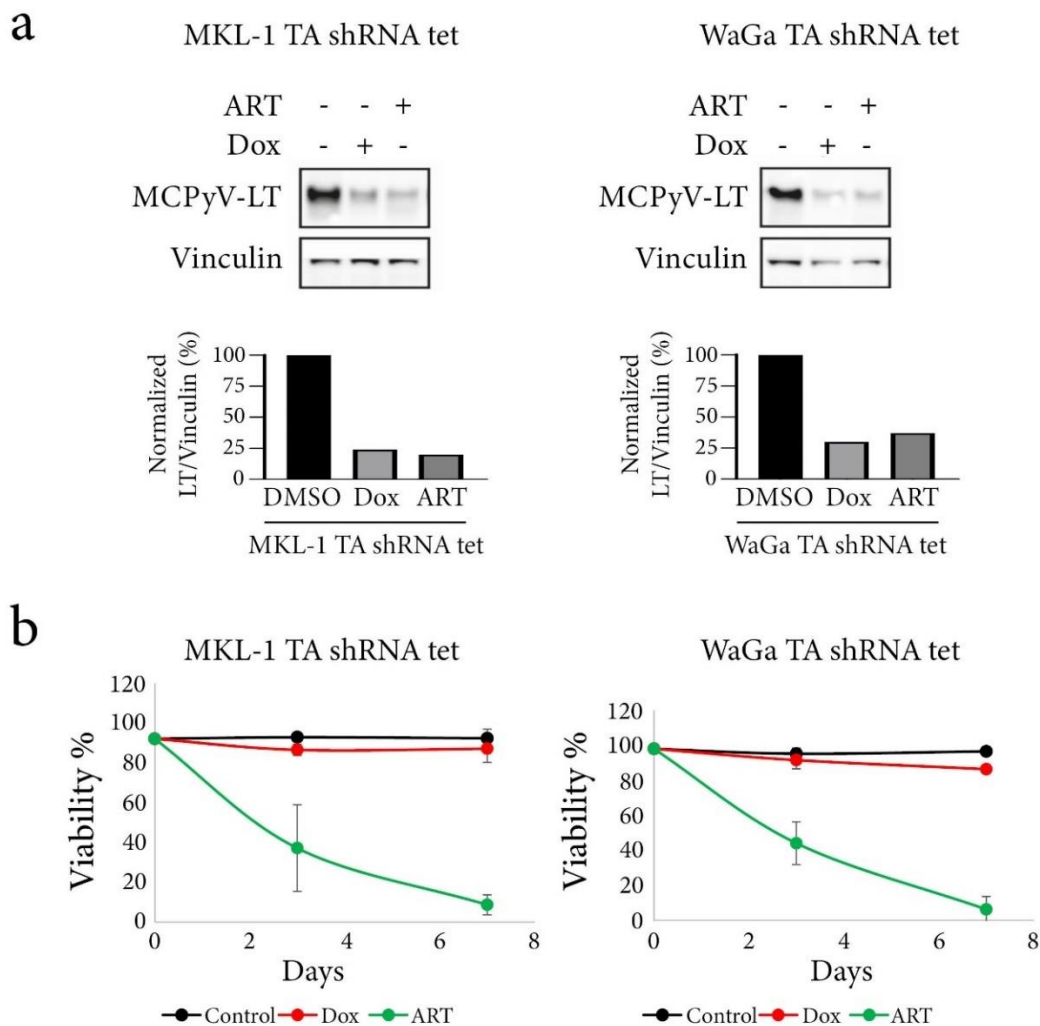


**Figure 25: Further mechanisms along with T antigen inhibition are involved in artesunate-induced cell death of MCPyV-positive MCCs.** MKL-1 and WaGa cells transduced with a vector enabling doxycycline (Dox) inducible TA shRNA expression were either treated with 1  $\mu$ M Dox or with 10  $\mu$ M artesunate (ART) for seven days. Cells treated with DMSO were used as a control. The bar graphs depict quantification for the immunoblot signals for LT normalized to vinculin and represented relative to the respective DMSO control treatments. a) After four days of treatment, immunoblots were performed for MCPyV-LT and vinculin was used as a loading control. b) Cell viability was assessed using the trypan blue assay over the time course of treatment and the percentage of viable cells were

plotted. The graphs depict mean values ( $\pm$  SD) derived from at least four independent experiments. Figures a and b adapted from [358].

### **3.2.4 WaGa cells are sensitized to artesunate by the expression of the T antigens**

Our initial experiments suggested a correlation of MCPyV-positivity and artesunate sensitivity (Fig. 23). Therefore, the next set of experiments was performed to elucidate whether the T antigens might sensitize MCC cells towards artesunate. Three MCPyV-positive MCC cell lines (MKL-1, MKL-2 and WaGa) transduced with a vector expressing a doxycycline-inducible TA shRNA and in addition a vector constitutively expressing an shRNA to RB1 [51] were used. The latter was essential to ensure their progression in the cell cycle following LT knockdown [51] and to thereby retain their sensitivity towards the anti-cancer drug, artesunate [205]. The cells were either treated with or without doxycycline for four days and LT knockdown was confirmed by immunoblot (Fig. 26a). Following treatment with a range of concentrations of artesunate, cell viability was measured using both the trypan blue exclusion assay and cell cycle analysis. Dose response curves were plotted to depict an increase in the percentage of trypan blue positive cells or sub-G1 fractions as measured from either assay. As analyzed by both viability assays, in the absence of the T antigens, the WaGa cells demonstrated reduced cell death following artesunate treatment (Fig. 26b). This implies that the presence of the T antigens rendered these cells sensitive to the drug. Such a protective effect of T antigen knockdown in response to artesunate was not observed for MKL-1 and MKL-2 (Fig. 26b).

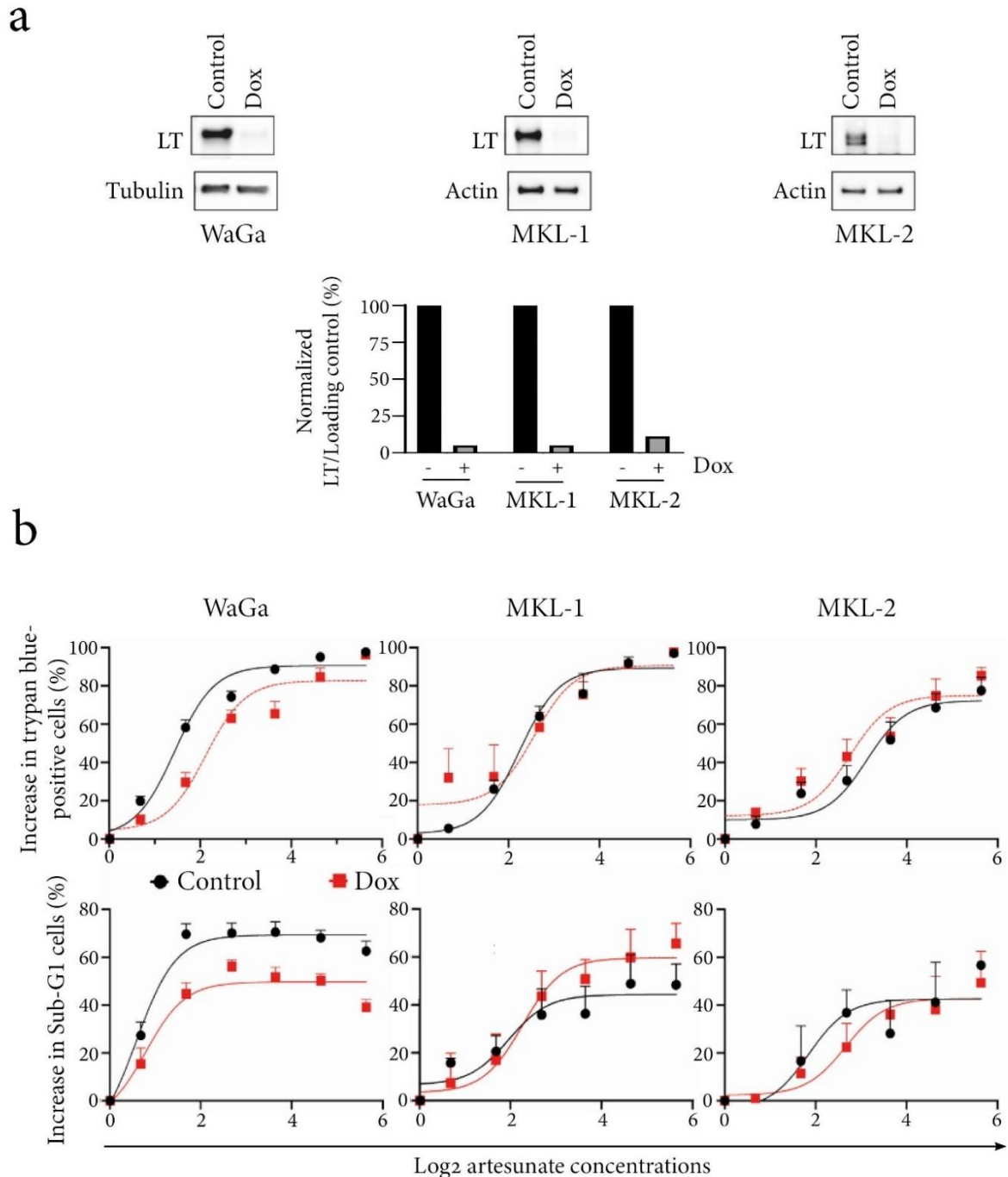


**Figure 26: T antigen expression sensitizes WaGa cells to artesunate.** The indicated MCPyV-positive MCC cell lines were transduced with a vector enabling doxycycline (Dox) inducible TA shRNA expression and a vector constitutively expressing an RB1 shRNA. a) After Dox (1  $\mu$ M) induction for five days, knockdown of T antigens was analyzed using immunoblot for MCPyV-LT. Tubulin and actin were used as loading controls. The bar graphs depict quantification for the immunoblot signals for LT normalized to the respective loading controls and represented relative to the respective control treatments without Dox. b) Following the knockdown, the cells were treated with a range of concentrations of artesunate (1.6  $\mu$ M, 3.125  $\mu$ M, 6.25  $\mu$ M, 12.5  $\mu$ M, 25  $\mu$ M and 50  $\mu$ M) and DMSO as a control. Cell viability was analyzed using the trypan blue assay and cell cycle analysis, four days after treatment. Comparison of the percentages of dead cells obtained without and with Dox induction was made using dose response curves (log<sub>2</sub> artesunate concentrations). The values obtained are derived

from three independent experiments and represent mean values (+ SE). Figures a and b adapted from [358].

### **3.2.5 Absence of typical apoptotic signatures in most artesunate-treated MCPyV-positive MCC cell lines**

Previous reports have shown that artesunate exerts its cytotoxic effects on various cancer entities by apoptosis induction [185, 188, 361-363]. Therefore, in the following experiments, the role of artesunate as a possible apoptosis inducer in MCPyV-positive MCC cell lines was investigated. Five MCPyV-positive MCC cell lines (MKL-1, MKL-2, WaGa, PeTa and MS-1) were treated with a range of concentrations of artesunate, and cell viability was compared between the trypan blue assay and cell cycle analysis. The principle behind the estimation of dead cells varies between the two assays. While the trypan blue assay determines a cell as dead due to its permeable cell membrane [364], the DNA intercalating agent, propidium iodide, used for cell cycle analysis provides information on the cellular DNA content, i.e. whether the genomic DNA within a cell is intact or degraded [365]. DNA degradation preceding membrane permeabilisation and cell death is a hallmark of apoptosis [366] while for some other modes of cell death loss of cellular DNA is observed later after execution of death [246]. Interestingly, a higher percentage of dead cells was detected by the trypan blue assay as compared to the percentage of cells with degraded DNA detected by DNA staining for four of the five cell lines tested (Fig. 27a). This observation was evident especially at the higher concentrations of artesunate treatment and implied that at least some of the cell death occurring was not apoptotic. MKL-2, however, was an exception with both curves (trypan blue and sub-G1) demonstrating equal kinetics (Fig. 27a).

To further the investigation into apoptotic cell death, the pan-caspase inhibitor benzyloxycarbonyl-Val-Ala-Asp (OMe) fluoromethylketone (Z-VAD-FMK) was used [367, 368]. The five MCPyV-positive MCC cell lines tested in the previous experiment were treated with artesunate alone or in combination with Z-VAD-FMK. The trypan blue assay was performed after two days of treatment. The data showed that Z-VAD-FMK was not able to rescue the cells from artesunate-induced cell death (Fig. 27b). Although MKL-2 displayed a tendency for increased survival in the presence of Z-VAD-FMK, no significant rescue could be documented.

In addition, the morphology of two artesunate-treated non-spheroidal MCPyV-positive MCC cell lines (WaGa and PeTa) was also studied using time lapse microscopy. Apoptosis is well-characterized by cell shrinkage, plasma membrane blebbing and formation of apoptotic bodies [245, 246] Quite contrary to these characteristics, cell swelling and subsequent rupture was observed upon artesunate treatment (Fig. 27c).

These results demonstrated that most MCPyV-positive MCC cell lines did not display any typical apoptotic features upon artesunate treatment indicating that there might exist an alternative mode of cell death induced by artesunate in these cell lines.

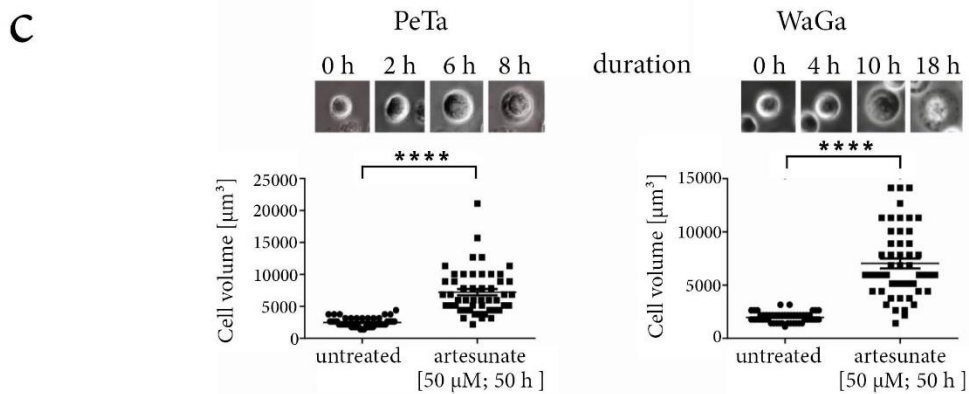
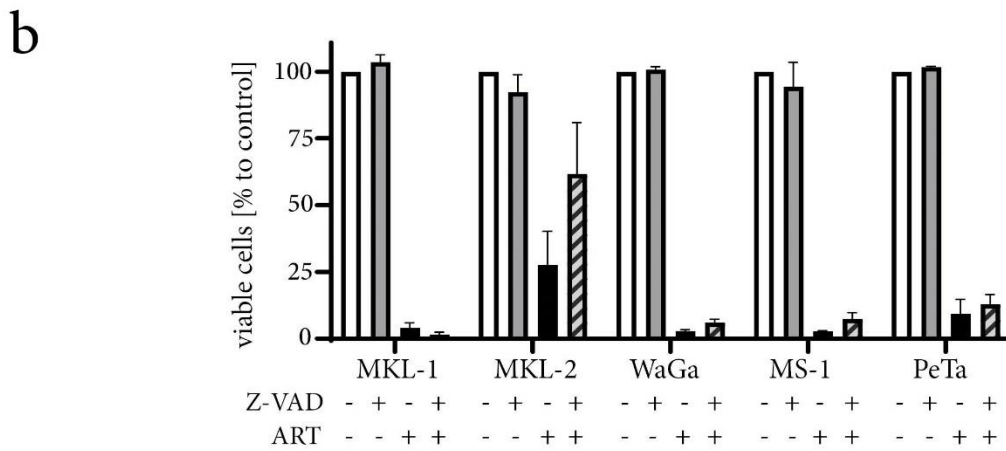
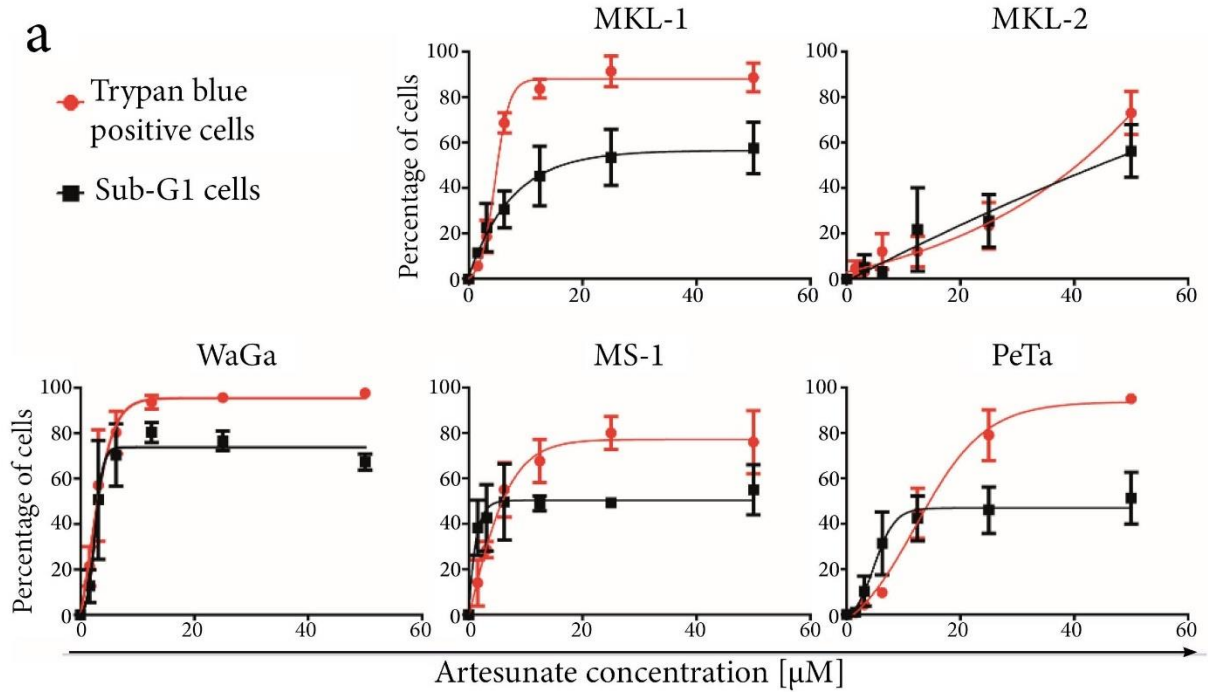


**Figure 27: Artesunate-induced cell death of MCPyV-positive MCCs is not associated with typical apoptotic signatures.** a) The indicated MCPyV-positive MCC cell lines were treated with a range of concentrations of artesunate (1.6  $\mu$ M, 3.125  $\mu$ M, 6.25  $\mu$ M, 12.5  $\mu$ M, 25  $\mu$ M and 50  $\mu$ M) and DMSO as a control. Following three days of treatment, cell viability was compared between the trypan blue assay and cell cycle analysis. The percentage of dead cells are plotted in the curves. b) The cell lines were treated with artesunate (ART) in the presence or absence of the pan-caspase inhibitor Z-VAD-FMK (20  $\mu$ M) and with DMSO as a control. After two days of treatment, the trypan blue assay was used to analyze cell viability. Bar graphs depicting the percentage of viable cells normalized to the respective DMSO controls are plotted. Mean values from at least three independent experiments are represented. Statistical analysis (ANOVA followed by Dunnett's multiple comparisons post hoc test) was used to compare each condition to that of the artesunate treatment for the individual cell lines and no significant differences were obtained. c) WaGa and PeTa cells were treated with 50  $\mu$ M artesunate and cellular morphology was monitored over 50 hours of treatment using time lapse microscopy. The graphs depict the cellular volume of 50 cells before and 50 cells after treatment. The Mann-Whitney test (\*\*\*\* $p < 0.0001$ ) was used to compare mean values. Figures a, b and c adapted from [358].

### **3.2.6 Artesunate induces a ferroptotic mode of cell death in MCPyV-positive MCC cell lines**

Besides apoptosis, artesunate has been described to induce ferroptosis, a non-apoptotic and iron-dependent form of cell death [227], in several types of cancer cells [186, 229, 369, 370]. Cells undergoing ferroptosis develop pores on their plasma membrane resulting in cell swelling, rupture and consequent death [232]. Since a similar morphological observation was made for artesunate-treated MCPyV-positive MCC cell lines, we speculated that these cells might be killed by ferroptosis.

Consequently, a panel of ferroptosis inhibitors targeting different parts of the ferroptotic pathway were used to test if they can dampen artesunate-induced cellular cytotoxicity. The iron chelator deferoxamine (DFO) and the lipid peroxide inhibitor and potent antioxidant ferrostatin-1 (Fer-1) were used owing to the characteristic iron accumulation and lipid peroxidation observed during ferroptosis [227, 371, 372]. Furthermore, lysosomes, which demonstrate iron accumulation [260], have also been shown to be involved in ferroptotic cell death [261]. In this regard, the inhibitor of the lysosomal vacuolar-type H<sup>+</sup>-ATPase BAF-A1 [265] was also included in this study. Artesunate treatment of five MCPyV-positive MCC cell lines (MKL-1, MKL-2, WaGa, PeTa and MS-1) was performed in the presence or absence of these ferroptosis inhibitors and cell viability was assessed using the trypan blue assay. Interestingly, combination of the ferroptosis inhibitors with artesunate had a strong protective effect on the MCPyV-positive MCC cell lines (Fig. 28a). The significant rescue from artesunate-induced cell death upon DFO addition suggested accumulation of iron in all cell lines. Moreover, increased survival of four of the five cell lines following artesunate cotreatment with BAF-A1 demonstrated the importance of functional lysosomes for artesunate-mediated cytotoxicity. All artesunate-treated cell lines were also protected upon using Fer-1 highlighting that artesunate was triggering increased

lipid peroxidation in the cells. Taken together, these inhibitor experiments argued in favor of a ferroptotic mode of cell death induced by artesunate in MCPyV-positive MCC cell lines.

Another important biomarker of ferroptosis is the enzyme Acyl-CoA synthetase long-chain family member 4 (ACSL4). It converts polyunsaturated fatty acids (PUFAs) to acyl CoA variants that serve as substrates for the production of pro-ferroptotic lipids [276-278]. To further support the obtained data which pointed towards artesunate-induced ferroptosis via lipid peroxidation, the effect of ACSL4 inhibition on artesunate's cytotoxic action was studied next. Three MCPyV-positive MCC cell lines (MKL-1, WaGa and PeTa) were treated with artesunate in the presence and absence of Rosiglitazone (Rosi), an ACSL4 inhibitor [373] and the trypan blue assay for cell viability was performed. ACSL4 inhibition was able to rescue artesunate-induced cell death in all three cell lines (Fig. 28b). Downstream of ACSL4 are the LOX enzymes which aid in the generation of lipid hydroperoxides [270, 276]. Hence, the anti-ferroptotic agent, vitamin E ( $\alpha$ -tocotrienol), that serves to inhibit LOXs [284] was also combined with artesunate treatment of five MCPyV-positive MCC cell lines (MKL-1, MKL-2, WaGa, PeTa and MS-1), and was also found to protect them against artesunate-induced cytotoxicity (Fig. 28c).

Suppression of the crucial antioxidant system, System  $X_c^-$  (cystine/glutamate antiporter) has also been reported as an important mechanism of ferroptosis action. Cystine import by this antiporter results in the generation of the antioxidant GSH which ultimately prevents oxidative damage and thereby ferroptosis [288, 374, 375]. The ferroptosis inhibitor  $\beta$ -mercaptoethanol alleviates ferroptotic cell damage by promoting cystine uptake [227, 294]. Upon combining artesunate treatment of five MCPyV-positive MCC cell lines with  $\beta$ -mercaptoethanol, four of the five cell lines demonstrated increased survival (Fig. 28d).

In conclusion, the observed morphology of cell death as well as a series of experiments applying diverse inhibitors of crucial molecular events in the ferroptotic process, strongly suggested that artesunate induces a ferroptotic mode of cell death in MCPyV-positive MCC cell lines.

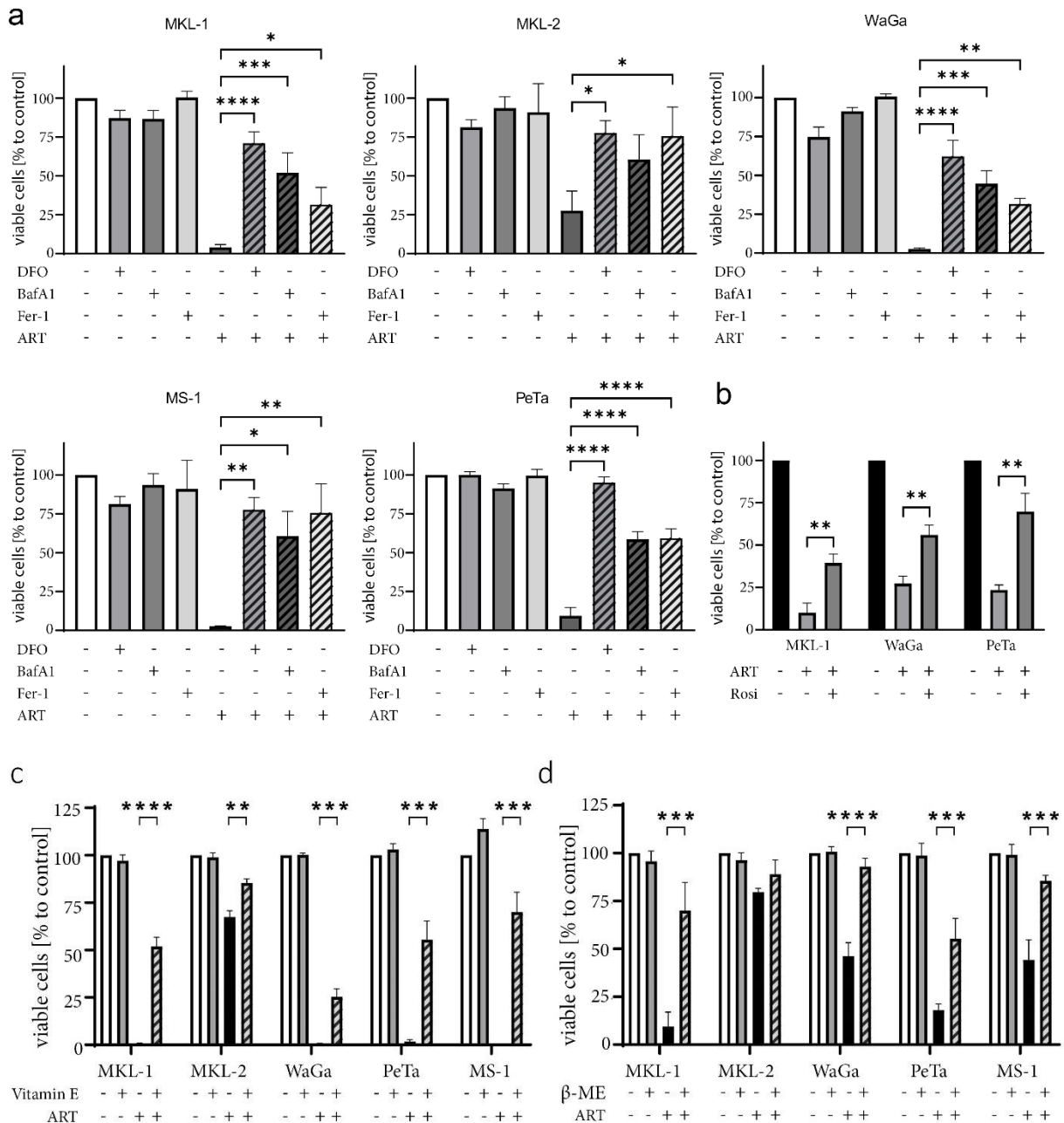
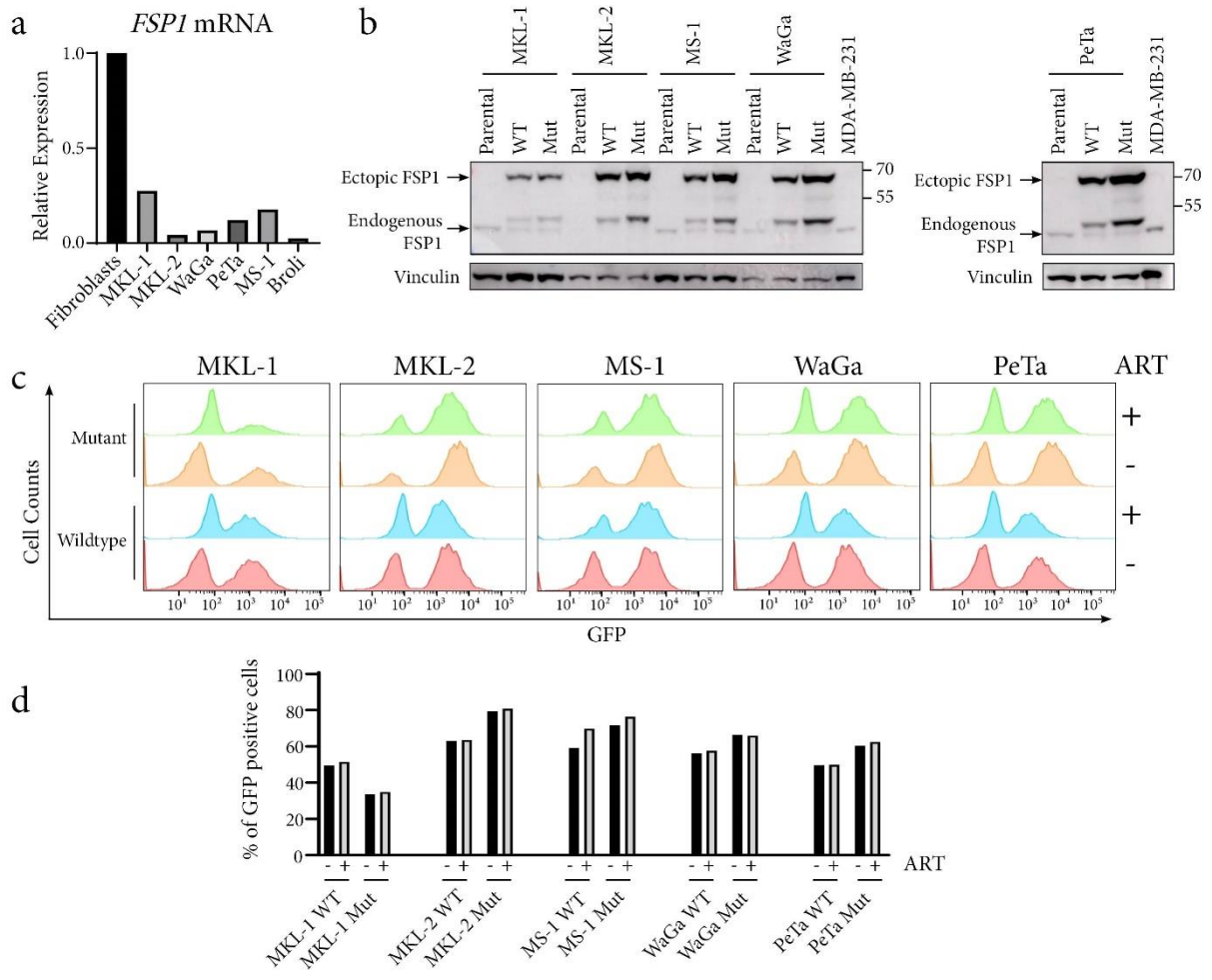


**Figure 28: The rescue of artesunate-induced cell death in MCPyV-positive MCCs by various ferroptosis inhibitors supports a ferroptotic mode of cell death.** The indicated MCPyV-positive MCC cell lines were treated with artesunate (ART) both in the presence and absence of ferroptosis inhibitors such as a) the iron chelator, DFO (100  $\mu$ M), the lysosomal vacuolar-type H<sup>+</sup>-ATPase, BAF-A1 (50 nM) or the lipid peroxide inhibitor, Fer-1 (10  $\mu$ M) b) the ACSL4 inhibitor Rosiglitazone (Rosi; 25  $\mu$ M) c) the LOX inhibitor, Vitamin E (10  $\mu$ M) and d) the promoter of cysteine uptake,  $\beta$ -mercaptoethanol (66  $\mu$ M). ART was used at a concentration of 50  $\mu$ M in Fig. 28a, 28c and 28d and 25  $\mu$ M in Fig. 28b. DMSO treatment served as controls. Cell viability was assessed using the trypan blue assay after two days of treatment in Fig 28a, 28b and 28c and after one day of treatment in Fig. 28d. Bar graphs display the percentage of viable cells normalized to the respective DMSO controls. Mean values of at least three independent experiments (+ SD) are represented. Statistical significance was estimated using ANOVA followed by Dunnett's multiple comparisons post hoc test by comparing each condition to that of the artesunate treatment for the individual cell lines (\* p < 0.05; \*\* p < 0.01; \*\*\* p < 0.001; \*\*\*\* p < 0.0001). Figures a, b and d adapted from [358].

### **3.2.7 Ferroptosis suppressor protein 1 (FSP1) does not suppress artesunate-induced ferroptosis in MCPyV-positive MCCs**

Ferroptosis suppressor protein 1 (FSP1) is part of an alternative antioxidant pathway acting in parallel with the GPX4-GSH pathway to prevent lipid peroxide-mediated ferroptosis [295, 296]. Research has shown that lung cancer cell lines expressing low levels of FSP1 display increased sensitivity to the ferroptosis inducer RSL3 [296]. In this context, levels of *FSP1* mRNA were first checked in MCPyV-positive MCC cell lines by qPCR. Indeed, all tested cell lines were found to express relatively low levels of *FSP1* mRNA compared to fibroblasts (Fig. 29a). This led to the speculation that these low levels of expression of FSP1 might contribute to the sensitivity of the MCPyV-positive MCC cells towards artesunate-induced ferroptosis. Therefore, we investigated whether overexpression of FSP1 might lower the sensitivity of the cells to artesunate. Five MCPyV-positive MCC cell lines (MKL-1, MKL-2, WaGa, PeTa and MS-1) were transduced with vectors encoding for FSP1 either as its wildtype version or as a loss of function (G2A) mutant version as a negative control [295, 296]. Overexpression was confirmed by immunoblotting (Fig. 29b). FSP1 was C-terminally fused to a GFP in both wildtype and mutant constructs. Following transduction, two cell populations were observed in the GFP channel upon flow cytometric analysis of these cells. The cells that were successfully infected and expressed the FSP1-GFP fusion constructs appeared as a GFP-positive population while the non-infected cells appeared as GFP-negative (Fig. 29c). These infected cell lines were treated with artesunate and analyzed on the flow cytometer. However, no marked enrichment of GFP-positive FSP1 expressing cells upon artesunate treatment was detected in all cell lines tested (Fig. 29c and d). In addition, the trypan blue assay for cell viability was also performed for these cell lines. No protective effect of wildtype FSP1 overexpression was observed also in this case (Fig. 29e). In order to ensure that the fusion of GFP with the FSP1 protein was not interfering with FSP1 function, three MCPyV-positive MCC cell lines (MKL-1, MKL-2 and PeTa) were infected with vectors overexpressing the wildtype and loss of function mutant (E156A) [296] versions of FSP1 without GFP fusion. The infected cells were selected in puromycin (the antibiotic selection marker in the FSP1 vectors) to enrich for the successfully transduced cells and an immunoblot for FSP1 was also performed (Fig. 29f). Subsequently, these cells were treated with artesunate and the trypan blue cell viability assay was performed. Overexpression of FSP1 lacking fusion with GFP also did not serve to rescue any of the cell lines from artesunate-induced cell death (Fig. 29g). In order to test whether FSP1 overexpression was able to protect the cells from ferroptosis induced by alternative ferroptosis inducers, two MCPyV-positive MCC cell lines (MKL-1 and PeTa) overexpressing the FSP1 wildtype and E156A mutant versions were treated with RSL-3. Interestingly, the cells expressing wildtype FSP1 demonstrated increased survival as compared to those expressing the mutant version and the corresponding parental cells (Fig. 29h). The results showed that FSP1 overexpression was able to protect the cells from RSL-3 but not artesunate-induced ferroptosis. Taken together, these results

suggest that FSP1 does not suppress artesunate-induced ferroptosis in MCPyV-positive MCCs.



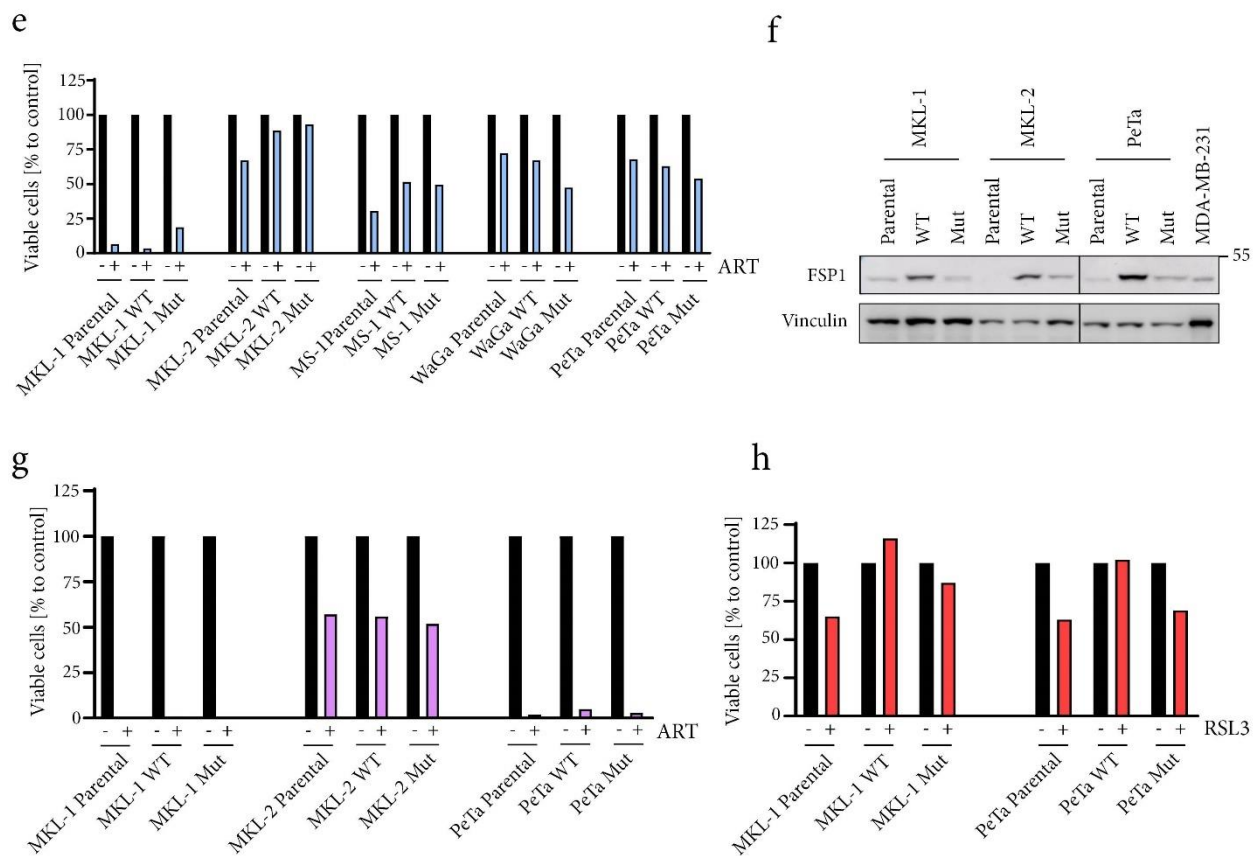


**Figure 29: Ferroptosis suppressor protein 1 (FSP1) does not suppress artesunate-induced ferroptosis in MCPyV-positive MCCs.** a) *FSP1* mRNA levels were determined in the indicated MCPyV-positive MCC cell lines in comparison to primary fibroblasts using qPCR. Bar graphs depicting expression of *FSP1* relative to that of primary fibroblasts are plotted. b) The indicated MCPyV-positive MCC cell lines were infected with either a wildtype (WT) or G2A mutant (Mut) FSP1 construct C-terminally fused to GFP, and overexpression was checked by immunoblotting. The expected size of endogenous FSP1 was 40 kDa while that of the fusion protein was 67 kDa. The breast cancer cell line MDA-MB-231 was included as a positive control for FSP1 expression. Vinculin was used as a loading control. c) WT and Mut FSP1-GFP-overexpressing MCPyV-positive MCC cell lines were treated with 12.5  $\mu$ M artesunate (ART) and DMSO as a control. After two days of treatment, GFP fluorescence was analyzed on the flow cytometer. d) The bar graph depicts the percentage of GFP-positive cells as obtained from the flow cytometric analysis shown in Fig. 29c. e) WT and Mut FSP1-GFP overexpressing MCPyV-positive MCC cell lines including the corresponding parental cell lines were treated with 50  $\mu$ M ART and DMSO as a control. The trypan blue assay for cell viability analysis was performed after one day of treatment. f) The indicated MCPyV-positive MCC cell lines were infected with either a wildtype (WT) or E156A mutant (Mut) FSP1 construct without GFP fusion. Overexpression was determined by immunoblotting. MDA-MB-231 was included as a positive control for FSP1 expression and vinculin was used as a loading control. g) WT and E156A mutant (Mut) FSP1 overexpressing MCPyV-positive MCC cell lines including the corresponding parental cell lines were treated with 50  $\mu$ M ART and DMSO as a control. The trypan blue assay for cell viability analysis was performed after two days of treatment. h) The indicated MCPyV-positive MCC cell lines infected with either a wildtype (WT) or E156A mutant (Mut) FSP1 construct without GFP fusion including the corresponding parental cell lines were treated with 200 nM RSL3 and DMSO as a control. After two days of treatment the trypan blue assay for cell viability analysis was performed.

### **3.2.8 Absence of a pro-ferroptotic role of p53 in MCPyV-positive MCCs**

While the tumor suppressor protein p53 is expressed in its wild type form in most MCPyV-positive MCCs [102], MKL-2 cells, which as per our studies, were found to be more resistant to artesunate-induced ferroptosis (Fig. 28a, c and d), lack p53 expression [102]. In this context, both, pro- and anti-ferroptotic functions have been described for p53 [243, 301, 302, 376, 377] and one of its pro-ferroptotic functions involves the inhibition of *SLC7A11*, a component of the antiporter System X<sub>c</sub><sup>-</sup> [243]. Since the data obtained for the other more artesunate-sensitive and p53-expressing MCPyV-positive MCCs, pointed towards suppression of system X<sub>c</sub><sup>-</sup> upon artesunate-induced ferroptosis (Fig. 28d), the role of p53 as a positive contributor of ferroptosis was tested next. To this end, p53 expression as well as p53 activity was analyzed in artesunate-treated MCPyV-positive MKL-1 and WaGa cells. First, immunoblot analysis did not reveal changes in the p53 expression levels of artesunate-treated cells (Fig. 30a). To confirm this data with a second method, MKL-1 and WaGa cells infected with a construct in which the expression of GFP is controlled by a p53 response element, were used [102]. The cells were either treated with artesunate or with Nutlin-3a (a p53 activator inhibiting MDM2 [378]) as a positive control, and green fluorescence was then monitored on the flow cytometer as a determinant for p53 activity. While Nutlin-3a was able to increase GFP expression in the cells, two different concentrations of artesunate treatment failed to induce an upregulation of p53 activity (Fig. 30b). Taken together, the data from these experiments suggest that ferroptosis induction by artesunate is not associated with p53 activation.

Although no further activation of p53 was observed in artesunate-treated MCC cells, we speculated that the presence of the protein might be essential for artesunate-induced cell death. To test this possibility, drug treatment was combined with shRNA knockdown of p53. Five MCPyV-positive MCC cell lines (MKL-1, MKL-2, WaGa, PeTa and MS-1) were transduced with a vector expressing a doxycycline-inducible shRNA targeting p53. Following doxycycline treatment for four days, knockdown of p53 was confirmed by immunoblotting (Fig. 30c). The cell lines including respective parental cells as controls were then treated with artesunate and the trypan blue assay for cell viability was performed. None of the cell lines with p53 knockdown demonstrated a rescue from artesunate-induced cell death (Fig. 30d) indicating that ferroptosis was able to occur in these cells despite lower levels of p53.

Taken together, the results demonstrated the lack of a pro-ferroptotic role of p53 in artesunate-induced ferroptosis in MCPyV-positive MCCs.

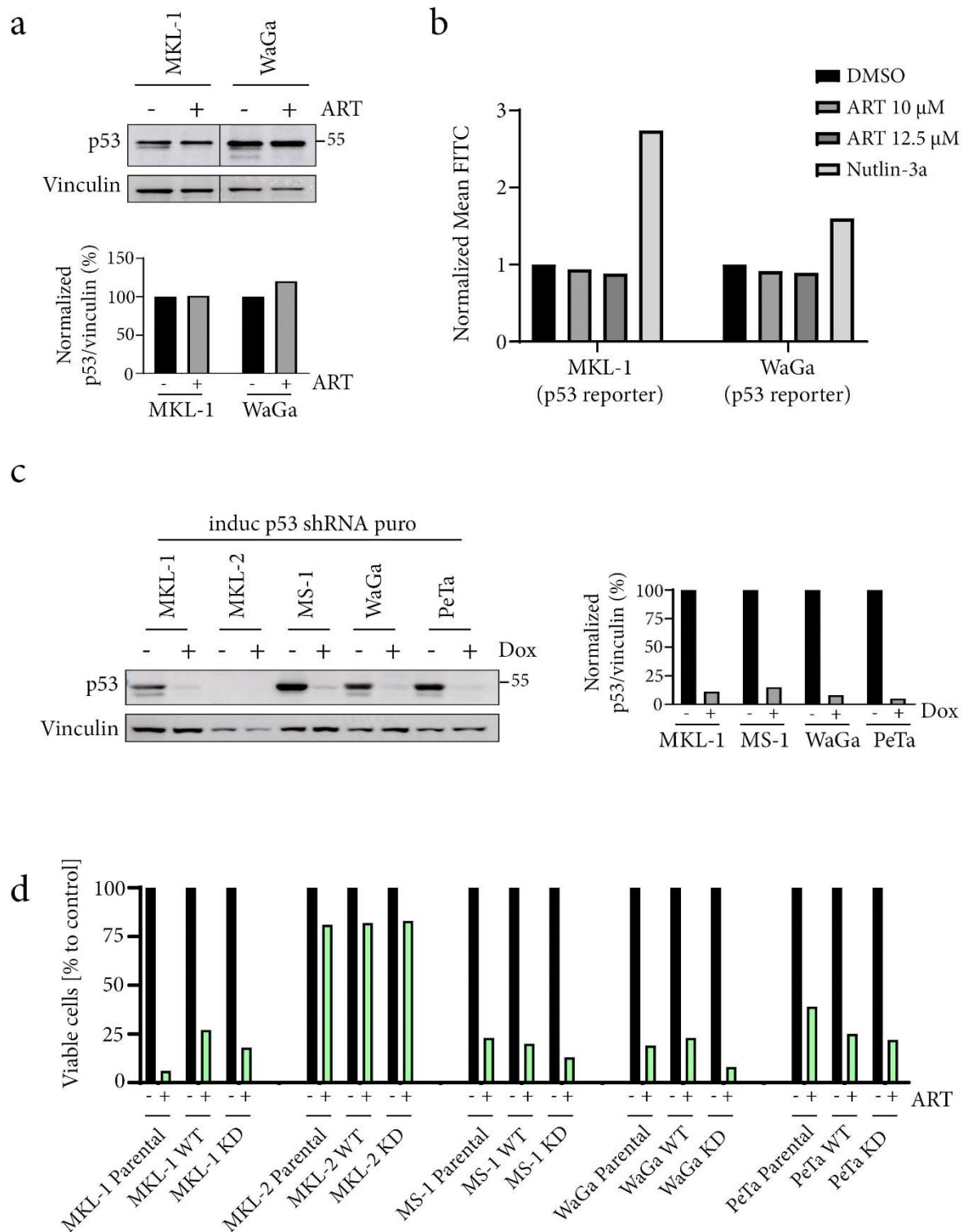


**Figure 30: p53 does not exhibit a pro-ferroptotic role in artesunate-induced ferroptosis of MCPyV-positive MCCs** a) The indicated MCPyV-positive MCC cell lines were treated either with 10  $\mu$ M artesunate (ART) or DMSO as a control. After three days of treatment, an immunoblot for p53 was performed. Vinculin was used as a loading control. The bar graphs depict quantification for the immunoblot signals for p53 normalized to vinculin and represented relative to the respective DMSO control treatments. b) The indicated MCPyV-positive MCC cell lines infected with a p53 reporter construct were treated with DMSO, ART (10  $\mu$ M and 12.5  $\mu$ M) and the p53 activator Nutlin-3a. After one day of treatment, p53 reporter activity in the cells was tested by measuring GFP fluorescence using flow cytometry. Mean FITC values were normalized to the respective DMSO treatments for both cell

lines. c) The indicated MCPyV-positive MCC cell lines were infected with a vector enabling doxycycline-inducible expression of an shRNA to p53. Following treatment with or without 1  $\mu$ M doxycycline (Dox) for four days, an immunoblot for was performed to confirm p53 knockdown. Vinculin was used as a loading control. The bar graphs depict quantification for the immunoblot signals for p53 normalized to the vinculin and represented relative to the respective control treatments without Dox (No p53 expression was detected for MKL-2 cells which were therefore excluded from the quantification analysis). d) The infected MCPyV-positive MCC cell lines expressing wildtype p53 (WT) or a knockdown of p53 (KD) along with the respective parental cell lines were treated either with 50  $\mu$ M ART or with DMSO as a control. The trypan blue assay for cell viability was performed after two days of treatment.

### **3.2.9 Artesunate suppresses MCC tumor growth *in vivo***

Since artesunate exerted strong cytotoxic effects towards MCPyV-positive MCCs *in vitro*, its efficacy in suppressing tumor growth *in vivo* was studied next. For this purpose, xenotransplantation mice models were used. The MCPyV-positive MCC cell line MKL-1 was subcutaneously injected into mice. After the tumors reached a size of approximately 150 mm<sup>3</sup>, intraperitoneal administration of 100 mg/kg artesunate was carried out over a period of 20 days. A control group of mice received the same concentration of the vehicle control. Evaluation of the tumor size during the course of treatment revealed a repression of tumor growth of artesunate-treated mice in comparison to control mice (Fig. 31). Moreover, we did not detect any abnormalities or limitations in the animal behaviour or toxic side effects in the artesunate-treated animals indicating that systemic delivery of artesunate at a dose sufficient to repress tumor growth was well tolerated. Therefore, the results demonstrated that artesunate can be applied in a living organism to inhibit MCC growth.

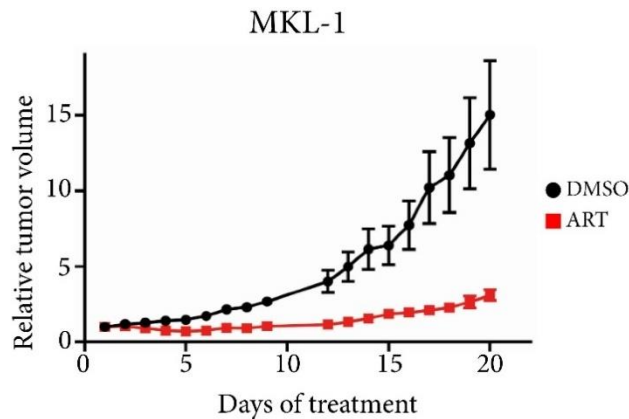
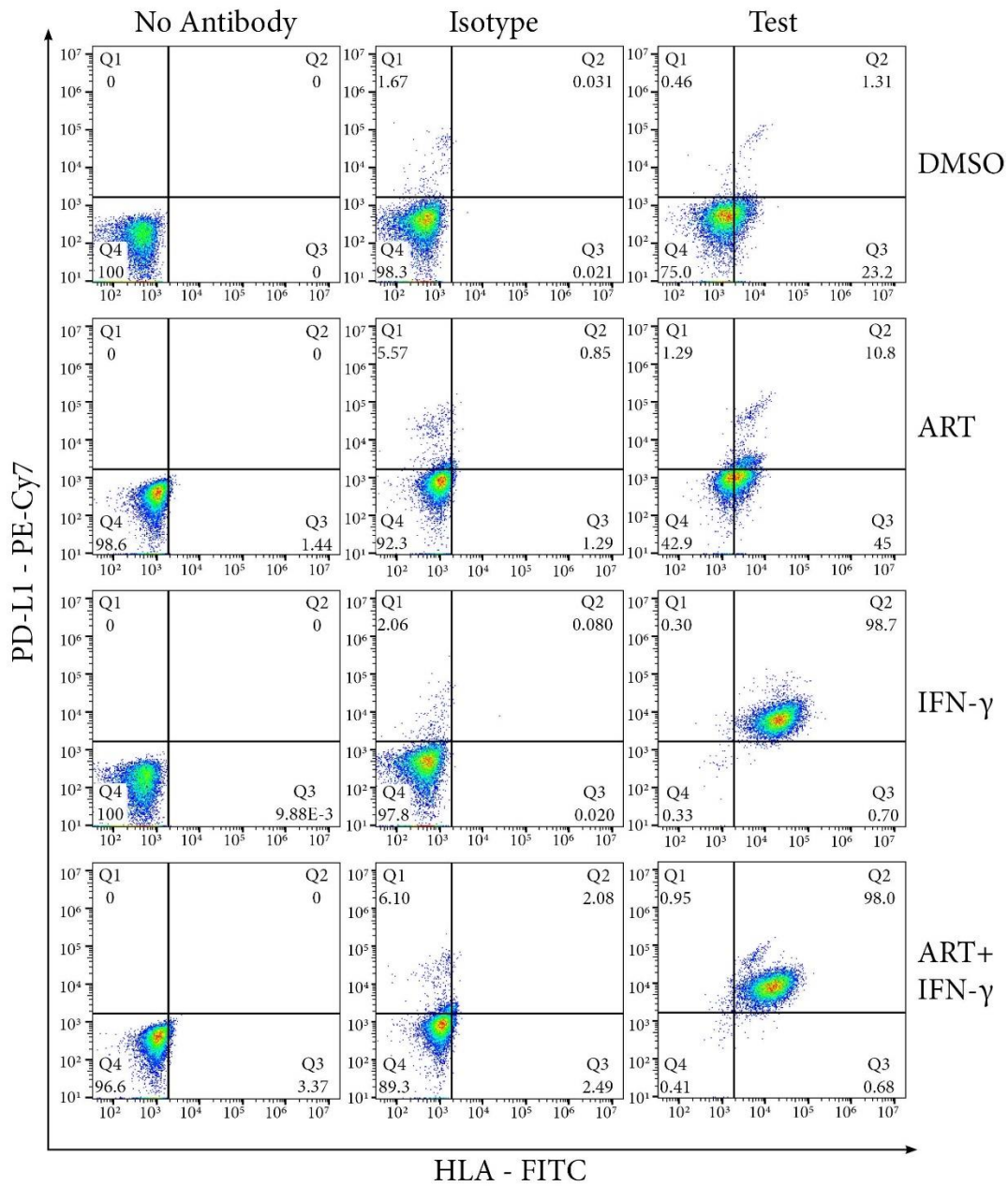


**Figure 31: Artesunate suppresses tumor growth *in vivo*** a) The MCPyV-positive MCC cell line MKL-1 was injected subcutaneously into immunodeficient NOD/SCID mice and tumor growth was monitored. Upon reaching a size of approximately 150 mm<sup>3</sup>, the mice were sorted either into control groups (n=5; one mouse did not show any tumor growth and was therefore excluded) or treatment groups (n=6). While the mice from the treatment group received daily intraperitoneal injections of artesunate (ART; 100 mg/kg), mice from the control group received an equal volume of solvent (2% DMSO in PBS). Tumor volumes were monitored and documented regularly for both groups over a period of 20 days until the maximum acceptable tumor sizes were reached. The graph depicts the mean values of tumor volume ( $\pm$  SEM) and the statistical testing of the area under the curves was performed (unpaired t-test;  $p < 0.001$ ). Figure adapted from [358].

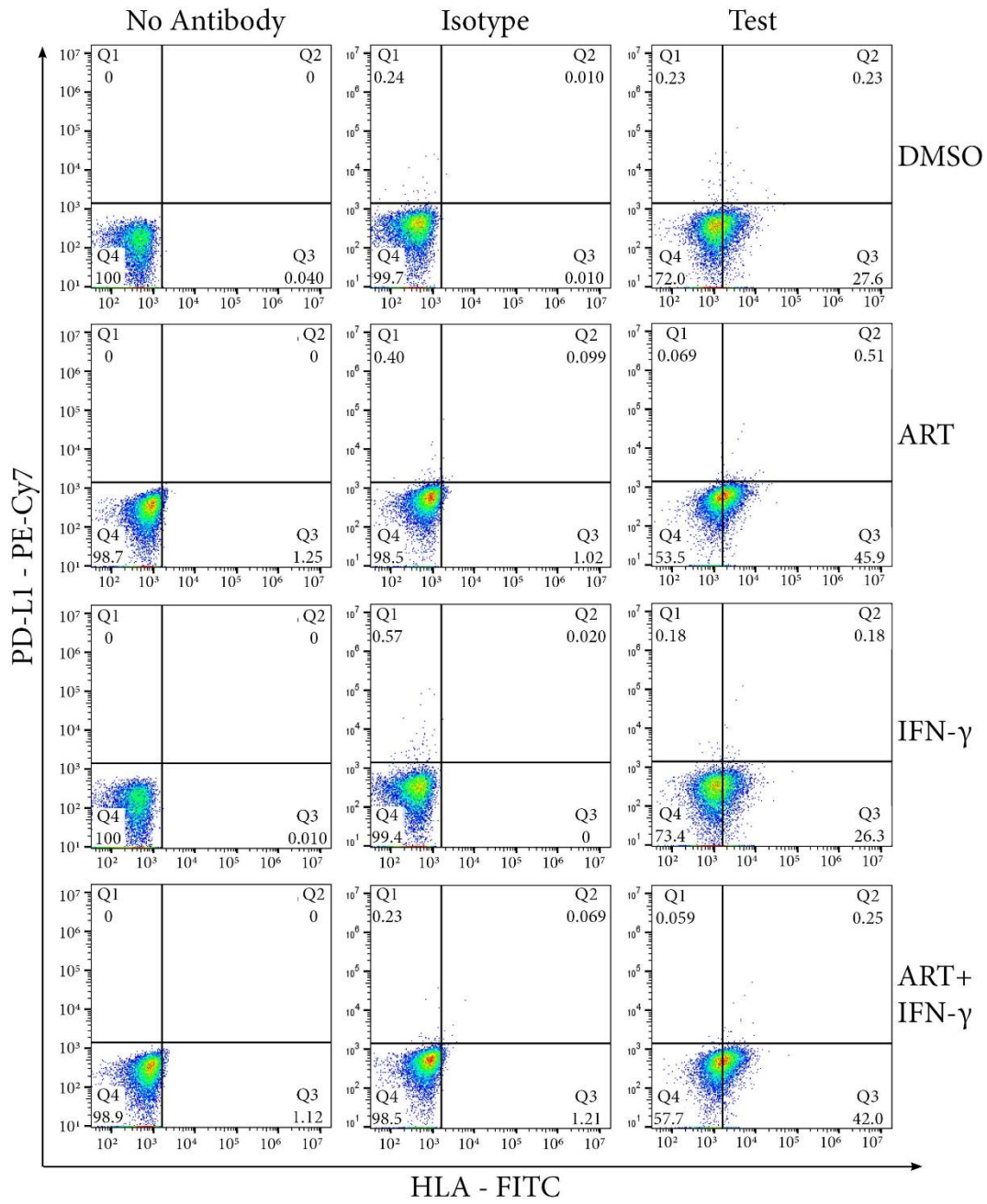
### **3.2.10 Artesunate does not interfere with upregulation of crucial immune-relevant molecules on MCPyV-positive MCC cells**

Checkpoint blockade immunotherapy has emerged as an effective approach for the treatment of MCC [147, 148, 379] demonstrating that MCC tumors can be controlled by boosting of the immune response. Therefore, any new therapeutic strategy for the treatment of MCC should not interfere with antitumor immune responses, in particular because it is likely to be used in combination with immune checkpoint blockade. Two key mechanisms of tumor cells to evade the immune system are down-regulation of MHC class I molecules which present immunogenic peptides to T-cells [141] and upregulation of repressors of T-cell function, like PD-L1 [146]. Consequently, the influence of artesunate on the expression of HLA and PD-L1 on MCC cells was investigated. Since their expression is largely modified by the presence of interferon gamma [141], cells were analyzed following treatment either with interferon gamma, artesunate or a combination of both. As expected, treatment with interferon gamma resulted in an increase of both HLA and PDL-1 expression in four of the five investigated cell lines (WaGa, Peta, MKL1 and MS-1) while expression was not changed on MKL-2 in accordance with previously obtained data [380] (Fig. 32). Importantly, artesunate treatment alone did not result in a substantial upregulation of PD-L1, and its use in combination with interferon gamma did not dampen the expression of HLA. The results provided a first positive indication regarding a possible use of artesunate in combinatorial immunotherapy for MCC.

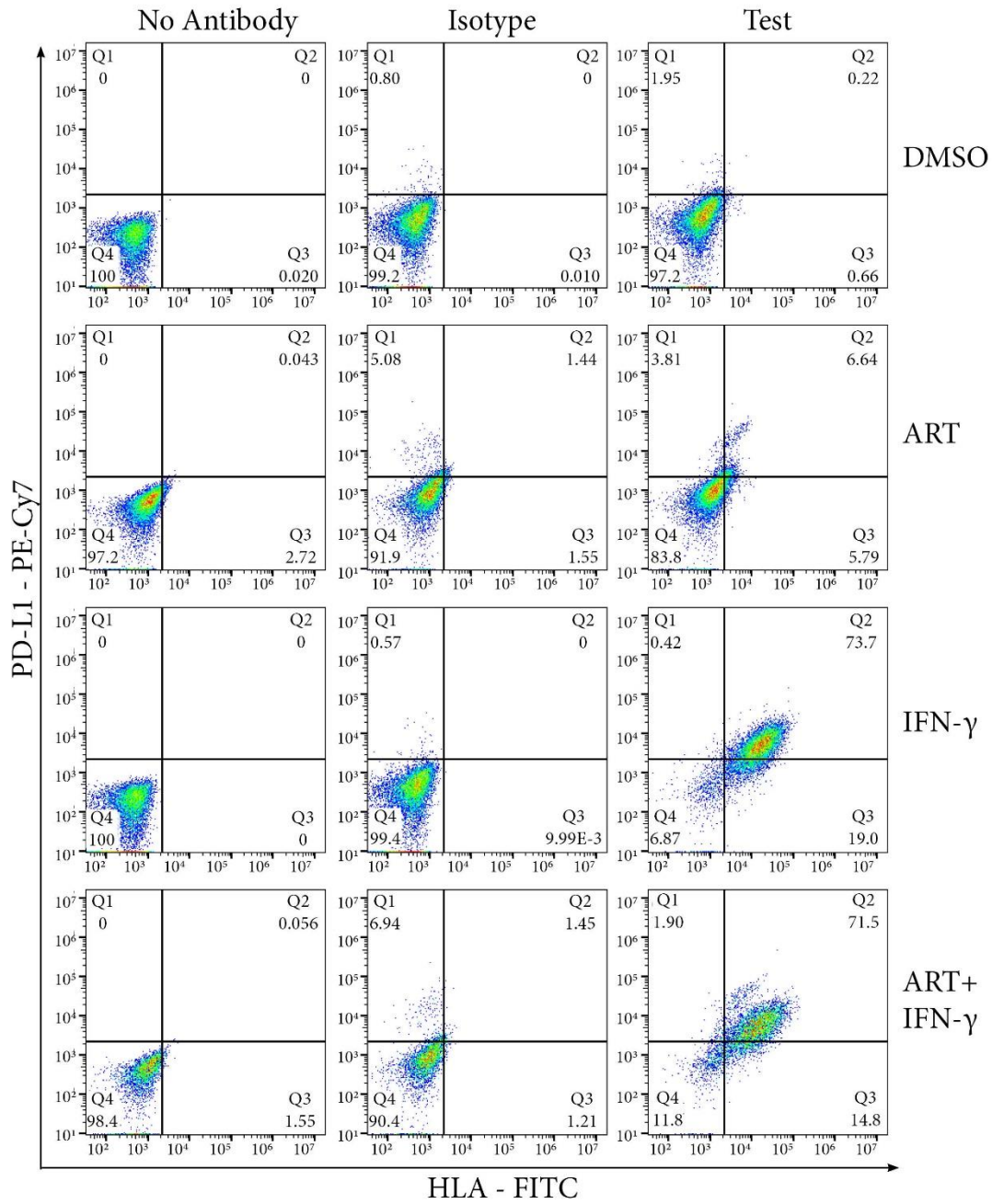
# MKL-1



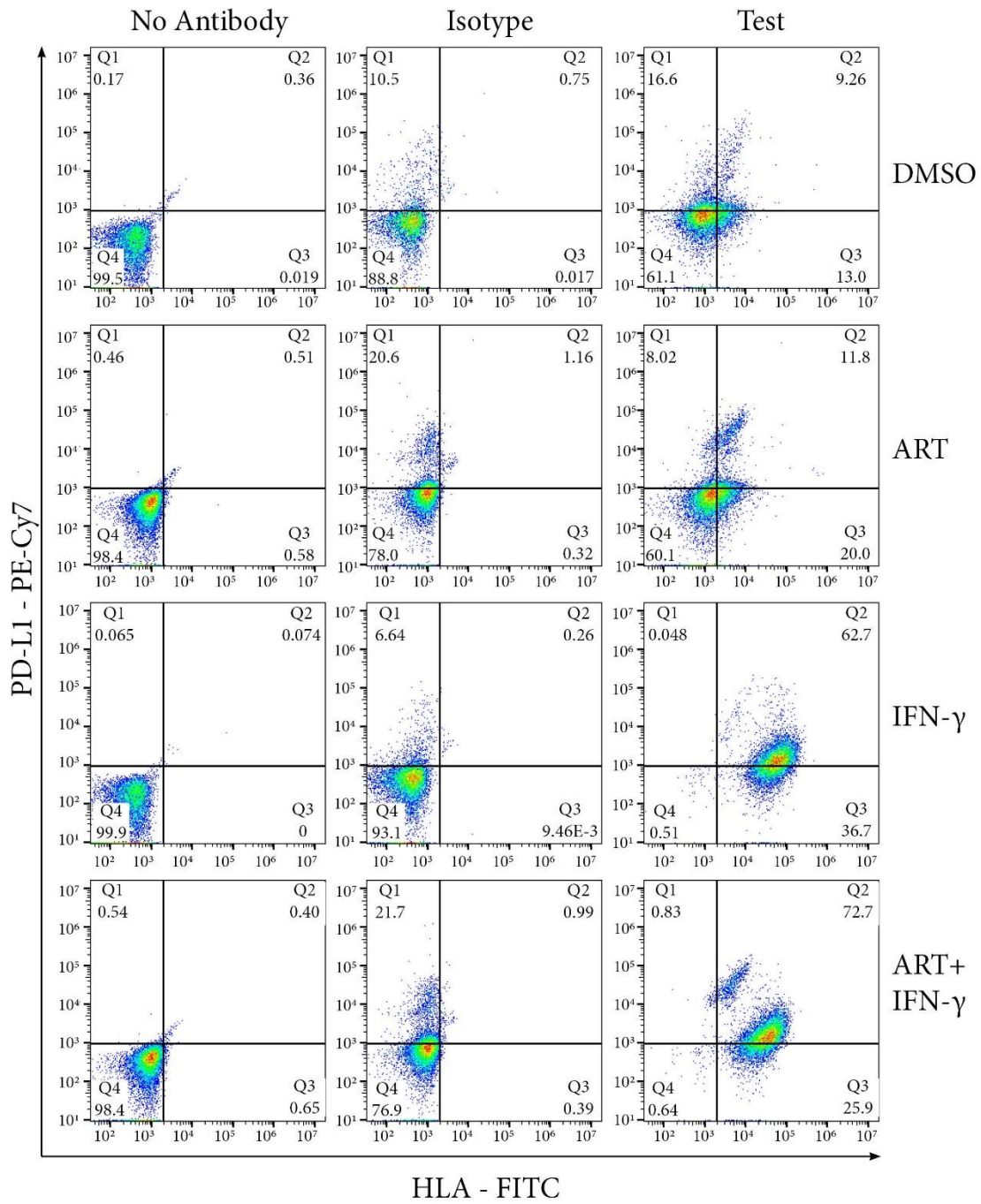
# MKL-2



# MS-1



# PeTa



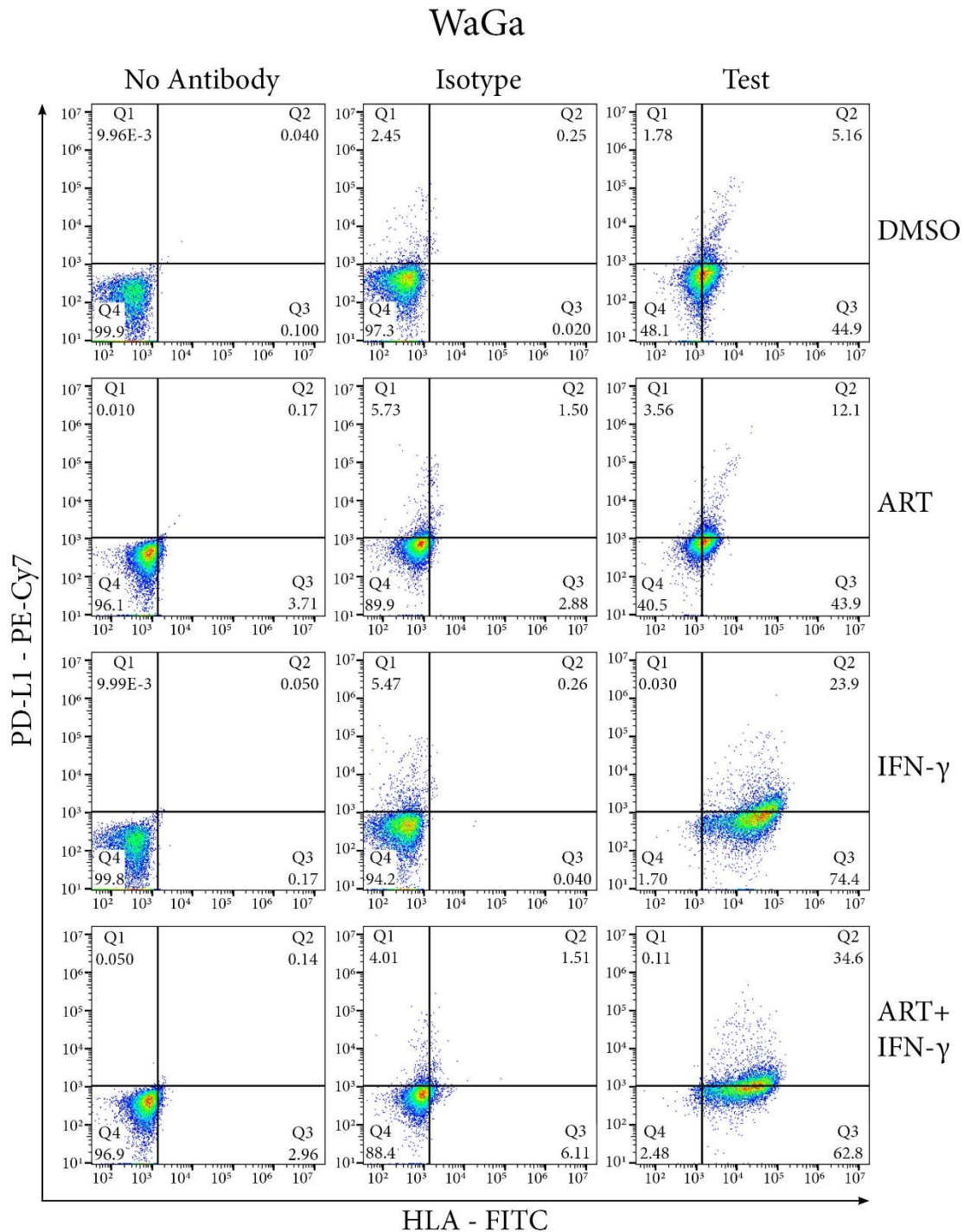


**Figure 32: Artesunate does not interfere with the upregulation of immune-relevant molecules on MCPyV-positive MCCs.** Five MCPyV-positive MCC cell lines (MKL-1, MKL-2, MS-1, PeTa and WaGa) were treated with DMSO, 10  $\mu$ M artesunate (ART), 200U/ml Interferon gamma (IFN- $\gamma$ ) or a combination of ART and IFN- $\gamma$ . Following two days of treatment, immunofluorescence staining was performed using HLA-A,B,C and PD-L1 antibodies conjugated to FITC (green) and PE-Cy7 (red) respectively. As controls, the cells were also stained without antibodies or with the corresponding isotype antibodies.

## **4. Discussion**

### **4.1 Models for MCC oncogenesis**

#### **4.1.1 Why has the cell of origin of MCC not yet been identified?**

The rising incidence of MCC [26] along with its aggressive nature [381, 382] demand for a thorough understanding of the oncogenesis of this cancer. An important finding in this regard, was the discovery of the MCPyV which was found to be integrated in the genome of MCC tumors [31] and is now known to be the causative agent for 80% of MCC cases [31-33]. Numerous reports have shown that the MCPyV-derived T antigens serve as oncoproteins which are crucial for driving MCPyV-positive MCC carcinogenesis [45, 46, 70]. In addition, various transcription factors such as ATOH1 [61, 82] and cell signaling pathways such as the Notch [36, 100] and Hedgehog pathways [89, 93] have also been implicated to influence the oncogenesis of MCPyV-positive MCC. For instance, ATOH1 was recently described as a lineage-dependency oncogene in MCC and was found to activate expression of miR-375, one of the most abundantly expressed microRNAs in MCC [83]. In addition, rare cancer-promoting mutations in tumor suppressor genes like *NOTCH1* and *NOTCH2* have been predicted to inactivate the Notch pathway in MCPyV-positive MCCs [36]. Moreover, recent studies also supported MCPyV-positive MCC development from an epithelial precursor cell expressing GLI1 [94], a downstream transcription factor of the Hedgehog pathway [87]. Despite these advances towards the understanding of MCPyV-positive MCC oncogenesis, several aspects of its oncogenesis remain unresolved such as the cell or origin of this cancer, the cellular tropism of the MCPyV and the precise differentiation pathways that are ultimately involved in MCPyV-positive MCC development [44]. To address these unanswered questions, several groups attempted the generation of mice models to study MCPyV-positive MCC oncogenesis. For instance, Spurgeon and colleagues analyzed the effect of MCPyV T antigen expression in keratin 14-expressing stratified squamous epithelial cells and Merkel cells in mouse skin epidermis [75]. Although hyperplasia, hyperkeratosis and papilloma formation were observed, MCC tumor development was not found to occur [75]. In the sT MCPyV transgenic mouse model generated by Shuda and colleagues, sT expression in Merkel cells in a p53-null setting increased embryonic merkel cell precursor cell proliferation only transiently and MCC tumorigenesis was not induced [126]. Interestingly, in the work by Verhaegen and colleagues, MCC-like intraepidermal tumors were found to develop in mice co-expressing sT and ATOH1 under the epidermis-specific keratin 5 promoter [61]. Notably, however, most MCC tumors are located within the dermis and lack a connection with the epidermis [106, 125, 383]. Taken together, despite the efforts until date, no perfect MCC models have been established. Therefore, further studies are required to identify the genuine cells

of origin of MCC which might aid in the generation of models closely mimicking MCC and in turn clarify further aspects of MCC oncogenesis [44].

#### **4.1.2 Generation of a vector system to aid in the study of MCC oncogenesis**

Since mouse models could not answer the unresolved aspects of MCC oncogenesis so far, it would be desirable to recapitulate some aspects of MCC carcinogenesis in human *in vitro* model systems. Ideally, several different candidate factors potentially contributing to MCC development would be independently regulatable in such a model. Therefore, we generated lentiviral vectors for the inducible expression of the crucial MCPyV-positive MCC oncoproteins (T antigens) and differentiation factors (ATOH1, GLI1 from the Hedgehog pathway and dnMAML1 from the Notch pathway) which have previously been implicated for MCPyV-positive MCC carcinogenesis [36, 61, 70, 94] in order to further the understanding of MCPyV-positive MCC development and differentiation. Each lentiviral vector was independently inducible and the previously established doxycycline [320, 321], RheoSwitch [330-332] and IPTG [340, 341] systems were made use of for the inducible expression of the T antigens, ATOH1 and GLI1/dnMAML1 respectively. In addition, each vector was independently selectable with its own antibiotic selection marker. The advantage of such a system is that it provides the ability to independently, temporally and reversibly regulate expression deriving from these MCPyV-positive MCC relevant factors and thereby the independent influence of each factor on MCPyV-positive MCC development can be investigated in any cell type in a temporal fashion. Moreover, it also well known that KRT20 is an important marker frequently used for the identification of MCPyV-positive MCC tumors [108, 109]. Therefore, as part of our study, we also successfully generated a KRT20 fluorescence reporter system which could be used for monitoring the induction of KRT20 expression and thereby serve as an indicator of MCC-like differentiation.

#### **4.1.3 Efficiency of the generated inducible expression vectors in primary fibroblasts and HaCaT cells**

While several recent reports have strongly supported the origin of MCC from an epithelial cell [84, 94], fibroblasts are known to be the only cells that support robust MCPyV replication [125]. Furthermore, fibroblasts are also known to be genetically amenable [384, 385] and can be dedifferentiated into iPSCs [343, 386] which provides the additional possibility to test such vector systems in iPSCs derived from dedifferentiated genetically manipulated cells. Accordingly, in our study, we went on to analyze the influence of our successfully established vectors in promoting MCC-like differentiation by introducing them into both primary fibroblasts and HaCaT

(immortalized human keratinocytes) cells. In this regard, we could successfully introduce the various inducible vectors into primary fibroblasts and HaCaT cells by lentiviral transduction and also observed correct integration of the KRT20 fluorescence reporter by CRISPR/Cas9 genome editing.

Upon analyzing inducible expression of the various vectors in primary fibroblasts and HaCaT cells, a striking observation was the excellent inducible expression of the T antigens from the doxycycline system (over 1000-fold as compared to the uninduced state) with minimal leaky expression. This observation was in accordance with previous studies in mammalian cell types such as SupT1 (T-cell lymphoma cells), wherein these cells, which were also transduced with doxycycline-inducible vectors, demonstrated high induction (up to 84-fold) with low background activity [387]. With respect to the IPTG system, a major drawback in our study was the high level of leaky expression observed in our cell types also in the absence of the inducer, IPTG. Such leaky expression deriving from IPTG systems has previously been described as problematic in prokaryotic cells (*E. coli*) [388] as well as in *in vivo* mice models [389]. A possible explanation for this phenomenon was described as the potential inefficient expression of the lac repressor [389] which is necessary for binding to lac operator sequences in the promoter thereby preventing transcription [340]. In this regard, in order to overcome the problem of leaky expression, alternative strategies have been developed [390]. For instance, Deans and colleagues designed a genetic switch which in addition to the lac repressor (for target gene repression), also expressed an RNA interference (RNAi) module to knockdown leaky gene transcripts only in the uninduced state, which was reversible upon addition of the inducer [390]. Such genetic modifications might be tested and implemented in further studies. In our studies, in addition to the leaky expression from the IPTG system, we also most often observed very low levels of induction between 1 to 5-fold from the uninduced state compared to the over 1000-fold induction frequently observed with the doxycycline-inducible system. In this context, recent experiments using the IPTG system in mammalian cells also described low expression levels of the target gene upon IPTG induction [341]. Interestingly, the authors showed that IPTG induction, when combined with lactose, an alternative inducer for this system, elevated inducible expression of the target gene [341]. Therefore, such methods might be tested and incorporated in future experiments in case that low inducible expression levels are observed in certain cell types. Concerning the RheoSwitch system, we observed variable levels of RSL1-induced expression of ATOH1 in the different cell types in which the system was analyzed. While the maximum inducible expression of ATOH1 was around 8-fold in one of the isolated fibroblast single cell clones, induction levels in the HaCaT cells were higher, reaching around 30-fold in some of the polyclonal populations generated as compared to the uninduced states. Moreover, it was possible to isolate a HaCaT clone which demonstrated inducible ATOH1 expression to a level of around one-third of the endogenous expression seen in WaGa cells which was not the case for fibroblasts. Notably, the sensitivity of the RheoSwitch system was recently shown to be cell type-dependent and was also influenced by cell density and contact inhibition

[391]. In NIH3T3 fibroblast cell lines, RSL1-induced target gene expression was greatly diminished when the cells were highly confluent and displayed contact inhibition [391]. However, such an observation was not made for NMuMG mammary epithelial cells [391]. In our studies, we frequently observed that primary fibroblasts encountered senescence when sparsely seeded and therefore had to be seeded at relatively high cell densities. Therefore, it is possible that the maintenance of these cells as nearly confluent over long periods of time in culture might have hampered induction from the RheoSwitch system [391]. On the other hand, HaCaT cells could rapidly proliferate also when seeded at low densities in our experimental set-up, which might potentially explain the slightly increased success in the isolation of HaCaT single cell clones with good RSL-1-inducible ATOH1 expression [391]. Therefore, the influence of various cell densities on inducible-ATOH1 expression by the RheoSwitch system for every cell type tested might be carefully analyzed in further studies. In addition to the points discussed above, a further explanation for the low levels of inducible expression seen in several cases might be a form of transcriptional interference between the promoters used in the inducible expression constructs, as has previously been evidenced in murine and human cell lines [392, 393]. In conclusion, analysis of our vector system in fibroblasts and HaCaT cells showed that we could obtain excellent inducible expression from the doxycycline-inducible system. The inductions achieved from the RheoSwitch and IPTG systems, on the other hand, could be further investigated and improved in these cell types in future studies.

#### **4.1.4 Challenges faced with primary fibroblast proliferation, single cell clone generation and the integrated KRT20 donor**

We faced several hurdles during the course of the genetic manipulations in primary fibroblasts. One of the challenges faced in our experiments, as discussed previously, was the fact that the primary fibroblasts, following several passages, frequently stopped proliferating and ran into senescence. In this regard, it has frequently been shown that hTERT can be used to rescue primary cells such as human dermal fibroblasts, keratinocytes and human lens epithelial cells from such a non-proliferative state and prolong cellular lifespan by enabling telomere synthesis [346, 394, 395]. Similarly, in our experiments, we were able to successfully generate and introduce an hTERT expression vector into the primary fibroblasts and improve their proliferative potential. Despite these genetic manipulations for prolonging the proliferative lifespan of the fibroblasts, we could not isolate proliferating single cell clones harbouring the TA construct in subsequent steps. In this context, it has been shown that the use of polybrene to increase viral transduction efficiency can have a negative impact on the proliferation of primary cells such as fibroblasts as well as in mesenchymal stem cells [396]. In addition, antibiotics such as penicillin and streptomycin, which are frequently used in cell culture media, have also been shown to suppress growth-rates of normal human keratinocytes [397] and embryonic stem cells [398]. Since our experiments

involved several polybrene-aided lentiviral transduction steps as well as extended periods of cell culture in antibiotic-containing media, it might be speculated that this line of fibroblasts harbouring the TA construct was negatively influenced by these factors. Although we could successfully isolate proliferating single cell clones harbouring the sT construct, we encountered the further challenge that these single cell clones demonstrated green fluorescence as detected on the flow cytometer which did not derive from an active KRT20 promoter. It is well known that CRISPR/Cas9 genome editing might result in off-target cleavage [399, 400] and random integration of the donor DNA into the host genome [401, 402], suggesting that there might have occurred a potential integration of the KRT20 donor in frame with alternative transcriptionally active promoters in the fibroblasts. Nevertheless, the observed fluorescence was not uniform in individual clones analyzed, suggesting that the observed fluorescence might derive from other sources. Accordingly, it was observed in previous reports that human fibroblasts with long passages in culture demonstrated an increase in autofluorescence owing to the onset of senescence [403, 404] which might serve as a potential explanation also in our case. Furthermore, no non-specific green fluorescence was observed upon prior testing of the KRT20 fluorescence reporter system in WaGa cells as well in subsequently transfected HaCaT cells supporting the correct integration of the KRT20 donor in these other cell types. In conclusion, the results from our experiments indicated that it was not trivial to introduce such vector systems into primary cells susceptible to senescence and rather implicated the use and testing of such a vector system in cells with extensive proliferating potential.

#### **4.1.5 Expression of potential MCC-promoting factors in HaCaT cells**

In addition to MCPyV-positive MCC cells, Merkel cells also express KRT20 at later stages of their differentiation process [78]. In studies analyzing merkel cell differentiation in neonatal mouse skin, an induction of KRT20 expression was found to occur in ATOH1-positive cells around 16 to 18 days post-embryonic development [78]. Moreover, recent reports analyzing the influence of T antigen and GLI1 coexpression in normal human keratinocytes demonstrated induction of KRT20 expression in a few cells following two weeks of co-expression [84]. Since we could successfully isolate a HaCaT single cell clone demonstrating good induction of the T antigens and ATOH1 as well as the highest achieved induction of dnMAML1 from the IPTG system in our experimental set-up, we analyzed the influence of the combined expression of these factors on the induction of KRT20 in these cells as an indication of MCC-like differentiation for up to 20 days post co-expression. However, we could not detect green fluorescence deriving from the KRT20 reporter system in these cells over the time point studied. Since recent studies have strongly implicated a role for the expression of GLI1 in promoting MCPyV T antigen-induced MCC development [94], subsequent overexpression of GLI1 and ATOH1 in polyclonal populations of HaCaT

cells expressing inducible T antigens was also tested, however, also in this case no KRT20 induction was observed. Therefore, our results showed that the combination of the T antigens, ATOH1 and either dnMAML1 or GLI1 in HaCaT cells in our experimental set-up did not promote the induction KRT20 expression. It is possible that this cell line, despite its keratinocytic origin [348], did not serve as an ideal model for studying MCPyV-positive MCC carcinogenesis. For instance, these cell lines have been found to harbour UV-indicative mutations in p53 [405] whereas MCPyV-positive MCCs typically express p53 in its wildtype form [102]. Interestingly, the recently characterized spontaneously immortalized keratinocytic cell line HaSKpw was found to harbour p53 in its wildtype form [405]. Therefore, future experiments to study MCPyV-positive MCC oncogenesis using our vector system might consider performing these studies in the HaSKpw cell line.

#### **4.1.6 Future implications for our lentiviral vector system for multiple independently-inducible factors**

Since iPSCs can proliferate indefinitely and can also be differentiated *in vitro* and *in vivo*, the use of these cells to study cancer oncogenesis has gained immense popularity [386, 406, 407]. For instance, human iPSCs were successfully used to model gliomagenesis by their initial differentiation into neural progenitor cells which were subsequently genetically manipulated to generate glioma tumor-initiating cells [408]. Similarly, iPSCs might serve as a potential cellular model for the testing of our generated vector system in future studies investigating MCPyV-positive MCC oncogenesis. In this context, a recent study described the interesting possibility to generate hair-bearing human skin from iPSCs [409]. These organoids were also found to generate KRT20-expressing Merkel cells from Merkel-cell like precursors expressing typical Merkel cell markers like ATOH1 [409]. Therefore, the availability of such human skin organoid models also provides the additional possibility to test the spatio-temporal expression of our generated inducible vectors in order to deepen the understanding of MCPyV-positive MCC oncogenesis.

#### **4.1.7 Conclusion**

As a conclusion to our study, we could successfully generate a lentiviral vector system expressing crucial factors implicated in MCPyV-positive MCC oncogenesis which might be tested in several different cellular contexts and experimental set-ups to provide insights into MCPyV-positive MCC carcinogenesis.

## **4.2 Artesunate as a potential MCC treatment**

### **4.2.1 The need for alternative treatments for MCC**

The high mortality rate associated with MCC (between 33 to 46%) [27] as well as its rising incidence [26] demand for the development of highly effective treatments for this cancer. Until recently, surgery, radiotherapy and chemotherapy were the available options to treat patients with advanced MCC, however, without providing significant survival benefit [137, 151]. With the advent of checkpoint blockade immunotherapies targeting immune checkpoints such as PD-1 and PD-L1, this has changed and many patients profit by this antibody treatment [137, 151]. For instance, treatment with the PD-1 inhibitor, pembrolizumab, has been associated with improved median progression free survival (up to 16.8 months) in MCC patients [149] as compared to chemotherapeutic treatments (median progression free survival up to 90 days) [139]. Nevertheless, despite these therapeutic advances, problems such as the lack of response to treatment in approximately 50% of MCC patients, the occurrence of immune-related adverse events, tumor relapse and chemotherapy-associated cytotoxicity still persist [140, 142, 410]. Therefore, there is a growing concern for the development of novel MCC therapies which are not only safe but highly effective. Moreover, since MCPyV is the oncogenic driver in approximately 80% of MCC cases [31-33], there is a demand for virus-specific treatments since the current checkpoint blockade immunotherapies function regardless of the viral state of the tumor [44, 147, 150]. These problems emphasize the need for alternative strategies for the treatment of MCC.

### **4.2.2 Artesunate as a potential treatment option for MCPyV-positive MCC**

In the context of developing novel therapies, 'drug repositioning' has become increasingly popular for the treatment of cancer [411]. This term refers to the use of an already established drug for new treatments linked to other diseases which is not only cost-effective but also associated with lesser risks for patients [411]. For instance, thalidomide, a drug initially used for the treatment of morning sickness, has now been repositioned for the treatment of multiple myeloma [412, 413]. Another drug, currently being tested for repositioning is artesunate, a derivative of artemisinin, which is a metabolite isolated from the ancient Chinese medicinal plant, *Artemisia annua* [154, 414]. At present, artesunate is approved as a safe and effective anti-malarial drug for the first line treatment of malaria [158, 161] however it additionally possesses anti-cancer and anti-viral properties [172, 184]. Consequently, several studies are already in process for testing the repositioning of artesunate for the treatment of cancer entities such as renal cell carcinoma [187, 414] as well as for the inhibition of pathogenic

viruses such as the Human Cytomegalovirus (HCMV) [174] and also the recently discovered severe acute respiratory syndrome coronavirus 2 (SARS-CoV-2) [415, 416]. On similar lines, in this study, we analyzed whether artesunate, by means of its anti-cancer and anti-viral properties, might be used as a treatment for MCPyV-positive MCCs. Notably, our experiments confirmed that artesunate was indeed cytotoxic towards MCPyV-positive MCC cell lines *in vitro* as per several different cell viability assays as well as *in vivo* in MCC xenotransplantation mice models. Importantly, artesunate did not show any signs of toxicity in mice upon the efficient repression of tumor growth indicating that artesunate might also be used for the treatment of patients with MCPyV-positive MCC following successful clinical trials. Therefore, our study is the first to highlight a potential role of artesunate as a treatment for MCPyV-positive MCC.

#### **4.2.3 Artesunate inhibits the growth of MCPyV-positive MCCs and represses MCPyV oncoproteins**

Our initial *in vitro* experiments showed that all the analyzed MCPyV-positive MCC cell lines and two of the three analyzed MCPyV-negative cell lines, MCC26 and UI50, were sensitive towards artesunate. Nevertheless, we observed that the MCPyV-positive MCC cell lines demonstrated an increased sensitivity towards artesunate as compared to the MCPyV-negative cell lines upon treatment for longer durations. While these results suggested that certain MCPyV-negative MCCs are also affected by artesunate, it appeared that the presence of the virus might be responsible for the increased sensitivity of the MCPyV-positive MCC cells towards artesunate probably owing to artesunate's additional anti-viral properties [172]. In this context, artesunate is currently being tested in clinical trials for the treatment of patients with epithelial cervical human papillomavirus (HPV) lesions indicating the possibility to exploit its dual anti-cancer and anti-viral properties for the treatment of viral-derived cancers [183]. Moreover, it is also known that artesunate can interfere with the replication of other members from the polyomavirus family like the BK and JC polyomaviruses [177, 179]. Therefore, we analyzed whether artesunate might also affect the MCPyV upon exerting its cytotoxic effects towards MCPyV-positive MCCs. It is well known that the MCPyV-derived T antigens are crucial for promoting growth of MCPyV-positive MCC cells [51, 53] and also some degree of cytotoxicity has been observed upon T antigen knockdown in MCPyV-positive MCC cells [70]. Consequently, upon looking for the effect of artesunate on the MCPyV T antigens, we found that total T antigen and LT mRNA as well as LT protein were repressed by artesunate in MCPyV-positive MCC cell lines. This observation was in line with previous experiments which showed that artesunate could repress LT mRNA and protein in the BK polyomavirus [179]. A similar observation was made also in recent studies showing that artesunate repressed expression of the rabies virus-derived nucleoprotein mRNA [355]. The mechanism of action of artesunate in the repression of viral gene transcription has also been

determined, for instance, in the case of the Human Cytomegalovirus (HCMV) [174]. HCMV has been found to activate the NF- $\kappa$ B pathway in the host which in turn promotes transcription from the HCMV major early immediate promoter, a process essential for HCMV pathogenesis [417]. In this regard, it has been shown that artesunate reduces NF- $\kappa$ B protein levels in the host, thereby blocking HCMV viral gene transcription [174]. Therefore, in our study, we went on to check whether the observed repression of MCPyV LT transcription by artesunate might be due to an influence of artesunate on NCCR-driven LT transcription. Our experiments using an NCCR reporter construct in MKL-1 cells showed that artesunate repressed expression from the early region (encoding the T antigens [31, 40]) while expression from the late region (encoding the coat proteins [31, 40]) was not affected suggesting that there might occur a specific regulation by artesunate on NCCR-driven early gene transcription. In this regard, similar experiments using such an MCPyV NCCR fluorescence reporter have shown that MCPyV NCCR-controlled early and late gene expression can differ based on the cellular context, suggesting differential bidirectional regulation of this promoter [418]. For instance, Ajuh and colleagues showed that following the transfection of this MCPyV NCCR fluorescence reporter construct into different cell types, while the highest expression from the early region occurred in skin-derived A375 cells, expression from the late region was the highest in cervix-derived HeLa cells [418]. Moreover, it is also well known that the MCPyV, like other DNA viruses, temporally regulates the expression of its early and late region genes by the NCCR upon infection [40, 356, 357]. While early proteins are expressed upon infection and are required to initiate viral replication, the late proteins are expressed post-replication so that the capsid proteins can aid in the progeny virion production [40, 356]. Therefore, it is possible that artesunate also bidirectionally regulates the MCPyV NCCR. Moreover, it would be interesting to understand whether artesunate regulates certain host cell transcription factors which might be involved in promoting transcription from the MCPyV NCCR as in the case of artesunate-induced HCMV gene repression [174]. Transcription factors such as NF- $\kappa$ B, NF-1 and Sp1 have been shown to regulate transcription from the promoters of other polyomaviruses like BK, JC and SV40 [41, 419-422]. However, despite *in silico* predictions revealing binding sites for these transcription factors within the MCPyV NCCR, it is not yet known whether these transcription factors mediate transcription from the MCPyV NCCR [41, 418]. Activation of the MAPK/ERK pathway has also been found to be important for MCPyV transcription, however, information is lacking regarding the transcription factors which might be activated by this pathway for MCPyV transcription [41, 125]. Therefore, further research is needed to obtain more information about the regulation of MCPyV transcription as it might prove valuable to further elucidate the mechanisms of transcriptional repression of LT by artesunate. Nevertheless, the role of MCPyV LT in autoregulating its expression from the NCCR has been described previously [48, 423, 424]. Several studies have shown that wildtype MCPyV LT represses its NCCR-controlled transcription [423, 424] while MCPyV truncated LT (tLT), on the other hand, stimulates the same [424]. Since our studies revealed that artesunate represses tLT in MCPyV-positive MCCs, it might be speculated that reduced tLT protein levels in the

cells might in turn result in the reduced stimulation of the NCCR thereby resulting in a decrease in LT transcription. A further study on bladder cancer showed that artesunate could induce a microRNA (miR-16) which inhibited the expression of COX2 (cyclooxygenase-2), a protein positively correlating with the growth of this cancer entity [362]. Therefore, a further possibility is that artesunate might post-transcriptionally regulate T antigen mRNA via the induction of MCPyV or host-derived inhibitory microRNAs, such as the MCPyV-derived MCV-miR-M1-5p, which is known to repress MCPyV LT expression [67, 69] and is therefore expressed at low levels in MCPyV-positive MCC tumors [69]. Interestingly, our subsequent overexpression experiments showed that LT protein which was overexpressed using an ectopic CMV promoter was also repressed by artesunate in two MCPyV-positive MCC cell lines. These results suggested that artesunate might additionally exert translational repression on the LT protein or affect its stability. In this regard, it has been shown that artesunate can exert an anti-cancer effect on malignant peripheral nerve sheath tumor cells by directly associating with and degrading TCTP (translationally controlled tumor protein), a protein correlating with tumorigenicity in neurofibromatosis type 1-associated tumors [425]. Therefore, similar mechanisms might exist in MCPyV-positive MCCs, wherein the oncoprotein LT might be targeted by artesunate for degradation. Nonetheless, since artesunate can repress HCMV transcription by modulating host cell proteins [174], a further possibility in the case of our experiment is that artesunate was able to repress CMV-derived transcription of ectopic LT also in the cellular context of MCCs. Importantly, our experiments showed that artesunate could exert a strong repression on LT upon exerting its cytotoxic effect on MCPyV-positive MCCs, transcriptionally and also potentially translationally. Once the details regarding the regulation of T antigen transcription and translation have been elucidated, the precise mechanism of this repression could be further investigated.

#### **4.2.4 Further mechanisms in addition to MCPyV T antigen repression are crucial in artesunate-induced cytotoxicity towards MCPyV-positive MCCs**

It is well known that cancer cells ensure their continued proliferation by deregulating the cell cycle [426]. Likewise, MCPyV-positive MCCs, express the oncoprotein LT which plays a crucial role in promoting cell cycle progression of these tumors [51, 70]. In most MCPyV-positive MCC cells, LT binds to and sequesters the pocket protein RB1 as a result of which the transcription factors of the E2F family can ensure continual entry of the tumor cells into the S phase of the cell cycle [51, 71]. In this regard, studies have shown that inhibition of the T antigens in MCPyV-positive MCCs results in decreased proliferation of these cells over time, cell cycle arrest in the G1 phase and subsequent cell death [70]. Therefore, upon observing a strong repression of LT by artesunate in our studies, we initially speculated that this might be the main mechanism of artesunate-induced growth inhibition of MCPyV-positive MCCs. Moreover, artesunate's cytotoxic and anti-proliferative effect towards certain cancer

entities has also frequently been associated with an inhibition of cell cycle progression [201, 427]. For instance, artesunate was found to reduce proliferation and induce cell cycle arrest in ovarian cancer cells by interfering with several important cell cycle regulatory proteins such as E2F-1 and cyclin D3 [427]. Interestingly, however, upon comparing cell death induced by T antigen knockdown with cell death induced by artesunate treatment in MCPyV-positive MCCs, we found that artesunate treatment was much more cytotoxic than T antigen knockdown over the time course studied. Moreover, only one of the three analyzed MCPyV-positive MCC cell lines (WaGa) was found to be sensitized by the presence of the T antigens to artesunate. These results implied that T antigen inhibition was not the sole mechanism of artesunate's cytotoxic action and that artesunate exerted further mechanisms in order to trigger cell death. Therefore, it is likely that other pathways promoting proliferation of MCPyV-positive MCCs independent of the T antigens are also affected by artesunate resulting in such a massive suppression of cell growth and induction of cell death. In this context, the PI3K/AKT/mTORC pathway is known to be upregulated in MCCs and promotes proliferation of these cells without correlating with the presence of the T antigens [428]. Interestingly artesunate is also known to induce cell death in cancer entities such as hepatocellular carcinoma cells and cervical carcinoma by inhibition of the PI3K/AKT/mTORC pathway [429, 430]. Therefore, it is possible that artesunate inhibits survival-promoting pathways such as the PI3K/AKT/mTORC pathway also in the cellular context of MCPyV-positive MCCs in addition to repressing T antigen expression. Furthermore, in several reports, artesunate has also been found to inhibit tumor growth and proliferation by directly promoting the induction of cell death pathways [202, 222]. For instance, as observed in human retinoblastoma cells, artesunate upregulated the expression of Kruppel-like factor 6 (KLF6) which promoted mitochondria-mediated apoptosis and KLF6 silencing inhibited artesunate-induced apoptosis [222]. Similarly, in another study in breast cancer cells, artesunate upregulated Beclin1, an initiator of autophagy and inhibition of Beclin1 attenuated artesunate-induced cell death [202]. Therefore, we also analyzed the association of artesunate with the induction of specific modes of cell death in MCPyV-positive MCCs in our study as discussed in the next section.

#### **4.2.5 Artesunate-induces ferroptosis in MCPyV-positive MCCs and does not depend on suppressing the FSP1 antioxidant pathway in these cells**

Research over the years has shown that artesunate, as an anti-cancer drug, can induce multiple modes of cell death depending upon the cellular context [201]. Apoptosis, ferroptosis, oncosis and autophagy are some of the forms of cell death often associated with artesunate-induced cellular cytotoxicity [186, 201, 202, 224, 225]. With respect to the modes of cell death observed in MCPyV-positive MCCs, studies have frequently demonstrated the induction of apoptosis following treatment with synthetic or small molecule inhibitors such as YM155, a survivin inhibitor or MAL3-

101, an HSP70 inhibitor, which target proteins that are crucial for the proliferation of these tumors [50, 431]. Nevertheless, our study argued against apoptosis being the major mode of cell death induced by artesunate in MCPyV-positive MCCs as observed by the lack of typical apoptotic signatures. While artesunate-induced apoptosis has been identified in cancer entities such as retinoblastoma and osteosarcoma via the activation of the caspases 3 and 9 [222, 432], the pan-caspase inhibitor Z-VAD-FMK failed to rescue artesunate-induced cell death in five different MCPyV-positive MCC cell lines in our study. Moreover, while apoptotic MCC cells have been characterized by the presence of nuclear condensation and fragmentation as well as the formation of apoptotic bodies [433], we observed cell swelling with increased cellular volume following artesunate treatment of two MCPyV-positive non-spheroidal MCC cell lines. In addition, the cell viability assays comparing cell death between the cell cycle analysis and trypan blue staining also supported the occurrence of another form of cell death distinct from apoptosis, especially induced at higher concentrations of artesunate treatment for the majority of MCPyV-positive MCC cell lines analyzed.

Interestingly, upon investigating other potential modes of cell death, our studies identified the involvement of ferroptosis, a more recently described caspase-independent and non-apoptotic form of cell death [227, 291], as the main mode of cell death induced by artesunate in MCPyV-positive MCCs. The swollen morphology of artesunate-treated MCPyV-positive MCCs cells provided the first hints regarding a ferroptotic mode of cell death [232]. This observation was in line with a previous study which described extensive cell swelling followed by rupture in chronic myelogenous leukemia cells treated with the ferroptosis-inducing agents ferric ammonium citrate (FAC) and buthionine sulfoxamine (BSO) [232]. Biochemically, ferroptosis is characterized by iron accumulation and lipid peroxidation [244, 257, 434]. In this regard, in several cancer entities such as pancreatic cancer and hepatocellular carcinoma, the induction of ferroptosis by artesunate was confirmed by the use of ferroptosis inhibitors including iron chelators and antioxidants which interfere with these typical biochemical features of ferroptosis [186, 370]. On similar lines, we checked for the inhibitory role of a panel of ferroptosis inhibitors targeting various aspects of the ferroptotic pathway in artesunate-induced cell death of MCPyV-positive MCCs. We found that both the iron chelator deferoxamine (DFO) [435] and the potent antioxidant and lipid peroxide inhibitor ferrostatin-1 (Fer-1) [227] blocked artesunate-induced cell death in all five tested MCPyV-positive MCC cell lines, suggesting the involvement of iron and lipid peroxides in this cell death process. Our findings were consistent with previous work in pancreatic ductal adenocarcinoma cells where iron-dependent and lipid peroxide-associated ferroptosis was found to be induced by artesunate and a rescue from cell death was observed upon using DFO and Fer-1 [186]. Moreover, in four of the five cell lines analyzed, we also found that the lysosomal vacuolar-type H(+)-ATPase inhibitor, BAF-A1 [265] protected the cells from artesunate-induced cell death suggesting that functional lysosomes are also crucial for artesunate-induced cytotoxicity in MCPyV-positive MCC cells. The importance of functional lysosomes for the ferroptotic process in cancer cells has already been

described [261] and in this regard, the use of BAF-A1 was found to protect cancer cell types such as pancreatic ductal adenocarcinoma from ferroptosis induced by erastin [266]. Interestingly, BAF-A1 is also known to inhibit autophagy [436], another mode of cell death which involves lysosomes [437], suggesting a link between ferroptosis and autophagy. Accordingly, in studies using the ferroptosis inducer erastin in human fibrosarcoma cells, autophagy was detected and was found to promote ferroptotic cell death [262, 267]. Furthermore, in another study, artesunate-induced ferroptosis in hepatocellular carcinoma could be inhibited not only with BAF-A1 but also with other inhibitors of autophagy [370] suggesting the involvement of autophagy in parallel with ferroptosis. Nevertheless, another report contradicting these studies showed that dihydroartemisinin, an active metabolite derived from artesunate [438, 439], induced a ferroptotic mode of cell death involving the lysosomes which was however independent of autophagy in human fibrosarcoma cells [440]. Therefore, future studies analyzing the involvement of crucial autophagy genes such as *ATG5* and *ATG7* [262, 441] upon artesunate treatment in the cellular context of MCPyV-positive MCCs could be performed to explore the contribution of autophagy to artesunate-induced ferroptosis in these cells.

Our experiments with the first set of ferroptosis inhibitors targeting iron, lysosomes and lipid peroxides [227, 266] suggested that artesunate induces a ferroptotic mode of cell death in MCPyV-positive MCCs. Our findings were further supported by using the next set of ferroptosis inhibitors targeting enzymes aiding in the generation of substrates which promote ferroptotic damage [270, 276]. In this regard, several studies have established a positive correlation of ACSL4 (acyl-CoA synthetase long-chain family member 4) with ferroptosis in cancer cells [276, 277]. ACSL4 is responsible for the synthesis of fatty acyl CoA variants, which are ideal substrates for lipid peroxidation, which in turn promotes ferroptosis [276, 277]. ACSL4 expression has been found to sensitize human hepatocellular carcinoma cells and human promyelocytic leukemia cells to ferroptosis induced by erastin [276] and breast cancer cells to ferroptosis induced by RSL3 [277]. Moreover, pharmacological inhibition of ACSL4 with Rosiglitazone [442] has also been found to delay mortality *in vivo* in a ferroptosis mouse model [277]. In accordance with these studies, we observed a rescue from artesunate-induced cell death in all three tested MCPyV-positive MCC cell lines upon co-treatment with Rosiglitazone. Therefore, our results further supported the occurrence of lipid peroxide-mediated ferroptosis by artesunate in MCPyV-positive MCCs. Moreover, vitamin E, the inhibitor of lipoxygenase (LOX) enzymes which generate ferroptosis-promoting oxygenated phospholipids [270, 284], also protected all five tested MCPyV-positive MCC cell lines from artesunate-induced cell death. Similar studies, demonstrating a protective role of vitamin E from ferroptotic damage induced by LOXs have been observed in GPX4 (a crucial antioxidant preventing ferroptosis [289])-deficient mouse embryonic fibroblasts [270]. Therefore, our experiments also suggested the involvement of LOX enzymes in artesunate-induced MCPyV-positive MCC cytotoxicity.

A crucial antioxidant pathway that has been described to prevent ferroptosis is the amino acid heterodimeric antiporter, System X<sub>c</sub><sup>-</sup>, which imports cystine to ultimately generate a potent antioxidant, GPX4, that prevents lipid peroxidation [375, 443]. Several well-known ferroptosis inducers have been described to target this antiporter or its downstream antioxidants upon promoting ferroptosis [227, 280, 444]. For instance, while erastin targets System X<sub>c</sub><sup>-</sup> by potentially regulating the levels of one of its components (SLC7A11) [227], RSL3 binds to and inactivates the antioxidant GPX4 [289, 444]. Interestingly, in this context, β-mercaptoethanol, a promoter of cystine uptake [294], has been found to rescue ferroptosis induced by erastin but not RSL3 as studied in fibrosarcoma cells [227, 280, 445]. In our study, all five tested MCPyV-positive MCC cell lines were protected from artesunate-induced cell death upon addition of β-mercaptoethanol to the medium. Therefore, not only did our experiment further confirm the induction of ferroptosis by artesunate in our cells but also suggested that artesunate might function similar to erastin and potentially inhibit one or more components of System X<sub>c</sub><sup>-</sup> [227]. Moreover, our studies also implicated the involvement of the crucial ferroptosis relevant-antioxidant system, System X<sub>c</sub><sup>-</sup>, [375, 443] in artesunate-induced cell death of MCPyV positive MCCs.

Interestingly, our assays to identify a specific mode of artesunate-induced cell death also revealed that the cell line MKL-2 deviated often from the responses observed in the other MCPyV-positive MCC cell lines. The trypan blue assays for cell viability showed that MKL-2 cells were more resistant to artesunate-induced cell death as compared to the other cell lines. Reports on the doubling time of these MCPyV-positive MCC cell lines have shown that MKL-2 cells have a slightly longer doubling time (three to five days as per two different studies) as compared to the more sensitive cell lines such as MKL-1 (two to three days as per two different studies) [70, 303]. In this regard, it has been shown that artesunate is more cytotoxic towards rapidly proliferating cells [205] which might serve as an explanation for this observation. Moreover, MKL-2 cells also exhibited a tendency towards an apoptotic mode of cell death which was not the case for the other cell lines. In this regard, artesunate has also been found to induce more than one form of cell death as observed in one study in ovarian cancer where caspase-dependent apoptosis and caspase-independent ferroptosis was evidenced [427]. Therefore, despite ferroptosis being the prominent mode of cell death, there might also be low levels of apoptosis induced by artesunate in MKL-2 cells.

In our study, we also found that the GPX4-independent FSP1–CoQ10–NAD(P)H antioxidant pathway [269, 295, 296, 446] did not play a crucial role in artesunate-induced ferroptosis in MCPyV-positive MCCs. It is known that myristoylated FSP1 in the plasma membrane functions to convert coenzyme Q10 (ubiquinone) to ubiquinol, a potent antioxidant that counteracts lipid peroxidation and importantly, functions independent of GPX4 [269, 295, 296]. The expression levels of FSP1 have been described to positively correlate with resistance to ferroptosis in many cancer cell lines as per data mined from the Cancer Therapeutics Response Portal (CTRP) [296, 447]. For instance, analysis of several lung cancer cell lines showed that those expressing

low levels of FSP1 were more sensitive to RSL3-induced ferroptosis as compared to those expressing higher levels of FSP1 [296]. Accordingly, overexpression of FSP1 in the sensitive cells increased their resistance to RSL3-induced ferroptosis by 10-20 fold [296]. Although we detected low levels of *FSP1* mRNA in MCPyV-positive MCC cell lines in our study, FSP1 overexpression did not increase their resistance to artesunate-induced ferroptosis, contrary to previously described reports [295, 296] suggesting that artesunate-induced ferroptosis in MCPyV-positive MCCs does not depend on suppression of the FSP1–CoQ10–NAD(P)H antioxidant pathway [295, 446]. It is known that FSP1 requires coenzyme Q10 in order to generate antioxidants for the mitigation of lipid peroxidation [296]. In this regard, low levels of coenzyme Q10 have been detected in other skin cancer types such as in melanoma cells as well as in the blood of melanoma patients [448-450]. Therefore, future studies could investigate whether MCPyV-positive MCCs also express low levels of coenzyme Q10, in which case, the failure of FSP1 overexpression to rescue artesunate-induced ferroptosis in these cells might be explained. In another study, the MDM2-MDMX complex, which normally functions to suppress the tumor suppressor p53's function [451], was found to promote ferroptosis (independent of p53) by altering the lipid profile of cells [452]. Importantly, this complex was found to negatively regulate FSP1 expression levels and the authors implicate a potential regulation of this complex on the stability of FSP1 [452]. Inhibition MDM2 or MDM4 was found to result in elevated levels of FSP1 and a concomitant increase in reduced coenzyme Q10 which helped to suppress ferroptosis [452]. Interestingly, the small T antigen expressed in MCPyV-positive MCCs is known to upregulate MDM2 expression and MDM4 is also known to be overexpressed in MCPyV-positive MCCs [103]. Therefore, is it possible that MDM2 and MDM4 interfere with FSP1 expression and/or stability in MCPyV-positive MCCs, which might explain the observed low levels of endogenous FSP1 expression in these cell lines and the lack of protection of overexpressed FSP1 from artesunate-induced ferroptosis in our study. In a subsequent experiment, we also observed increased survival in RSL3-treated MCPyV-positive MCCs overexpressing wild type FSP1 as compared to the corresponding parental cells and those overexpressing mutant FSP1. This was consistent with findings from several reports in the literature which have demonstrated the rescue of RSL3-induced ferroptosis in FSP1 overexpressing cancer cells such as fibrosarcoma and lung cancer cells [295, 296] as well as FSP1 overexpressing mouse embryonic fibroblasts with a knockout of GPX4 [295, 453, 454]. These results, on the other hand, indicate that it might indeed be possible to activate the FSP1 antioxidant pathway in MCPyV-positive MCCs. In addition, these results also suggest that FSP1 overexpression in MCPyV-positive MCCs might rescue these cells from ferroptosis induced by RSL3 but not artesunate. In this regard, it is known that different ferroptosis inducers can function differentially to target one or more antioxidant pathways upon promoting the induction of ferroptosis [280, 455]. While most ferroptosis inducers like erastin, RSL3, FIN56 and FINO<sub>2</sub> induce ferroptosis by suppressing the crucial antioxidant GPX4 [227, 280, 289, 456, 457], some of these inducers additionally target further antioxidants in the process [280, 456]. For instance, while RSL3 induces ferroptosis primarily by inhibiting the antioxidant GPX4 [289], the

other potent ferroptosis inducer FIN56, can induce ferroptosis by degradation of GPX4 as well as by depletion of the antioxidant enzyme coenzyme Q10 [456]. Our studies already implicated a role for artesunate in suppressing the GPX4 generating antiporter System X<sub>c</sub><sup>-</sup> [289, 375] in MCPyV-positive MCCs. It is possible that artesunate might additionally possess the ability to deplete coenzyme Q10 in MCPyV-positive MCCs which might explain the inability of FSP1 overexpression to rescue artesunate-induced ferroptosis in these cells. Upstream activators of coenzyme Q10 synthesis such as farnesyl pyrophosphate [456, 458, 459] could be combined with artesunate treatment of FSP1 overexpressing MCPyV-positive MCCs in future experiments to look for a protection from artesunate-induced ferroptosis in MCPyV-positive MCCs. Thereby, the lack of involvement of the FSP1 antioxidant pathway in artesunate-induced ferroptosis of MCPyV-positive MCCs might be further investigated.

Taken together, our study showed that ferroptosis is the main mode of cell death induced by artesunate in MCPyV-positive MCC cells and we also found that the suppression of the FSP1 antioxidant pathway is not crucial for this process.

#### **4.2.6 The tumor suppressor protein p53 does not promote artesunate-induced ferroptosis in MCPyV-positive MCCs**

The tumor suppressor protein p53 which is largely known for its ability to suppress tumor growth by inducing cell cycle arrest and apoptosis [460, 461] is frequently mutated in several cancer entities [462, 463]. In the majority of MCPyV-positive MCCs on the other hand, p53 is expressed in its wild type form which however, exhibits only limited transcriptional activity, insufficient to restrict tumor proliferation [102]. In this context, reactivation p53 transcriptional activity by the inhibition of MDM2 and MDM4 (inhibitors of p53) in MCPyV-positive MCCs has been shown to promote cell cycle arrest and apoptosis of these tumor cells [102, 103] showing that p53 can induce cell death also in the cellular context of MCPyV-positive MCCs. Interestingly, MKL-2 cells lack p53 protein expression [102] and our studies showed that this cell line was the most resistant to artesunate-induced ferroptosis which led us to analyze whether p53 might positively contribute also to a ferroptotic mode of cell death induced by artesunate in our cells. In this regard, studies have shown that p53 can indeed also promote ferroptosis in several cancer entities [243, 464, 465]. For instance, overexpression of wild type p53 in ovarian cancer cells was found to downregulate the expression of ferroptosis-preventive proteins such as xCT and GPX4 and thereby p53 was found to synergize with superparamagnetic iron oxide treatment to promote ferroptosis [464]. Moreover, p53 has also been described to promote ferroptosis by suppressing transcription of *SLC7A11*, one of the components of System X<sub>c</sub><sup>-</sup>, a crucial antioxidant generating amino acid antiporter [243]. Interestingly, our experiments using β-mercaptoethanol as a ferroptosis inhibitor also implicated a role for System X<sub>c</sub><sup>-</sup> in preventing artesunate-induced ferroptosis of MCPyV-positive MCCs, which

further served as a basis for testing for a pro-ferroptotic role for p53. Nevertheless, contrary to our speculations and findings from some previous reports [243, 464], we found that p53 did not promote artesunate-induced ferroptosis in MCPyV-positive MCCs. We initially found that artesunate did not increase the transcriptional activity of p53 in MCPyV-positive MCCs, however, p53 expression persisted in the MCPyV-positive MCC cell lines in the presence of artesunate, implicating a potential role of this protein in artesunate-induced ferroptosis. Nevertheless, p53 knockdown did not rescue artesunate-induced ferroptosis in MCPyV-positive MCC cell lines, suggesting that artesunate-induced ferroptosis could occur independent of the presence of p53 in these cells. Our studies were similar to previous reports analyzing the role of p53 in artesunate-induced cellular cytotoxicity [205]. Although the authors did not specifically analyze artesunate-induced ferroptosis, they found that artesunate-induced inhibition of proliferation did not significantly differ between wildtype and p53 knockout colon cancer cells showing that artesunate could exert its cytotoxic effects in the presence and absence of p53 in the context of these cells [205]. However, in a study in renal carcinoma cell lines, artesunate was found to specifically induce ferroptosis in those cell lines expressing p53 [465]. Therefore, artesunate can induce both p53-dependent and independent pathways for tumor cell inhibition [205, 465]. With respect to the role of p53 in ferroptosis, it is known to be highly context-dependent, varying with the cellular context as well as with the ferroptosis inducer used [300, 302]. Interestingly, in this regard, studies have demonstrated a p53-independent ferroptosis-promoting role of MDM2 and MDM4 in human fibrosarcoma and hepatocellular carcinoma cell lines [300, 452]. The authors showed that the inhibition of MDM2 and MDM4 in these cell lines in the context of both p53-wildtype and knockout backgrounds, prevented ferroptosis induced by imidazole ketone erastin [452]. As discussed in section 4.2.5, MCPyV-positive MCCs indeed express high levels of MDM2 and MDM4 [103] and therefore, it might be speculated that this in turn could sensitize them to p53-independent, artesunate-induced ferroptosis [300]. The role of mutant p53 with regards to the sensitivity of tumor cells to anti-cancer drugs has also been studied [205]. In this respect, analysis of the ferroptosis-sensitizing ability of p53 in a panel of colorectal cancer cells showed that cell lines expressing mutant p53 were strongly sensitized to erastin-induced ferroptosis as compared to those expressing wild type p53 [302]. It was observed that knock-in of a p53 hotspot mutation (R175H) in the wild type p53 expressing cell lines, restored their sensitivity to ferroptosis [302]. On the other hand, a study in a panel of 55 artesunate-sensitive cancer cell lines of the NCI (National Cancer Institute) showed that p53 mutational status of these cells did not correlate with the IC<sub>50</sub> values for artesunate [205]. Therefore, experiments addressing the sensitivity of MCPyV-positive MCCs overexpressing mutant p53 to artesunate-induced ferroptosis might be performed in the future to further understand the contribution of p53 mutational status in the context of artesunate-induced ferroptosis in MCPyV-positive MCCs. Importantly, p53 is also known to suppress ferroptosis in certain cancer cell types [301, 302]. For instance, the authors who identified the pro-ferroptotic role of mutant p53 in colorectal cancer cells found that wild type p53 in fact inhibited erastin-induced ferroptosis in these cells by binding to and blocking the

activity of the lipid peroxidation-promoting protease DPP4 [302]. The authors describe the p53 wild type cells in their study as resistant to artesunate [302] which however was contrary to our study wherein the wild type p53-expressing MCPyV-positive MCCs were highly sensitive to artesunate. Therefore, while it appears unlikely that wild type p53 might suppress artesunate-induced ferroptosis in the context of MCPyV-positive MCCs, future studies might also address this question by looking for a decrease in the sensitivity of wildtype p53 overexpressing MCPyV-positive MCCs to artesunate-induced ferroptosis. In conclusion, taking into account that p53 has multifaceted roles in the context of ferroptosis induction, our study points towards the lack of a pro-ferroptotic role of p53 in artesunate-induced cell death of MCPyV-positive MCCs.

#### **4.2.7 First positive indications for the potential use of artesunate in combinatorial MCPyV-positive MCC immunotherapy**

Our studies showed that artesunate was highly effective in inhibiting MCPyV-positive MCC cell lines *in vitro* and MCPyV-positive MCC xenografts *in vivo* identifying it as a potential compound for future MCC therapies. Notably, new candidate anti-cancer drugs are frequently tested to ensure that they do not interfere with chemotherapeutic drugs or immunotherapeutic regimens already used to treat a specific cancer type [466-468]. Therefore, we also investigated whether artesunate might affect the currently most effective approach for the treatment of MCC, i.e. immunotherapy with checkpoint inhibiting antibodies [147, 148, 379]. In fact, artesunate has already been shown to demonstrate synergistic anti-tumor effects when used in combination with chemotherapeutic drugs like cisplatin for the treatment of lung cancer [469] and carboplatin for the treatment of non-small cell lung cancer [470]. Furthermore, artemisinin and some of its derivatives have also been found to harmonize with immune therapy *in vivo* [471, 472]. For instance, dihydroartemisinin in combination with the chemotherapeutic drug oxaliplatin was found to synergize with anti-PD-L1 antibody treatment to eradicate colorectal cancers in mice [472]. A similar observation was also made upon combining artemisinin and anti-PD-L1 monoclonal antibody therapy which efficiently reduced the growth of T-cell lymphoma tumors in mice [471]. With respect to artesunate's role in immunomodulation, both pro and anti-immunogenic functions have been described [191, 215, 473-477]. Human primary monocytes pretreated with artesunate were found to convert into an inflammatory phenotype and enhanced apoptosis of leukemia cells [473]. However, in models of sepsis and neuroinflammation, artesunate was found to attenuate pro-inflammatory cytokine release [475, 476]. In our study, artesunate did not interfere with externally induced immune stimulation in MCPyV-positive MCCs, thereby providing the first positive indications regarding its potential use in combinatorial MCPyV-positive MCC immunotherapy. The influence of artesunate on some crucial immune-relevant molecules, i.e. human MHC class I molecules (human leukocyte antigen HLA-A,-B,-C) [478] and PD-L1 [479], was analyzed in this study. Notably, PD-L1 is often

expressed by several cancers as a mechanism to evade the host immune system [479, 480] and in this regard, studies have already shown the ability of dihydroartemisinin to inhibit PD-L1 expression in non-small cell lung cancer cell lines and mice models [481]. PD-L1 is also expressed by MCPyV-positive MCCs [146] which serves as the basis for anti-PD-L1 immunotherapies such as avelumab [148, 151]. Although, in our study, we did not observe artesunate-induced inhibition of PD-L1 as previously observed for dihydroartemisinin [481], we found that artesunate treatment alone did not result in a substantial upregulation of PD-L1 in the MCPyV-positive MCC cell lines analyzed. This observation was a positive indication that artesunate might not compromise MCPyV-positive MCC immunotherapies by upregulating expression of this immune suppressive marker on MCPyV-positive MCCs. With respect to MHC class I molecules, since they primarily function to present immunogenic peptides to cytotoxic CD8+ T cells to promote immune responses [478], their expression is downregulated in 40-90% of human cancers [482]. MHC class I expression is also downregulated in MCPyV-positive MCC tumors [141]. Nevertheless, this downregulation is reversible and treatment with immune response-stimulating cytokines such as interferon gamma (IFN- $\gamma$ ) have been shown to increase MHC class I expression in MCPyV-positive MCCs [141, 380, 483]. Similarly, in our study, we could reproduce the previously observed upregulation of MHC class I (HLA) expression upon IFN- $\gamma$  treatment in most MCPyV-positive MCC cell lines analyzed. Importantly, MCC immunotherapies, for instance those involving PD-L1 inhibition with avelumab, are often associated with increases in pro-inflammatory cytokines like IFN- $\gamma$  [484, 485]. Therefore, in this context, a crucial finding in our study was that artesunate, when used in combination with IFN- $\gamma$ , did not suppress IFN- $\gamma$ -induced upregulation of HLA expression, implicating that artesunate might not interfere with this aspect of activation of an immune response. Moreover, our finding that artesunate induces ferroptosis in MCPyV-positive MCCs has also to be noted with respect to immune therapy since a pro-inflammatory and immunogenic role of ferroptosis in the context of diseases such as alcoholic liver disease [486] and ischemia-reperfusion injury [487, 488] has already been demonstrated. Therefore, although the role of ferroptosis in inflammation and immunity is still under exploration [489], it is likely that artesunate might not hinder or even support immune responses towards MCPyV-positive MCCs. In summary, the results from our experiments as well as reported evidence suggest that artesunate might be used in combination with current immunotherapies to treat MCPyV-positive MCC [484].

#### **4.2.8 Conclusion**

In conclusion, our study highlights the potential of the safe, efficient and cost-effective anti-malarial drug, artesunate for the treatment of MCPyV-positive MCC. Following further research regarding its use in combination with immunotherapy, it might be considered for its inclusion in clinical trials for testing its efficacy in MCPyV-positive MCC patients.

## **5. References**

1. Yousef, H., M. Alhajj, and S. Sharma, *Anatomy, Skin (Integument), Epidermis*, in *StatPearls*. 2021, StatPearls Publishing

Copyright © 2021, StatPearls Publishing LLC.: Treasure Island (FL).

2. Kolarsick, P.A.J., M.A. Kolarsick, and C. Goodwin, *Anatomy and Physiology of the Skin*. Journal of the Dermatology Nurses' Association, 2011. **3**(4).
3. Watt, F.M., *Mammalian skin cell biology: at the interface between laboratory and clinic*. Science, 2014. **346**(6212): p. 937-40.
4. Reichelt, J., et al., *Formation of a normal epidermis supported by increased stability of keratins 5 and 14 in keratin 10 null mice*. Molecular biology of the cell, 2001. **12**(6): p. 1557-1568.
5. Santos, M., et al., *The expression of keratin k10 in the basal layer of the epidermis inhibits cell proliferation and prevents skin tumorigenesis*. J Biol Chem, 2002. **277**(21): p. 19122-30.
6. Fuchs, E. and H. Green, *Changes in keratin gene expression during terminal differentiation of the keratinocyte*. Cell, 1980. **19**(4): p. 1033-42.
7. Moll, I., *Merkel cell distribution in human hair follicles of the fetal and adult scalp*. Cell Tissue Res, 1994. **277**(1): p. 131-8.
8. Delevoye, C., *Melanin Transfer: The Keratinocytes Are More than Gluttons*. Journal of Investigative Dermatology, 2014. **134**(4): p. 877-879.
9. Clayton, K., et al., *Langerhans Cells—Programmed by the Epidermis*. Frontiers in Immunology, 2017. **8**(1676).
10. Heath, W.R. and F.R. Carbone, *The skin-resident and migratory immune system in steady state and memory: innate lymphocytes, dendritic cells and T cells*. Nature Immunology, 2013. **14**(10): p. 978-985.
11. Blanpain, C. and E. Fuchs, *Epidermal stem cells of the skin*. Annual review of cell and developmental biology, 2006. **22**: p. 339-373.
12. Boehnke, K., et al., *Stem cells of the human epidermis and their niche: composition and function in epidermal regeneration and carcinogenesis*. Carcinogenesis, 2012. **33**(7): p. 1247-1258.
13. Nguyen, M.B., et al., *FGF signalling controls the specification of hair placode-derived SOX9 positive progenitors to Merkel cells*. Nature Communications, 2018. **9**(1): p. 2333.
14. Woo, S.-H., et al., *Identification of epidermal progenitors for the Merkel cell lineage*. Development (Cambridge, England), 2010. **137**(23): p. 3965-3971.
15. Doucet, Yanne S., et al., *The Touch Dome Defines an Epidermal Niche Specialized for Mechanosensory Signaling*. Cell Reports, 2013. **3**(6): p. 1759-1765.
16. Erickson, J.R. and K. Echeverri, *Learning from regeneration research organisms: The circuitous road to scar free wound healing*. Developmental biology, 2018. **433**(2): p. 144-154.
17. Peterson, S.C., et al., *Basal cell carcinoma preferentially arises from stem cells within hair follicle and mechanosensory niches*. Cell Stem Cell, 2015. **16**(4): p. 400-12.
18. Houben, R., D. Schrama, and J.C. Becker, *Molecular pathogenesis of Merkel cell carcinoma*. Experimental Dermatology, 2009. **18**(3): p. 193-198.
19. Toker, C., *Trabecular carcinoma of the skin*. Arch Dermatol, 1972. **105**(1): p. 107-10.
20. Rywlin, A.M., *Malignant Merkel-cell tumor is a more accurate description than trabecular carcinoma*. Am J Dermatopathol, 1982. **4**(6): p. 513-5.
21. Toker, C., *Trabecular carcinoma of the skin. A question of title*. Am J Dermatopathol, 1982. **4**(6): p. 497-500.

22. Miller, R.W. and C.S. Rabkin, *Merkel Cell Carcinoma and Melanoma: Etiological Similarities and Differences*. *Cancer Epidemiology Biomarkers & Prevention*, 1999. **8**(2): p. 153.
23. Pellitteri, P.K., et al., *Merkel cell carcinoma of the head and neck*. *Head Neck*, 2012. **34**(9): p. 1346-54.
24. DeCaprio, J.A., *Molecular Pathogenesis of Merkel Cell Carcinoma*. *Annu Rev Pathol*, 2021. **16**: p. 69-91.
25. Zwijnenburg, E.M., et al., *Merkel Cell Carcinoma: New Trends*. *Cancers (Basel)*, 2021. **13**(7).
26. Paulson, K.G., et al., *Merkel cell carcinoma: Current US incidence and projected increases based on changing demographics*. *Journal of the American Academy of Dermatology*, 2018. **78**(3): p. 457-463.e2.
27. Schadendorf, D., et al., *Merkel cell carcinoma: Epidemiology, prognosis, therapy and unmet medical needs*. *European Journal of Cancer*, 2017. **71**: p. 53-69.
28. Harms, K.L., et al., *Analysis of Prognostic Factors from 9387 Merkel Cell Carcinoma Cases Forms the Basis for the New 8th Edition AJCC Staging System*. *Ann Surg Oncol*, 2016. **23**(11): p. 3564-3571.
29. Buonerba, L., et al., *Hematological Toxicity During Concomitant Treatment With Ruxolitinib and Avelumab for Merkel Cell Carcinoma*. *Frontiers in Oncology*, 2020. **10**(1849).
30. Engels, E.A., et al., *Merkel cell carcinoma and HIV infection*. *Lancet*, 2002. **359**(9305): p. 497-498.
31. Feng, H., et al., *Clonal integration of a polyomavirus in human Merkel cell carcinoma*. *Science*, 2008. **319**(5866): p. 1096-100.
32. Kassem, A., et al., *Frequent detection of Merkel cell polyomavirus in human Merkel cell carcinomas and identification of a unique deletion in the VP1 gene*. *Cancer Res*, 2008. **68**(13): p. 5009-13.
33. Becker, J.C., et al., *MC Polyomavirus Is Frequently Present in Merkel Cell Carcinoma of European Patients*. *Journal of Investigative Dermatology*, 2009. **129**(1): p. 248-250.
34. Bhatia, K., et al., *Merkel cell carcinoma subgroups by Merkel cell polyomavirus DNA relative abundance and oncogene expression*. *International Journal of Cancer*, 2010. **126**(9): p. 2240-2246.
35. Wong, S.Q., et al., *UV-Associated Mutations Underlie the Etiology of MCV-Negative Merkel Cell Carcinomas*. *Cancer Res*, 2015. **75**(24): p. 5228-34.
36. Goh, G., et al., *Mutational landscape of MCPyV-positive and MCPyV-negative Merkel cell carcinomas with implications for immunotherapy*. *Oncotarget*, 2016. **7**(3): p. 3403-15.
37. Harms, P.W., et al., *The Distinctive Mutational Spectra of Polyomavirus-Negative Merkel Cell Carcinoma*. *Cancer research*, 2015. **75**(18): p. 3720-3727.
38. Knepper, T.C., et al., *The Genomic Landscape of Merkel Cell Carcinoma and Clinicogenomic Biomarkers of Response to Immune Checkpoint Inhibitor Therapy*. *Clinical cancer research : an official journal of the American Association for Cancer Research*, 2019. **25**(19): p. 5961-5971.
39. John, R., et al., *Taxonomical developments in the family Polyomaviridae*. *Archives of virology*, 2011. **156**(9): p. 1627-1634.
40. Spurgeon, M.E. and P.F. Lambert, *Merkel cell polyomavirus: a newly discovered human virus with oncogenic potential*. *Virology*, 2013. **435**(1): p. 118-130.
41. Yang, J.F. and J. You, *Regulation of Polyomavirus Transcription by Viral and Cellular Factors*. *Viruses*, 2020. **12**(10): p. 1072.
42. Coursaget, P., et al., *Human Merkel cell polyomavirus: virological background and clinical implications*. *APMIS*, 2013. **121**(8): p. 755-769.
43. Carter, J.J., et al., *Identification of an overprinting gene in Merkel cell polyomavirus provides evolutionary insight into the birth of viral genes*. *Proceedings of the National Academy of Sciences*, 2013. **110**(31): p. 12744.

44. Pietropaolo, V., C. Prezioso, and U. Moens, *Merkel Cell Polyomavirus and Merkel Cell Carcinoma*. *Cancers*, 2020. **12**(7): p. 1774.
45. Shuda, M., et al., *T antigen mutations are a human tumor-specific signature for Merkel cell polyomavirus*. *Proc Natl Acad Sci U S A*, 2008. **105**(42): p. 16272-7.
46. Wendzicki, J.A., P.S. Moore, and Y. Chang, *Large T and small T antigens of Merkel cell polyomavirus*. *Current opinion in virology*, 2015. **11**: p. 38-43.
47. Kwun, H.J., et al., *The minimum replication origin of merkel cell polyomavirus has a unique large T-antigen loading architecture and requires small T-antigen expression for optimal replication*. *Journal of virology*, 2009. **83**(23): p. 12118-12128.
48. Nwogu, N., L.E. Ortiz, and H.J. Kwun, *Merkel Cell Polyomavirus Large T Antigen Unique Domain Regulates Its Own Protein Stability and Cell Growth*. *Viruses*, 2020. **12**(9).
49. Liu, X., et al., *Merkel cell polyomavirus large T antigen disrupts lysosome clustering by translocating human Vam6p from the cytoplasm to the nucleus*. *The Journal of biological chemistry*, 2011. **286**(19): p. 17079-17090.
50. Arora, R., et al., *Survivin is a therapeutic target in Merkel cell carcinoma*. *Science translational medicine*, 2012. **4**(133): p. 133ra56-133ra56.
51. Hesbacher, S., et al., *RB1 is the crucial target of the Merkel cell polyomavirus Large T antigen in Merkel cell carcinoma cells*. *Oncotarget*, 2016. **7**(22): p. 32956-68.
52. Schrama, D., et al., *Serine 220 phosphorylation of the Merkel cell polyomavirus large T antigen crucially supports growth of Merkel cell carcinoma cells*. *Int J Cancer*, 2016. **138**(5): p. 1153-62.
53. Houben, R., et al., *Characterization of functional domains in the Merkel cell polyoma virus Large T antigen*. *Int J Cancer*, 2015. **136**(5): p. E290-300.
54. Harrison, C.J., et al., *Asymmetric assembly of Merkel cell polyomavirus large T-antigen origin binding domains at the viral origin*. *J Mol Biol*, 2011. **409**(4): p. 529-42.
55. Li, J., et al., *Phosphorylation of Merkel cell polyomavirus large tumor antigen at serine 816 by ATM kinase induces apoptosis in host cells*. *The Journal of biological chemistry*, 2015. **290**(3): p. 1874-1884.
56. Cheng, J., et al., *Merkel cell polyomavirus large T antigen has growth-promoting and inhibitory activities*. *Journal of virology*, 2013. **87**(11): p. 6118-6126.
57. Li, J., et al., *Merkel Cell Polyomavirus Large T Antigen Disrupts Host Genomic Integrity and Inhibits Cellular Proliferation*. *Journal of Virology*, 2013. **87**(16): p. 9173.
58. Kwun, H.J., et al., *Restricted protein phosphatase 2A targeting by Merkel cell polyomavirus small T antigen*. *Journal of virology*, 2015. **89**(8): p. 4191-4200.
59. Chen, W., et al., *Identification of specific PP2A complexes involved in human cell transformation*. *Cancer Cell*, 2004. **5**(2): p. 127-36.
60. Shuda, M., et al., *Human Merkel cell polyomavirus small T antigen is an oncoprotein targeting the 4E-BP1 translation regulator*. *The Journal of clinical investigation*, 2011. **121**(9): p. 3623-3634.
61. Verhaegen, M.E., et al., *Merkel Cell Polyomavirus Small T Antigen Initiates Merkel Cell Carcinoma-like Tumor Development in Mice*. *Cancer Res*, 2017. **77**(12): p. 3151-3157.
62. Kwun, H.J., et al., *Merkel cell polyomavirus small T antigen controls viral replication and oncoprotein expression by targeting the cellular ubiquitin ligase SCFFbw7*. *Cell host & microbe*, 2013. **14**(2): p. 125-135.
63. Dye, K.N., et al., *Merkel cell polyomavirus Tumor antigens expressed in Merkel cell carcinoma function independently of the ubiquitin ligases Fbw7 and  $\beta$ -TrCP*. *PLoS pathogens*, 2019. **15**(1): p. e1007543-e1007543.
64. Nwogu, N., L.E. Ortiz, and H.J. Kwun, *Surface charge of Merkel cell polyomavirus small T antigen determines cell transformation through allosteric FBW7 WD40 domain targeting*. *Oncogenesis*, 2020. **9**(5): p. 53.

65. Griffiths, D.A., et al., *Merkel Cell Polyomavirus Small T Antigen Targets the NEMO Adaptor Protein To Disrupt Inflammatory Signaling*. Journal of Virology, 2013. **87**(24): p. 13853.
66. Knight, L.M., et al., *Merkel Cell Polyomavirus Small T Antigen Mediates Microtubule Destabilization To Promote Cell Motility and Migration*. Journal of Virology, 2015. **89**(1): p. 35.
67. Seo, G.J., C.J. Chen, and C.S. Sullivan, *Merkel cell polyomavirus encodes a microRNA with the ability to autoregulate viral gene expression*. Virology, 2009. **383**(2): p. 183-187.
68. Stakaitytė, G., et al., *Merkel cell polyomavirus: molecular insights into the most recently discovered human tumour virus*. Cancers (Basel), 2014. **6**(3): p. 1267-97.
69. Lee, S., et al., *Identification and validation of a novel mature microRNA encoded by the Merkel cell polyomavirus in human Merkel cell carcinomas*. Journal of clinical virology : the official publication of the Pan American Society for Clinical Virology, 2011. **52**(3): p. 272-275.
70. Houben, R., et al., *Merkel cell polyomavirus-infected Merkel cell carcinoma cells require expression of viral T antigens*. J Virol, 2010. **84**(14): p. 7064-72.
71. Houben, R., et al., *Merkel Cell Polyomavirus Large T Antigen is Dispensable in G2 and M-Phase to Promote Proliferation of Merkel Cell Carcinoma Cells*. Viruses, 2020. **12**(10).
72. Angermeyer, S., et al., *Merkel cell polyomavirus-positive Merkel cell carcinoma cells do not require expression of the viral small T antigen*. J Invest Dermatol, 2013. **133**(8): p. 2059-64.
73. Verhaegen, M.E., et al., *Merkel cell polyomavirus small T antigen is oncogenic in transgenic mice*. The Journal of investigative dermatology, 2015. **135**(5): p. 1415-1424.
74. Berrios, C., et al., *Merkel Cell Polyomavirus Small T Antigen Promotes Pro-Glycolytic Metabolic Perturbations Required for Transformation*. PLoS Pathog, 2016. **12**(11): p. e1006020.
75. Spurgeon, M.E., et al., *Tumorigenic activity of merkel cell polyomavirus T antigens expressed in the stratified epithelium of mice*. Cancer research, 2015. **75**(6): p. 1068-1079.
76. Spurgeon, M.E., et al., *The Merkel Cell Polyomavirus T Antigens Function as Tumor Promoters in Murine Skin*. Cancers, 2021. **13**(2): p. 222.
77. Boyland, E., *Tumour initiators, promoters, and complete carcinogens*. British journal of industrial medicine, 1985. **42**(10): p. 716-718.
78. Perdigoto, C.N., et al., *Embryonic maturation of epidermal Merkel cells is controlled by a redundant transcription factor network*. Development, 2014. **141**(24): p. 4690.
79. Van Keymeulen, A., et al., *Epidermal progenitors give rise to Merkel cells during embryonic development and adult homeostasis*. Journal of Cell Biology, 2009. **187**(1): p. 91-100.
80. Maricich, S.M., et al., *Merkel Cells Are Essential for Light-Touch Responses*. Science, 2009. **324**(5934): p. 1580.
81. Bossuyt, W., et al., *Atonal homolog 1 is a tumor suppressor gene*. PLoS Biol, 2009. **7**(2): p. e39.
82. Gambichler, T., et al., *Prognostic relevance of high atonal homolog-1 expression in Merkel cell carcinoma*. Journal of Cancer Research and Clinical Oncology, 2017. **143**(1): p. 43-49.
83. Fan, K., et al., *MCPyV Large T Antigen-Induced Atonal Homolog 1 Is a Lineage-Dependency Oncogene in Merkel Cell Carcinoma*. J Invest Dermatol, 2020. **140**(1): p. 56-65.e3.
84. Kervarrec, T., et al., *Merkel Cell Polyomavirus T Antigens Induce Merkel Cell-Like Differentiation in GLI1-Expressing Epithelial Cells*. Cancers (Basel), 2020. **12**(7).
85. Harold, A., et al., *Conversion of Sox2-dependent Merkel cell carcinoma to a differentiated neuron-like phenotype by T antigen inhibition*. Proceedings of the National Academy of Sciences, 2019. **116**(40): p. 20104.
86. Park, D.E., et al., *Merkel cell polyomavirus activates LSD1-mediated blockade of non-canonical BAF to regulate transformation and tumorigenesis*. Nature Cell Biology, 2020. **22**(5): p. 603-615.
87. Murone, M., A. Rosenthal, and F.J. de Sauvage, *Hedgehog signal transduction: from flies to vertebrates*. Exp Cell Res, 1999. **253**(1): p. 25-33.

88. Ingham, P.W. and A.P. McMahon, *Hedgehog signaling in animal development: paradigms and principles*. Genes Dev, 2001. **15**(23): p. 3059-87.
89. Brunner, M., et al., *Expression of hedgehog signaling molecules in Merkel cell carcinoma*. Head Neck, 2010. **32**(3): p. 333-40.
90. Perdigoto, C.N., et al., *Polycomb-Mediated Repression and Sonic Hedgehog Signaling Interact to Regulate Merkel Cell Specification during Skin Development*. PLoS Genet, 2016. **12**(7): p. e1006151.
91. Xiao, Y., et al., *A Cascade of Wnt, Eda, and Shh Signaling Is Essential for Touch Dome Merkel Cell Development*. PLoS genetics, 2016. **12**(7): p. e1006150-e1006150.
92. Xiao, Y., et al., *Neural Hedgehog signaling maintains stem cell renewal in the sensory touch dome epithelium*. Proceedings of the National Academy of Sciences, 2015. **112**(23): p. 7195.
93. Kuromi, T., et al., *Association of expression of the hedgehog signal with Merkel cell polyomavirus infection and prognosis of Merkel cell carcinoma*. Hum Pathol, 2017. **69**: p. 8-14.
94. Kervarrec, T., et al., *Polyomavirus-Positive Merkel Cell Carcinoma Derived from a Trichoblastoma Suggests an Epithelial Origin of this Merkel Cell Carcinoma*. J Invest Dermatol, 2020. **140**(5): p. 976-985.
95. Penton, A.L., L.D. Leonard, and N.B. Spinner, *Notch signaling in human development and disease*. Seminars in Cell & Developmental Biology, 2012. **23**(4): p. 450-457.
96. Hori, K., A. Sen, and S. Artavanis-Tsakonas, *Notch signaling at a glance*. Journal of Cell Science, 2013. **126**(10): p. 2135-2140.
97. Blanpain, C., et al., *Canonical notch signaling functions as a commitment switch in the epidermal lineage*. Genes & development, 2006. **20**(21): p. 3022-3035.
98. Zheng, X., et al., *Suppression of hath1 gene expression directly regulated by hes1 via notch signaling is associated with goblet cell depletion in ulcerative colitis*. Inflamm Bowel Dis, 2011. **17**(11): p. 2251-60.
99. Logan, G.J., et al., *Notch pathway signaling in the skin antagonizes Merkel cell development*. Developmental Biology, 2018. **434**(2): p. 207-214.
100. Abraham, K.J., et al., *Roles for miR-375 in Neuroendocrine Differentiation and Tumor Suppression via Notch Pathway Suppression in Merkel Cell Carcinoma*. The American Journal of Pathology, 2016. **186**(4): p. 1025-1035.
101. Wardhani, L.O., et al., *Expression of Notch 3 and Jagged 1 Is Associated With Merkel Cell Polyomavirus Status and Prognosis in Merkel Cell Carcinoma*. Anticancer Res, 2019. **39**(1): p. 319-329.
102. Houben, R., et al., *Mechanisms of p53 restriction in Merkel cell carcinoma cells are independent of the Merkel cell polyoma virus T antigens*. J Invest Dermatol, 2013. **133**(10): p. 2453-2460.
103. Park, D.E., et al., *Dual inhibition of MDM2 and MDM4 in virus-positive Merkel cell carcinoma enhances the p53 response*. Proc Natl Acad Sci U S A, 2019. **116**(3): p. 1027-1032.
104. Cheng, J., et al., *Merkel cell polyomavirus recruits MYCL to the EP400 complex to promote oncogenesis*. PLoS Pathog, 2017. **13**(10): p. e1006668.
105. Kraft, S. and S.R. Granter, *Molecular Pathology of Skin Neoplasms of the Head and Neck*. Archives of Pathology & Laboratory Medicine, 2014. **138**(6): p. 759-787.
106. Kervarrec, T., et al., *Histogenesis of Merkel Cell Carcinoma: A Comprehensive Review*. Frontiers in oncology, 2019. **9**: p. 451-451.
107. Brown, H.A., D.M. Sawyer, and T. Woo, *Intraepidermal Merkel Cell Carcinoma With No Dermal Involvement*. The American Journal of Dermatopathology, 2000. **22**(1).
108. Scott, M.P. and K.F. Helm, *Cytokeratin 20: A Marker For Diagnosing Merkel Cell Carcinoma*. The American Journal of Dermatopathology, 1999. **21**(1).

109. Chan, J.K., et al., *Cytokeratin 20 immunoreactivity distinguishes Merkel cell (primary cutaneous neuroendocrine) carcinomas and salivary gland small cell carcinomas from small cell carcinomas of various sites*. *Am J Surg Pathol*, 1997. **21**(2): p. 226-34.
110. Moll, R., D.L. Schiller, and W.W. Franke, *Identification of protein IT of the intestinal cytoskeleton as a novel type I cytokeratin with unusual properties and expression patterns*. *J Cell Biol*, 1990. **111**(2): p. 567-80.
111. Leech, S.N., et al., *Merkel cell carcinoma can be distinguished from metastatic small cell carcinoma using antibodies to cytokeratin 20 and thyroid transcription factor 1*. *Journal of Clinical Pathology*, 2001. **54**(9): p. 727.
112. Cheuk, W., et al., *Immunostaining for thyroid transcription factor 1 and cytokeratin 20 aids the distinction of small cell carcinoma from Merkel cell carcinoma, but not pulmonary from extrapulmonary small cell carcinomas*. *Arch Pathol Lab Med*, 2001. **125**(2): p. 228-31.
113. Koljonen, V., et al., *Neuroendocrine differentiation in primary Merkel cell carcinoma-- possible prognostic significance*. *Anticancer Res*, 2005. **25**(2a): p. 853-8.
114. Lilo, M.T., Y. Chen, and R.E. LeBlanc, *INSM1 Is More Sensitive and Interpretable than Conventional Immunohistochemical Stains Used to Diagnose Merkel Cell Carcinoma*. *Am J Surg Pathol*, 2018. **42**(11): p. 1541-1548.
115. Kurokawa, M., et al., *CD56: a useful marker for diagnosing Merkel cell carcinoma*. *J Dermatol Sci*, 2003. **31**(3): p. 219-24.
116. Kervarrec, T., et al., *Diagnostic accuracy of a panel of immunohistochemical and molecular markers to distinguish Merkel cell carcinoma from other neuroendocrine carcinomas*. *Modern Pathology*, 2019. **32**(4): p. 499-510.
117. Fukuhara, M., et al., *SATB2 is expressed in Merkel cell carcinoma*. *Arch Dermatol Res*, 2016. **308**(6): p. 449-54.
118. Dellambra, E., et al., *Merkel Cell Carcinoma*. *Biomedicines*, 2021. **9**(7): p. 718.
119. Tang, C.K. and C. Toker, *Trabecular carcinoma of the skin: an ultrastructural study*. *Cancer*, 1978. **42**(5): p. 2311-21.
120. Moll, I., C. Kuhn, and R. Moll, *Cytokeratin 20 is a general marker of cutaneous Merkel cells while certain neuronal proteins are absent*. *J Invest Dermatol*, 1995. **104**(6): p. 910-5.
121. Gambichler, T., et al., *Prognostic relevance of high atonal homolog-1 expression in Merkel cell carcinoma*. *J Cancer Res Clin Oncol*, 2017. **143**(1): p. 43-49.
122. Hartschuh, W., E. Weihe, and U. Egner, *Chromogranin A in the mammalian Merkel cell: cellular and subcellular distribution*. *J Invest Dermatol*, 1989. **93**(5): p. 641-8.
123. García-Caballero, T., et al., *Synaptophysinlike immunoreactivity in the Merkel cells of pig-snout skin*. *Ultrastruct Pathol*, 1989. **13**(1): p. 55-61.
124. Visvader, J.E., *Cells of origin in cancer*. *Nature*, 2011. **469**(7330): p. 314-22.
125. Liu, W., et al., *Identifying the Target Cells and Mechanisms of Merkel Cell Polyomavirus Infection*. *Cell host & microbe*, 2016. **19**(6): p. 775-787.
126. Shuda, M., et al., *Merkel Cell Polyomavirus Small T Antigen Induces Cancer and Embryonic Merkel Cell Proliferation in a Transgenic Mouse Model*. *PloS one*, 2015. **10**(11): p. e0142329-e0142329.
127. Tilling, T. and I. Moll, *Which are the cells of origin in merkel cell carcinoma?* *Journal of skin cancer*, 2012. **2012**: p. 680410-680410.
128. Toma, J.G., et al., *Isolation of multipotent adult stem cells from the dermis of mammalian skin*. *Nat Cell Biol*, 2001. **3**(9): p. 778-84.
129. Kwok, C.K., P.K. Tam, and E.S. Ngan, *Potential use of skin-derived precursors (SKPs) in establishing a cell-based treatment model for Hirschsprung's disease*. *J Pediatr Surg*, 2013. **48**(3): p. 619-28.
130. Sauer, C.M., et al., *Reviewing the current evidence supporting early B-cells as the cellular origin of Merkel cell carcinoma*. *Critical Reviews in Oncology/Hematology*, 2017. **116**: p. 99-105.

131. zur Hausen, A., et al., *Early B-Cell Differentiation in Merkel Cell Carcinomas: Clues to Cellular Ancestry*. Cancer Research, 2013. **73**(16): p. 4982.
132. Koljonen, V., et al., *Joint occurrence of Merkel cell carcinoma and non-Hodgkin lymphomas in four Nordic countries*. Leuk Lymphoma, 2015. **56**(12): p. 3315-9.
133. Tadmor, T., A. Aviv, and A. Polliack, *Merkel cell carcinoma, chronic lymphocytic leukemia and other lymphoproliferative disorders: an old bond with possible new viral ties*. Annals of Oncology, 2011. **22**(2): p. 250-256.
134. Popovic, L., et al., *Concurrent chronic lymphocytic leukemia and merkel cell carcinoma in primary skin tumor and metastatic lymph node*. Indian journal of hematology & blood transfusion : an official journal of Indian Society of Hematology and Blood Transfusion, 2014. **30**(Suppl 1): p. 422-424.
135. Pantulu, N.D., et al., *Detection of a novel truncating Merkel cell polyomavirus large T antigen deletion in chronic lymphocytic leukemia cells*. Blood, 2010. **116**(24): p. 5280-5284.
136. Hagg, A.M., et al., *Fluorescence in situ hybridization confirms the presence of Merkel cell polyomavirus in chronic lymphocytic leukemia cells*. Blood, 2011. **117**(21): p. 5776-5777.
137. Villani, A., et al., *Merkel Cell Carcinoma: Therapeutic Update and Emerging Therapies*. Dermatol Ther (Heidelb), 2019. **9**(2): p. 209-222.
138. Jouary, T., et al., *Adjuvant prophylactic regional radiotherapy versus observation in stage I Merkel cell carcinoma: a multicentric prospective randomized study*. Ann Oncol, 2012. **23**(4): p. 1074-80.
139. Iyer, J.G., et al., *Response rates and durability of chemotherapy among 62 patients with metastatic Merkel cell carcinoma*. Cancer medicine, 2016. **5**(9): p. 2294-2301.
140. Nghiem, P., et al., *Systematic literature review of efficacy, safety and tolerability outcomes of chemotherapy regimens in patients with metastatic Merkel cell carcinoma*. Future Oncol, 2017. **13**(14): p. 1263-1279.
141. Paulson, K.G., et al., *Downregulation of MHC-I expression is prevalent but reversible in Merkel cell carcinoma*. Cancer Immunol Res, 2014. **2**(11): p. 1071-9.
142. Nghiem, P., et al., *Durable Tumor Regression and Overall Survival in Patients With Advanced Merkel Cell Carcinoma Receiving Pembrolizumab as First-Line Therapy*. Journal of Clinical Oncology, 2019. **37**(9): p. 693-702.
143. D'Angelo, S.P., et al., *Efficacy and Safety of First-line Avelumab Treatment in Patients With Stage IV Metastatic Merkel Cell Carcinoma: A Preplanned Interim Analysis of a Clinical Trial*. JAMA Oncol, 2018. **4**(9): p. e180077.
144. Han, Y., D. Liu, and L. Li, *PD-1/PD-L1 pathway: current researches in cancer*. American journal of cancer research, 2020. **10**(3): p. 727-742.
145. Jiang, Y., et al., *PD-1 and PD-L1 in cancer immunotherapy: clinical implications and future considerations*. Hum Vaccin Immunother, 2019. **15**(5): p. 1111-1122.
146. Lipson, E.J., et al., *PD-L1 expression in the Merkel cell carcinoma microenvironment: association with inflammation, Merkel cell polyomavirus and overall survival*. Cancer immunology research, 2013. **1**(1): p. 54-63.
147. Nghiem, P.T., et al., *PD-1 Blockade with Pembrolizumab in Advanced Merkel-Cell Carcinoma*. New England Journal of Medicine, 2016. **374**(26): p. 2542-2552.
148. Kaufman, H.L., et al., *Avelumab in patients with chemotherapy-refractory metastatic Merkel cell carcinoma: a multicentre, single-group, open-label, phase 2 trial*. Lancet Oncol, 2016. **17**(10): p. 1374-1385.
149. Nghiem, P., et al., *Three-year survival, correlates and salvage therapies in patients receiving first-line pembrolizumab for advanced Merkel cell carcinoma*. Journal for ImmunoTherapy of Cancer, 2021. **9**(4): p. e002478.
150. Kaufman, H.L., et al., *Updated efficacy of avelumab in patients with previously treated metastatic Merkel cell carcinoma after ≥1 year of follow-up: JAVELIN Merkel 200, a phase 2 clinical trial*. Journal for immunotherapy of cancer, 2018. **6**(1): p. 7-7.

151. Baker, M., L. Cordes, and I. Brownell, *Avelumab: a new standard for treating metastatic Merkel cell carcinoma*. *Expert Review of Anticancer Therapy*, 2018. **18**(4): p. 319-326.
152. Glutsch, V., et al., *Activity of ipilimumab plus nivolumab in avelumab-refractory Merkel cell carcinoma*. *Cancer Immunology, Immunotherapy*, 2021.
153. Marin-Acevedo, J.A., et al., *Next generation of immune checkpoint therapy in cancer: new developments and challenges*. *Journal of hematology & oncology*, 2018. **11**(1): p. 39-39.
154. Efferth, T., *From ancient herb to modern drug: Artemisia annua and artemisinin for cancer therapy*. *Semin Cancer Biol*, 2017. **46**: p. 65-83.
155. Lisgarten, J.N., et al., *Structure, absolute configuration, and conformation of the antimalarial drug artesunate*. *Journal of Chemical Crystallography*, 2002. **32**(1): p. 43-48.
156. Zoller, T., et al., *Intravenous artesunate for severe malaria in travelers, Europe*. *Emerging infectious diseases*, 2011. **17**(5): p. 771-777.
157. Li, Q. and P. Weina, *Artesunate: The Best Drug in the Treatment of Severe and Complicated Malaria*. *Pharmaceuticals (Basel, Switzerland)*, 2010. **3**(7): p. 2322-2332.
158. Roussel, C., et al., *Artesunate to treat severe malaria in travellers: review of efficacy and safety and practical implications*. *Journal of Travel Medicine*, 2017. **24**(2).
159. Bosman, A. and K.N. Mendis, *A major transition in malaria treatment: the adoption and deployment of artemisinin-based combination therapies*. *Am J Trop Med Hyg*, 2007. **77**(6 Suppl): p. 193-7.
160. Nosten, F. and N.J. White, *Artemisinin-based combination treatment of falciparum malaria*. *Am J Trop Med Hyg*, 2007. **77**(6 Suppl): p. 181-92.
161. Khanal, P., *Antimalarial and anticancer properties of artesunate and other artemisinins: current development*. *Monatshefte für Chemie - Chemical Monthly*, 2021. **152**(4): p. 387-400.
162. Kremsner, P.G., et al., *Intramuscular Artesunate for Severe Malaria in African Children: A Multicenter Randomized Controlled Trial*. *PLoS Med*, 2016. **13**(1): p. e1001938.
163. Fanello, C., et al., *Pharmacokinetic Study of Rectal Artesunate in Children with Severe Malaria in Africa*. *Antimicrob Agents Chemother*, 2021. **65**(4).
164. Asawamahasakda, W., et al., *Reaction of antimalarial endoperoxides with specific parasite proteins*. *Antimicrobial agents and chemotherapy*, 1994. **38**(8): p. 1854-1858.
165. Wang, J., et al., *Artemisinin directly targets malarial mitochondria through its specific mitochondrial activation*. *PloS one*, 2010. **5**(3): p. e9582-e9582.
166. Gopalakrishnan, A.M. and N. Kumar, *Antimalarial Action of Artesunate Involves DNA Damage Mediated by Reactive Oxygen Species*. *Antimicrobial Agents and Chemotherapy*, 2015. **59**(1): p. 317.
167. Meshnick, S.R., et al., *Artemisinin (qinghaosu): the role of intracellular hemin in its mechanism of antimalarial action*. *Molecular and Biochemical Parasitology*, 1991. **49**(2): p. 181-189.
168. Adebayo, J.O., et al., *Enhancing the antimalarial activity of artesunate*. *Parasitology Research*, 2020. **119**(9): p. 2749-2764.
169. Septembre-Malaterre, A., et al., *Artemisia annua, a Traditional Plant Brought to Light*. *International journal of molecular sciences*, 2020. **21**(14): p. 4986.
170. Wu, Y., et al., *Facile Preparation of N-Glycosylated 10-Piperazinyl Artemisinin Derivatives and Evaluation of Their Antimalarial and Cytotoxic Activities*. *Molecules*, 2018. **23**(7).
171. D'Alessandro, S., et al., *The Use of Antimalarial Drugs against Viral Infection*. *Microorganisms*, 2020. **8**(1).
172. Efferth, T., et al., *The antiviral activities of artemisinin and artesunate*. *Clin Infect Dis*, 2008. **47**(6): p. 804-11.
173. Kaptein, S.J., et al., *The anti-malaria drug artesunate inhibits replication of cytomegalovirus in vitro and in vivo*. *Antiviral Res*, 2006. **69**(2): p. 60-9.

174. Efferth, T., et al., *Antiviral activity of artesunate towards wild-type, recombinant, and ganciclovir-resistant human cytomegaloviruses*. J Mol Med (Berl), 2002. **80**(4): p. 233-42.
175. Hwang, E.-S., et al., *Human cytomegalovirus IE1-72 protein interacts with p53 and inhibits p53-dependent transactivation by a mechanism different from that of IE2-86 protein*. Journal of virology, 2009. **83**(23): p. 12388-12398.
176. Shapira, M.Y., et al., *Artesunate as a potent antiviral agent in a patient with late drug-resistant cytomegalovirus infection after hematopoietic stem cell transplantation*. Clin Infect Dis, 2008. **46**(9): p. 1455-7.
177. Sharma, B.N., M. Marschall, and C.H. Rinaldo, *Antiviral effects of artesunate on JC polyomavirus replication in COS-7 cells*. Antimicrob Agents Chemother, 2014. **58**(11): p. 6724-34.
178. Ciotti, M., C. Prezioso, and V. Pietropaolo, *An overview on human polyomaviruses biology and related diseases*. Future Virology, 2019. **14**(7): p. 487-501.
179. Sharma, B.N., et al., *Antiviral effects of artesunate on polyomavirus BK replication in primary human kidney cells*. Antimicrob Agents Chemother, 2014. **58**(1): p. 279-89.
180. Auerochs, S., K. Korn, and M. Marschall, *A reporter system for Epstein-Barr virus (EBV) lytic replication: anti-EBV activity of the broad anti-herpesviral drug artesunate*. J Virol Methods, 2011. **173**(2): p. 334-9.
181. Romero, M.R., et al., *Effect of artemisinin/artesunate as inhibitors of hepatitis B virus production in an "in vitro" replicative system*. Antiviral Res, 2005. **68**(2): p. 75-83.
182. Obeid, S., et al., *Artemisinin analogues as potent inhibitors of in vitro hepatitis C virus replication*. PloS one, 2013. **8**(12): p. e81783-e81783.
183. Trimble, C.L., et al., *A first-in-human proof-of-concept trial of intravaginal artesunate to treat cervical intraepithelial neoplasia 2/3 (CIN2/3)*. Gynecol Oncol, 2020. **157**(1): p. 188-194.
184. Efferth, T., et al., *The anti-malarial artesunate is also active against cancer*. Int J Oncol, 2001. **18**(4): p. 767-73.
185. Jiang, F., et al., *Artesunate induces apoptosis and autophagy in HCT116 colon cancer cells, and autophagy inhibition enhances the artesunate-induced apoptosis*. Int J Mol Med, 2018. **42**(3): p. 1295-1304.
186. Eling, N., et al., *Identification of artesunate as a specific activator of ferroptosis in pancreatic cancer cells*. Oncoscience, 2015. **2**(5): p. 517-532.
187. Jeong, D.E., et al., *Repurposing the anti-malarial drug artesunate as a novel therapeutic agent for metastatic renal cell carcinoma due to its attenuation of tumor growth, metastasis, and angiogenesis*. Oncotarget, 2015. **6**(32): p. 33046-33064.
188. Hamacher-Brady, A., et al., *Artesunate activates mitochondrial apoptosis in breast cancer cells via iron-catalyzed lysosomal reactive oxygen species production*. The Journal of biological chemistry, 2011. **286**(8): p. 6587-6601.
189. Greenshields, A.L., W. Fernando, and D.W. Hoskin, *The anti-malarial drug artesunate causes cell cycle arrest and apoptosis of triple-negative MDA-MB-468 and HER2-enriched SK-BR-3 breast cancer cells*. Exp Mol Pathol, 2019. **107**: p. 10-22.
190. Wang, B., et al., *Artesunate sensitizes ovarian cancer cells to cisplatin by downregulating RAD51*. Cancer biology & therapy, 2015. **16**(10): p. 1548-1556.
191. Chen, X., et al., *Artesunate promotes Th1 differentiation from CD4+ T cells to enhance cell apoptosis in ovarian cancer via miR-142*. Brazilian journal of medical and biological research = Revista brasileira de pesquisas medicas e biologicas, 2019. **52**(5): p. e7992-e7992.
192. Li, B., et al., *Artemisinin derivatives inhibit epithelial ovarian cancer cells via autophagy-mediated cell cycle arrest*. Acta Biochimica et Biophysica Sinica, 2018. **50**(12): p. 1227-1235.
193. Efferth, T., et al., *Combination treatment of glioblastoma multiforme cell lines with the anti-malarial artesunate and the epidermal growth factor receptor tyrosine kinase inhibitor OSI-774*. Biochem Pharmacol, 2004. **67**(9): p. 1689-700.

194. Dou, C.-Y., et al., *Cytotoxic effect of Artesunate on myeloid leukemia cell lines through up-regulating miR-29c expression*. *Translational Cancer Research*, 2018. **7**(6): p. 1748-1750.
195. Chen, S., et al., *Artesunate induces apoptosis and inhibits the proliferation, stemness, and tumorigenesis of leukemia*. *Annals of Translational Medicine*, 2020. **8**(12): p. 767.
196. Li, L.N., et al., *Artesunate attenuates the growth of human colorectal carcinoma and inhibits hyperactive Wnt/beta-catenin pathway*. *Int J Cancer*, 2007. **121**(6): p. 1360-5.
197. Zhao, F., et al., *Artesunate Impairs Growth in Cisplatin-Resistant Bladder Cancer Cells by Cell Cycle Arrest, Apoptosis and Autophagy Induction*. *Cells*, 2020. **9**(12): p. 2643.
198. Deeken, J.F., et al., *A phase I study of intravenous artesunate in patients with advanced solid tumor malignancies*. *Cancer Chemother Pharmacol*, 2018. **81**(3): p. 587-596.
199. von Hagens, C., et al., *Prospective open uncontrolled phase I study to define a well-tolerated dose of oral artesunate as add-on therapy in patients with metastatic breast cancer (ARTIC M33/2)*. *Breast Cancer Res Treat*, 2017. **164**(2): p. 359-369.
200. Augustin, Y., H.M. Staines, and S. Krishna, *Artemisinins as a novel anti-cancer therapy: Targeting a global cancer pandemic through drug repurposing*. *Pharmacol Ther*, 2020. **216**: p. 107706.
201. Xu, C., et al., *Artemisinins as Anticancer Drugs: Novel Therapeutic Approaches, Molecular Mechanisms, and Clinical Trials*. *Frontiers in Pharmacology*, 2020. **11**(1608).
202. Chen, K., et al., *Artesunate induces G2/M cell cycle arrest through autophagy induction in breast cancer cells*. *Anticancer Drugs*, 2014. **25**(6): p. 652-62.
203. Wen, L., et al., *Artesunate promotes G2/M cell cycle arrest in MCF7 breast cancer cells through ATM activation*. *Breast Cancer*, 2018. **25**(6): p. 681-686.
204. Fei, Z., et al., *Artesunate enhances radiosensitivity of esophageal cancer cells by inhibiting the repair of DNA damage*. *Journal of Pharmacological Sciences*, 2018. **138**(2): p. 131-137.
205. Efferth, T., et al., *Molecular Modes of Action of Artesunate in Tumor Cell Lines*. *Molecular Pharmacology*, 2003. **64**(2): p. 382.
206. Efferth, T., et al., *Artesunate induces ROS-mediated apoptosis in doxorubicin-resistant T leukemia cells*. *PloS one*, 2007. **2**(8): p. e693-e693.
207. Beccafico, S., et al., *Artesunate induces ROS- and p38 MAPK-mediated apoptosis and counteracts tumor growth in vivo in embryonal rhabdomyosarcoma cells*. *Carcinogenesis*, 2015. **36**(9): p. 1071-1083.
208. DeBerardinis, R.J., et al., *The Biology of Cancer: Metabolic Reprogramming Fuels Cell Growth and Proliferation*. *Cell Metabolism*, 2008. **7**(1): p. 11-20.
209. Seliger, B., *Strategies of tumor immune evasion*. *BioDrugs*, 2005. **19**(6): p. 347-54.
210. Li, L.N., et al., *Differential sensitivity of colorectal cancer cell lines to artesunate is associated with expression of beta-catenin and E-cadherin*. *Eur J Pharmacol*, 2008. **588**(1): p. 1-8.
211. Haynes, R.K., *From artemisinin to new artemisinin antimalarials: biosynthesis, extraction, old and new derivatives, stereochemistry and medicinal chemistry requirements*. *Curr Top Med Chem*, 2006. **6**(5): p. 509-37.
212. Mi, Y.-j., et al., *Dihydroartemisinin inhibits glucose uptake and cooperates with glycolysis inhibitor to induce apoptosis in non-small cell lung carcinoma cells*. *PloS one*, 2015. **10**(3): p. e0120426-e0120426.
213. Ma, H., et al., *The effects of artesunate on the expression of EGFR and ABCG2 in A549 human lung cancer cells and a xenograft model*. *Molecules (Basel, Switzerland)*, 2011. **16**(12): p. 10556-10569.
214. Cheng, H., et al., *Targeting the PI3K/AKT/mTOR pathway: potential for lung cancer treatment*. *Lung cancer management*, 2014. **3**(1): p. 67-75.
215. Kumar, V.L., S. Verma, and P. Das, *Artesunate suppresses inflammation and oxidative stress in a rat model of colorectal cancer*. *Drug Development Research*, 2019. **80**(8): p. 1089-1097.
216. Fisher, D.E., *Apoptosis in cancer therapy: crossing the threshold*. *Cell*, 1994. **78**(4): p. 539-42.

217. Su, Y., et al., *Ferroptosis, a novel pharmacological mechanism of anti-cancer drugs*. Cancer Letters, 2020. **483**: p. 127-136.
218. Vakifahmetoglu-Norberg, H., H.-g. Xia, and J. Yuan, *Pharmacologic agents targeting autophagy*. The Journal of clinical investigation, 2015. **125**(1): p. 5-13.
219. Galluzzi, L., et al., *Molecular mechanisms of cell death: recommendations of the Nomenclature Committee on Cell Death 2018*. Cell Death & Differentiation, 2018. **25**(3): p. 486-541.
220. Koren, E. and Y. Fuchs, *Modes of Regulated Cell Death in Cancer*. Cancer Discov, 2021. **11**(2): p. 245-265.
221. Van der Meeren, L., et al., *AFM Analysis Enables Differentiation between Apoptosis, Necroptosis, and Ferroptosis in Murine Cancer Cells*. iScience, 2020. **23**(12): p. 101816.
222. Yang, Y., et al., *Artesunate induces mitochondria-mediated apoptosis of human retinoblastoma cells by upregulating Kruppel-like factor 6*. Cell Death & Disease, 2019. **10**(11): p. 862.
223. Zhou, X., et al., *Artesunate inhibits the growth of gastric cancer cells through the mechanism of promoting oncosis both in vitro and in vivo*. Anticancer Drugs, 2013. **24**(9): p. 920-7.
224. Zhang, P., et al., *Artesunate inhibits the growth and induces apoptosis of human gastric cancer cells by downregulating COX-2*. OncoTargets and therapy, 2015. **8**: p. 845-854.
225. Du, J.H., et al., *Artesunate induces oncosis-like cell death in vitro and has antitumor activity against pancreatic cancer xenografts in vivo*. Cancer Chemother Pharmacol, 2010. **65**(5): p. 895-902.
226. Zhou, X., et al., *Artesunate induces autophagy dependent apoptosis through upregulating ROS and activating AMPK-mTOR-ULK1 axis in human bladder cancer cells*. Chem Biol Interact, 2020. **331**: p. 109273.
227. Dixon, S.J., et al., *Ferroptosis: an iron-dependent form of nonapoptotic cell death*. Cell, 2012. **149**(5): p. 1060-72.
228. Wang, N., et al., *Artesunate activates the ATF4-CHOP-CHAC1 pathway and affects ferroptosis in Burkitt's Lymphoma*. Biochemical and Biophysical Research Communications, 2019. **519**(3): p. 533-539.
229. Roh, J.-L., et al., *Nrf2 inhibition reverses the resistance of cisplatin-resistant head and neck cancer cells to artesunate-induced ferroptosis*. Redox Biology, 2017. **11**: p. 254-262.
230. Fink, S.L. and B.T. Cookson, *Apoptosis, pyroptosis, and necrosis: mechanistic description of dead and dying eukaryotic cells*. Infection and immunity, 2005. **73**(4): p. 1907-1916.
231. Mou, Y., et al., *Ferroptosis, a new form of cell death: opportunities and challenges in cancer*. Journal of Hematology & Oncology, 2019. **12**(1): p. 34.
232. Riegman, M., et al., *Ferroptosis occurs through an osmotic mechanism and propagates independently of cell rupture*. Nature Cell Biology, 2020. **22**(9): p. 1042-1048.
233. Yan, G., M. Elbadawi, and T. Efferth, *Multiple cell death modalities and their key features (Review)*. World Acad Sci J, 2020. **2**(2): p. 39-48.
234. Weerasinghe, P. and L.M. Buja, *Oncosis: an important non-apoptotic mode of cell death*. Exp Mol Pathol, 2012. **93**(3): p. 302-8.
235. Mills, E.M., et al., *Regulation of cellular oncosis by uncoupling protein 2*. J Biol Chem, 2002. **277**(30): p. 27385-92.
236. Liu, X., T. Van Vleet, and R.G. Schnellmann, *The role of calpain in oncotic cell death*. Annu Rev Pharmacol Toxicol, 2004. **44**: p. 349-70.
237. Menon, M.B. and S. Dhamija, *Beclin 1 Phosphorylation – at the Center of Autophagy Regulation*. Frontiers in Cell and Developmental Biology, 2018. **6**(137).
238. Gao, M., et al., *Glutaminolysis and Transferrin Regulate Ferroptosis*. Mol Cell, 2015. **59**(2): p. 298-308.
239. Yoshida, M., et al., *Involvement of cigarette smoke-induced epithelial cell ferroptosis in COPD pathogenesis*. Nat Commun, 2019. **10**(1): p. 3145.

240. Reichert, C.O., et al., *Ferroptosis Mechanisms Involved in Neurodegenerative Diseases*. International journal of molecular sciences, 2020. **21**(22): p. 8765.
241. Stockwell, B.R., X. Jiang, and W. Gu, *Emerging Mechanisms and Disease Relevance of Ferroptosis*. Trends Cell Biol, 2020. **30**(6): p. 478-490.
242. Zhang, Y., et al., *BAP1 links metabolic regulation of ferroptosis to tumour suppression*. Nature Cell Biology, 2018. **20**(10): p. 1181-1192.
243. Jiang, L., et al., *Ferroptosis as a p53-mediated activity during tumour suppression*. Nature, 2015. **520**(7545): p. 57-62.
244. Tang, D., et al., *Ferroptosis: molecular mechanisms and health implications*. Cell Research, 2021. **31**(2): p. 107-125.
245. Bortner, C.D. and J.A. Cidlowski, *Uncoupling cell shrinkage from apoptosis reveals that Na<sup>+</sup> influx is required for volume loss during programmed cell death*. J Biol Chem, 2003. **278**(40): p. 39176-84.
246. Tang, D., et al., *The molecular machinery of regulated cell death*. Cell Research, 2019. **29**(5): p. 347-364.
247. Challa, S. and F.K.-M. Chan, *Going up in flames: necrotic cell injury and inflammatory diseases*. Cellular and molecular life sciences : CMLS, 2010. **67**(19): p. 3241-3253.
248. Kim, S.E., et al., *Ultrasmall nanoparticles induce ferroptosis in nutrient-deprived cancer cells and suppress tumour growth*. Nature Nanotechnology, 2016. **11**(11): p. 977-985.
249. Fanzani, A. and M. Poli, *Iron, Oxidative Damage and Ferroptosis in Rhabdomyosarcoma*. International journal of molecular sciences, 2017. **18**(8): p. 1718.
250. Phaniendra, A., D.B. Jestadi, and L. Periyasamy, *Free radicals: properties, sources, targets, and their implication in various diseases*. Indian journal of clinical biochemistry : IJCB, 2015. **30**(1): p. 11-26.
251. Li, J., et al., *Ferroptosis: past, present and future*. Cell Death & Disease, 2020. **11**(2): p. 88.
252. Nemeth, E., et al., *Hepcidin Regulates Cellular Iron Efflux by Binding to Ferroportin and Inducing Its Internalization*. Science, 2004. **306**(5704): p. 2090.
253. Habashy, H.O., et al., *Transferrin receptor (CD71) is a marker of poor prognosis in breast cancer and can predict response to tamoxifen*. Breast Cancer Res Treat, 2010. **119**(2): p. 283-93.
254. Jeong, D.E., et al., *Repurposing the anti-malarial drug artesunate as a novel therapeutic agent for metastatic renal cell carcinoma due to its attenuation of tumor growth, metastasis, and angiogenesis*. Oncotarget, 2015. **6**(32): p. 33046-64.
255. Basuli, D., et al., *Iron addiction: a novel therapeutic target in ovarian cancer*. Oncogene, 2017. **36**(29): p. 4089-4099.
256. Kong, Y., et al., *Ferroportin downregulation promotes cell proliferation by modulating the Nrf2-miR-17-5p axis in multiple myeloma*. Cell Death & Disease, 2019. **10**(9): p. 624.
257. Chen, X., et al., *Iron Metabolism in Ferroptosis*. Frontiers in cell and developmental biology, 2020. **8**: p. 590226-590226.
258. Ooko, E., et al., *Artemisinin derivatives induce iron-dependent cell death (ferroptosis) in tumor cells*. Phytomedicine, 2015. **22**(11): p. 1045-54.
259. Wu, J., et al., *Intercellular interaction dictates cancer cell ferroptosis via NF2-YAP signalling*. Nature, 2019. **572**(7769): p. 402-406.
260. Kurz, T., et al., *Lysosomes in iron metabolism, ageing and apoptosis*. Histochemistry and cell biology, 2008. **129**(4): p. 389-406.
261. Torii, S., et al., *An essential role for functional lysosomes in ferroptosis of cancer cells*. Biochemical Journal, 2016. **473**(6): p. 769-777.
262. Hou, W., et al., *Autophagy promotes ferroptosis by degradation of ferritin*. Autophagy, 2016. **12**(8): p. 1425-8.
263. Yambire, K.F., et al., *Impaired lysosomal acidification triggers iron deficiency and inflammation in vivo*. Elife, 2019. **8**.

264. Yao, X., et al., *Deferoxamine promotes recovery of traumatic spinal cord injury by inhibiting ferroptosis*. *Neural regeneration research*, 2019. **14**(3): p. 532-541.
265. Yoshimori, T., et al., *Bafilomycin A1, a specific inhibitor of vacuolar-type H(+)-ATPase, inhibits acidification and protein degradation in lysosomes of cultured cells*. *J Biol Chem*, 1991. **266**(26): p. 17707-12.
266. Gao, H., et al., *Ferroptosis is a lysosomal cell death process*. *Biochem Biophys Res Commun*, 2018. **503**(3): p. 1550-1556.
267. Gao, M., et al., *Ferroptosis is an autophagic cell death process*. *Cell research*, 2016. **26**(9): p. 1021-1032.
268. Yang, N.D., et al., *Artesunate induces cell death in human cancer cells via enhancing lysosomal function and lysosomal degradation of ferritin*. *J Biol Chem*, 2014. **289**(48): p. 33425-41.
269. Hadian, K., *Ferroptosis Suppressor Protein 1 (FSP1) and Coenzyme Q10 Cooperatively Suppress Ferroptosis*. *Biochemistry*, 2020. **59**(5): p. 637-638.
270. Kagan, V.E., et al., *Oxidized arachidonic and adrenic PEs navigate cells to ferroptosis*. *Nature chemical biology*, 2017. **13**(1): p. 81-90.
271. Küch, E.M., et al., *Differentially localized acyl-CoA synthetase 4 isoenzymes mediate the metabolic channeling of fatty acids towards phosphatidylinositol*. *Biochim Biophys Acta*, 2014. **1841**(2): p. 227-39.
272. Forcina, G.C. and S.J. Dixon, *GPX4 at the Crossroads of Lipid Homeostasis and Ferroptosis*. *Proteomics*, 2019. **19**(18): p. e1800311.
273. Wang, L., X. Chen, and C. Yan, *Ferroptosis: An emerging therapeutic opportunity for cancer*. *Genes & Diseases*, 2020.
274. Han, C., et al., *Ferroptosis and Its Potential Role in Human Diseases*. *Frontiers in Pharmacology*, 2020. **11**(239).
275. Dixon, S.J., et al., *Human Haploid Cell Genetics Reveals Roles for Lipid Metabolism Genes in Nonapoptotic Cell Death*. *ACS chemical biology*, 2015. **10**(7): p. 1604-1609.
276. Yuan, H., et al., *Identification of ACSL4 as a biomarker and contributor of ferroptosis*. *Biochem Biophys Res Commun*, 2016. **478**(3): p. 1338-43.
277. Doll, S., et al., *ACSL4 dictates ferroptosis sensitivity by shaping cellular lipid composition*. *Nature Chemical Biology*, 2017. **13**(1): p. 91-98.
278. Moerke, C., et al., *ACSL4 as the First Reliable Biomarker of Ferroptosis Under Pathophysiological Conditions*, in *Ferroptosis in Health and Disease*, D. Tang, Editor. 2019, Springer International Publishing: Cham. p. 111-123.
279. Henry, R.R., *Thiazolidinediones*. *Endocrinol Metab Clin North Am*, 1997. **26**(3): p. 553-73.
280. Lei, P., T. Bai, and Y. Sun, *Mechanisms of Ferroptosis and Relations With Regulated Cell Death: A Review*. *Frontiers in Physiology*, 2019. **10**(139).
281. Kutzner, L., et al., *Mammalian ALOX15 orthologs exhibit pronounced dual positional specificity with docosahexaenoic acid*. *Biochim Biophys Acta Mol Cell Biol Lipids*, 2017. **1862**(7): p. 666-675.
282. Shintoku, R., et al., *Lipoxygenase-mediated generation of lipid peroxides enhances ferroptosis induced by erastin and RSL3*. *Cancer science*, 2017. **108**(11): p. 2187-2194.
283. Shah, R., M.S. Shchepinov, and D.A. Pratt, *Resolving the Role of Lipoxygenases in the Initiation and Execution of Ferroptosis*. *ACS central science*, 2018. **4**(3): p. 387-396.
284. Hinman, A., et al., *Vitamin E hydroquinone is an endogenous regulator of ferroptosis via redox control of 15-lipoxygenase*. *PLoS one*, 2018. **13**(8): p. e0201369-e0201369.
285. Mao, G., et al., *Tocopherols and tocotrienols prevent lipoxygenase-driven phospholipid oxidation in ferroptosis*. *The FASEB Journal*, 2017. **31**(S1): p. 946.3-946.3.
286. Zilka, O., et al., *On the Mechanism of Cytoprotection by Ferrostatin-1 and Lipoxstatin-1 and the Role of Lipid Peroxidation in Ferroptotic Cell Death*. *ACS Central Science*, 2017. **3**(3): p. 232-243.

287. Sato, H., et al., *Cloning and expression of a plasma membrane cystine/glutamate exchange transporter composed of two distinct proteins*. J Biol Chem, 1999. **274**(17): p. 11455-8.
288. Dixon, S.J., et al., *Pharmacological inhibition of cystine-glutamate exchange induces endoplasmic reticulum stress and ferroptosis*. Elife, 2014. **3**: p. e02523.
289. Yang, W.S., et al., *Regulation of ferroptotic cancer cell death by GPX4*. Cell, 2014. **156**(1-2): p. 317-331.
290. Conrad, M. and J.P. Friedmann Angeli, *Glutathione peroxidase 4 (Gpx4) and ferroptosis: what's so special about it?* Molecular & cellular oncology, 2015. **2**(3): p. e995047-e995047.
291. Yagoda, N., et al., *RAS-RAF-MEK-dependent oxidative cell death involving voltage-dependent anion channels*. Nature, 2007. **447**(7146): p. 865-869.
292. Dolma, S., et al., *Identification of genotype-selective antitumor agents using synthetic lethal chemical screening in engineered human tumor cells*. Cancer Cell, 2003. **3**(3): p. 285-96.
293. Imai, H., et al., *Lipid Peroxidation-Dependent Cell Death Regulated by GPx4 and Ferroptosis*. Curr Top Microbiol Immunol, 2017. **403**: p. 143-170.
294. Ishii, T., S. Bannai, and Y. Sugita, *Mechanism of growth stimulation of L1210 cells by 2-mercaptoethanol in vitro. Role of the mixed disulfide of 2-mercaptoethanol and cysteine*. J Biol Chem, 1981. **256**(23): p. 12387-92.
295. Doll, S., et al., *FSP1 is a glutathione-independent ferroptosis suppressor*. Nature, 2019. **575**(7784): p. 693-698.
296. Bersuker, K., et al., *The CoQ oxidoreductase FSP1 acts parallel to GPX4 to inhibit ferroptosis*. Nature, 2019. **575**(7784): p. 688-692.
297. Pietsch, E.C., et al., *The p53 family and programmed cell death*. Oncogene, 2008. **27**(50): p. 6507-6521.
298. Fridman, J.S. and S.W. Lowe, *Control of apoptosis by p53*. Oncogene, 2003. **22**(56): p. 9030-9040.
299. Ou, Y., et al., *Activation of SAT1 engages polyamine metabolism with p53-mediated ferroptotic responses*. Proceedings of the National Academy of Sciences of the United States of America, 2016. **113**(44): p. E6806-E6812.
300. Liu, J., et al., *The Regulation of Ferroptosis by Tumor Suppressor p53 and its Pathway*. Int J Mol Sci, 2020. **21**(21).
301. Tarangelo, A., et al., *p53 Suppresses Metabolic Stress-Induced Ferroptosis in Cancer Cells*. Cell Reports, 2018. **22**(3): p. 569-575.
302. Xie, Y., et al., *The Tumor Suppressor p53 Limits Ferroptosis by Blocking DPP4 Activity*. Cell Reports, 2017. **20**(7): p. 1692-1704.
303. Schrama, D., et al., *Characterization of six Merkel cell polyomavirus-positive Merkel cell carcinoma cell lines: Integration pattern suggest that large T antigen truncating events occur before or during integration*. Int J Cancer, 2019. **145**(4): p. 1020-1032.
304. Rosen, S.T., et al., *Establishment and characterization of a neuroendocrine skin carcinoma cell line*. Lab Invest, 1987. **56**(3): p. 302-12.
305. Van Gele, M., et al., *Combined karyotyping, CGH and M-FISH analysis allows detailed characterization of unidentified chromosomal rearrangements in Merkel cell carcinoma*. International Journal of Cancer, 2002. **101**(2): p. 137-145.
306. Guastafierro, A., et al., *Characterization of an early passage Merkel cell polyomavirus-positive Merkel cell carcinoma cell line, MS-1, and its growth in NOD scid gamma mice*. J Virol Methods, 2013. **187**(1): p. 6-14.
307. Leonard, J.H., et al., *Characterisation of four merkel cell carcinoma adherent cell lines*. International Journal of Cancer, 1995. **60**(1): p. 100-107.
308. Ronan, S.G., et al., *Merkel cell carcinoma: in vitro and in vivo characteristics of a new cell line*. J Am Acad Dermatol, 1993. **29**(5 Pt 1): p. 715-22.
309. Boukamp, P., et al., *Normal keratinization in a spontaneously immortalized aneuploid human keratinocyte cell line*. The Journal of cell biology, 1988. **106**(3): p. 761-771.

310. Todaro, G.J. and H. Green, *Quantitative studies of the growth of mouse embryo cells in culture and their development into established lines*. J Cell Biol, 1963. **17**(2): p. 299-313.
311. Niforou, K.N., et al., *The Proteome Profile of the Human Osteosarcoma U2OS Cell Line*. Cancer Genomics - Proteomics, 2008. **5**(1): p. 63.
312. Lin, Y.-C., et al., *Genome dynamics of the human embryonic kidney 293 lineage in response to cell biology manipulations*. Nature Communications, 2014. **5**(1): p. 4767.
313. Cailleau, R., et al., *Breast tumor cell lines from pleural effusions*. Journal of the National Cancer Institute, 1974. **53**(3): p. 661-674.
314. Sieiro, D., et al., *Cytoplasmic NOTCH and membrane-derived  $\beta$ -catenin link cell fate choice to epithelial-mesenchymal transition during myogenesis*. Elife, 2016. **5**.
315. Livak, K.J. and T.D. Schmittgen, *Analysis of Relative Gene Expression Data Using Real-Time Quantitative PCR and the  $2^{-\Delta\Delta CT}$  Method*. Methods, 2001. **25**(4): p. 402-408.
316. Sakuma, T., et al., *MMEJ-assisted gene knock-in using TALENs and CRISPR-Cas9 with the PITCh systems*. Nat Protoc, 2016. **11**(1): p. 118-33.
317. Moll, R., et al., *Cytokeratin 20 in human carcinomas. A new histodiagnostic marker detected by monoclonal antibodies*. Am J Pathol, 1992. **140**(2): p. 427-47.
318. Higashimoto, T., et al., *The woodchuck hepatitis virus post-transcriptional regulatory element reduces readthrough transcription from retroviral vectors*. Gene Therapy, 2007. **14**(17): p. 1298-1304.
319. Cole, C.N. and T.P. Stacy, *Identification of sequences in the herpes simplex virus thymidine kinase gene required for efficient processing and polyadenylation*. Mol Cell Biol, 1985. **5**(8): p. 2104-13.
320. Das, A.T., L. Tenenbaum, and B. Berkhout, *Tet-On Systems For Doxycycline-inducible Gene Expression*. Current gene therapy, 2016. **16**(3): p. 156-167.
321. Gossen, M., et al., *Transcriptional activation by tetracyclines in mammalian cells*. Science, 1995. **268**(5218): p. 1766.
322. Biswas, T.K. and G.S. Getz, *Promoter-promoter interactions influencing transcription of the yeast mitochondrial gene, *Oli 1*, coding for ATPase subunit 9. Cis and trans effects*. J Biol Chem, 1988. **263**(10): p. 4844-51.
323. Hoque, M.O., et al., *Aquaporin 1 Is Overexpressed in Lung Cancer and Stimulates NIH-3T3 Cell Proliferation and Anchorage-Independent Growth*. The American Journal of Pathology, 2006. **168**(4): p. 1345-1353.
324. Wang, C., et al., *TCRP1 promotes NIH/3T3 cell transformation by over-activating PDK1 and AKT1*. Oncogenesis, 2017. **6**(4): p. e323-e323.
325. *NIH3T3 Transformation Assay*, in *Encyclopedia of Cancer*, M. Schwab, Editor. 2009, Springer Berlin Heidelberg: Berlin, Heidelberg. p. 2081-2081.
326. Alvarez, A., G.A. Barisone, and E. Diaz, *Focus formation: a cell-based assay to determine the oncogenic potential of a gene*. Journal of visualized experiments : JoVE, 2014(94): p. 51742.
327. Oikonomou, E., et al., *BRAF(V600E) efficient transformation and induction of microsatellite instability versus KRAS(G12V) induction of senescence markers in human colon cancer cells*. Neoplasia (New York, N.Y.), 2009. **11**(11): p. 1116-1131.
328. Davies, H., et al., *Mutations of the BRAF gene in human cancer*. Nature, 2002. **417**(6892): p. 949-54.
329. Wright, M.C., et al., *Unipotent, Atoh1+ progenitors maintain the Merkel cell population in embryonic and adult mice*. The Journal of cell biology, 2015. **208**(3): p. 367-379.
330. Cress, D.E., P. Kumar, and J. Friz, *The RheoSwitch system for inducible up- and down-regulation of gene expression*. Cancer Research, 2006. **66**(8 Supplement): p. 27.
331. Palli, S.R., et al., *Improved ecdysone receptor-based inducible gene regulation system*. European Journal of Biochemistry, 2003. **270**(6): p. 1308-1315.

332. Barrett, J.A., et al., *Regulated intratumoral expression of IL-12 using a RheoSwitch Therapeutic System® (RTS®) gene switch as gene therapy for the treatment of glioma*. *Cancer Gene Therapy*, 2018. **25**(5): p. 106-116.
333. Webster, N., et al., *The yeast UASG is a transcriptional enhancer in human hela cells in the presence of the GAL4 trans-activator*. *Cell*, 1988. **52**(2): p. 169-178.
334. Pfeiffer, B.D., et al., *Refinement of Tools for Targeted Gene Expression in Drosophila*. *Genetics*, 2010. **186**(2): p. 735.
335. Liu, J., et al., *Notch signaling in the regulation of stem cell self-renewal and differentiation*. *Curr Top Dev Biol*, 2010. **92**: p. 367-409.
336. Kopan, R., et al., *Signal transduction by activated mNotch: importance of proteolytic processing and its regulation by the extracellular domain*. *Proceedings of the National Academy of Sciences*, 1996. **93**(4): p. 1683.
337. Chillakuri, C.R., et al., *Notch receptor-ligand binding and activation: insights from molecular studies*. *Seminars in cell & developmental biology*, 2012. **23**(4): p. 421-428.
338. Wu, L., et al., *MAML1, a human homologue of Drosophila mastermind, is a transcriptional co-activator for NOTCH receptors*. *Nat Genet*, 2000. **26**(4): p. 484-9.
339. Maillard, I., et al., *Mastermind critically regulates Notch-mediated lymphoid cell fate decisions*. *Blood*, 2004. **104**(6): p. 1696-1702.
340. Hu, M.C.T. and N. Davidson, *The inducible lac operator-repressor system is functional in mammalian cells*. *Cell*, 1987. **48**(4): p. 555-566.
341. Myung, S.H., et al., *Development of the Mammalian Expression Vector System that can be Induced by IPTG and/or Lactose*. *J Microbiol Biotechnol*, 2020. **30**(8): p. 1124-1131.
342. Meissner, A., M. Wernig, and R. Jaenisch, *Direct reprogramming of genetically unmodified fibroblasts into pluripotent stem cells*. *Nature Biotechnology*, 2007. **25**(10): p. 1177-1181.
343. Lowry, W.E., et al., *Generation of human induced pluripotent stem cells from dermal fibroblasts*. *Proceedings of the National Academy of Sciences*, 2008. **105**(8): p. 2883.
344. Takahashi, K. and S. Yamanaka, *Induction of pluripotent stem cells from mouse embryonic and adult fibroblast cultures by defined factors*. *Cell*, 2006. **126**(4): p. 663-76.
345. Alvero, A.B., et al., *Telomerase prolongs the lifespan of normal human ovarian surface epithelial cells without inducing neoplastic phenotype*. *J Soc Gynecol Investig*, 2004. **11**(8): p. 553-61.
346. Kang, M.K. and N.H. Park, *Extension of cell life span using exogenous telomerase*. *Methods Mol Biol*, 2007. **371**: p. 151-65.
347. Milyavsky, M., et al., *Prolonged Culture of Telomerase-Immortalized Human Fibroblasts Leads to a Premalignant Phenotype*. *Cancer Research*, 2003. **63**(21): p. 7147.
348. Boukamp, P., et al., *Normal keratinization in a spontaneously immortalized aneuploid human keratinocyte cell line*. *J Cell Biol*, 1988. **106**(3): p. 761-71.
349. Lehman, T.A., et al., *p53 Mutations in human immortalized epithelial cell lines*. *Carcinogenesis*, 1993. **14**(5): p. 833-839.
350. Galvin, K.E., et al., *Gli1 Induces G2/M Arrest and Apoptosis in Hippocampal but Not Tumor-Derived Neural Stem Cells*. *STEM CELLS*, 2008. **26**(4): p. 1027-1036.
351. Isaka, F., et al., *Ectopic expression of the bHLH gene Math1 disturbs neural development*. *European Journal of Neuroscience*, 1999. **11**(7): p. 2582-2588.
352. DeCaprio, J.A., *Merkel cell polyomavirus and Merkel cell carcinoma*. *Philos Trans R Soc Lond B Biol Sci*, 2017. **372**(1732).
353. Eling, N., et al., *Identification of artesunate as a specific activator of ferroptosis in pancreatic cancer cells*. *Oncoscience*, 2015. **2**(5): p. 517-32.
354. Våtsveen, T.K., et al., *Artesunate shows potent anti-tumor activity in B-cell lymphoma*. *J Hematol Oncol*, 2018. **11**(1): p. 23.
355. Luo, J., et al., *Artesunate and Dihydroartemisinin Inhibit Rabies Virus Replication*. *Virologica Sinica*, 2021.

356. Feng, H., et al., *Cellular and viral factors regulating Merkel cell polyomavirus replication*. PLoS One, 2011. **6**(7): p. e22468.
357. White, M.K., M. Safak, and K. Khalili, *Regulation of Gene Expression in Primate Polyomaviruses*. Journal of Virology, 2009. **83**(21): p. 10846.
358. Sarma, B., et al., *Artesunate Affects T Antigen Expression and Survival of Virus-Positive Merkel Cell Carcinoma*. Cancers (Basel), 2020. **12**(4).
359. Houben, R., et al., *Merkel cell carcinoma and Merkel cell polyomavirus: evidence for hit-and-run oncogenesis*. J Invest Dermatol, 2012. **132**(1): p. 254-6.
360. Houben, R., et al., *An intact retinoblastoma protein-binding site in Merkel cell polyomavirus large T antigen is required for promoting growth of Merkel cell carcinoma cells*. International Journal of Cancer, 2012. **130**(4): p. 847-856.
361. Zhou, C., et al., *Artesunate induces apoptosis via a Bak-mediated caspase-independent intrinsic pathway in human lung adenocarcinoma cells*. J Cell Physiol, 2012. **227**(12): p. 3778-86.
362. Zuo, W., Z.Z. Wang, and J. Xue, *Artesunate induces apoptosis of bladder cancer cells by miR-16 regulation of COX-2 expression*. Int J Mol Sci, 2014. **15**(8): p. 14298-312.
363. Liu, L., et al., *Artesunate induces apoptosis and inhibits growth of Eca109 and Ec9706 human esophageal cancer cell lines in vitro and in vivo*. Mol Med Rep, 2015. **12**(1): p. 1465-1472.
364. Strober, W., *Trypan Blue Exclusion Test of Cell Viability*. Current protocols in immunology, 2015. **111**: p. A3.B.1-A3.B.3.
365. Pozarowski, P. and Z. Darzynkiewicz, *Analysis of cell cycle by flow cytometry*. Methods Mol Biol, 2004. **281**: p. 301-11.
366. Compton, M.M., *A biochemical hallmark of apoptosis: internucleosomal degradation of the genome*. Cancer Metastasis Rev, 1992. **11**(2): p. 105-19.
367. Galluzzi, L., et al., *Molecular definitions of cell death subroutines: recommendations of the Nomenclature Committee on Cell Death 2012*. Cell Death & Differentiation, 2012. **19**(1): p. 107-120.
368. Slee, E.A., et al., *Benzyloxycarbonyl-Val-Ala-Asp (OMe) fluoromethylketone (Z-VAD.FMK) inhibits apoptosis by blocking the processing of CPP32*. Biochem J, 1996. **315 ( Pt 1)**(Pt 1): p. 21-4.
369. Wang, N., et al., *Artesunate activates the ATF4-CHOP-CHAC1 pathway and affects ferroptosis in Burkitt's Lymphoma*. Biochem Biophys Res Commun, 2019. **519**(3): p. 533-539.
370. Li, Z.-j., et al., *Artesunate synergizes with sorafenib to induce ferroptosis in hepatocellular carcinoma*. Acta Pharmacologica Sinica, 2021. **42**(2): p. 301-310.
371. Ursini, F. and M. Maiorino, *Lipid peroxidation and ferroptosis: The role of GSH and GPx4*. Free Radical Biology and Medicine, 2020. **152**: p. 175-185.
372. Doll, S. and M. Conrad, *Iron and ferroptosis: A still ill-defined liaison*. IUBMB Life, 2017. **69**(6): p. 423-434.
373. Kim, J.-H., T.M. Lewin, and R.A. Coleman, *Expression and Characterization of Recombinant Rat Acyl-CoA Synthetases 1, 4, and 5: SELECTIVE INHIBITION BY TRIACSIN C AND THIAZOLIDINEDIONES\**. Journal of Biological Chemistry, 2001. **276**(27): p. 24667-24673.
374. Sato, M., et al., *The ferroptosis inducer erastin irreversibly inhibits system x c – and synergizes with cisplatin to increase cisplatin's cytotoxicity in cancer cells*. Scientific Reports, 2018. **8**(1): p. 968.
375. Liu, M.-r., W.-t. Zhu, and D.-s. Pei, *System Xc – : a key regulatory target of ferroptosis in cancer*. Investigational New Drugs, 2021.
376. Wang, S.-J., et al., *Acetylation Is Crucial for p53-Mediated Ferroptosis and Tumor Suppression*. Cell Reports, 2016. **17**(2): p. 366-373.
377. Kang, R., G. Kroemer, and D. Tang, *The tumor suppressor protein p53 and the ferroptosis network*. Free Radical Biology and Medicine, 2019. **133**: p. 162-168.

378. Vassilev, L.T., et al., *In Vivo Activation of the p53 Pathway by Small-Molecule Antagonists of MDM2*. Science, 2004. **303**(5659): p. 844.
379. Samimi, M., *Immune Checkpoint Inhibitors and Beyond: An Overview of Immune-Based Therapies in Merkel Cell Carcinoma*. American Journal of Clinical Dermatology, 2019. **20**(3): p. 391-407.
380. Gavvovidis, I., et al., *Targeting Merkel Cell Carcinoma by Engineered T Cells Specific to T-Antigens of Merkel Cell Polyomavirus*. Clinical cancer research : an official journal of the American Association for Cancer Research, 2018. **24**(15): p. 3644-3655.
381. Datta, C.K. and C.B. Mendoza, Jr., *Merkel cell carcinoma: an aggressive neoplasm*. W V Med J, 1999. **95**(3): p. 127-9.
382. Pergolizzi, J., Jr., et al., *Merkel cell carcinoma: an aggressive malignancy*. Am Surg, 1997. **63**(5): p. 450-4.
383. Calder, K.B. and B.R. Smoller, *New Insights Into Merkel Cell Carcinoma*. Advances in Anatomic Pathology, 2010. **17**(3).
384. Auburger, G., et al., *Primary Skin Fibroblasts as a Model of Parkinson's Disease*. Molecular Neurobiology, 2012. **46**(1): p. 20-27.
385. Ichim, T.E., P. O'Heeron, and S. Kesari, *Fibroblasts as a practical alternative to mesenchymal stem cells*. Journal of Translational Medicine, 2018. **16**(1): p. 212.
386. Takahashi, K., et al., *Induction of pluripotent stem cells from adult human fibroblasts by defined factors*. Cell, 2007. **131**(5): p. 861-72.
387. Das, A.T., et al., *Selecting the optimal Tet-On system for doxycycline-inducible gene expression in transiently transfected and stably transduced mammalian cells*. Biotechnology Journal, 2016. **11**(1): p. 71-79.
388. Gomes, L., G. Monteiro, and F. Mergulhão, *The Impact of IPTG Induction on Plasmid Stability and Heterologous Protein Expression by Escherichia coli Biofilms*. Int J Mol Sci, 2020. **21**(2).
389. Grespi, F., et al., *Generation and Evaluation of an IPTG-Regulated Version of Vav-Gene Promoter for Mouse Transgenesis*. PLOS ONE, 2011. **6**(3): p. e18051.
390. Deans, T.L., C.R. Cantor, and J.J. Collins, *A Tunable Genetic Switch Based on RNAi and Repressor Proteins for Regulating Gene Expression in Mammalian Cells*. Cell, 2007. **130**(2): p. 363-372.
391. Wallbaum, S., et al., *Cell cycle quiescence can suppress transcription from an ecdysone receptor-based inducible promoter in mammalian cells*. BioTechniques, 2009. **46**(6): p. 433-440.
392. Curtin, J.A., et al., *Bidirectional promoter interference between two widely used internal heterologous promoters in a late-generation lentiviral construct*. Gene Therapy, 2008. **15**(5): p. 384-390.
393. Shearwin, K.E., B.P. Callen, and J.B. Egan, *Transcriptional interference--a crash course*. Trends in genetics : TIG, 2005. **21**(6): p. 339-345.
394. Bodnar, A.G., et al., *Extension of life-span by introduction of telomerase into normal human cells*. Science, 1998. **279**(5349): p. 349-52.
395. Huang, X.-Q., et al., *hTERT Extends Proliferative Lifespan and Prevents Oxidative Stress-Induced Apoptosis in Human Lens Epithelial Cells*. Investigative Ophthalmology & Visual Science, 2005. **46**(7): p. 2503-2513.
396. Griukova, A., et al., *P38 MAPK inhibition prevents polybrene-induced senescence of human mesenchymal stem cells during viral transduction*. PloS one, 2018. **13**(12): p. e0209606-e0209606.
397. Nygaard, U.H., et al., *Antibiotics in cell culture: friend or foe? Suppression of keratinocyte growth and differentiation in monolayer cultures and 3D skin models*. Experimental Dermatology, 2015. **24**(12): p. 964-965.
398. *Antibiotics Reduce the Growth Rate and Differentiation of Embryonic Stem Cell Cultures*. Tissue Engineering, 2006. **12**(7): p. 2025-2030.

399. Fu, Y., et al., *High-frequency off-target mutagenesis induced by CRISPR-Cas nucleases in human cells*. Nature Biotechnology, 2013. **31**(9): p. 822-826.
400. Zhang, X.-H., et al., *Off-target Effects in CRISPR/Cas9-mediated Genome Engineering*. Molecular Therapy - Nucleic Acids, 2015. **4**: p. e264.
401. Lino, C.A., et al., *Delivering CRISPR: a review of the challenges and approaches*. Drug delivery, 2018. **25**(1): p. 1234-1257.
402. Yang, H., et al., *One-step generation of mice carrying reporter and conditional alleles by CRISPR/Cas-mediated genome engineering*. Cell, 2013. **154**(6): p. 1370-1379.
403. Rattan, S.I.S., et al., *Autofluorescence as an index of ageing in human fibroblasts in culture*. Bioscience Reports, 1982. **2**(8): p. 561-567.
404. Poot, M., et al., *Autofluorescence of Human Skin Fibroblasts during Growth Inhibition and in vitro Ageing*. Gerontology, 1985. **31**(3): p. 158-165.
405. Pavez Lorie, E., et al., *Characterisation of the novel spontaneously immortalized and invasively growing human skin keratinocyte line HaSKpw*. Scientific Reports, 2020. **10**(1): p. 15196.
406. Curry, E.L., et al., *Using induced pluripotent stem cells as a tool for modelling carcinogenesis*. World journal of stem cells, 2015. **7**(2): p. 461-469.
407. Kim, J.J., *Applications of iPSCs in Cancer Research*. Biomarker insights, 2015. **10**(Suppl 1): p. 125-131.
408. Sancho-Martinez, I., et al., *Establishment of human iPSC-based models for the study and targeting of glioma initiating cells*. Nature Communications, 2016. **7**(1): p. 10743.
409. Lee, J., et al., *Hair-bearing human skin generated entirely from pluripotent stem cells*. Nature, 2020. **582**(7812): p. 399-404.
410. Colunga, A., T. Pulliam, and P. Nghiem, *Merkel Cell Carcinoma in the Age of Immunotherapy: Facts and Hopes*. Clinical cancer research : an official journal of the American Association for Cancer Research, 2018. **24**(9): p. 2035-2043.
411. Serafin, M.B., et al., *Drug Repositioning in Oncology*. Am J Ther, 2021. **28**(1): p. e111-e117.
412. Masuda, T., et al., *Drug repositioning in cancer: The current situation in Japan*. Cancer science, 2020. **111**(4): p. 1039-1046.
413. Shim, J.S. and J.O. Liu, *Recent advances in drug repositioning for the discovery of new anticancer drugs*. International journal of biological sciences, 2014. **10**(7): p. 654-663.
414. Li, Y.-Q., et al., *Repositioning of Antiparasitic Drugs for Tumor Treatment*. Frontiers in Oncology, 2021. **11**(1539).
415. Firestone, T.M., et al., *Repurposing Quinoline and Artemisinin Antimalarials as Therapeutics for SARS-CoV-2: Rationale and Implications*. ACS Pharmacology & Translational Science, 2021. **4**(2): p. 613-623.
416. Cao, R., et al., *Anti-SARS-CoV-2 Potential of Artemisinins In Vitro*. ACS Infectious Diseases, 2020. **6**(9): p. 2524-2531.
417. DeMeritt, I.B., L.E. Milford, and A.D. Yurochko, *Activation of the NF- $\kappa$ B Pathway in Human Cytomegalovirus-Infected Cells Is Necessary for Efficient Transactivation of the Major Immediate-Early Promoter*. Journal of Virology, 2004. **78**(9): p. 4498-4507.
418. Ajuh, E.T., et al., *Novel Human Polyomavirus Noncoding Control Regions Differ in Bidirectional Gene Expression according to Host Cell, Large T-Antigen Expression, and Clinically Occurring Rearrangements*. Journal of virology, 2018. **92**(7): p. e02231-17.
419. Dynan, W.S. and R. Tjian, *The promoter-specific transcription factor Sp1 binds to upstream sequences in the SV40 early promoter*. Cell, 1983. **35**(1): p. 79-87.
420. Raj, G.V., et al., *Transcriptional regulation of human polyomavirus JC: evidence for a functional interaction between RelA (p65) and the Y-box-binding protein, YB-1*. J Virol, 1996. **70**(9): p. 5944-53.

421. Kumar, K.U., A. Pater, and M.M. Pater, *Human JC virus perfect palindromic nuclear factor 1-binding sequences important for glial cell-specific expression in differentiating embryonal carcinoma cells*. J Virol, 1993. **67**(1): p. 572-6.
422. Kraus, R.J., L. Shadley, and J.E. Mertz, *Nuclear factor 1 family members mediate repression of the BK virus late promoter*. Virology, 2001. **287**(1): p. 89-104.
423. Kwun, H.J., Y. Chang, and P.S. Moore, *Protein-mediated viral latency is a novel mechanism for Merkel cell polyomavirus persistence*. Proceedings of the National Academy of Sciences of the United States of America, 2017. **114**(20): p. E4040-E4047.
424. Abdulsalam, I., et al., *Promoter activity of Merkel cell Polyomavirus variants in human dermal fibroblasts and a Merkel cell carcinoma cell line*. Virology journal, 2020. **17**(1): p. 54-54.
425. Kobayashi, D., et al., *Translationally Controlled Tumor Protein Is a Novel Biological Target for Neurofibromatosis Type 1-associated Tumors\**. Journal of Biological Chemistry, 2014. **289**(38): p. 26314-26326.
426. Williams, G.H. and K. Stoeber, *The cell cycle and cancer*. The Journal of Pathology, 2012. **226**(2): p. 352-364.
427. Greenshields, A.L., T.G. Shepherd, and D.W. Hoskin, *Contribution of reactive oxygen species to ovarian cancer cell growth arrest and killing by the anti-malarial drug artesunate*. Molecular Carcinogenesis, 2017. **56**(1): p. 75-93.
428. Hafner, C., et al., *Activation of the PI3K/AKT pathway in Merkel cell carcinoma*. PloS one, 2012. **7**(2): p. e31255-e31255.
429. Jing, W., et al., *Artesunate promotes sensitivity to sorafenib in hepatocellular carcinoma*. Biochemical and Biophysical Research Communications, 2019. **519**(1): p. 41-45.
430. Thanaketpaisarn, O., et al., *Artesunate enhances TRAIL-induced apoptosis in human cervical carcinoma cells through inhibition of the NF- $\kappa$ B and PI3K/Akt signaling pathways*. Int J Oncol, 2011. **39**(1): p. 279-85.
431. Adam, C., et al., *The HSP70 modulator MAL3-101 inhibits Merkel cell carcinoma*. PLoS One, 2014. **9**(4): p. e92041.
432. Xu, Q., et al., *Artesunate inhibits growth and induces apoptosis in human osteosarcoma HOS cell line in vitro and in vivo*. Journal of Zhejiang University. Science. B, 2011. **12**(4): p. 247-255.
433. Mori, Y., et al., *A study of apoptosis in Merkel cell carcinoma: an immunohistochemical, ultrastructural, DNA ladder, and TUNEL labeling study*. Am J Dermatopathol, 2001. **23**(1): p. 16-23.
434. Conrad, M., et al., *Regulation of lipid peroxidation and ferroptosis in diverse species*. Genes & development, 2018. **32**(9-10): p. 602-619.
435. Jones, G., et al., *Combating iron overload: a case for deferoxamine-based nanochelators*. Nanomedicine, 2020. **15**(13): p. 1341-1356.
436. Yamamoto, A., et al., *Bafilomycin A1 prevents maturation of autophagic vacuoles by inhibiting fusion between autophagosomes and lysosomes in rat hepatoma cell line, H-4-II-E cells*. Cell Struct Funct, 1998. **23**(1): p. 33-42.
437. Jiang, X., M. Overholtzer, and C.B. Thompson, *Autophagy in cellular metabolism and cancer*. J Clin Invest, 2015. **125**(1): p. 47-54.
438. Morris, C.A., et al., *Review of the clinical pharmacokinetics of artesunate and its active metabolite dihydroartemisinin following intravenous, intramuscular, oral or rectal administration*. Malaria Journal, 2011. **10**(1): p. 263.
439. Gautam, A., et al., *Pharmacokinetics and pharmacodynamics of endoperoxide antimalarials*. Curr Drug Metab, 2009. **10**(3): p. 289-306.
440. Chen, G.-Q., et al., *Artemisinin compounds sensitize cancer cells to ferroptosis by regulating iron homeostasis*. Cell Death & Differentiation, 2020. **27**(1): p. 242-254.
441. Xie, Y., et al., *Posttranslational modification of autophagy-related proteins in macroautophagy*. Autophagy, 2015. **11**(1): p. 28-45.

442. Askari, B., et al., *Rosiglitazone inhibits acyl-CoA synthetase activity and fatty acid partitioning to diacylglycerol and triacylglycerol via a peroxisome proliferator-activated receptor-gamma-independent mechanism in human arterial smooth muscle cells and macrophages*. *Diabetes*, 2007. **56**(4): p. 1143-52.
443. Koppula, P., L. Zhuang, and B. Gan, *Cystine transporter SLC7A11/xCT in cancer: ferroptosis, nutrient dependency, and cancer therapy*. *Protein & Cell*, 2020.
444. Yang, W.S., et al., *Peroxidation of polyunsaturated fatty acids by lipoxygenases drives ferroptosis*. *Proceedings of the National Academy of Sciences of the United States of America*, 2016. **113**(34): p. E4966-E4975.
445. Gaschler, M.M., et al., *FINO(2) initiates ferroptosis through GPX4 inactivation and iron oxidation*. *Nature chemical biology*, 2018. **14**(5): p. 507-515.
446. Chen, J., et al., *The Potential Value of Targeting Ferroptosis in Early Brain Injury After Acute CNS Disease*. *Frontiers in Molecular Neuroscience*, 2020. **13**(110).
447. Rees, M.G., et al., *Correlating chemical sensitivity and basal gene expression reveals mechanism of action*. *Nature Chemical Biology*, 2016. **12**(2): p. 109-116.
448. Picardo, M., et al., *Imbalance in the antioxidant pool in melanoma cells and normal melanocytes from patients with melanoma*. *J Invest Dermatol*, 1996. **107**(3): p. 322-6.
449. Rusциani, L., et al., *Low plasma coenzyme Q10 levels as an independent prognostic factor for melanoma progression*. *Journal of the American Academy of Dermatology*, 2006. **54**(2): p. 234-241.
450. Thapa, M. and G. Dallmann, *Role of coenzymes in cancer metabolism*. *Seminars in Cell & Developmental Biology*, 2020. **98**: p. 44-53.
451. Karni-Schmidt, O., M. Lokshin, and C. Prives, *The Roles of MDM2 and MDMX in Cancer*. *Annual review of pathology*, 2016. **11**: p. 617-644.
452. Venkatesh, D., et al., *MDM2 and MDMX promote ferroptosis by PPAR $\alpha$ -mediated lipid remodeling*. *Genes & development*, 2020. **34**(7-8): p. 526-543.
453. Friedmann Angeli, J.P., et al., *Inactivation of the ferroptosis regulator Gpx4 triggers acute renal failure in mice*. *Nature cell biology*, 2014. **16**(12): p. 1180-1191.
454. Seiler, A., et al., *Glutathione peroxidase 4 senses and translates oxidative stress into 12/15-lipoxygenase dependent- and AIF-mediated cell death*. *Cell Metab*, 2008. **8**(3): p. 237-48.
455. Zuo, S., et al., *Novel insights on targeting ferroptosis in cancer therapy*. *Biomarker Research*, 2020. **8**(1): p. 50.
456. Shimada, K., et al., *Global survey of cell death mechanisms reveals metabolic regulation of ferroptosis*. *Nature Chemical Biology*, 2016. **12**(7): p. 497-503.
457. Gaschler, M.M., et al., *FINO2 initiates ferroptosis through GPX4 inactivation and iron oxidation*. *Nature Chemical Biology*, 2018. **14**(5): p. 507-515.
458. Turunen, M., J. Olsson, and G. Dallner, *Metabolism and function of coenzyme Q*. *Biochimica et Biophysica Acta (BBA) - Biomembranes*, 2004. **1660**(1): p. 171-199.
459. Grünler, J., J. Ericsson, and G. Dallner, *Branch-point reactions in the biosynthesis of cholesterol, dolichol, ubiquinone and prenylated proteins*. *Biochimica et Biophysica Acta (BBA) - Lipids and Lipid Metabolism*, 1994. **1212**(3): p. 259-277.
460. Zilfou, J.T. and S.W. Lowe, *Tumor suppressive functions of p53*. *Cold Spring Harbor perspectives in biology*, 2009. **1**(5): p. a001883-a001883.
461. Murphy, M., *The Thousand Doors that Lead to Death: p53-Dependent Repression and Apoptosis*. *Cancer Biology & Therapy*, 2003. **2**(4): p. 381-382.
462. Rivlin, N., et al., *Mutations in the p53 Tumor Suppressor Gene: Important Milestones at the Various Steps of Tumorigenesis*. *Genes & cancer*, 2011. **2**(4): p. 466-474.
463. Toyooka, S., T. Tsuda, and A.F. Gazdar, *The TP53 gene, tobacco exposure, and lung cancer*. *Hum Mutat*, 2003. **21**(3): p. 229-39.
464. Zhang, Y., et al., *p53 Promoted Ferroptosis in Ovarian Cancer Cells Treated with Human Serum Incubated-Superparamagnetic Iron Oxides*. *Int J Nanomedicine*, 2021. **16**: p. 283-296.

465. Markowitsch, S.D., et al., *Artesunate Inhibits Growth of Sunitinib-Resistant Renal Cell Carcinoma Cells through Cell Cycle Arrest and Induction of Ferroptosis*. *Cancers (Basel)*, 2020. **12**(11).
466. Gonzalez-Aparicio, M., et al., *Oxaliplatin in combination with liver-specific expression of interleukin 12 reduces the immunosuppressive microenvironment of tumours and eradicates metastatic colorectal cancer in mice*. *Gut*, 2011. **60**(3): p. 341.
467. Ebert, P.J.R., et al., *MAP Kinase Inhibition Promotes T Cell and Anti-tumor Activity in Combination with PD-L1 Checkpoint Blockade*. *Immunity*, 2016. **44**(3): p. 609-621.
468. Kumar, S., et al., *A Phase I Study of the Chinese Herbal Medicine PHY906 as a Modulator of Irinotecan-based Chemotherapy in Patients with Advanced Colorectal Cancer*. *Clinical Colorectal Cancer*, 2011. **10**(2): p. 85-96.
469. Li, W., et al., *Artesunate exhibits synergistic anti-cancer effects with cisplatin on lung cancer A549 cells by inhibiting MAPK pathway*. *Gene*, 2021. **766**: p. 145134.
470. Wang, Z., et al., *The combination of artesunate and carboplatin exerts a synergistic anti-tumour effect on non-small cell lung cancer*. *Clinical and Experimental Pharmacology and Physiology*, 2020. **47**(6): p. 1083-1091.
471. Yan, D., et al., *Artemisinin improves the efficiency of anti-PD-L1 therapy in T-cell lymphoma*. *The Journal of Immunology*, 2020. **204**(1 Supplement): p. 241.46.
472. Duan, X., et al., *Immunostimulatory nanomedicines synergize with checkpoint blockade immunotherapy to eradicate colorectal tumors*. *Nature Communications*, 2019. **10**(1): p. 1899.
473. Mancuso, R.I., S.T. Olalla Saad, and J.H. Azambuja, *Artesunate Switches Monocytes to an Inflammatory Phenotype with the Ability to Kill Leukemic Cells*. *Int J Mol Sci*, 2021. **22**(2).
474. Shang, S., et al., *Artesunate interacts with the vitamin D receptor to reverse sepsis-induced immunosuppression in a mouse model via enhancing autophagy*. *British Journal of Pharmacology*, 2020. **177**(18): p. 4147-4165.
475. Kuang, M., et al., *Artesunate Attenuates Pro-Inflammatory Cytokine Release from Macrophages by Inhibiting TLR4-Mediated Autophagic Activation via the TRAF6-Beclin1-PI3KC3 Pathway*. *Cellular Physiology and Biochemistry*, 2018. **47**(2): p. 475-488.
476. Wang, D., et al., *Artesunate Attenuates Lipopolysaccharide-Stimulated Proinflammatory Responses by Suppressing TLR4, MyD88 Expression, and NF- $\kappa$ B Activation in Microglial Cells*. *Inflammation*, 2015. **38**(5): p. 1925-32.
477. Qian, P., et al., *Artesunate enhances  $\gamma\delta$  T-cell-mediated antitumor activity through augmenting  $\gamma\delta$  T-cell function and reversing immune escape of HepG2 cells*. *Immunopharmacology and Immunotoxicology*, 2018. **40**(2): p. 107-116.
478. Wieczorek, M., et al., *Major Histocompatibility Complex (MHC) Class I and MHC Class II Proteins: Conformational Plasticity in Antigen Presentation*. *Frontiers in Immunology*, 2017. **8**(292).
479. Gou, Q., et al., *PD-L1 degradation pathway and immunotherapy for cancer*. *Cell Death & Disease*, 2020. **11**(11): p. 955.
480. Ritprajak, P. and M. Azuma, *Intrinsic and extrinsic control of expression of the immunoregulatory molecule PD-L1 in epithelial cells and squamous cell carcinoma*. *Oral Oncology*, 2015. **51**(3): p. 221-228.
481. Zhang, H., et al., *Eliminating Radiation Resistance of Non-Small Cell Lung Cancer by Dihydroartemisinin Through Abrogating Immunity Escaping and Promoting Radiation Sensitivity by Inhibiting PD-L1 Expression*. *Frontiers in oncology*, 2020. **10**: p. 595466-595466.
482. Cornel, A.M., I.L. Mimpfen, and S. Nierkens, *MHC Class I Downregulation in Cancer: Underlying Mechanisms and Potential Targets for Cancer Immunotherapy*. *Cancers*, 2020. **12**(7): p. 1760.

483. Chapuis, A.G., et al., *Regression of metastatic Merkel cell carcinoma following transfer of polyomavirus-specific T cells and therapies capable of re-inducing HLA class-I*. *Cancer Immunol Res*, 2014. **2**(1): p. 27-36.
484. Angelo, S.P., et al., *Avelumab in patients with previously treated metastatic Merkel cell carcinoma: long-term data and biomarker analyses from the single-arm phase 2 JAVELIN Merkel 200 trial*. *Journal for ImmunoTherapy of Cancer*, 2020. **8**(1): p. e000674.
485. Chin, K., V.K. Chand, and D.S.A. Nuyten, *Avelumab: clinical trial innovation and collaboration to advance anti-PD-L1 immunotherapy*. *Annals of oncology : official journal of the European Society for Medical Oncology*, 2017. **28**(7): p. 1658-1666.
486. Zhou, Z., et al., *Intestinal SIRT1 Deficiency Protects Mice from Ethanol-Induced Liver Injury by Mitigating Ferroptosis*. *The American Journal of Pathology*, 2020. **190**(1): p. 82-92.
487. Li, W., et al., *Ferroptotic cell death and TLR4/Trif signaling initiate neutrophil recruitment after heart transplantation*. *J Clin Invest*, 2019. **129**(6): p. 2293-2304.
488. Sun, Y., et al., *The emerging role of ferroptosis in inflammation*. *Biomedicine & Pharmacotherapy*, 2020. **127**: p. 110108.
489. Proneth, B. and M. Conrad, *Ferroptosis and necroinflammation, a yet poorly explored link*. *Cell Death & Differentiation*, 2019. **26**(1): p. 14-24.

## **6. Appendix**

### **6.1 List of tables**

**Table 1:** Characteristics of various modes of cell death.

### **6.2 List of figures**

**Figure 1:** Schematic representation of the skin and location of epidermal stem cells.

**Figure 2:** Appearance of MCC tumors on the skin.

**Figure 3:** Schematic representation of the MCPyV genome and its early region transcripts/proteins.

**Figure 4:** Histology of MCC tumors.

**Figure 5:** Speculated cells of origin of MCC.

**Figure 6:** The source and structure of artesunate.

**Figure 7:** Important aspects of ferroptosis.

**Figure 8:** Schematic representation of a potential approach to study *in vitro* oncogenesis and differentiation processes of MCPyV-positive MCC.

**Figure 9:** Gene expression of ten MCPyV-positive MCC cell surface markers shortlisted post-RNA sequencing.

**Figure 10:** Flow cytometric staining for the ten cell surface markers shortlisted post-RNA sequencing.

**Figure 11:** Design of the KRT20 donor and confirmation of the functionality of the KRT20 fluorescence reporter system in WaGa cells.

**Figure 12:** Design and confirmation of inducibility and functionality of the T antigen expression vectors.

**Figure 13:** Design and functionality of the RheoSwitch-inducible lentiviral vector intended for the inducible expression of ATOH1.

**Figure 14:** Design and functionality of the IPTG-inducible lentiviral vector intended for the inducible expression of GLI1 and dnMAML1.

**Figure 15:** Introduction of the KRT20 donor construct in primary fibroblasts.

**Figure 16:** hTERT expression increased the proliferative potential of primary fibroblasts.

**Figure 17:** Inducibility testing of the various vectors in KRT20-fibroblasts.

**Figure 18:** Inducibility testing of representative single cell clones of genetically manipulated KRT20-fibroblasts.

**Figure 19:** Introduction of the KRT20 donor construct in HaCaT cells.

**Figure 20:** Inducibility testing of the various vectors in genetically manipulated KRT20-HaCaT cells.

**Figure 21:** Testing of the genetically manipulated KRT20-HaCaT single cell clone 3 as a precursor for MCC-like cell formation.

**Figure 22:** Testing of the genetically manipulated KRT20-HaCaT cells expressing inducible T antigens and overexpressing ATOH1 and GLI1 as precursors for MCC-like cell formation.

**Figure 23:** Artesunate is strongly cytotoxic towards MCPyV-positive MCC cell lines *in vitro*.

**Figure 24:** Artesunate downregulates LT expression in MCPyV-positive MCC cell lines.

**Figure 25:** Further mechanisms along with T antigen inhibition are involved in artesunate-induced cell death of MCPyV-positive MCCs.

**Figure 26:** T antigen expression sensitizes WaGa cells to artesunate.

**Figure 27:** Artesunate-induced cell death of MCPyV-positive MCCs is not associated with typical apoptotic signatures.

**Figure 28:** The rescue of artesunate-induced cell death in MCPyV-positive MCCs by various ferroptosis inhibitors supports a ferroptotic mode of cell death.

**Figure 29:** Ferroptosis suppressor protein 1 (FSP1) does not play a crucial role in artesunate-induced ferroptosis of MCPyV-positive MCCs.

**Figure 30:** p53 does not exhibit a pro-ferroptotic role in artesunate-induced ferroptosis of MCPyV-positive MCCs.

**Figure 31:** Artesunate suppresses tumor growth *in vivo*.

**Figure 32:** Artesunate does not interfere with the upregulation of immune-relevant molecules on MCPyV-positive MCCs.

### **6.3 Abbreviations**

4E-BP1	4E-binding protein 1
$\beta$ -ME	$\beta$ -Mercaptoethanol
$\mu$ g	microgram
$\mu$ l	microlitre
$\mu$ m	micrometer
$\mu$ M	micromolar
ACSL4	Acyl-CoA synthetase long-chain family member 4
ADRA2C	Adrenoceptor Alpha 2C
AKT	AKT serine/threonine kinase
ALTO	alternate frame of the large T open reading frame
ART	Artesunate
ASXL1	ASXL transcriptional regulator 1
ATM	ATM serine/threonine kinase
ATOH1	Atonal BHLH Transcription Factor 1
ATP	Adenosine triphosphate
BAF-A1	Bafilomycin A1
BSA	Bovine serum albumin
BSD	Blasticidin
CA9	Carbonic Anhydrase 9
Cas9	CRISPR associated protein 9
cDNA	Complementary DNA
CELSR3	Cadherin EGF LAG Seven-Pass G-Type Receptor 3
CNTN2	Contactin 2
CoQ10	coenzyme Q10
CRISPR	Clustered regularly interspaced short palindromic repeats
DFO	Deferoxamine
DHA	Dihydroartemisinin
DLL3	Delta Like Canonical Notch Ligand 3
DMSO	Dimethyl sulfoxide
DNA	Deoxyribonucleic acid
dnMAML1	dominant-negative Mastermind-like1
Dox	Doxycycline
DPP4	Dipeptidyl peptidase-4
eGFP	Enhanced green fluorescent protein
FBS	Fetal Bovine Serum
Fer-1	Ferrostatin-1
FPKM	Fragments per Kilobase per Million mapped reads
FSP1	Ferroptosis suppressor protein 1
g	gram
GFP	Green fluorescent protein

GLI1	GLI family zinc finger 1
GPC3	Glypican 3
GPX4	Glutathione peroxidase 4
GSH	glutathione
HCMV	Human cytomegalovirus
HES1	Hes family bHLH transcription factor 1
HLA	Human leukocyte antigen
hTERT	Human telomerase reverse transcriptase
IFN $\gamma$	Interferon gamma
iPSC	Induced pluripotent stem cells
IPTG	Isopropyl $\beta$ -D-1-thiogalactopyranoside
KD	knockdown
kg	kilogram
KRT17	Keratin 17
KRT20	Keratin 20
l	litre
LINGO1	Leucine Rich Repeat And Ig Domain Containing Protein 1
LOX	Lipoxygenase
LSD	LT-Stabilization Domain
LT	Large T antigen
M	molar
MCC	Merkel cell carcinoma
MCPyV	Merkel cell polyomavirus
mg	milligram
MHC I	Major histocompatibility complex class I
miRNA	microRNA
ml	millilitre
mM	millimolar
mTORC	Mammalian target of rapamycin complex
MUR	MCPyV unique regions
NCCR	Non-coding control region
NCOA4	Nuclear receptor coactivator 4
NEMO	NF- $\kappa$ B essential modulator
ng	nanogram
NIC	Notch intracellular domain
NLS	Nuclear localization signal
nM	nanomolar
NOTCH (1-4)	Notch receptor (1-4)
NRN1	Neuritin 1
NRSN1	Neurensin 1
OBD	origin binding domain
OE	overexpression

PBS	Phosphate buffered saline
PCR	Polymerase chain reaction
PD-1	Programmed cell death protein 1
PD-L1	Programmed death-ligand 1
Pen/Strep	Penicillin/streptomycin
PI3K	Phosphoinositide 3-kinase
PP2A	Protein phosphatase 2A
PP4C	Protein phosphatase 4C
PUFA	Polyunsaturated fatty acid
qPCR	quantitative polymerase chain reaction
RB1	Retinoblastoma protein 1
RNA	Ribonucleic acid
ROS	Reactive oxygen species
Rosi	Rosiglitazone
RPLP0	Ribosomal protein lateral stalk subunit P0
RSL1	RheoSwitch ligand 1
RSL3	RAS-selective lethal 3
RT	Room temperature
shRNA	short hairpin RNA
SLC7A11	Solute carrier family 7 member 11
SLIT1	Slit Guidance Ligand 1
SOX 2	SRY-box transcription factor 2
SOX 9	SRY-box transcription factor 9
sT	Small T antigen
TA	T antigen
TBS	Tris buffered saline
TBS-T	Tris buffered saline - Tween 20
T/E	Trypsin/EDTA
TFR1	Transferrin receptor 1
TP53	Tumor protein p53
UV	Ultraviolet
V-ATPase	Vacuolar H <sup>+</sup> -ATPase
VP1	Viral protein 1
VP2	Viral protein 2
WT	Wild type
Z-VAD-FMK	Benzyloxycarbonyl-Val-Ala-Asp (OMe) fluoromethylketone

## **6.4 Copyright clearance**

Parts of this work were published in the following article as indicated in the thesis:

Artesunate Affects T Antigen Expression and Survival of Virus-Positive Merkel Cell Carcinoma. Sarma B, Willmes C, Angerer L, Adam C, Becker JC, Kervarrec T, Schrama D, Houben R. *Cancers (Basel)*. 2020 Apr 9;12(4). pii: E919. doi: 10.3390/cancers12040919.

The following figures used in this thesis were adapted or reused after obtaining permission from the respective publishers as mentioned in the respective figure legends:

- Figure 1: Schematic representation of the skin and location of epidermal stem cells. (a and b)
- Figure 3: Schematic representation of the MCPyV genome and its early region transcripts/proteins. (b and c)
- Figure 7: Important aspects of ferroptosis. (c)

## 6.5 Affidavit

I hereby confirm that my thesis entitled “**Merkel Cell Carcinoma: Investigations on its carcinogenesis and new therapeutic approaches**” is the result of my own work. I did not receive any help or support from commercial consultants. All sources and/or and materials applied are listed and specified in the thesis.

Furthermore, I confirm that this thesis has not yet been submitted as part of another examination process neither in identical nor in similar form.

---

Place, Date

---

Signature

### Eidesstattliche Erklärung

Hiermit erkläre ich an Eides statt, dass ich die Dissertation mit dem Titel „**Merkel Zellkarzinom: Untersuchungen zur Karzinogenese und neue Therapieansätze**“ eigenständig, d.h. insbesondere selbstständig und ohne Hilfe eines kommerziellen Promotionspartners angefertigt und keine anderen als die von mir angegebenen Quellen und Hilfsmittel verwendet zu haben.

Ich erkläre außerdem, dass die Dissertation weder in gleicher noch in ähnlicher Form bereits in einem anderen Prüfungsverfahren vorgelegen hat.

---

Ort, Datum

---

Unterschrift

## **6.6 Acknowledgements**

At first, I would like to thank my primary supervisors, Roland and David, for giving me the opportunity to pursue my PhD in tumor biology in the TBFL research group. I am also very thankful to Prof. Dr. med. Matthias Goebeler for having me as a part of the research unit of the University Skin Clinic in Würzburg. Moreover, I am grateful to Prof. Dr. med. Lars Dölken and PD Dr. Matthias Becker for agreeing to co-supervise my PhD thesis and for their valuable inputs at every group meeting.

Roland and David, it was a pleasure for me to be a part of your TBFL lab family. I appreciate the amount of effort and time that you invested to teach and to guide me. I thank you for your constant support throughout, especially during times when experiments would fail and tough decisions were to be made about our projects. Under your guidance, I was able to learn a lot from my PhD experience and thoroughly enjoyed this learning path. Roland, I also especially thank you for going over my PhD thesis in detail and for the advice on scientific writing. David, with immense patience, you taught me how to use not one but several softwares for processing my results, for which I am also very grateful. Moreover, life in the TBFL lab was more than just science. Roland, I enjoyed the darts competitions organized by you as well as the singing of Christmas carols before Winter holidays! All in all, the atmosphere in TBFL was a perfect mixture of science and fun which helped me learn in a relaxed manner.

Thank you Sonja, Eva and Lena for patiently showing me how every technique in the lab is performed. Sonja, you have been a pillar of support during my PhD. I owe you a big thank you for extending a helping hand and for performing several experiments. You had magic in your hands because experiments always worked when you would perform them! Your motivating words also made me do better at every step. Eva, thank you for making my very first PCR in the lab a success! It was fun to work by your side at the cell culture bench and it was definitely very easy to communicate with you at all times. Lena, your humorous nature and funny stories were perfect to bring a smile to my face. Thank you for showing me around the lab especially during my first few months there. Sabine, thank you for being so kind and cheerful and also for supporting me with my experiments whenever I needed help.

I am also very grateful to all the TBFL PhD students and master students with whom I had the pleasure to share my working time in the lab with. Kristina, you were my first office buddy and you made me very welcome and comfortable in my initial days in the lab. Thibault, not only did I learn a lot from you but we also had some really fun times in the lab especially because of your jokes! Clara, you were like a lab-sister as we would share all our successes and failures with each other and of course the short time you spent in the lab was very memorable for me. Laura, it was a good first experience for me to supervise you and I am very thankful to you for helping me out with my experiments. Marlies, with you as my lab office partner, you gave me the opportunity to practice my German and I definitely enjoyed the delicious cakes you

would bring to the lab! Fati and Tanzeela, although Corona restrictions made it complicated to socialize, it was very nice to get to know you, and Tanzeela to supervise you, towards the end of my PhD studies.

As our partners working on the same floor, I am thankful to the AG Schilling and AG Schmidt groups for sharing antibodies and reagents with me when required. Claudia, I'm glad I could communicate with you in my 'not yet perfect' German and thanks for helping me with those extra blotting chambers when I needed them! Simone, you helped me right from my starting days in the lab and were extremely friendly. I really enjoyed the scientific retreats we attended together and our weekly sports. Playing darts with you as well as with Marion, Jonas, and at times with Anne and Corinna was also a great way to take a pause from lab work! Thank you Christian, the king of the mice, for working with me as a team for our mice experiments and Lorenza, for the nice conversations while our Western blots would develop! I would also like to thank the AG Friedmann-Angeli group from the Rudolf-Virchow-Zentrum for sharing plasmids and antibodies with me.

At last, I would also like to thank my family and friends for their constant love and support and for standing by my side through every success and failure of mine.

## **6.7 Publication list**

- **Artesunate Affects T Antigen Expression and Survival of Virus-Positive Merkel Cell Carcinoma.** Sarma B, Willmes C, Angerer L, Adam C, Becker JC, Kervarrec T, Schrama D, Houben R. *Cancers (Basel)*. 2020 Apr 9;12(4). pii: E919. doi: 10.3390/cancers12040919.
- **Merkel Cell Polyomavirus T Antigens Induce Merkel Cell-Like Differentiation in GLI1-Expressing Epithelial Cells.** Kervarrec T, Samimi M, Hesbacher S, Berthon P, Wobser M, Sallot A, Sarma B, Schweinitzer S, Gandon T, Destrieux C, Pasqualin C, Guyétant S, Touzé A, Houben R, Schrama D. *Cancers (Basel)*. 2020 Jul 21; 12(7):1989 doi: 10.3390/cancers12071989.
- **Polyomavirus-positive Merkel cell carcinoma derived from a trichoblastoma suggests an epithelial origin of this Merkel cell carcinoma.** Kervarrec T, Aljundi M, Appenzeller S, Samimi M, Maubec E, Cribier B, Deschamps L, Sarma B, Sarosi EM, Berthon P, Levy A, Bousquet G, Tallet A, Touzé A, Guyétant S, Schrama D, Houben R. *J Invest Dermatol*. 2019 Nov 21. pii: S0022-202X(19)33387-1. doi: 10.1016/j.jid.2019.09.026. [Epub ahead of print]
- **Matrix Metalloproteinase-3 is Key Effector of TNF- $\alpha$ -Induced Collagen Degradation in Skin.** Mirastschijski U, Lupše B, Maedler K, Sarma B, Radtke A, Belge G, Dorsch M, Wedekind D, McCawley LJ, Boehm G, Zier U, Yamamoto K, Kelm S, Ågren MS. *Int J Mol Sci*. 2019 Oct 22;20(20). pii: E5234. doi: 10.3390/ijms20205234.
- **Histogenesis of Merkel Cell Carcinoma: A Comprehensive Review.** Kervarrec T, Samimi M, Guyétant S, Sarma B, Chéret J, Blanchard E, Berthon P, Schrama D, Houben R, Touzé A. *Front Oncol*. 2019 Jun 10;9:451. doi: 10.3389/fonc.2019.00451. eCollection 2019. Review.



